Title
Modern Methods of QCD Tomography for Electron-Ion Collder Phenomenology

Author
Terry, John David

Publication Date
2022

Peer reviewed|Thesis/dissertation

UNIVERSITY OF CALIFORNIA
Los Angeles

Modern Methods of QCD Tomography for Electron-Ion Collider Phenomenology

A dissertation submitted in partial satisfaction
of the requirements for the degree
Doctor of Philosophy in Physics

by

John Terry

2022

ABSTRACT OF THE DISSERTATION

Modern Methods of QCD Tomography for Electron-Ion Collider Phenomenology

by

John Terry
Doctor of Philosophy in Physics
University of California, Los Angeles, 2022
Professor Zhongbo Kang, Chair

Hadrons are the bound states of QCD and are a fundamental building block of nature. Through dedicated experimental and theoretical endeavors over the past century, the field of nuclear physics has begun to understand the three-dimensional structure of hadrons in momentum space, which is encoded in Transverse Momentum Dependent PDFs (TMD PDFs). To perform full three dimensional imaging within hadrons, one must note that TMD PDFs contain a mixture of perturbative and non-perturbative contributions. To de-couple these two contributions, theorists rely on factorization theorems, which allow us to write QCD cross sections as a convolution of a perturbative and non-perturbative contributions. Factorization theorems have long since been understood at leading power (LP) for Semi-Inclusive DIS, Drell-Yan, and double inclusive leptonic annihilation. With the use of these formalisms, in the past decade the imaging of the unpolarized quark TMD PDF has moved into an era of precision, where the perturbative contributions are close to N^4LL accuracy and non-perturbative extractions have been performed at the accuracy of NNLO+N^3LL. Despite this progress, many questions remain to be addressed in the field of TMDs. How does the introduction of spin affect the transverse dynamics of the quarks? What processes are optimal perform imaging of the gluons and how do we establish factorization theorems for these processes? How do we establish factorization theorems beyond LP? The interest in understanding the underlying structure of hadrons has led to the development of the Electron-Ion

Collider (EIC), a future facility which will allow us to measure the internal structure of protons at never before seen precision. Due to the high-luminosity, high center of mass energy, and precision beam control, this new facility opens the possibility of measuring spin-dependent TMDs in a wide range of new processes. Furthermore, the high luminosity open the possibility of performing high precision measurements of angular correlations which will allow us to probe the next-to-leading power (NLP) structure of hadrons.

To measure the spin-dependent structure of hadrons, experimental measurements are performed for azimuthal spin asymmetries. In this dissertation, I quantify the extent to which we understand the quark Sivers function, a spin-dependent TMD PDF, by performing the first ever global analysis of this function from Semi-Inclusive DIS and Drell-Yan. To allow for a future global analysis of the gluon Sivers asymmetry, I establish a factorization and resummation formalism for heavy-flavor di-jet production at the future EIC using Soft-Collinear Effective Theory (SCET). I then establish a factorization and resummation formalism for the Sivers asymmetry in di-jet production at RHIC and discuss how such a process can be used to test factorization breaking effects and the extent to which theorist understand the universality arguments of the Sivers function. Additionally, while spin asymmetries can be generated by the spin of initial-state particles, they also arise due to hadronization effect. However, probing the spin-dependent final-state hadrons introduces additional experimental complications associated with reconstructing the spin of the hadron. In the past several years, Λ baryons, which undergo self-analyzing decay, have been explored as a method of probing spin-dependent fragmentation functions. In this dissertation, I perform one of the first global analyses of the TMD Polarizing Fragmentation Function (TMD PFF) and the first global analysis of the transversity TMD FF. Using SCET, I establish a factorization and resummation formalism for the distribution of hadrons in a jet and use this formalism to make predictions at the EIC. Lastly, I perform direct calculations of the evolution equations of kinematic and intrinsic sub-leading twist distribution functions for the first time.

The dissertation of John Terry is approved.

Graciela B. Gelmini

Huan Z. Huang

E. Terry Tomboulis

Zhongbo Kang, Committee Chair

University of California, Los Angeles

2022

To Maria

Table of Contents

List of Figures

Preface

During my academic career, I have been very fortunate in terms of my advisors. Mostly I am thankful to my PhD advisor, Professor Zhong-Bo Kang. The majority of the field theory that I know originated from conversations with him. But I am also thankful for his patience, his kindness, his guidance, and his support for these past five years. I would also like to thank Professor Gerald Miller at the University of Washington. Jerry taught me how remarkable nuclear theory could be and has always supported me. I would like to thank Professor Dirk Bouwmeester at UCSB, who gave me my first research experience, who brought me to Leiden for a summer, and who inspired in me a love of quantum mechanics. Finally, I would like to thank Mr. Havard at Redlands High School for always challenging me to be a better mathematician.

I have also been very lucky in terms of my collaborators. First I'd like to thank Nobuo Sato and Alexei Prokudin for working with me when I was first starting out. The lessons that the two of you taught me early on served as proved to be fundamental skills in this dissertation. I'd like to thank Maarten Buffing for teaching me formal aspects of TMD physics. I'd also like to thank Miguel Echevarria for his guidance early on in my academic career. I'd like to thank Dingyu Shao for teaching me many aspects of effective field theory and resummation. I'd like to thank Hongxi Xing for his generosity as a collaborator. I would especially like to thank Leonard Gamberg and Jianwei Qiu for their support in my postdoc applications and for the professional guidance that they have so often given. Lastly, I would like to thank Chris Lee and Duff Neill for their support in my application to Los Alamos National Lab.

I'd also like to thank the many members of the UCLA physics department. My academic siblings, Jared Reiten, Fanyi Zhao, and Sasza Czajka, who have always been great friends, been supportive, and have also inspired me to be a better scientist. Additionally, I'd like to thank Kyle Lee, my academic great-uncle/uncle/brother, who always served as a role model in research and who has also been a good friend. I'd like to thank Steven Durr, Kevin Chen,

Dimitris Kosmopoulos, and Ji Zou for their friendship during the PhD program. I'd like to also thank the many UCLA undergrads that I had the pleasure of working with these past 5 years, namely Andrew Gordeev, Daniel Callos, Amanda Wei and Mishary Alrashed, for their hard work and dedication. The undergrads at UCLA always inspired me with their persistence and talent.

I'd also like to thank my friends and family who taught me many life lessons that served me during this academic journey. I like to thank my mother for teaching me that while life will be challenging, to be strong and to always find way to persevere. I'd like to thank Scott, who has the kindest heart of anyone that I know. You taught me the impact that kindness can make, which has always inspired me to try to be a good mentor to students. I'd like to thank my older sister Tabatha, who taught me to think independently and to always raise questions. I'd like to thank my older brother Tim for always looking out for me growing up. I'd like to thank my younger brother Adam, who inspired me to do better in life and who has always helped me to take care of our family. I'd like to thank my youngest brother Matthew, who showed me how rewarding caring for someone could be. Lastly and most importantly, I'd like to thank Maria, whose kind heart, patience, and support taught me to love.

Lastly, there are many friends that I would like to thank. I'd like to thank Jordan Grace for convincing me to change my major from bio-med to physics. I'd also like to thank Chris Snapp-Kolas and Jordan Grace for their many years of friendship and support while we learned math and physics, and also while we played chess and Fortnite during Covid. I'd like to thank Paul Steward, and Christian Willis, and especially Dr. George Phandthong for their support and friendship while I was in college. I'd like to thank Chris Morton, Oliver Keane, Kait Cunningham, Gladys Ferrero Sanchez, Jeremiah Baca, Kati Nguyen, Kimia Nader, and Kyle Evans for their friendship and support for Maria and myself during our PhD programs.

Curriculum Vitae

2013 – 2015	B.S. in Physics, University of California, Santa Barbara
2016 – Present	Ph.D. Student in Physics University of California, Los Angeles
2022 – 2025	Postdoctoral Scholar T-2 Division, Los Alamos National Lab
07/2018 – Present	National Science Foundation Graduate Research Fellow
10/2021 – Present	UCLA Dissertation Year Fellow
09/2022	Director's Fellow, Los Alamos National Lab

Publications

M. Alrashed, D. Anderle, Z.-B. Kang, J. Terry and H. Xing, Nuclear Modified Transverse Momentum Distributions and 3D Imaging in Nuclei, in 24th International Symposium on Spin Physics, 3, 2022, 2203.09112.

Z.-B. Kang, J. Reiten, D. Y. Shao and J. Terry, Resummation of the Sivers asymmetry in heavy flavor dijet production at the Electron-Ion Collider, SciPost Phys. Proc. 8 (2022) 175, [2108.07257].

Z.-B. Kang, J. Terry, A. Vossen, Q. Xu and J. Zhang, Transverse Lambda production at the future Electron-Ion Collider, Phys. Rev. D 105 (2022) 094033, [2108.05383].

M. Alrashed, D. Anderle, Z.-B. Kang, J. Terry and H. Xing, Three-dimensional imaging in nuclei, 2107.12401.

R. Abdul Khalek et al., Science Requirements and Detector Concepts for the Electron-Ion Collider: EIC Yellow Report, 2103.05419.

L. Gamberg, Z.-B. Kang, D. Y. Shao, J. Terry and F. Zhao, Transverse Lambda polarization in e+ e- collisions, Phys. Lett. B 818 (2021) 136371, [2102.05553].

Z.-B. Kang, J. Reiten, D. Y. Shao and J. Terry, QCD evolution of the gluon Sivers function in heavy flavor dijet production at the Electron-Ion Collider, JHEP 05 (2021) 286, [2012.01756].

M. G. Echevarria, Z.-B. Kang and J. Terry, Global analysis of the Sivers functions at NLO+NNLL in QCD, JHEP 01 (2021) 126, [2009.10710].

Z.-B. Kang, K. Lee, D. Y. Shao and J. Terry, The Sivers Asymmetry in Hadronic Dijet Production, JHEP 02 (2021) 066, [2008.05470].

D. Callos, Z.-B. Kang and J. Terry, Extracting the transverse momentum dependent polarizing fragmentation functions, Phys. Rev. D 102 (2020) 096007, [2003.04828].

Z.-B. Kang, K. Lee, J. Terry and H. Xing, Jet fragmentation functions for Z-tagged jets, Phys. Lett. B 798 (2019) 134978, [1906.07187].

Z.-B. Kang, A. Prokudin, N. Sato and J. Terry, Efficient Fourier Transforms for Transverse Momentum Dependent Distributions, Comput. Phys. Commun. 258 (2021) 107611, [1906.05949].

J. D. Terry and G. A. Miller, Meaning of the nuclear wave function, Phys. Rev. C 94 (2016) 014002, [1603.07032].

CHAPTER 1

Introduction

1.1 Motivation

Quantum tomography is the study of the dynamics of elementary particles in bound systems, and seeks to address the question as to how these dynamics give rise to global properties. This goal is the field theoretical continuation of the millennia old pursuit to address the nature of matter. It can be argued that quantum tomography began in 1897, when J.J. Thompson discovered the electron. Within the next decade, the scientists of the early 20th century began endeavoring to understand how the properties of the electron were tied to the structure of the Hydrogen atom. To address this question, scientists were forced change their perception of small scale physics and quantum mechanics was born. Schrodinger, who was exploring the wave nature of non-relativistic particles, solved this puzzle and changed our understanding of the world. To this day, technological and scientific advancements related to these discoveries influence our society. Due to the developments of our understanding of Quantum Field Theory (QFT) and the standard model in the last century, the scientist of today continue to address the structure of matter by asking the question as to how the dynamics of the point-like constituents of hadrons are related to the hadron's global properties.

Quantum tomography of hadrons is infinitely more complex than atomic tomography. Electrons can be isolated from atoms and their properties can be measured by introducing electromagnetic fields. However, no experiments have been able to measure isolated charges associated with the strong interaction. This 'color confinement' indicated that the size of the coupling constant associated with the strong interaction was so large that perturbative

techniques could not be used to address the theory. By the late 1960s however, Bjorken predicted that structure functions in DIS at sufficiently high energies should depend on the ratio $x = Q^2/2P \cdot q$ in Ref. [14]. Within the next year, SLAC verified this approximation and Feynman presented his formulation of the parton model in Ref. [15], in which he illustrated that Bjorken scaling indicated that hadrons were composed of point-like non-interacting particles, which he named 'partons'. However, this theory conflicted with our understanding that hadrons were strongly coupled. Ultimately in Ref. [16] Gross and Wilczek discovered that non-Abelian gauge theories give rise to 'asymptotic freedom', which states that while the coupling for non-Abelian gauge theories can be large at small energy scales, at large energy scales the coupling decreases and perturbative techniques become feasible. This remarkable work served to bridge Feynman's parton model with color confinement. While partons exist as asymptotically free particles, the non-perturbative interactions form the asymptotic color neutral states of QCD which we call hadrons.

This formulation of the strong interaction indicated that perturbative techniques in QCD can be used to calculate partonic cross sections. But to perform precision QCD, one is forced to address the question as to whether or not non-perturbative interactions could drastically affect purely perturbative contributions to the cross section. After ten years of work, the authors Collins, Soper, and Sterman carried out the first proof of 'QCD factorization' in Ref. [17], in which the perturbative and non-perturbative contributions are proven to decouple from one another. Using their formalism, cross sections could be written as a convolution of perturbative and non-perturbative contributions. Since their demonstration of factorization theorems, the methodology for quantum tomography of hadrons has relied on their analysis. Modern day theorists calculate perturbative contributions to cross sections and then either extract the non-perturbative contributions from lattice or fit experimental data. This procedure allows us being understanding the dynamics of the non-perturbative contributions to the cross sections.

The ultimate goal of QCD tomography is to address the question as to how the global quantities of hadrons, such as the hadron's mass and spin, emerge from the dynamics of

quarks and gluons. As hadrons account for the vast majority of the mass of the visible universe, addressing such a question is vital for our greater understanding of the universe. A fundamental shortcoming of previous theoretical descriptions of hadron structure is that they only provide information longitudinal to the beam direction. The field of QCD holography has been pushing for more differential measurements of the internal structure of the hadrons. The full information for the distributions of hadrons in momentum space and impact parameter space is encoded in Generalize Transverse Momentum Distribution Functions (GTMDs), see for instance Refs. [18, 19, 20, 21, 22, 23, 24]. Within the past few years, researchers have been exploring QCD factorization theorems which can be used to probe these distributions in [25, 26, 27, 28, 29, 30, 31, 32]. Transverse Momentum Dependent Parton Distribution Functions (TMD PDFs), are GTMDs in which the impact parameter space has been integrated over. A major strength of TMD PDFs are that factorization theorems for TMDs have been established in double inclusive hadron production in leptonic annihilation in [17], Drell-Yan in [33], and Semi-Inclusive DIS in [34]. These TMD PDFs allow us to address how the spin of the parent hadron distorts the distribution of momentum in hadrons. As a result, TMDs are an attractive distribution to understand how the spin properties of the hadron and the transverse dynamics are correlated with one another.

Following the endorsement by the National Academy of Sciences, the Department of Energy officially started the Electron-Ion Collider (EIC) project in 2020. This high-energy, high-luminosity, polarized EIC will allow physicists to perform measure the both polarized and unpolarized TMDs at unprecedented precision. Due to the high collision energies, this device will allow physicists to measure the gluon TMD PDFs, while previous colliding facilities have mainly measured quark TMD PDFs. The high luminosity, high center of mass energy, and freedom to use polarized beams at the EIC will open new possible avenues for probing hadron structure. To interpret experimental data, QCD theorists rely on factorization theorems, in which the perturbative and non-perturbative contributions in a cross section decouple from one another. As such, the methodology of this dissertation has been to use existing data to extract non-perturbative information associated with the polarized

hadron structure at the highest precision possible, to establish factorization theorems for novel processes, to calculate the perturbative contributions to novel processes, and to provide first predictions for this new facility.

1.2 Organization of this Thesis

In Chapter 2, formal background in QCD is provided. In Chapter 3, I perform the first global extraction of the quark Sivers function, a spin-dependent TMD PDF. I also perform this analysis at NLO+NNLL resummation, which had never been done before. Using this analysis, I provide high precision projections at the future EIC. In Chapter 4, I use SCET to derive factorization and resummation formalisms which can be used to probe the spin-dependent structure of the proton using jets. In Chapter 5, I perform one of the first global extractions of the TMD Polarizing Fragmentation Function (TMD PFF) and the transversity TMD FF, two spin-dependent fragmentation function, and perform an EIC impact study for these distributions. In Chapter 6, I derive QCD evolution equations for sub-leading TMDs. I'll conclude this dissertation in Chapter 7.

CHAPTER 2

QCD Background

2.1 Overview of Factorization and Resummation

The major obstacle in QCD tomography is that while perturbation theory can be used to describe partonic interactions, detectors measure physical quantities of hadrons. To describe and interpret experimental data, one then needs to understand how to transition between partons and hadrons. However, this transition involves interactions at the energy scale $\Lambda_{\rm QCD}$ where perturbative techniques fail. To address this issue, QCD factorization theorems must be established. The central idea behind factorization theorems is that if the partonic scale Q is much larger than $\Lambda_{\rm QCD}$, the relevant time scale for hard interactions happen is much smaller time scale than the time scale for inter-partonic interactions. We could examine Deep Inelastic Scattering (DIS) as an illustrative example, $e\left(\ell\right) + p\left(P\right) \rightarrow e\left(\ell'\right) + X$. In this process, the two relevant scales are Q, the virtuality of the photon, and $\Lambda_{\rm QCD}$ which is associated with the interaction between partons in the hadron. In the laboratory frame, the proton is stationary and the relevant time scale for the interaction of partons in the target hadron is therefore $1/\Lambda_{\rm QCD}$. The photon on the other hand has virtuality Q, and thus the interaction time scale for the photon with the parton is $1/Q$. In the rest frame of the virtual photon, the hadron moves toward the photon with an energy Q. If $Q \gg \Lambda_{\rm QCD}$, the lifetime of the partons, which were of order $1/\Lambda_{\rm QCD}$, undergo time dilation and are therefore extended. As a result, up to power corrections of order $\Lambda_{\rm QCD}/Q$, the partons which are resolved by the virtual photon are on their mass shell. The central idea behind factorization theorems is to treat the particles which communicate information between the hard and soft regions to be on shell and therefore classical. In doing so, the hard and soft regions are insensitive

to the dynamics driven by the quantum corrections of the other region. As we still need to integrate over the classical momentum of the particle which communicated the information between the two regions, the factorization theorem for DIS can be written in the usual way as

$$\frac{d\sigma_{\rm DIS}}{dx\,dy} = \sum_a \int d\hat{x}\, f_{a/p}\left(\hat{x};Q;\mu\right) \frac{d\hat{\sigma}_{\rm DIS}}{dy}\left(\frac{x}{\hat{x}};\mu\right) + \mathcal{O}\left(\frac{\Lambda_{\rm QCD}}{Q}\right) . \tag{2.1}$$

In this expression x is the usual Bjorken variable associated with the longitudinal momentum component of the quark, Q is the virtuality of the photon, y is related to the angle of the final state quark, and μ is the renormalization scale. $f_{a/p}$ is the PDF, which we will find contains a mixture of interactions at long and short distance interactions. The purely short time scale interaction is given by $d\hat{\sigma}_{\rm DIS}/dy$, which represents the partonic interaction of a quark and lepton. Within factorization theorems, the short distance interactions can be computed in perturbative QCD, while the long distance interactions are obtained through lattice methods or by fitting experimental data.

QCD factorization theorems also introduce the property of 'universality'. This immensely powerful property states that for processes which are factorized, the non-perturbative information encoded in the PDFs is independent of the underlying process. All the predictive power and discovery potential of QCD is built upon this property. In the case of DIS, the simple relation between the DIS cross section and the PDF allows one to extract the non-perturbative information of the PDFs in a clean way. However, to discover physics at high energy scales, processes with high energies are required. In the case of DIS, synchrotron radiation prevents high energy electron beams from reaching high enough energies to probe the high energy region. For this reason, proton-proton collisions serve as the main mechanism for discovering new physics. For this reason, Drell-Yan, $p_1(P_1)\,p_2(P_2) \to q(q)$ represents the main QCD background for many events. Neglecting power corrections, the factorized expression for the Drell-Yan cross section can be written as

$$\frac{d\sigma_{\rm DY}}{dy\,dQ^2} = \sum_{a,b} \int_{x_A}^1 d\hat{x}_A \int_{x_A}^1 d\hat{x}_B\, f_{a/p}\left(\hat{x}_A;Q,\mu\right)\, f_{b/p}\left(\hat{x}_B;Q,\mu\right)\, \frac{d\hat{\sigma}_{\rm DY}}{dy\,dQ^2}\left(\frac{x_A}{\hat{x}_A},\frac{x_B}{\hat{x}_B};Q,\mu\right) , \tag{2.2}$$

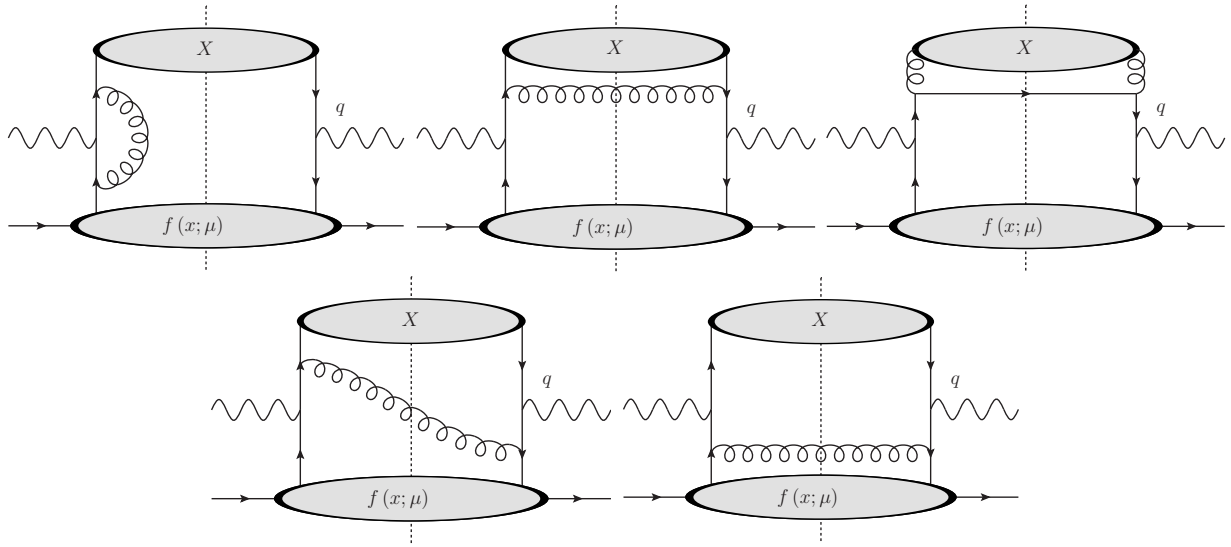

Figure 2.1: Top row: Example hard correction to the cross section. Bottom Row: Diagrams related to the evolution of the PDF.

where y and Q represent the rapidity and invariant mass of the produced vector boson. The Bjorken variables of the PDFs are related to the Q, and y, and the hadronic COM energy through the relations

$$x_A = \frac{Q}{\sqrt{S}} e^{y}\,, \qquad x_B = \frac{Q}{\sqrt{S}} e^{-y}\,. \tag{2.3}$$

Due to the principle of universality, the PDFs which enter into the cross section for Drell-Yan are identical to those in DIS. Therefore, global fits from DIS data can be used to obtain the precise non-perturbative behavior of PDFs. These extracted PDFs can then be used to describe the QCD background at high energy Drell-Yan collisions. In this way, QCD factorization theorems and universality drive the predictive power and discovery potential of QCD.

An important and yet overlooked detail in going from low energy data to high energy data is the role of effects associated with renormalization. In both the case for Drell-Yan and DIS, the PDFs and the partonic cross sections will suffer from divergences beyond tree level. In Fig. 2.1, a subset of the total one loop corrections to the DIS cross section have been included. There are two possible approaches for dealing with these divergences. In one case, the divergences of all the diagrams are added. Due to renormalization group

consistency, the divergences will cancel and the PDF and partonic cross sections can be defined as subtracted quantities. One could then simply replace the renormalization scale μ with the hard scale Q. There are many shortcomings of this procedure, however. Firstly if there are additional scales entering into the cross section, large logarithms that enter into the perturbative expressions will destroy the convergence of the perturbative series. Secondly, to describe the cross section in this way, one needs the behavior of the PDF at exactly Q. Thus for each value of Q, a new global fit would need to be performed. Fortunately the alternative to this approach is much more powerful. In this case, each loop integral can be written as a sum of contributions from the collinear and hard regions. The collinear contributions are used to define the perturbative part of the PDF and the hard contributions are the loop corrections to the partonic cross section. Each contribution will suffer from divergences and the PDF and the partonic cross section are then defined as divergent quantities. We can then perform renormalization group evolution of these divergent quantities and obtain QCD evolution equations. By using this method, we can resum any large logarithms that enter from radiative corrections to all orders. This procedure allows us to understand how the PDF and partonic cross section evolve to arbitrary μ. As a result, a single global analysis provides substantially more information than in the previous case. In Sec. 2.5, I will outline this procedure for the TMD case in Drell-Yan.

2.2 Pinch Surfaces and the QCD Mode Analysis

Bound partons within hadrons interact with one another, driving one another off their mass shell and generating inter-parton correlations. In the previous section, I discussed how time dilation of boosted hadrons extended the lifetime of these off shell modes. As a result, QCD factorization theorems are valid up to power corrections of $\Lambda_{\rm QCD}/Q$. While this simple picture provides intuition for QCD factorization theorems, in this section, I will provide a more rigorous mathematical formalism for this treatment following the work of Collins, Soper, and Sterman. Within this treatment, the authors treated loop integrals as contour integrals. IR poles arose in their analysis through the appearance of 'pinch singular surfaces', in which

contours could not be deformed away from poles entering into the complex plane. By characterizing the kinematic regions where these pinch surfaces arose, the authors were able to demonstrate that pinch surface singularities were generated by soft and collinear interactions, which are both on shell. The authors then demonstrated that the asymptotic contribution of the cross section emerge from the dynamics of these on-shell modes. Thus these authors provided a mathematical framework verifying the intuition for the factorization theorem. In this section, I will review the appearance and interpretation of these IR divergences.

For this analysis, I will use the virtual diagram in Fig. 2.1 as an illustrative example. Furthermore, to simplify the calculations, I will treat the quarks and gluons as scalar fields. Using Feynman parameters, the expression for the vertex can be written as

$$\Gamma(p_1, p_2) = i\pi^2 \int_0^1 d\alpha_1\, d\alpha_2\, d\alpha_3 \int \frac{d^4 l}{(2\pi)^4} \frac{\delta\left(1 - \alpha_1 - \alpha_2 - \alpha_3\right)}{\left[\alpha_1 l^2 + \alpha_2 \left(p_1 + l\right)^2 + \alpha_3 \left(p_2 - l\right)^2 - i\epsilon\right]^3} \,. \tag{2.4}$$

The asymptotic behavior of this integral is obtained by finding the kinematic regions in l where the denominator is minimized. This can be obtained by setting the gradient of the denominator with respect to l^μ to zero, which leads to the Landau equation from Ref. [35]

$$\alpha_1 l^\mu + \alpha_2 \left(p_1 + l\right)^\mu - \alpha_3 \left(p_2 - l\right)^\mu = 0 \,. \tag{2.5}$$

Two particular regions which satisfy this condition are the collinear and anti-collinear regions: where the gluon becomes collinear to the incoming or outgoing quarks. For the case of the incoming quark, the Landau condition will hold where $l^\mu = \zeta p_1^\mu$, $\alpha_3 = 0$, and $\alpha_1 \zeta = -\alpha_2 \left(1 + \zeta\right)$. In this case, the denominator of the vertex is proportional to the mass of the incoming quark. In general, the incoming quark can have a non-zero virtuality. However, one would need to integrate over the quark mass to obtain the full QCD amplitude. Thus the asymptotic contribution of the cross section is obtained in the neighborhood in which the mass of the quark and virtual gluon vanishes. As the incoming quark is close to its mass shell and the plus component of the momentum is large, the momentum of the incoming quark scales as

$$p_1^\mu \sim Q\left(\frac{\bar{n}^\mu}{2} + \lambda^2 \frac{n^\mu}{2} + \lambda \hat{x}^\mu + \lambda \hat{y}^\mu\right) = Q\left(1_+, \lambda_-^2, \lambda_\perp\right) \,. \tag{2.6}$$

In this expression, I have introduce the light-cone directions $n^\mu = \hat{t} - \hat{z}$, $\bar{n}^\mu = \hat{t} + \hat{z}$ and taken the normalization $n \cdot \bar{n} = 2$. Furthermore, $\hat{t}^\mu$, $\hat{x}^\mu$, $\hat{y}^\mu$, $\hat{z}^\mu$ are unit four vectors. In the expression for the scaling of the momentum p_1^μ, I have introduced the parameter $\lambda = M/Q$ where M is the mass of the incoming hadron. This scaling can be thought of as follows: the plus component is fixed to be large while there is some freedom for the transverse momentum of the incoming quark. In general, the transverse momentum will affect how close the integration gets to the appearance of the collinear IR divergence. Since singularities occur for all values $0 < \zeta < 1$, one would need to integrate over all values of ζ. Furthermore, while the collinear IR pole emerges as $l_\perp \to 0$, to obtain the asymptotic behavior of the cross section, one would need to integrate over the region $0 < l_\perp < \lambda Q$. For this reason, Collins frequently refers to these pinch surfaces as 'skeletons' of the integrals, see Ref. [36]. They provide the overall structure by not the full picture.

Another IR divergence occurs where the components of l^μ are much smaller than Q such that $p_1^\mu + l^\mu \sim p_1^\mu$ and $p_2^\mu + l^\mu \sim p_2^\mu$ so that the interaction of the soft gluons with the collinear quarks leaves the quarks on their mass shell up to power corrections. To satisfy these conditions, the required scaling for the soft gluon is $l^\mu \sim Q\,(\lambda^2, \lambda^2, \lambda^2)$. This scaling is is known to give rise to the soft eikonal approximation. In this case, the denominator of the vertex will depend only on l^2 and an IR pole will once again be generated for a gluon which is on its mass shell. Analogous to the collinear case, the asymptotic behavior of the soft contribution is obtained by integrating a region of l^μ, namely $l^2 < Q^2\lambda^4$.

In Ref. [37], Coleman and Norton interpreted this analysis to indicated that the dominant contributions from the cross section enter from on shell partons. As a result, information is passed from the collinear and soft regions to the hard region only through classical particles. Therefore, the complicated quantum corrections associated with collinear and soft interactions are then decoupled from the quantum corrections of the hard region. Furthermore, since the soft particles do not take the collinear particles off their mass shell, the soft and collinear contributions also decouple from one another. As a result, each region evolves independently. The breaking of factorization effects occur due to off shell propagators entangle these differ-

ent kinematic regions. While so far I have discussed how soft and collinear regions generate IR divergences, there is one additional region which can generate IR divergences, known as the Glauber region. Glauber gluons have momenta which scale as $l^\mu \sim Q\left(\lambda^2, \lambda^2, \lambda\right)$, which are off shell and therefore can break factorization theorems. The proof of the cancellation of Glaubers has been performed for TMD factorization in Drell-Yan, Semi-Inclusive DIS and double inclusive leptonic annihilation (DIA), see for instance Refs. [38, 39, 40]. For many processes however, Glauber cancellation has not been explicitly verified. Even more dramatically, Glauber gluons are known to drive the dynamics involved in parton propagation through QCD media, such as the Quark-Gluon-Plasma (QGP), cold nuclear matter, and the Color-Glass Condensate (CGC). In these systems, the media become entangled with the partonic cross section. Recently the paradigm has been to treat this coupled behavior as an open quantum system in Refs. [41, 42]. This gives rise to Lindblad equations, or equivalently the BK equation, see for instance Ref. [43]. Due to the interest in understanding media effects, Glauber gluons remains an active area of research. In fact, several effective field theories have been developed in this direction, see for instance Refs. [44, 45, 46] For the remainder of this thesis however, Glauber gluons will not be treated.

So far, I have demonstrated that the vertex graph contains IR divergences, which contains part of the asymptotic behavior of the vertex integral. However, if the IR divergences were left uncancelled, the differential cross section would be sensitive to the mass of the partons, which is not physical as the mass scale of the quarks is much smaller than the Λ_{QCD}. As a result, there must be additional contributions to this vertex which have so far not been calculation. We saw however, that these divergences originate from the soft and collinear regions. As a result, the appearance of IR divergences provide us some insight as to which QCD modes need to be considered in our formulation of QCD factorization theorems. Namely to formulate the cross section for DIS, one also needs to consider the contributions from the soft and collinear regions. In the following section, I will demonstrate this.

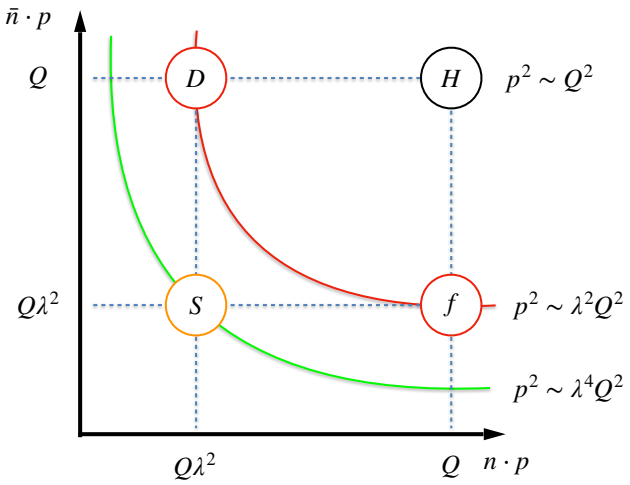

Figure 2.2: Organization of modes entering into the example according to their scaling in $n \cdot p$, $\bar{n} \cdot p$, and their invariant masses.

2.3 The Method of Regions

To calculate the soft, collinear, and hard contributions to the vertex, I will closely follow the analysis that was performed in Ref. [47] to use the method of regions from Refs. [48, 49], where the asymptotic behavior of the loop integrals is obtained by expanding the integrand in each area which gives a large contribution. This method is related to the integration over the pinch surfaces. Namely by asymptotically expanding the integrand, we capture the asymptotic behavior around the pinch surfaces. To demonstrate the delicate cancellation between IR and UV divergences, I will use a simple model which treats the quarks as massive scalars and treats the gluon as massless.

To obtain the hard contribution to the cross section, we assume that the virtuality of the gluon goes like Q^2 and that the virtuality of the quarks goes like $\lambda^2 Q^2$ from the power counting in the previous section. To obtain the asymptotic behavior of the loop integral in this region, we retain only the leading power behavior in the denominator. In this region, the asymptotic behavior of the vertex is therefore given by

$$\Gamma_h(p_1, p_2) = i\pi^{d/2}\mu^{4-d} \int \frac{d^d l}{l^2\,(l^2 + 2p_1 \cdot l)\,(l^2 - 2p_2 \cdot l)}\,. \tag{2.7}$$

The behavior of this integral in the soft and collinear limits is the same as the massless loop

integral in the previous section and therefore gives rise to IR divergences in those regions. This loop integral can be easily performed using a Passarino-Veltman reduction, the exact expression is obtained as

$$\Gamma_h(p_1,p_2) = \frac{\Gamma(1+\epsilon)}{Q^2}\left(\frac{1}{\epsilon^2}+\frac{1}{\epsilon}\ln\left(\frac{\mu^2}{Q^2}\right)+\frac{1}{2}\ln^2\left(\frac{\mu^2}{Q^2}\right)-\frac{\pi^2}{6}\right), \tag{2.8}$$

where the ϵ enter from the IR poles.

To obtain the contribution in the soft region, l^μ is taken to scale as $Q(\lambda^2,\lambda^2,\lambda^2)$. Expanding the denominator and retaining only the leading terms, the integrand becomes

$$\Gamma_s(p_1,p_2) = i\pi^{d/2}\mu^{4-d}\int \frac{d^dl}{l^2(p_1^2+2p_1\cdot l)(p_2^2-2p_2\cdot l)}. \tag{2.9}$$

This expression is one graph that enters into the 'soft function', which contains the soft contribution to the differential cross section. From this expression, several interesting features can be observed. Note that the invariant mass of the virtual gluon is of order λ^4 while the invariant mass of the external quarks are of order λ^2. As a result, as l approaches zero, the terms associated with the quark masses regulate the IR divergences. In the UV region however, where the virtuality of the gluon becomes larger, the denominator will scale as l^4, giving rise to a UV divergence. This UV divergence can be regarded as the hard contributions contaminating the soft contributions. Furthermore, in principle one would also need to deal with soft contamination into the collinear and anti-collinear regions. I will cover this later when I discuss 'rapidity renormalization group evolution'. The expression for the soft contribution to the vertex integral is given by

$$\Gamma_s(p_1,p_2) = \frac{\Gamma(1+\epsilon)}{Q^2}\left(\frac{1}{\epsilon^2}+\frac{1}{\epsilon}\ln\left(\frac{\mu^2}{Q^2\lambda^4}\right)+\frac{1}{2}\ln^2\left(\frac{\mu^2}{Q^2\lambda^4}\right)+\frac{\pi^2}{6}\right). \tag{2.10}$$

In this expression, the ϵ are associated with UV divergences. I would like to also note that in this expression, a large logarithm enters into the finite part. These large logarithms can in principle become so large that they spoil the convergence of perturbative calculations. These large logarithms can handled through resummation which I will cover in Sec. 2.5.

The expressions for the collinear and anti-collinear contributions to the vertex interaction

can be obtained in a similar way. In the collinear sector, the cross section is given by

$$\Gamma_c(p_1,p_2) = i\pi^{d/2}\mu^{4-d}\int \frac{d^dl}{l^2\left(p_1-l\right)^2\left(2p_2\cdot l\right)}\,. \tag{2.11}$$

I note at this point, that this interaction is exactly a Wilson line interaction which enters into the calculation for the DGLAP evolution equations. By studying this integral, we can see that there is a UV divergence that appears as the virtuality of the gluon grows large and there are potentially also IR divergences associated with moving into the region where the virtuality grows small. These regions represent the two contribution associated with collinear gluons contaminating the hard and soft regions, respectively. The expression for the collinear and anti-collinear contributions is given by

$$\Gamma_c(p_1,p_2) = \frac{\Gamma\left(1+\epsilon\right)}{Q^2}\left(-\frac{1}{\epsilon^2}-\frac{1}{\epsilon}\ln\left(\frac{\mu^2}{\lambda^2}\right)-\frac{1}{2}\ln^2\left(\frac{\mu^2}{\lambda^2}\right)+\frac{\pi^2}{6}\right)\,. \tag{2.12}$$

$$\Gamma_{\bar{c}}(p_1,p_2) = \frac{\Gamma\left(1+\epsilon\right)}{Q^2}\left(-\frac{1}{\epsilon^2}-\frac{1}{\epsilon}\ln\left(\frac{\mu^2}{\lambda^2}\right)-\frac{1}{2}\ln^2\left(\frac{\mu^2}{\lambda^2}\right)+\frac{\pi^2}{6}\right)\,, \tag{2.13}$$

where we once again see the appearance of large logarithms.

Since we have performed these integrals using dimensional regularization, we have introduced the scale μ, which serves as a cutoff between modes of different virtuality, see for instance Fig. 2.2. For the method of regions to accurately produce the full contribution of the loop vertex, it must not depend on the scale μ. Furthermore, since we have introduced masses to regularize the IR divergences of the full vertex, the full vertex must be free of both UV and IR divergences. After summing the contributions of each region, the total vertex contribution is given by

$$\Gamma(p_1,p_2) = \frac{1}{Q^2}\left(\ln\left(\frac{Q^2}{\lambda^2}\right)\ln\left(\frac{Q^2}{\lambda^2}\right)+\frac{\pi^2}{3}\right)\,, \tag{2.14}$$

which satisfies these two criteria.

I note that in principle the cancellation of the UV and IR divergences in full QCD is much more delicate than this simple model. In general the IR divergences in the virtual diagrams must cancel against the UV divergences entering into the virtual emissions. Thus

the cancellation will not involve just one of the diagrams in Fig. 2.1 but all of them. However, this model serves to demonstrate the intuition associated with performing calculations associated with each region and the appearances of divergences. To be precise, in deriving factorization theorems, we first catalog the different QCD modes. We can then calculate the contribution of each mode using the method of regions and dimensional regularization which introduces a scale μ in the virtuality. Overlap between the various regions enters as divergences which cancel when we have summed over the contributions of the different modes. While I have demonstrated this procedure works at NLO, so long as the observable is infrared and collinear safe, the KLN theorem [50, 51, 52] guarantees the cancellation of the IR divergence to all orders.

2.4 Soft-Collinear Effective Theory

2.4.1 SCET Lagrangian

While the asymptotic behavior of the loop integrals in the previous sections are dominated by the soft and collinear regions, the QCD Lagrangian takes into consideration all possible momenta configurations. In this sense, QCD contains more information than what is required to describe many processes. Effective field theories (EFTs) are a field theoretical language which formulate the Lagrangian of a system to only contain the asymptotic degrees of freedom. Heavy quarks for instance can be neglected when describing collisions with energies below the quark mass. In a path integral formulation, the fluctuations associated with the heavy quark field are 'integrated out'. Soft-Collinear Effective Theory (SCET), Refs. [53, 54, 55, 56, 57, 58, 59] is an EFT that contains the degrees of freedom associated with soft and collinear QCD modes and integrates out the contributions from outside regions. Due to this simplification, SCET allows us to organize and calculate perturbative contributions to high perturbative accuracy. In this section, I will provide an overview of the key features of SCET.

By integrating out fields with momenta scaling outside of the soft and collinear regions,

the fields which enter into the Lagrangian reduce to

$$A^{\mu}(x) = A_c^{\mu}(x) + A_s^{\mu}(x) \;, \qquad \psi(x) = \psi_c(x) + \psi_s(x) \;, \tag{2.15}$$

where the c subscript denotes fields with momenta that scale as $Q(1, \lambda^2, \lambda)$ while the subscript s denotes fields with momenta that scale as $Q(\lambda^2, \lambda^2, \lambda^2)$. To arrive at this expression, I have assumed that there is only one collinear mode for simplicity. In processes with energetic modes in another direction, one would simply need to add additional modes to the right side of these expressions. A key feature of these replacements are that Glauber modes, which provide asymptotic behavior for processes with QCD media and which break QCD factorization theorems, are not considered. In general SCET is useful for processes in which Glauber contributions have been demonstrated to vanish. After integrating out the modes beyond the collinear and soft regions, the number of degrees of freedom for the system can be further reduced through the equations of motion. Namely the quark spinors can be projected into two subspaces as follows

$$\psi_c(x) = \left(\frac{\bar{\not{n}} \not{n}}{4} + \frac{\not{n} \bar{\not{n}}}{4} \right) \psi_c(x) = \xi_c(x) + \varphi_c(x) \,.$$

Through the equations of motion of the ξ field, the φ field can be integrated out.

SCET also systematically removes sub-leading field contributions to the Lagrangian. In the formulation of SCET, it is then necessary to obtain the precise power counting associated with each field. The power counting of the ξ_c field for instance can be obtained by examining the two point correlation functions

$$\begin{aligned} \left\langle 0 \left| T\left\{ \xi_c(x)\, \bar{\xi}_c(0) \right\} \right| 0 \right\rangle &= \int \frac{d^4p}{(2\pi)^4} \frac{i}{p^2 + i\epsilon} e^{-ip\cdot x} \frac{\bar{\not{n}} \not{n}}{4} \not{p} \frac{\not{n} \bar{\not{n}}}{4} \\ &= \int \frac{d^4p}{(2\pi)^4} \frac{i}{p^2 + i\epsilon} e^{-ip\cdot x} p^+ \frac{\bar{\not{n}}}{2} \sim \lambda^2 \,. \end{aligned} \tag{2.16}$$

Performing the same procedure for the soft quark field, we obtain the power counting $\psi_s \sim \lambda^3$. The power counting for the gluons depends on the choice of gauge. The traditional formulation of SCET is done using covariant gauges and have scaling $A_c^{\mu} \sim p_c^{\mu} \sim Q(1, \lambda^2, \lambda)$ and $A_s^{\mu} \sim p_s^{\mu} \sim Q(\lambda^2, \lambda^2, \lambda^2)$ in which Lorentz invariance manifests naturally. We can see

from the scaling of the soft modes that the soft gluons vary in minus and transverse direction more slowly than the collinear gluons.

After integrating out the fields and using the power counting, the SCET Lagrangian is given by

$$\begin{aligned}\mathcal{L}_{\rm SCET}(x) = \bar{\psi}_s(x) i \not{D}_s(x) \psi_s(x) - \frac{1}{4}\left[F^{s\,a}_{\mu\nu}(x)\right]^2 \\ + \bar{\xi}(x)\frac{\not{n}}{2}\left[in\cdot D(x) + i\not{D}_{c\perp}(x)\frac{1}{in\cdot D_c(x)} i\not{D}_{c\perp}(x)\right]\xi(x) - \frac{1}{4}\left[F^{c\,a}_{\mu\nu}(x)\right]^2 .\end{aligned} \tag{2.17}$$

In this expression, we have introduced the various covariant derivatives

$$\begin{aligned} iD^s_\mu &= i\partial_\mu + gA^s_\mu\,, \\ iD^c_\mu &= i\partial_\mu + gA^s_\mu\,, \\ i\bar{n}\cdot D &= i\bar{n}\cdot\partial + g\bar{n}\cdot A_c(x) + g\bar{n}\cdot A_s(n\cdot x)\,, \\ in\cdot D &= in\cdot\partial + gn\cdot A_c(x)\,, \\ iD^\perp_\mu &= i\partial^\perp_\mu + gn\cdot A^{c\,\perp}_\mu(x)\,, \end{aligned} \tag{2.18}$$

and we define the gluon field strength tensor as

$$igF^s_{\mu\nu} = \left[iD^s_\mu, iD^s_\nu\right] \qquad igF^c_{\mu\nu} = \left[iD_\mu, iD_\nu\right] \tag{2.19}$$

An important feature of the SCET Lagrangian at this point, is that the soft and collinear sectors communicate with one another due to the kinetic term for the collinear gluons and the $i\bar{n}\cdot D$ term. In the formulation of the SCET Lagrangian, field redefinitions are then performed to decouple these two contributions.

2.4.2 Gauge Invariance in SCET and the Decoupling Transformation

Within traditional QCD, the gauge invariance of non-local operators manifests from Wilson lines. In the construction of the SCET Lagrangian, we introduced two types of fields, the soft and collinear. As a result, this will lead to the introduction of two types of Wilson lines with distinct behaviors. Namely we can denote two types of gauge transformations

$$U_n(x) = \exp\left(i\alpha^a_n(x)t^a\right) \qquad U_{us}(x) = \exp\left(i\alpha^a_{us}(x)t^a\right)\,, \tag{2.20}$$

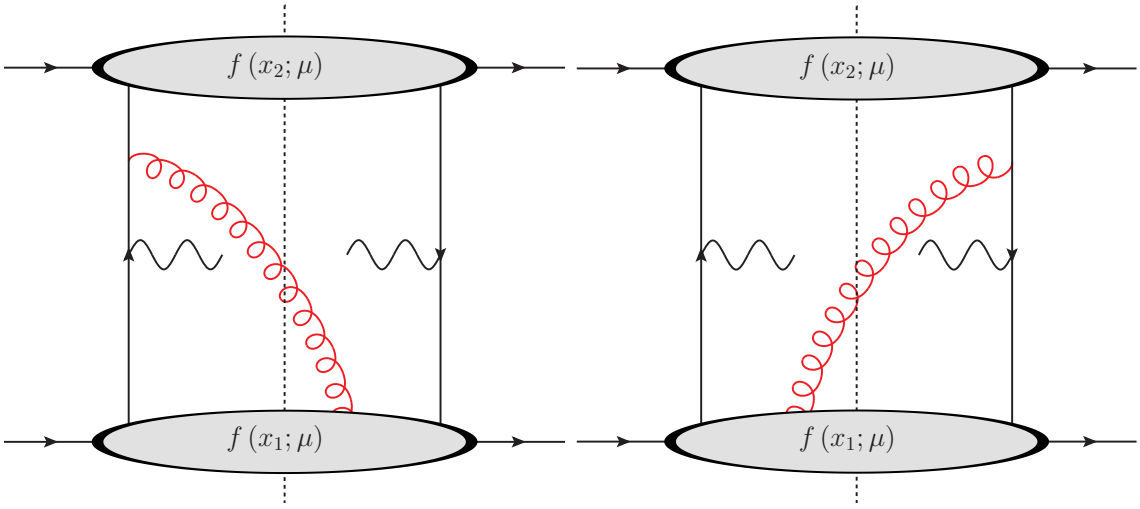

Figure 2.3: Representation of how the Wilson lines enter for the collinear PDF. Left: The Wilson line $W^{\bar{n}}(x^-,-\infty;\mathbf{0}_\perp)$. Right: The Wilson line $W^{\bar{n}}(-\infty,0;\mathbf{0}_\perp)$

which must obey different scalings

$$i\partial^\mu U_n(x) \sim Q\left(1,\lambda^2,\lambda\right) U_n(x) \qquad i\partial^\mu U_{us}(x) \sim Q\left(\lambda^2,\lambda^2,\lambda^2\right) U_{us}(x)\,. \tag{2.21}$$

The collinear Wilson lines enter into the definition of bi-local operators such as the unpolarized PDF for example

$$f(x;\mu) = \int \frac{d^4x}{(2\pi)^4} e^{ik\cdot x}\delta\left(x^+\right) \left\langle P \left| \bar{\xi}(x)\, W^{\bar{n}}(x^-,-\infty;\mathbf{0}_\perp)\, \frac{\not{n}}{2}\, W^{\bar{n}}(-\infty,0;\mathbf{0}_\perp)\, \xi(0) \right| P \right\rangle , \tag{2.22}$$

while the soft functions can be defined as vacuum matrix elements of a soft Wilson loop.

In the case of Drell-Yan, these Wilson lines enter due to the scattering of collinear gluons with the anti-collinear quark and serve to transport the quark in the $\bar{n}$ direction. In Fig. 2.3, we provide a picture of this interaction. The exact mathematical form for the Wilson lines can be obtained by examining the interaction of the anti-collinear quark with the collinear gluons, which is given by

$$\bar{\xi}_{\bar{c}}(p)\ (-ig\gamma^\mu t^a)\ \frac{-i\left(\not{p}+\not{l}\right)}{(p+l)^2} A^c_\mu(l) = -gt^a \frac{n\cdot A^c(l)}{n\cdot l} \bar{\xi}_{\bar{c}}(p) + \mathcal{O}(\lambda)\ . \tag{2.23}$$

We can see from this interaction that the interaction of the anti-collinear quark with the collinear gluons leads to a propagator which is far off its mass shell. This results in an

effective vertex in SCET. Furthermore, we see from the power counting of the collinear gluon field, we see that the attachment of a collinear gluon to the anti-collinear quark is not power suppressed. As a result, there is no difference between attaching one gluon or attaching an infinite number of gluons. In momentum space, this leads to the all order sum of the interactions as

$$W^{\bar{n}} = \sum_{k=0}^{\infty} \sum_{\text{perms}} \frac{(-g)^k}{k!} \frac{n \cdot A^c(l_1)\, n \cdot A^c(l_2) \ldots n \cdot A^c(l_k)}{[n \cdot l_1]\,[n \cdot (l_1 + l_2)] \ldots \left[n \cdot \sum_{i=1}^{k} l_i\right]} \,. \tag{2.24}$$

Fourier transforming into position space results in the simple expression

$$W^{\bar{n}}(a, b, \boldsymbol{c}_\perp) = \mathcal{P} \exp\left(ig \int_a^b ds\, \bar{n} \cdot A^c\left(x + \bar{n}s\right)\right) \,, \tag{2.25}$$

where $\mathcal{P}$ denotes the path ordering and I'll note that there in an analogous Wilson line in the n direction. In fact, we could also define a Wilson line in the $\perp$ direction as well. However, these transverse Wilson lines tend to enter at plus or minus infinity, where the field

Analogously, we could consider attaching soft gluons to the anti-collinear quark to obtain the soft Wilson lines. It's important to note however that because of the power counting of the soft gluons, these interactions do not knock the anti-collinear gluons off their mass shell and thus do note form effective vertices in SCET. The soft Wilson line is given by

$$Y^{\bar{n}}(a, b, \boldsymbol{c}_\perp) = \mathcal{P} \exp\left(ig \int_a^b ds\, \bar{n} \cdot A^s(x + \bar{n}s)\right) \,. \tag{2.26}$$

The decoupling of the soft and collinear modes at the Lagrangian level is obtained by defining new fields

$$\xi(x) = Y_n(x)\xi^{(0)}(x) \qquad A^c_\mu(x) = Y_n(x) A^c_{(0)\,\mu}(x) \,. \tag{2.27}$$

After the field redefinitions, we can write

$$\bar{\xi}_c(x) \frac{\bar{n}\!\!\!/}{2} i\bar{n} \cdot D(x) \xi_c(x) \to \bar{\xi}^{(0)}_c(x) \frac{\bar{n}\!\!\!/}{2} i\bar{n} \cdot D^{(0)}_c(x) \xi^{(0)}_c(x) \,. \tag{2.28}$$

The kinetic term for the collinear gluons also becomes

$$F^c_{\mu\nu}\, F^{\mu\nu\, c} \to F^{(0)\, c}_{\mu\nu}\, F^{(0)\, \mu\nu\, c} \,. \tag{2.29}$$

As a result, the soft and collinear sectors decouple at the Lagrangian level.

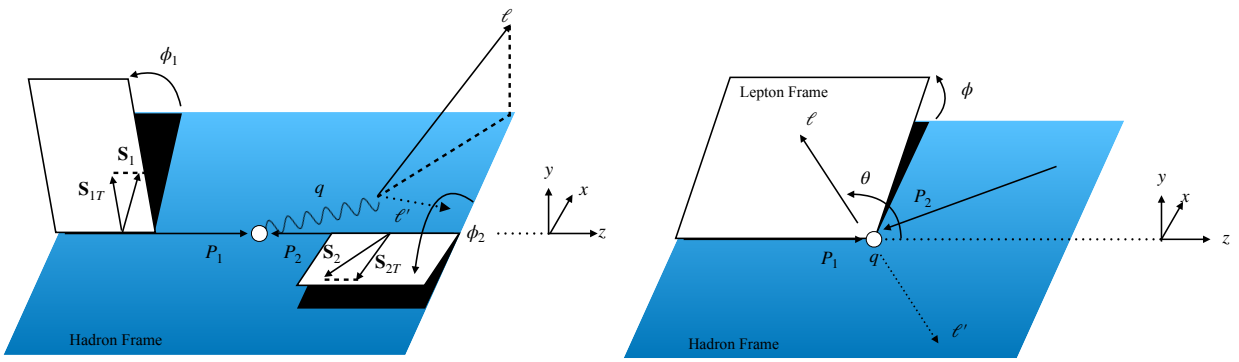

Figure 2.4: Left: The Drell-Yan cross section in the proton-proton COM frame. Right: the Drell-Yan cross section in the Gottfried-Jackson frame.

2.5 TMD Factorization and Resummation in Drell-Yan

Having summarized the ingredients of factorization theorems, I will now discuss resummation by examining Drell-Yan in the TMD region as an example. Within TMD factorization and resummation, the observable is sensitive to contributions to the two scales $q_\perp \ll Q$. This scale separation introduces large logarithms $\ln(q_\perp/Q)$ in the perturbative contributions which need to be resummed. In this section, I will demonstrate the procedure for performing this resummation. I would like to note at this point, that the formalism that is entering into this section follows directly from an upcoming paper of ours that considers higher twist contributions to the Drell-Yan and Semi-Inclusive DIS cross sections. Here is summarize only the twist-2 contributions however.

2.5.1 Kinematics

The transverse momentum dependent Drell-Yan cross section can be written in terms of its hadronic and leptonic contributions as [60]

$$\frac{d\sigma}{dQ^2\, dy\, d^2\boldsymbol{q}_\perp\, d\Omega} = \frac{\alpha_{\rm em}^2}{4sQ^4} L_{\mu\nu} W^{\mu\nu} \tag{2.30}$$

where $d\Omega = d\cos\theta\, d\phi$ is the solid angle of the lepton l and Q^2, y, and $\boldsymbol{q}_\perp$ are the invariant mass, rapidity, and transverse momentum of the produced photon in the hadronic COM

frame. Furthermore, $L^{\mu\nu}$ is the leptonic tensor which has the form

$$\begin{aligned} L^{\mu\nu} &= \langle 0|J^{\mu}(0)|\ell,\,\ell'\rangle\langle \ell,\,\ell'|J^{\mu\,\dagger}(0)|0\rangle \\ &= 4\ell^{\mu}\ell'^{\nu} + 4\ell^{\nu}\ell'^{\mu} - 2Q^2 g^{\mu\nu}\,, \end{aligned} \tag{2.31}$$

where ℓ and ℓ' are the momenta of the produced leptons and I have summed over the spin configurations of the final-state leptons. This cross section contains power corrections which scale as M/Q and $q_\perp/Q$. To formulate the leading power (LP) cross section, we drop the masses and kinematic corrections associated with $q_\perp$. After dropping these contributions, we can define a complete set of spatial coordinates in the leptonic COM frame as

$$\hat{t}^{\mu} = \frac{q^{\mu}}{Q}, \qquad \hat{x}^{\mu} = \frac{q_t^{\mu}}{q_\perp}\,, \qquad \hat{z}^{\mu} = \frac{2x_1}{Q}P_1^{\mu} - \hat{t}^{\mu}\,, \qquad \hat{y}^{\mu} = \epsilon^{\mu\nu\rho\sigma}\hat{t}_{\nu}\hat{x}_{\rho}\hat{z}_{\sigma}\,, \tag{2.32}$$

where $P_1^{\mu} = x_1 Q\bar{n}^{\mu}/2$ and $P_2^{\mu} = x_2 Q n^{\mu}/2$. Using these coordinates, the leptonic momenta can be defined as

$$\ell^{\mu} = \frac{Q}{2}\left(\hat{t}^{\mu} + \hat{z}^{\mu} + \hat{x}^{\mu}\cos\phi\sin\theta + \hat{y}^{\mu}\sin\phi\sin\theta\right)\,, \tag{2.33}$$

$$\ell'^{\mu} = \frac{Q}{2}\left(\hat{t}^{\mu} - \hat{z}^{\mu} - \hat{x}^{\mu}\cos\phi\sin\theta - \hat{y}^{\mu}\sin\phi\sin\theta\right)\,. \tag{2.34}$$

In the definition of the leptonic tensor, we have taken the normalization condition to be such that the sum over the spin configurations of the final-state leptons is absorbed into the definition of the leptonic tensor. Using the unit vectors defined previously, we can define projectors of the leptonic tensor as

$$\begin{aligned} \mathcal{V}_1^{\mu\nu} &= \hat{x}^{\mu}\hat{x}^{\nu} + \hat{y}^{\mu}\hat{y}^{\nu}, & \mathcal{V}_2^{\mu\nu} &= \hat{t}^{\mu}\hat{t}^{\nu}, \\ \mathcal{V}_3^{\mu\nu} &= \hat{x}^{\mu}\hat{z}^{\nu} + \hat{z}^{\mu}\hat{x}^{\nu}, & \mathcal{V}_4^{\mu\nu} &= \hat{x}^{\mu}\hat{x}^{\nu} - \hat{y}^{\mu}\hat{y}^{\nu}, \\ \mathcal{V}_5^{\mu\nu} &= \hat{x}^{\mu}\hat{z}^{\nu} - \hat{z}^{\mu}\hat{x}^{\nu}, & \mathcal{V}_6^{\mu\nu} &= \hat{x}^{\mu}\hat{y}^{\nu} - \hat{y}^{\mu}\hat{x}^{\nu}, \\ \mathcal{V}_7^{\mu\nu} &= \hat{y}^{\mu}\hat{z}^{\nu} - \hat{z}^{\mu}\hat{y}^{\nu}, & \mathcal{V}_8^{\mu\nu} &= \hat{y}^{\mu}\hat{z}^{\nu} + \hat{z}^{\mu}\hat{y}^{\nu}, \\ \mathcal{V}_9^{\mu\nu} &= \hat{x}^{\mu}\hat{y}^{\nu} + \hat{y}^{\mu}\hat{x}^{\nu}\,. \end{aligned} \tag{2.35}$$

We can also define the conjugate operators which are given by $\mathcal{V}_i^{\mu\nu}\,\bar{\mathcal{V}}_j^{\alpha\beta}g_{\mu\alpha}g_{\nu\beta} = \delta_{ij}$. Using this set of operators, the leptonic tensor can be decomposed as

$$L^{\mu\nu} = \sum_i L_i\left(\phi,\theta\right)\,\bar{\mathcal{V}}_i^{\mu\nu}\,, \tag{2.36}$$

where $L_i(\phi,\theta) = L_{\mu\nu}\mathcal{V}_i^{\mu\nu}$ are angular coefficients which are given by

$$\begin{aligned}
&L_1(\phi,\theta) = Q^2\,(1+\cos^2\theta), && L_2(\phi,\theta) = 0, \\
&L_3(\phi,\theta) = -Q^2\cos\phi\sin2\theta, && L_4(\phi,\theta) = -Q^2\cos2\phi\sin^2\theta, \\
&L_5(\phi,\theta) = 0, && L_6(\phi,\theta) = 0, \\
&L_7(\phi,\theta) = 0, && L_8(\phi,\theta) = -Q^2\sin\phi\sin2\theta, \\
&L_9(\phi,\theta) = -Q^2\sin2\phi\sin^2\theta\,.
\end{aligned} \tag{2.37}$$

From these coordinates, we can also define the transverse metric

$$g_{\mu\nu}^{\perp} = g_{\mu\nu} - \hat{t}^\mu\hat{t}^\nu + \hat{z}^\mu\hat{z}^\nu\,. \tag{2.38}$$

$W^{\mu\nu}$ represents the hadronic tensor, which is given by the expression

$$W_{\mu\nu} = \frac{1}{(2\pi)^4}\int d^4x\, e^{-iqx}\left\langle P_1\,, P_2\left|J_\mu^\dagger(x)\,J_\nu(0)\right|P_1\,, P_2\right\rangle\,, \tag{2.39}$$

where $J_\mu(x) = \sum_f e_f\bar{\psi}_f^c(x)\gamma_\mu\psi_f^c(x)$ denotes the quark current in QCD. In SCET, the interaction of the quark and the photon is given by

$$J_\mu(x) = \sum_f\int ds\,dt\,C_V(s,t)\,\bar{\chi}_c(x+s\bar{n})\gamma_\mu\chi_{\bar{c}}(x+tn)S_n^\dagger(x)\,S_{\bar{n}}^\dagger(x)\,. \tag{2.40}$$

$$\xi(x) = W^{\bar{n}}(x^-,-\infty,\boldsymbol{x}_\perp)\,, \tag{2.41}$$

where $C_V(s,t)$ represent Wilson coefficient functions which match SCET onto QCD in the UV region. The non-local interaction is a consequence of the scaling of the momentum scaling of collinear modes. Namely emissions of collinear gluons in the collinear region are not power suppressed since $p_c^\mu \sim Q(1,\lambda^2,\lambda)$.

2.5.2 Factorization in QCD

In full QCD, the hadronic tensor can be simplified as follows. Using the momentum space representation of the interaction and noting that the hard contribution is generated through

the interaction of collinear and anti-collinear modes, the hadronic tensor can be written as

$$W_{\mu\nu} = \sum_q \frac{e_q^2}{N_c} \int_\perp \mathrm{Tr}\Big[\Phi_q^{\mathrm{unsub}}\left(x_1, \boldsymbol{k}_{1\perp}, \boldsymbol{S}_1; \mu, \zeta_1/\nu^2\right) V^\mu\left(Q;\mu\right) \times \Phi_{\bar{q}}^{\mathrm{unsub}}\left(x_2, \boldsymbol{k}_{2\perp}, \boldsymbol{S}_2; \mu, \zeta_2/\nu^2\right) V^\nu\left(Q;\mu\right)\Big] S(\boldsymbol{\lambda}_\perp;\mu,\nu)\,, \tag{2.42}$$

$$\int_\perp = \int d^2\boldsymbol{k}_{1\perp}\, d^2\boldsymbol{k}_{2\perp}\, d^2\boldsymbol{\lambda}_\perp\, \delta^{(2)}\left(\boldsymbol{q}_\perp - \boldsymbol{k}_{1\perp} - \boldsymbol{k}_{2\perp} - \boldsymbol{\lambda}_\perp\right)\,. \tag{2.43}$$

In these expressions $\boldsymbol{k}_{1\perp}$, $\boldsymbol{k}_{2\perp}$, and $\boldsymbol{\lambda}_\perp$ denote the transverse momenta of the collinear, anti-collinear, and soft modes. Furthermore μ is the renormalization scale while ν and ζ represent the rapidity scale and the Collin-Soper parameter. The term $V^\mu\left(Q;\mu\right)$ is the photon quark vertex which contains QCD loop corrections. Φ_q denotes the quark-quark correlator, which is explicitly given in momentum space as

$$\Phi_{jj'}^{\mathrm{unsub}}(x,\boldsymbol{k}_\perp,\boldsymbol{S};\mu,\zeta/\nu^2) = \int \frac{d^4\xi}{(2\pi)^4}\, e^{ik\cdot\xi}\,\delta\left(\xi^+\right) \times \left\langle P,\boldsymbol{S}\left|\bar{\psi}_{j'}^c(\xi)\, W^{\bar{n}}(\xi^-,-\infty;\boldsymbol{\xi}_\perp)\, W^\perp(\boldsymbol{\xi}_\perp,\boldsymbol{0}_\perp;-\infty) W^{\bar{n}}(-\infty,\xi^-;\boldsymbol{0}_\perp)\,\psi_j^c(0)\right| P,\boldsymbol{S}\right\rangle\,. \tag{2.44}$$

The superscript unsub is used to say that 'soft subtraction' of the TMDs has not been performed yet. I will cover this soft subtraction in Sec. 2.5.7. In this expression ψ^c are quark fields with the momentum scaling $k^\mu \sim Q\left(1,\lambda^2,\lambda\right)$ where $\lambda = q_\perp/Q$. The Wilson lines are the same as those in Fig. 2.3 except that I have introduced a transverse collinear Wilson line which is defined as

$$W^\perp(\boldsymbol{a}_\perp,\boldsymbol{b}_\perp,c) = \mathcal{P}\exp\left(ig\int_{\boldsymbol{a}_\perp}^{\boldsymbol{b}_\perp} ds\, A_\perp^c\left(x+s\hat{\boldsymbol{s}}_\perp\right)\right)\,, \tag{2.45}$$

where $\hat{\boldsymbol{s}}_\perp$ is a perpendicular unit vector. Additionally, the function S in Eq. 2.42 contains the soft contribution to the cross section. We will discuss this contribution in more detail in Sec. 2.5.5. The trace that enters into this expression contains a mixture of interactions from the collinear, anti-collinear, and hard regions. To factorize these contributions it is useful to perform a Fierz decomposition of the hadronic tensor using the identity

$$\delta_{ij}\delta_{kl} = \sum_a \Gamma_{il}^a\,\bar{\Gamma}_{kj}^a\,, \tag{2.46}$$

to decompose the quark lines. Here, Γ^a are gamma matrices of the set

$$\Gamma^a \in \left\{1, \gamma_5, \gamma^\mu, \gamma^\mu\gamma^5, \sigma^{\mu\nu}\gamma^5\right\} . \tag{2.47}$$

A diagrammatic representation of this factorization is given in Fig. 2.5. After performing the Fierz decomposition, the hadronic tensor can be written as

$$W_{\mu\nu} = \sum_{a,b}\sum_q \frac{e_q^2}{N_c}\int_\perp \mathrm{Tr}\left[\gamma^\mu\,\bar\Gamma_1^a\,\gamma^\nu\,\bar\Gamma_1^b\right] \tag{2.48}$$

$$\times\,\Phi_{\rm unsub}^{[\Gamma^a]}\left(x_1, \boldsymbol{k}_{1\perp}, \boldsymbol{S}_1; \mu, \zeta_1/\nu^2\right)\,\bar\Phi_{\rm unsub}^{\left[\Gamma^b\right]}\left(x_2, \boldsymbol{k}_{2\perp}, \boldsymbol{S}_2; \mu, \zeta_2/\nu^2\right)\,S\left(\boldsymbol{\lambda}_\perp; \mu, \nu\right) . \tag{2.49}$$

In this expression, we have defined the trace of the quark-quark correlators as

$$\Phi^{[\Gamma^a]}\left(x_1, \boldsymbol{k}_{1\perp}, \boldsymbol{S}_1; \mu, \zeta_1/\nu^2\right) = \mathrm{Tr}\left[\Phi\left(x_1, \boldsymbol{k}_{1\perp}, \boldsymbol{S}_1; \mu, \zeta_1/\nu^2\right)\Gamma^a\right] . \tag{2.50}$$

The general structure of the quark-quark correlator can be obtained by performing a Fierz and Lorentz decomposition and retaining terms which are leading in power, and which are hermitician and satisfy parity transformations. At LP, the decomposition is given by

$$\Phi_{\rm unsub}\left(x, \boldsymbol{k}_\perp, \boldsymbol{S}; \mu, \zeta/\nu^2\right) = \left(f - \frac{\epsilon_\perp^{\rho\sigma} k_{\perp\rho} S_{\perp\sigma}}{M} f_{1T}^\perp\right)\frac{\not{\bar n}}{4} + \left(\lambda g_{1L} - \frac{\boldsymbol{k}_\perp\cdot\boldsymbol{S}_\perp}{M} g_{1T}\right)\frac{\gamma^5\not{\bar n}}{4}$$

$$+\left(S_\perp^k h_1 + \frac{\lambda k_\perp^k}{M} h_{1L}^\perp - \frac{\epsilon_\perp^{kj} k_{\perp j}}{M} h_1^\perp - \frac{k_\perp^k k_\perp^j - \frac{1}{2}k_\perp^2 g_\perp^{kj}}{M^2} S_{\perp j} h_{1T}^\perp\right)\frac{i\gamma^5\sigma_{-k}}{4} . \tag{2.51}$$

We can see in this expression the Dirac structure associated with the unpolarized TMD PDF, f. As a result, the unpolarized differential cross section can be obtained by setting $\bar\Gamma^a = \not{\bar n}/4$ and $\bar\Gamma^b = \not{n}/4$. Finally, we note that the convolution in transverse momentum in the hadronic tensor are simplified when working in $\boldsymbol{b}$ space, which is conjugate to $\boldsymbol{q}_\perp$ space. The final expression for the hadronic tensor is then

$$W_{\mu\nu} = -g_{\mu\nu}^\perp \sum_q \frac{e_q^2}{N_c}\int \frac{d^2b}{(2\pi)^2} e^{i\boldsymbol{b}\cdot\boldsymbol{q}_\perp} \tag{2.52}$$

$$\times\, f_{q/P_1}^{\rm unsub}\left(x_1, b; \mu, \zeta_1/\nu^2\right)\, f_{\bar q/P_2}^{\rm unsub}\left(x_2, b; \mu, \zeta_2/\nu^2\right)\, S\left(b; \mu, \nu\right) ,$$

$$\Theta(b) = \int d^2\boldsymbol{k}_\perp e^{-i\boldsymbol{k}\cdot\boldsymbol{b}}\Theta(k_\perp) , \tag{2.53}$$

for $\Theta = f, S$. The leading order contribution from the hard interaction can be obtained through the contraction

$$L_{\mu\nu}\,\mathrm{Tr}\left[\gamma^{\mu}\,\frac{\bar{\not{n}}}{4}\,\gamma^{\nu}\,\frac{\not{n}}{4}\right] = N_c\,Q^2\left(1+\cos^2\theta\right)\,H_{\mathrm{DIS}}^{(0)}(Q;\mu)\,, \tag{2.54}$$

where $H_{\mathrm{DIS}}^{(0)}(Q;\mu) = 1$ is the tree level hard function. As a result, the final expression for the differential cross section can be written as

$$\frac{d\sigma}{dQ^2\,dy\,d^2\boldsymbol{q}_{\perp}\,d\Omega} = \frac{\alpha_{\mathrm{em}}^2}{4sQ^2}\left(1+\cos^2\theta\right)\,H_{\mathrm{DIS}}(Q;\mu)\sum_q e_q^2\int\frac{bdb}{(2\pi)}J_0\left(bq_{\perp}\right) \tag{2.55}$$

$$\times\, f_{q/P_1}^{\mathrm{unsub}}\left(x_1,b;\mu,\zeta_1/\nu^2\right)\,f_{\bar{q}/P_2}^{\mathrm{unsub}}\left(x_2,b;\mu,\zeta_2/\nu^2\right)\,S\left(b;\mu,\nu\right)\,. \tag{2.56}$$

Where the Hankel transform was obtained through the relation

$$\int d\phi e^{i\boldsymbol{b}\cdot\boldsymbol{q}_{\perp}} = 2\pi J_0\left(bq_{\perp}\right)\,. \tag{2.57}$$

2.5.3 Hard Contribution

The NLO hard contribution will contain all diagrams which contain momentum scaling $l^{\mu}\sim Q\,(1,1,1)$. In principle, one would need to consider both real and virtual emissions. However, a real hard emission would lead to a final-state vector boson with transverse momentum $q_{\perp}\sim Q$ which would be outside of the TMD region. As a result, we can simply replace the vertex with the one loop virtual vertex. The expression for the one loop vertex is given by

$$V_{\mu}^{(1)}(Q;\mu) = e_q g_s^2\left(\frac{\mu^2 e^{\gamma_E}}{4\pi}\right)^{\epsilon}\int\frac{d^dl}{(2\pi)^d}\frac{\left(\gamma_{\alpha}t^a\right)\left(\not{l}-\not{k}_1\right)\gamma_{\mu}\left(\not{k}_2+\not{l}\right)\gamma^{\alpha}}{l^2\left(k_1-l\right)^2\left(k_2+l\right)^2}\,. \tag{2.58}$$

The expression can be obtained using through a Passarino-Veltman reduction. From this loop diagram, we obtain the hard contribution

$$\hat{H}(Q;\mu) = 1+\frac{\alpha_s C_F}{2\pi}\left[-\frac{2}{\epsilon^2}-\frac{3}{\epsilon}-L_Q^2-\frac{2L_Q}{\epsilon}-3L_Q+\frac{7\pi^2}{6}-8\right]\,, \tag{2.59}$$

where the hat indicates that the hard function is bare and the divergences are once again IR in origin, see for instance [61] for a discussion on this point. Additionally, note that the double pole term is associated with contributions which are simultaneously soft and collinear. In this expression, I have also defined the logarithm $L_Q = \ln\left(\mu^2/Q^2\right)$

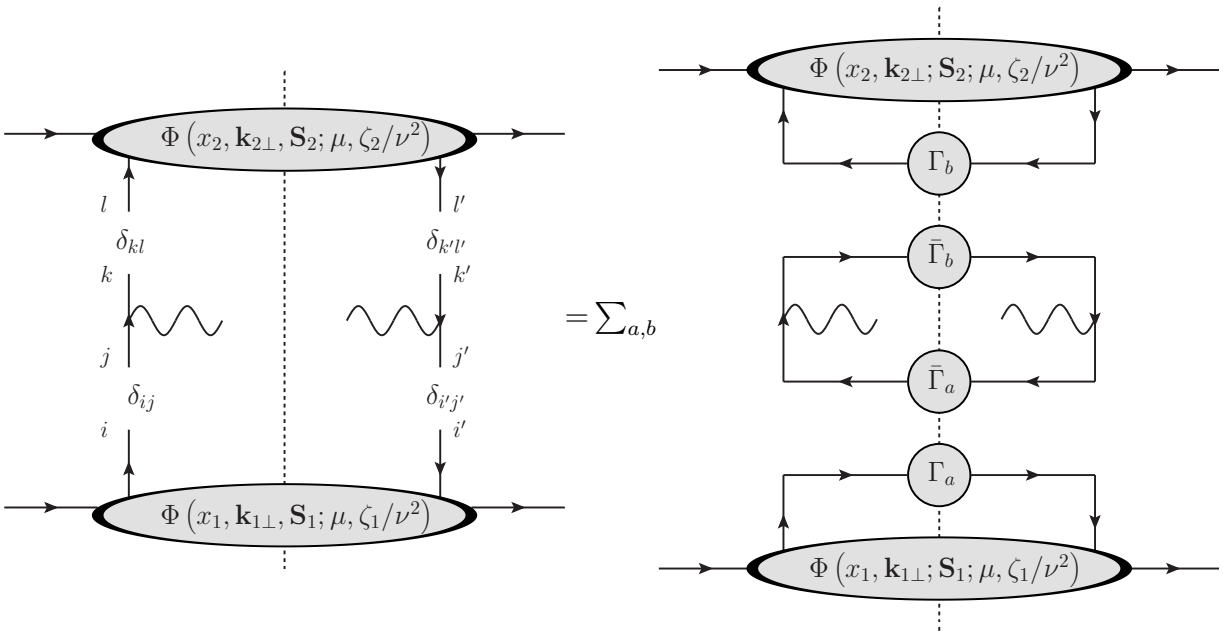

Figure 2.5: Diagrammatic representation of the Fierz decomposition of the hadronic tensor at tree level. Left: The broken lines are used to separate the hard interaction from the definition of the quark-quark correlation function. Right: The Fierz decomposition where Γ_i represent the operators which give rise to the parton densities while $\bar{\Gamma}_i$ represent the operators which enter into the hard function.

Using the definition of the unsubtracted hard function, we can obtained the subtracted hard function through multiplicative renormalization as

$$\hat{H}(Q;\mu) = Z(Q;\mu)H(Q;\mu) + \mathcal{O}(\alpha_s^2)\,, \tag{2.60}$$

where the divergences are contained in the multiplicative renormalization factor $Z(Q;\mu)$. This allows us to obtain the subtracted hard functions

$$H(Q;\mu) = 1 + \frac{\alpha_s C_F}{2\pi}\left[-L_Q^2 - 3L_Q + \frac{7\pi^2}{6} - 8\right], \tag{2.61}$$

and the multiplicative renormalization factors

$$Z(Q;\mu) = 1 + \frac{\alpha_s C_F}{2\pi}\left[-\frac{2}{\epsilon^2} - \frac{3}{\epsilon} - \frac{2L_Q}{\epsilon}\right]. \tag{2.62}$$

By exploiting the scale invariance of the hard function, we can obtain the evolution equation

$$\frac{\partial H\,(Q;\mu)}{\partial \ln\mu} = \Gamma_H^{\mu}(Q;\mu) H\,(Q;\mu)\,, \tag{2.63}$$

$$\Gamma_H^{\mu}(Q;\mu) = -\frac{1}{Z(Q;\mu)}\frac{\partial}{\partial \ln\mu} Z(Q;\mu)\,. \tag{2.64}$$

where this evolution equation holds to all orders. At NLO, the only non-vanishing contribution enters from taking the Z which is being acted on in the derivative to NLO. The explicit one loop expression for the hard anomalous dimension is then given by

$$\Gamma_H(Q;\mu) = -\frac{\alpha_s\,(\mu)\,C_F}{\pi}\left(2L_Q + 3\right). \tag{2.65}$$

This expression is often re-written in terms of the cusp and non-cusp anomalous dimensions, Γ_{cusp} and γ^V, as

$$\Gamma_H(Q;\mu) = \Gamma_{\text{cusp}}(\alpha_s)\ln\left(\frac{Q^2}{\mu^2}\right) + \gamma^V(\alpha_s)\,, \tag{2.66}$$

where the anomalous dimensions can organized by the number of loops as

$$\Gamma_{\text{cusp}}(\alpha_s) = \sum_{n=1}^{\infty}\Gamma_{n-1}\left(\frac{\alpha_s}{4\pi}\right)^n \qquad \gamma^V(\alpha_s) = \sum_{n=1}^{\infty}\gamma^V_{n-1}\left(\frac{\alpha_s}{4\pi}\right)^n \tag{2.67}$$

where $\Gamma_0 = 4C_F$, and $\gamma_0^V = -6C_F$. In the appendix of this chapter, we include these anomalous dimensions up to three loops. To obtain the expression for the anomalous dimension, I have related the bare and renormalized strong coupling constants at LO through the relation

$$\alpha_s(\mu) \left(\frac{\mu^2 e^{\gamma_E}}{4\pi} \right)^{\epsilon} = \alpha_s \,. \tag{2.68}$$

Using the definition of the hard anomalous dimension, we can solve for the evolution of the hard function as

$$H(Q;\mu) = H(Q;\mu_Q) \, \exp\left(\int_{\mu_Q}^{\mu} \frac{d\mu'}{\mu'} \Gamma_H^{\mu} \left(Q;\mu'\right) \right) . \tag{2.69}$$

Now please note that the logarithms L_Q can destroy the convergences of a perturbative sum. However, by solving the renormalization group equations, we introduce the auxiliary scale μ_Q, which can be anything. If we take $\mu_Q = Q$ then these logarithms in $H(Q;\mu_Q)$ go to zero. The large logarithms with argument μ/Q are then 'resummed' in the Sudakov exponential. I would like to note however at this point, that there is a subtlety associated with the organization of the anomalous dimension. At one loop, we saw the appearance of the term $\alpha_s \ln(Q^2/\mu^2)$. If μ is taken to be largely different than Q, than these logarithms can grow to be large. As a result, the larger contribution for the anomalous dimension will come from the term containing Γ_{cusp}. For this reason, it is conventional to take Γ_{cusp} to be one order higher than γ^V. Upon using the two loop expression for Γ_{cusp}, we reach an accuracy of next-to-leading order (NLO) and next-to-leading-log (NLL). In general the number of Ns that enter into logarithmic resummation is the same as the order of the non-cusp anomalous dimension. An interesting thought is how does the perturbative accuracy of the resummation relate to the perturbative accuracy of the fixed order contributions, such as the log independent terms in hard contribution. To demonstrate this comparison, consider that at LL we resum contributions which go like $\alpha_s^m \ln^{m+1}(Q^2/\mu^2) > \alpha_s$, at NLL we resum contributions which go like $\alpha_s^m \ln^m(Q^2/\mu^2) \sim \alpha_s^0$, and finally at NNLL we resum contributions which go like $\alpha_s^m \ln^{m-1}(Q^2/\mu^2) \sim \alpha_s$. Therefore to match the perturbative accuracy of NLO, it is conventional to work at NLO+NNLL accuracy.

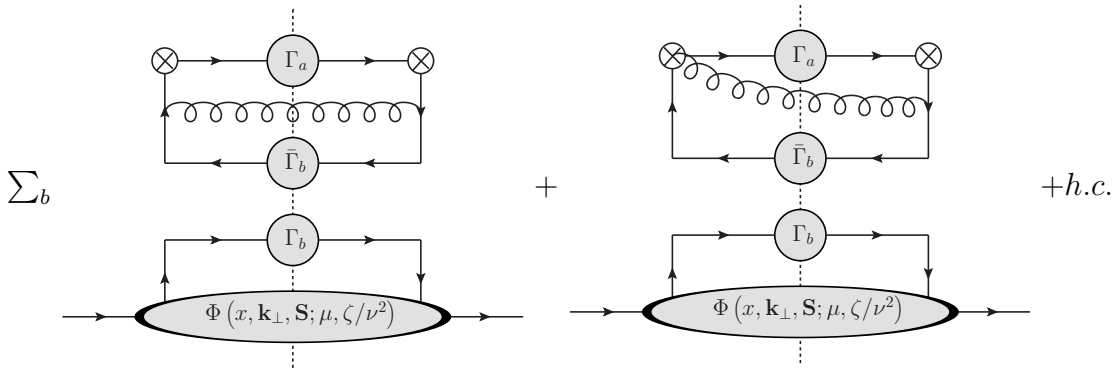

Figure 2.6: The graphs for the TMD PDFs at NLO. The upper part of the broken line represents the perturbative contribution to the one loop expression while the lower portion represents the un-renormalized TMD PDF. The $\otimes$ represents the Wilson line for the TMD PDFs while the second term on the contains a hermitian conjugate.

2.5.4 Collinear Contributions

To obtain the anomalous dimensions of the TMD PDF, we must obtain the UV divergences associated with the graphs in Fig. 2.6. We note that while there are additional graphs that contribute to this function, they all vanish in dimensional regularization. The graph on the right side has a hermitian conjugate and these two graphs emerge from the Wilson line associated with the collinear quark scattering against the anti-collinear gluon field from the other incoming hadron. The explicit expression for these graphs in momentum space are

$$\hat{f}\left(x, k_\perp; \mu, \zeta_1/\nu\right) = -g_s^2 C_F \left(\frac{\mu^2 e^{\gamma_E}}{4\pi}\right)^\epsilon \int d^2 p_\perp \int \frac{dx'}{x'} f\left(x', p_\perp; \mu, \zeta_1/\nu\right) \int \frac{d^d l}{(2\pi)^d} e^{i\boldsymbol{l}_\perp \cdot \boldsymbol{b}}$$
$$\delta\left(\left(x - x'\right) P^+ + l^+\right) \delta^2\left(\boldsymbol{p}_\perp - \boldsymbol{k}_\perp - \boldsymbol{l}_\perp\right) \mathrm{Tr}\left[x' \frac{\bar{\not{n}}}{4} \gamma^\mu \frac{\not{k}}{k^2} \frac{\not{n}}{2} \left(\frac{\not{k}}{k^2} \gamma_\mu + 2 \frac{n_\mu}{n \cdot l}\right)\right] (2\pi) \delta\left(l^2\right) . \tag{2.70}$$

In this expression, the momentum k represents the momentum of the quark entering the hard process and is given by

$$k^\mu = (p - l)^+ \frac{\bar{n}^\mu}{2} + (p - l)^- \frac{n^\mu}{2} - l_t^\mu - l_{\perp\epsilon}^\mu \tag{2.71}$$

where l is the momentum of the radiated gluon while p is the momentum of the incoming quark and the ϵ subscript on $l_{\perp\epsilon}^\mu$ denotes that the momentum is in a $d - 4$ direction in

dimensional regularization. Furthermore, x' is the momentum fraction of the incoming quark relative to the parent hadron while x is the momentum fraction of the outgoing quark. I would like to note that since the observable is sensitive to the scale Q, the cross section is sensitive to the value of x as a result, to calculate this distribution, I have inserted the δ function in x. Additionally, since the observable is sensitive to $q_\perp$, I have inserted a δ function which is sensitive to the generated transverse momentum. These δ functions are known as 'measurement functions' since their appearance occurs due to the sensitivity of the measurement. Additionally, I would like to point out that besides the δ function in the transverse momentum, these graphs are exactly the ones that enter into the expression for DGLAP evolution.

If we are interested in matching the TMD onto a collinear PDF, we can take on the right hand side

$$f^{\text{unsub}}\left(x', p_\perp; \mu, \zeta_1/\nu^2\right) = f(x';\mu)\,\delta^2\left(\boldsymbol{p}_\perp\right) . \tag{2.72}$$

Performing the integration over $p_\perp$, we obtain

$$\begin{aligned}\hat{f}\left(x, k_\perp; \mu, \zeta_1/\nu\right) = -g_s^2 C_F \left(\frac{\mu^2 e^{\gamma_E}}{4\pi}\right)^\epsilon \int \frac{dx'}{x'} f\left(x';\mu\right) \int \frac{d^d l}{(2\pi)^d}\, e^{i\boldsymbol{l}_\perp\cdot\boldsymbol{b}} \\ \delta\left(\left(x-x'\right)P^+ + l^+\right)\,\delta^2\left(\boldsymbol{k}_\perp + \boldsymbol{l}_\perp\right)\mathrm{Tr}\left[x'\frac{\bar{\not{n}}}{4}\gamma^\mu\frac{\not{k}}{k^2}\frac{\not{n}}{2}\left(\frac{\not{k}}{k^2}\gamma_\mu + 2\frac{n_\mu}{n\cdot l}\right)\right]\,(2\pi)\delta\left(l^2\right) .\end{aligned} \tag{2.73}$$

These types of calculation provide two valuable information for two separate contributions to the cross section. The UV divergences provide information for the evolution of the TMDs. The finite and IR parts of these graphs provide information for how the TMDs are matched onto collinear PDFs. However, to perform the full matching, I would also need to consider gluon to quark diagrams.

As in the case for the cross section, the convolution integral on the right-hand side of this expression is simplified by working in b-space.

$$\begin{aligned}\hat{f}\left(x, b; \mu, \zeta_1/\nu\right) = -g_s^2 C_F \left(\frac{\mu^2 e^{\gamma_E}}{4\pi}\right)^\epsilon \int \frac{dx'}{x'} f\left(x';\mu\right) \int \frac{d^d l}{(2\pi)^d}\, e^{i\boldsymbol{l}_\perp\cdot\boldsymbol{b}} \\ \times\,\delta\left(l^+ - \left(1-\hat{x}\right)\sqrt{\zeta_1}\right)\,\mathrm{Tr}\left[x'\frac{\bar{\not{n}}}{4}\gamma^\mu\frac{\not{k}}{k^2}\frac{\not{n}}{2}\left(\frac{\not{k}}{k^2}\gamma_\mu + 2\frac{n_\mu}{n\cdot l}\right)\right]\,(2\pi)\delta\left(l^2\right) .\end{aligned} \tag{2.74}$$

In this expression, we have introduced $\hat{x} = x/x'$ and the Collins-Soper scale $\zeta_1 = (x'P^+)^2$. After performing the integration, we are left with

$$\hat{f}(x,b;\mu,\zeta_1/\nu) = \frac{\alpha_s C_F}{2}\frac{\left(\mu^2 e^{\gamma_E}\right)^\epsilon}{\Gamma(1-\epsilon)}\csc(\pi\epsilon)\int\frac{dx'}{x'}f(x';\mu) \times\left[(1-\epsilon)(1-\hat{x})+\frac{2\hat{x}}{(1-\hat{x})}\right]\left(\frac{b^2}{4}\right)^\epsilon. \tag{2.75}$$

At this point, we can see that a divergence occurs where $x' = x$, and therefore this divergence occurs in the infrared limit of l^+. Because this divergence is in the plus direction, these are known as 'rapidity divergences'. As in the case of the factorization of the cross section, IR divergences indicates the presence of an unaccounted for mode. Namely, this mode must have a scaling $l^\mu \sim Q(\lambda,\lambda,\lambda)$, which is strikingly similar to the soft contribution but with a higher invariant mass. In the next section, we will provide a physical interpretation for this mode. For this section, we will simply acknowledge the presence of this mode and discuss regularizing the l^+ integral. While in principle this integration can be performed by introducing a hard cutoff, this would lead to a Wilsonian RGE for the rapidity. In Ref. [62], a regularization procedure was introduced which emulates the characteristics of dimensional regularization. The procedure outlined in that paper originates by noting that the $\hat{x}\to 1$ issue occurs only from the Wilson line interaction. The authors then replaced the Wilson lines with

$$W_n(x) \to \sum_{\text{perms}}\exp\left[-\frac{g\omega^2}{n\cdot P}\frac{|2P_{g3}|^{-\eta}}{\nu^{-\eta}}n\cdot A_n\right], \tag{2.76}$$

where ω acts as a coupling strength between the Wilson line and the gluon, ν acts as a cutoff scale similar to μ, η is a regulator, and P_{g3} and $n\cdot P$ are derivative operators in the z and plus directions, respectively.

Using this regularization procedure, the integral becomes

$$\hat{f}(x,b;\mu,\zeta_1/\nu) = \frac{\alpha_s C_F}{2}\frac{\left(\mu^2 e^{\gamma_E}\right)^\epsilon}{\Gamma(1-\epsilon)}\csc(\pi\epsilon)\int\frac{dx'}{x'}f(x';\mu) \times\left[(1-\epsilon)(1-\hat{x})+\frac{2\hat{x}\omega^2}{(1-\hat{x})^{1+\eta}}\left(\frac{\nu}{\zeta_1}\right)^\eta\right]\left(\frac{b^2}{4}\right)^\epsilon. \tag{2.77}$$

To perform the integration, we use the relation

$$(1-\hat{x})^{-1-\eta} = -\frac{1}{\eta}\delta(1-\hat{x}) + \frac{1}{(1-\hat{x})^{+}} + \mathcal{O}(\eta)\,. \tag{2.78}$$

The plus distribution can then be related to the splitting kernel and the expression for the TMD PDF becomes

$$\begin{aligned}\hat{f}^{\text{unsub}}\left(x,b;\mu,\zeta_1/\nu^2\right) = \frac{\alpha_s C_F}{2\pi}\int\frac{dx'}{x'}f(x;\mu)\Bigg[&-\left(L+\frac{1}{\epsilon}\right)P_{qq}(\hat{x}) \\ &+\left[\frac{2\omega^2}{\eta}L+\frac{2\omega^2}{\eta\epsilon}+\frac{\omega^2}{\epsilon}L_{\zeta_1}+\frac{3}{2\epsilon}\right]\delta(1-\hat{x}) \\ &+L\,L_{\zeta_1}\,\delta(1-\hat{x})+\frac{3}{2}L\delta(1-\hat{x})+(1-\hat{x})\Bigg]\,.\end{aligned} \tag{2.79}$$

The top line of this expression contains the IR divergences, the second line contains the UV divergences, and the third line contains the finite parts. Notice that in the second line, we have the appearance of a double pole. This double pole is associated with a mode at sufficiently small rapidity but with a large invariant mass. In this expression, we have introduced the logarithms

$$L = \ln\left(\frac{\mu^2}{\mu_b^2}\right)\,, \qquad \mu_b = \frac{2e^{-\gamma_E}}{b}\,, \qquad L_{\zeta_1} = \ln\left(\frac{\nu^2}{\zeta_1}\right)\,. \tag{2.80}$$

We see from the one loop expression that the scale that enters into the L term goes like $\ln b\mu$ in b-space. In momentum space, this will result in logarithms which go like $\ln\mu/q_\perp$, which can be very large and spoil the convergence of the perturbative cross section. Additionally, we see the appearance of the L_{ζ_1} logarithms. Analogous to the case for the hard function, we can perform resummation of these logarithms through a multiplicative renormalization procedure. This multiplicative procedure can be thought of as performing an all order resummation of the ladder diagrams. To perform this procedure we write

$$\hat{f}^{\text{unsub}}(x,b;\mu,\zeta_1/\nu^2) = \left[Z\otimes f^{\text{unsub}}\right]\left(x,b;\mu,\zeta_1/\nu^2\right) \tag{2.81}$$

$$\left[A\otimes B\right]\left(x,b;\mu,\zeta_1/\nu^2\right) = \int_x^1\frac{dx'}{x'}A(x'\dots)\;B(\hat{x},\dots)\,, \tag{2.82}$$

where ... refers to additional dependence. From this expression, we can exploit the scale invariance of the bare TMD PDF to obtain the evolution equations

$$\left[Z \otimes \frac{\partial f^{\text{unsub}}}{\partial \ln \mu}\right]\left(x, b; \mu, \zeta_1/\nu^2\right) = -\left[\frac{\partial Z}{\partial \ln \mu} \otimes f^{\text{unsub}}\right]\left(x, b; \mu, \zeta_1/\nu^2\right) , \tag{2.83}$$

$$\left[Z \otimes \frac{\partial f^{\text{unsub}}}{\partial \ln \nu}\right]\left(x, b; \mu, \zeta_1/\nu^2\right) = -\left[\frac{\partial Z}{\partial \ln \nu} \otimes f^{\text{unsub}}\right]\left(x, b; \mu, \zeta_1/\nu^2\right) . \tag{2.84}$$

We see from these expressions that since the TMDs require a renormalization and rapidity scale, that this leads to a coupled differential equation for the evolution. The evolution in ν is known as the Collins-Soper equation. Additionally, we note that due to the convolution, the $\partial f/\partial \ln \mu$ and $\partial f/\partial \ln \nu$ terms cannot be isolated to all orders in perturbation theory, as we had done for the hard function. However, at NLO this can easily be inverted by obtaining the expressions for the renormalized TMD PDF and the multiplicative renormalization factor, which are given by

$$Z\left(x', b; \mu, \zeta_1/\nu^2\right) = \delta\left(1 - x'\right) + \frac{\alpha_s C_F}{2\pi}\left[\frac{2\omega^2}{\eta} L + \frac{2\omega^2}{\eta\epsilon} + \frac{\omega^2}{\epsilon} L_{\zeta_1} + \frac{3}{2\epsilon}\right]\delta\left(1 - x'\right) \tag{2.85}$$

$$\begin{aligned} f^{\text{unsub}}\left(x, b; \mu, \zeta_1/\nu^2\right) = f\left(x; \mu\right) &- \int \frac{dx'}{x'} f\left(x'; \mu\right) \frac{\alpha_s C_F}{2\pi}\left(L + \frac{1}{\epsilon}\right) P_{qq}\left(\hat{x}\right) \\ &+ \frac{\alpha_s C_F}{2\pi} \int \frac{dx'}{x'} f\left(x'; \mu\right)\left[L\, L_{\zeta_1}\, \delta\left(1 - \hat{x}\right) + \frac{3}{2} L \delta\left(1 - \hat{x}\right) + \left(1 - \hat{x}\right)\right] . \end{aligned} \tag{2.86}$$

The evolution equations become at one loop

$$\frac{\partial f^{\text{unsub}}\left(x, b; \mu, \zeta_1/\nu^2\right)}{\partial \ln \mu} = \Gamma^c_\mu(\mu, \nu) f\left(x, b; \mu, \zeta_1/\nu^2\right) , \tag{2.87}$$

$$\frac{\partial f^{\text{unsub}}\left(x, b; \mu, \zeta_1/\nu^2\right)}{\partial \ln \nu} = \Gamma^c_\nu(\mu)\, f\left(x, b; \mu, \zeta_1/\nu^2\right) . \tag{2.88}$$

$$\Gamma^c_\mu(\mu, \nu, \zeta) = \frac{\alpha_s(\mu) C_F}{\pi}\left(L_{\zeta_1} + \frac{3}{2}\right) \qquad \Gamma^c_\nu(\mu) = \frac{\alpha_s(\mu) C_F}{\pi} L . \tag{2.89}$$

To obtain this contribution, I have written ω as a bare quantity that is related to a renormalized ω as

$$\omega^2 = \nu^\eta \omega^2(\nu) . \tag{2.90}$$

By solving these evolution equations, we are performing a resummation at all orders for a single emission. This is why in the expansion for the Wilson line, we expanded only to first order. By solving the renormalization group evolution equations, we are summing these contributions to all orders. The solution to these equations is

$$f^{\text{unsub}}\left(x,b;\mu,\zeta_1/\nu^2\right) = f\left(x,b;\mu_c,\zeta_1/\nu_c^2\right)\exp\left[\int_{\mu_c}^{\mu}\frac{d\mu'}{\mu'}\Gamma^c_\mu(\mu,\nu)\right]\left(\frac{\nu}{\nu_c}\right)^{\Gamma^c_\nu(\mu)} . \tag{2.91}$$

We see from the expression for the renormalized f, that logarithms, $L = \ln\left(\mu_c^2/\mu_b^2\right)$ and $L_{\zeta_1} = \ln\left(\nu_c^2/\zeta_1\right)$ enter. Analogous to the case for the hard function, we can evaluate the distribution on the right hand side at any scales μ_c, and ν_c and evolve the distribution up to the renormalization and rapidity scales μ and ν. To minimize the contributions of the logarithms in the perturbative expressions, we could take $\mu_c = \mu_b$ and $\nu_c^2 = \zeta_1$. Furthermore we can turn our attention to the IR divergence and the finite part. The general procedure is to write the UV finite TMD PDF in terms of the UV finite PDF through the relation

$$f^{\text{unsub}}\left(x,b;\mu,\zeta_1/\nu^2\right) = \left[C\otimes f^{\text{unsub}}\right]\left(x,b;\mu,\zeta_1/\nu^2\right) . \tag{2.92}$$

We then expand the TMD PDF and PDF to NLO. Upon performing this analysis, one finds that the IR divergences of the TMD PDF and PDF are the same at NLO. We can then absorb these IR divergences into the definition of the collinear PDF and obtain a finite and renormalized TMD PDF. We also recover the one loop coefficient function for quark to quark splitting

$$\begin{aligned} C_{q/q'}\left(x,b;\mu,\zeta_1/\nu^2\right) &= \delta_{q/q'}\delta\left(1-x\right) \\ &\quad + \delta_{q/q'}\frac{\alpha_s C_F}{2\pi}\left[L\,L_{\zeta_1}\,\delta\left(1-x\right) + \frac{3}{2}L\delta\left(1-x\right) + \left(1-x\right)\right] . \end{aligned}$$

$$C_{q/g}(x,b;\mu,\zeta_1/\nu^2) = \frac{\alpha_s}{\pi}\left[x(1-x)T_F - \frac{1}{2}P_{q\leftarrow g}(x)L\right] .$$

In the second line, I have included the one loop matching coefficient for quarks matched onto gluons for completeness.

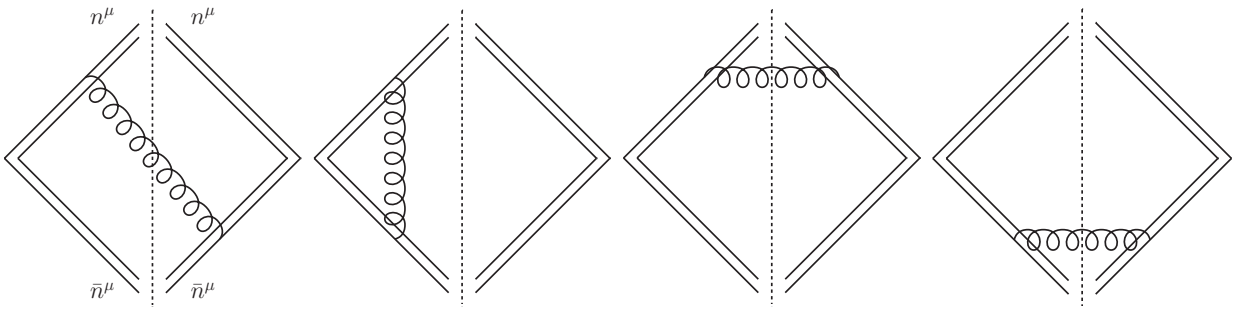

Figure 2.7: The graphs which provide the soft contributions to the cross section. The two graphs on the left have hermitian conjugates.

2.5.5 Soft Contribution

In the previous section, I demonstrated that an infrared rapidity divergence enters into the collinear distributions and discussed that this divergence indicated that a new soft mode was contributing to the cross section. The scaling of this mode was found to be $l^\mu \sim Q\left(\lambda, \lambda, \lambda\right)$ while the scaling of the traditional soft gluons is $l^\mu \sim Q\left(\lambda^2, \lambda^2, \lambda^2\right)$. To differentiate these two contributions, we will call the gluons which scale as $l^\mu \sim Q\left(\lambda, \lambda, \lambda\right)$ soft and the gluons which scale as $l^\mu \sim Q\left(\lambda^2, \lambda^2, \lambda^2\right)$ ultra soft.

The ultra-soft contribution to the cross section can be obtained by considering ultra-soft gluon emissions from the incoming quarks. The interaction of a collinear quark with a soft gluon is given by

$$\frac{-i\left(\not{p}+\not{l}\right)}{(p+l)^2}\left(-ig\gamma^\mu t^a\right)\xi_c\left(p\right) = -gt^a\frac{\bar{n}^\mu}{\bar{n}\cdot l}\xi_c\left(p\right) + \mathcal{O}\left(\lambda\right) , \tag{2.93}$$

which is an eikonal vertex, which is represented graphically by a gluon attaching to a double line. Similar Feynman rules can be obtained through the interaction with anti-collinear quarks and anti-quarks. By considering all possible interactions of the soft gluons with the incoming quarks, you obtain the graphs in Fig. 2.7. In those graphs, the left two diagrams contain hermitian conjugates. The right two diagrams vanish since $n \cdot n = \bar{n} \cdot \bar{n} = 0$. Furthermore, the first and second integrals are shown in the appendix to be proportional to scaleless integrals and therefore vanishes in dimensional regularization. Thus there is no ultra-soft contribution to the cross section. This behavior is a consequence of the fact that the

observable is not in any way sensitive to the dynamics of the ultra soft gluon radiation. The observable is sensitive to y and Q^2, and therefore gains access to x_1, the collinear component of the momenta which scales $Q\,\lambda^0$. The observable also has sensitivity to $q_\perp$ which scales as $Q\,\lambda$. However, the dynamics of the ultra soft gluons scale as λ^2. These soft gluons are then also integrated out and give a zero contribution above tree level.

In the case of the soft gluons, we can see that the observable will be sensitive to the transverse momentum of the soft gluons, which scales the same as $q_\perp$. Let's first begin by introducing the Wilson lines for these soft gluons. These Wilson lines will enter an an analogous way to the collinear Wilson lines as effective vertices. Their precise expressions in position space are

$$S_n = \sum_{\text{perms}} \exp\left[-\frac{g\omega}{n\cdot P}\frac{|2P_{g\,3}|^{-\eta/2}}{\nu^{-\eta/2}} n\cdot A_n\right] \tag{2.94}$$

Applying the Feynman rules to the graphs in Fig. 2.7, we obtain the explicit expression for the soft function contribution

$$\hat{S}(\lambda_\perp) = 2g_s^2\left(\frac{\mu^2 e^{\gamma_E}}{4\pi}\right)^\epsilon \int \frac{d^dl}{(2\pi)^d}(2\pi)\,\delta\left(l^2\right)(-g_{\mu\nu})\,\delta^2\left(\boldsymbol{\lambda}_\perp - \boldsymbol{l}_\perp\right)\frac{n^\mu\bar{n}^\nu}{n\cdot l\,\bar{n}\cdot l}\,. \tag{2.95}$$

After carefully considering this integral, it can be seen that there are two sources of UV rapidity divergences associated with $l^+\to\infty$ and $l^-\to\infty$. These divergences represent the contamination of the collinear gluons into the soft region. Replacing the Wilson line Feynman rules with the regularized ones, we obtain

$$\hat{S}(\lambda_\perp) = 2g_s^2\,\omega^2\left(\frac{\mu^2 e^{\gamma_E}}{4\pi}\right)^\epsilon \int \frac{d^dl}{(2\pi)^d}(2\pi)\,\delta\left(l^2\right)(-g_{\mu\nu})\,\delta^2\left(\boldsymbol{\lambda}_\perp - \boldsymbol{l}_\perp\right)\frac{n^\mu\bar{n}^\nu}{n\cdot l\,\bar{n}\cdot l}\left|\frac{2l_z}{\nu}\right|^{-\eta}\,. \tag{2.96}$$

The exact details for the calculation are in the appendix of this section. After performing the integration, Fourier transforming into b-space and expanding in η and ϵ, we are left with

$$\hat{S}(b;\mu,\nu) = 1 + \frac{\alpha_s C_F}{2\pi}\omega^2\left[\frac{4}{\eta}\left(-\frac{1}{\epsilon}-L\right)+\frac{2}{\epsilon^2}-\frac{2}{\epsilon}L_\nu - 2L\,L_\nu - L^2 - \frac{\pi^2}{6}\right]. \tag{2.97}$$

The intuition for the double divegences is the same as for the hard and collinear functions. The double poles $\eta\epsilon$ are associated with large rapidity modes with high invariant mass while

the ϵ^2 poles are associated with small rapidity modes with a large invariant mass. To obtain the evolution of the soft function, we perform the same procedure that was done for the TMD PDF. Namely, we write

$$\hat{S}(b;\mu,\nu) = Z(b;\mu,\nu)\, S(b;\mu,\nu)\,, \tag{2.98}$$

where S is the renormalized soft function. Exploiting the scale invariance of the bare soft function. The evolution equations become

$$\frac{\partial S(b;\mu,\nu)}{\partial \ln\mu} = \Gamma^s_\mu S(b;\mu,\nu) \qquad \frac{\partial S(b;\mu,\nu)}{\partial \ln\nu} = \Gamma^s_\nu S(b;\mu,\nu)\,. \tag{2.99}$$

The full exponentiation of the Wilson line is obtained by solving these renormalization group evolution equation. The anomalous dimensions for the soft function are defined as

$$\Gamma^s_\mu(b;\mu,\nu) = -\frac{1}{Z(b;\mu,\nu)}\frac{\partial Z(b;\mu,\nu)}{\partial \ln\mu} = 2\frac{\alpha_s(\mu)C_F}{\pi}L_\nu\,, \tag{2.100}$$

$$\Gamma^s_\nu(b;\mu) = -\frac{1}{Z(b;\mu,\nu)}\frac{\partial Z(b;\mu,\nu)}{\partial \ln\mu} = -\frac{2\alpha_s(\mu)C_F}{\pi}L\,. \tag{2.101}$$

Solving the evolution equations, the soft function can be written as

$$S(b;\mu,\nu) = S(b;\mu_s,\nu_s)\exp\left[\int_{\mu_s}^{\mu}\frac{d\mu'}{\mu'}\left(\Gamma^s_\mu(b;\mu,\nu)\right)\right]\left(\frac{\nu}{\nu_s}\right)^{\Gamma^s_\nu(b;\mu)}\,. \tag{2.102}$$

To minimize the contributions of the large logarithms, we can take $\mu_s = \nu_s = \mu_b$.

2.5.6 Renormalization Group Consistency

In formulating the cross section, we have introduced two scales μ and ν, which are associated with factorizing off the IR from the UV physics, and associated with factorizing the collinear from the soft physics. However, this separation is simply an organization tool and does not represent the underlying physics of the interactions. If we were to decrease μ as an example, a sample of the contributions which were previously defined as soft and collinear would be re-labeled as hard. Nevertheless, the contributions to the sum of total diagrams entering into

the cross section would remain unchanged. The renormalization group consistency condition is then

$$\frac{d\sigma}{d\ln\mu} = \frac{d\sigma}{d\ln\nu} = 0\,. \tag{2.103}$$

Since the cross section is related to the functions H, S, f_q and $f_{\bar{q}}$ through a convolution, the requirement for RG consistency can be written as

$$\sum_i \Gamma_\mu^{\Theta_i} = 0 \qquad \sum_i \Gamma_\nu^{\Theta_i} = 0\,, \tag{2.104}$$

where $\theta_i = f_q$, $f_{\bar{q}}$, H, and S. Summing twice the contribution of Eq. 2.89 with Eqs. 2.100, 2.101, and 2.66, we one can easily show that the renormalization group consistency conditions holds since $\zeta_1\zeta_2 = Q^4$.

2.5.7 Resummed Cross Section

In the literature, it is common to define 'proper TMDs' through the relation

$$f\left(x, b; \mu, \zeta_1\right) = f^{\text{unsub}}\left(x, b; \mu, \zeta_1/\nu^2\right)\sqrt{S(b;\mu,\nu)}\,, \tag{2.105}$$

where one can show that the product of these contributions no longer depends on the rapidity scale ν. The idea behind such a combination is that one hemisphere of the soft radiation is absorbed into each of the TMD PDFs so that there is no need for a rapidity cutoff scale. From our expression of the TMD PDF and the soft functions, we can define the proper TMD PDF as

$$\begin{aligned} f^{\text{TMD}}\left(x, b; \mu, \zeta_1\right) &= f\left(x, b; \mu_c, \zeta_1/\nu_c^2\right)\sqrt{S(b;\mu_s,\nu_s)} \\ &\times \exp\left[\int_{\mu_c}^{\mu}\frac{d\mu'}{\mu'}\Gamma_\mu^c(\mu,\nu)\right]\left(\frac{\nu}{\nu_c}\right)^{\Gamma_\nu^c(\mu)} \exp\left[\int_{\mu_s}^{\mu}\frac{d\mu'}{\mu'}\left(\frac{1}{2}\Gamma_\mu^s(b;\mu,\nu)\right)\right]\left(\frac{\nu}{\nu_s}\right)^{\frac{1}{2}\Gamma_\nu^s(b;\mu)}\,. \end{aligned} \tag{2.106}$$

We note that the scales μ_c and μ_s both minimize the logarithms in the perturbative expansions for $\mu_c = \mu_s = \mu_b$. It is common in the literature to then take $\mu_c = \mu_s$. After introducing the expressions for the anomalous dimensions and the fixed order contributions, the expression for the proper TMD is given by

$$f^{\text{TMD}}\left(x, b; \mu, \zeta_1\right) = \left[C^{\text{TMD}} \otimes f\right]\left(x, b; \mu, \zeta_1\right) \tag{2.107}$$

$$\times \exp\left\{\int_{\mu_c}^{\mu}\frac{d\mu'}{\mu'}\frac{\alpha_s\left(\mu'\right)\,C_F}{\pi}\left[\ln\left(\frac{\mu'^2}{\zeta_1}\right)+\frac{3}{2}\right]+\frac{\alpha_s(\mu)C_F}{\pi}L\ln\left(\frac{\nu_s}{\nu_c}\right)\right\}\,.$$

where the coefficient function is given by

$$C_{q/q'}^{\mathrm{TMD}}\left(x,b;\mu,\zeta_1\right)=\delta_{q/q'}\delta\left(1-x\right)$$
$$+\,\delta_{q/q'}\frac{\alpha_s C_F}{2\pi}\left[L\ln\left(\frac{\mu^2}{\zeta_1}\right)\,\delta\left(1-x\right)-\frac{1}{2}L^2\delta\left(1-x\right)+\frac{3}{2}L\delta\left(1-x\right)+\left(1-x\right)-\frac{\pi^2}{12}\delta\left(1-x\right)\right]\,.$$

Using the properly defined TMDs, the expression for the resummed cross section becomes

$$\frac{d\sigma}{dQ^2\,dy\,d^2\boldsymbol{q}_\perp\,d\Omega}=\frac{\alpha_{\mathrm{em}}^2}{4sQ^2}\left(1+\cos^2\theta\right)\,H_{\mathrm{DIS}}(Q;\mu_Q)\sum_q e_q^2\int\frac{bdb}{(2\pi)}J_0\left(b\,q_\perp\right) \tag{2.108}$$
$$\left[C^{\mathrm{TMD}}\otimes f\right]\left(x_1,b;\mu_c,\zeta_1\right)\,\left[C^{\mathrm{TMD}}\otimes f\right]\left(x_2,b;\mu_c,\zeta_2\right)\exp\left\{-S_{\mathrm{pert}}\left(b;\mu_c,\mu_Q,\nu_s,\nu_c\right)\right\}\,.$$

In this expression, we have introduced the perturbative Sudakov for the cross section which is defined as

$$S_{\mathrm{pert}}\left(b;\mu_c,\mu_Q,\zeta_i,\zeta_f\right)=\int_{\mu_c}^{\mu_Q}\frac{d\mu'}{\mu'}\left[\Gamma_{\mathrm{cusp}}\left(\mu'\right)\ln\left(\frac{\zeta_1}{\mu'^2}\right)+\gamma^V\left(\mu'\right)\right]+D(b;\mu_c)\ln\left(\frac{\zeta_1}{\zeta_i}\right)\,, \tag{2.109}$$

where $D(b;\mu_c)$ is the Collins-Soper kernel, which is also known as the rapidity anomalous dimension. The expressions along with the organization in powers of α_s is given in the appendix of this chapter.

2.5.8 Non-perturbative contributions

In the previous section, I outlined a procedure for factorizing cross section and calculating the perturbative contributions. To perform full tomography however, we must also address the non-perturbative contributions. To study how non-perturbative contributions related to the cross sections, it is instructive to study Eq. 2.108, where the range $b \geq 0$ is integrated over. We note in that expression that the logarithms are minimized by taking $\mu_c = \mu_b = c/b$. At small b, the scale μ_b becomes perturbative. As a result, the non-perturbative Sudakov evolves the distribution from μ_b to μ_Q, both of which are perturbative. However, at sufficiently large b, the scale μ_b becomes non-perturbative. The intuitive understanding of factorized cross

sections in b-space is that the small b physics is dominated by perturbative contributions while the large b physics is dominated by the non-perturbative contributions.

The non-perturbative contributions to the cross sections enter from three sources. The first source that I will address are those stemming from the collinear distributions. We saw in the previous section that TMDs are matched onto collinear distributions. As a result, these non-perturbative collinear contributions must be accounted for. These PDFs can in principle be used from previous global analyses within a purely collinear framework. We note that within this method, the main PDFs which are available are the unpolarized PDF f, the helicity PDF g, and the transversity PDF h. As I will demonstrate in this thesis however, there are several TMD PDFs which do not match onto either any of these mentioned PDFs. In this case, the TMD PDF of interest will be matched onto a collinear PDF in the usual way

$$\varphi\left(x,b;\mu,\zeta\right)=\left[C^{\varphi}\otimes\phi\right]\left(x,b;\mu,\zeta\right)\,, \tag{2.110}$$

where φ is a TMD PDF and ϕ is a collinear PDF. In this case, we would need to parameterize ϕ and obtain its behavior in a global analysis. Typically this is done by taking a parameterization

$$\phi_f(x)\sim N_f x^{\alpha_f}\left(1-x\right)^{\beta_f}\,, \tag{2.111}$$

and fitting the parameters N_f, α_f, and β_f.

The second source of non-perturbative contributions that I will discuss enters due to the intrinsic transverse momentum of the quarks. We discussed in the previous chapter that the solutions of the CSS equations account for the transverse momentum which is generated through perturbative radiation. The so-called 'intrinsic' transverse momentum is the transverse momentum which is generated through non-perturbative radiation and tends to be around $\Lambda_{\rm QCD}$. While such a transverse momentum seems quite small, I'll note that in Z boson production in Drell-Yan collisions, the average transverse momentum which is produced perturbatively tends to be close to 3 GeV, while for collisions with smaller Q, the perturbative transverse momentum is much smaller. This intrinsic transverse momentum

is accounted for through the ad-hoc introduction of an intrinsic non-perturbative Sudakov factor into the b dependent integrand for the Drell-Yan collisions. The expression for the intrinsic non-perturbative Sudakov is given by

$$\exp\left[S_{\rm NP}^{\rm int}(x_1,x_2,b,Q,Q_0)\right]=\exp\left[-g_q(x_1,b^2,Q,Q_0)-g_q(x_2,b^2,Q,Q_0)\right]\,. \tag{2.112}$$

The function g_q serves to smear the transverse momentum of the incoming quark in momentum space and is usually parameterized so that the non-perturbative Sudakov resembles a Gaussian or exponential distribution.

The final source of non-perturbative contributions to the cross section that I will discuss originates from the evolution equations. If we study the anomalous dimensions of the soft and collinear distributions, we see that the rapidity anomalous dimensions scale as $L=\ln\left(\mu^2/\mu_b^2\right)$. From this behavior, we see that if b grows large, that the rapidity anomalous dimension becomes non-perturbative. This behavior is an indication that the rapidity evolution of the TMDs contains a non-perturbative contribution. To account for effect the non-perturbative rapidity evolution Sudakov is introduced

$$\exp\left[S_{\rm NP}^{\rm rap}(x_1,x_2,b,Q,Q_0)\right]=\left[-\frac{1}{4}g_K(b)\ln\left(\frac{\zeta_1\zeta_2}{Q_0^4}\right)\right]\,. \tag{2.113}$$

This Sudakov provides information for the non-perturbative evolution from the initial rapidity scale Q_0 to the hard rapidity scale Q.

To implement the Sudakov contributions into the cross section, we note that the perturbative Sudakov terms contain contributions associated with generating transverse momenta through perturbative radiation. Up to power corrections of order $q_\perp/Q$, the contributions of the perturbative and non-perturbative momenta should be additive and the resulting Sudakov for the system becomes

$$S_{\rm pert}\left(b;\mu_c,\mu_Q,\nu_s,\nu_c\right)\to S_{\rm pert}\left(b;\mu_c,\mu_Q,\nu_s,\nu_c\right)+S_{\rm NP}(x_1,x_2,b,Q,Q_0)\,, \tag{2.114}$$

$$S_{\rm NP}(x_1,x_2,b,Q,Q_0)=S_{\rm NP}^{\rm rap}(x_1,x_2,b,Q,Q_0)+S_{\rm NP}^{\rm int}(x_1,x_2,b,Q,Q_0)\,, \tag{2.115}$$

Conventionally, we can define the non-perturbative contribution to each TMD as

$$S^f_{\rm NP}(x_1,b,Q_0,Q) = -g_q\left(x_1,b^2,Q,Q_0\right) - \frac{1}{4}g_K(b)\ln\left(\frac{\zeta_1}{Q_0^2}\right)\,, \tag{2.116}$$

$$S^f_{\rm NP}(x_2,b,Q_0,Q) = -g_q\left(x_2,b^2,Q,Q_0\right) - \frac{1}{4}g_K(b)\ln\left(\frac{\zeta_2}{Q_0^2}\right)\,. \tag{2.117}$$

In this paper, I will always take g_q to be independent of x so it's depenence will be dropped from this point forward.

2.6 Appendix

2.6.1 TMD evolution ingredients

The following expansions, numbers, etc, can be found in the 2013 PDG [63]. First of all, we need the expansion of the strong coupling in terms of $\Lambda_{\rm QCD}$:

$$\frac{\alpha_s(\mu)}{4\pi} = \frac{1}{\beta_0 x} - \frac{\beta_1}{\beta_0^3}\frac{\ln x}{x^2} + \frac{\beta_1^2}{\beta_0^5}\frac{\ln^2 x - \ln x - 1}{x^3} + \frac{\beta_2}{\beta_0^4}\frac{1}{x^3} + \cdots\,, \tag{2.118}$$

where $x = \ln\left(\mu^2/\Lambda^2_{\rm QCD}\right)$, and the coefficients of the β-function are given as

$$\beta_0 = \frac{11}{3}\,C_A - \frac{4}{3}\,T_F n_f\,, \tag{2.119}$$

$$\beta_1 = \frac{34}{3}\,C_A^2 - \frac{20}{3}\,C_A T_F n_f - 4C_F T_F n_f\,, \tag{2.120}$$

$$\beta_2 = \frac{2857}{54}\,C_A^3 + \left(2C_F^2 - \frac{205}{9}\,C_F C_A - \frac{1415}{27}\,C_A^2\right)T_F n_f + \left(\frac{44}{9}\,C_F + \frac{158}{27}\,C_A\right)T_F^2 n_f^2\,. \tag{2.121}$$

Since we want the resummation up to NNLL, we take the expansion of α_s with β_0, β_1 and β_2. Depending on the number of active flavours, the value of $\Lambda_{\rm QCD}$ changes. For $n_f = 4$ we have $\Lambda_{\rm QCD} = 0.297$ GeV, and for $n_f = 5$ we have $\Lambda_{\rm QCD} = 0.214$ GeV. The pole-mass for bottom-quark is $m_b = 4.7$ GeV.

The rapidity anomalous dimension, Collins-Soper kernel, is defined perturbatively as

$$D(b;\mu) = \sum_{n=1}^{\infty}\sum_{k=0}^{n} d^{(n,k)}\left(\frac{\alpha_s}{4\pi}\right)^n L^k\,, \tag{2.122}$$

where the coefficients up to NNLL are given by

$$\begin{aligned} d^{(1,0)} =&0\,, \qquad d^{(1,1)} = \Gamma_0/2\,, \\ d^{(2,0)} =&C_A C_F \left(\frac{404}{27} - 14\zeta_3\right) - \frac{112}{27} C_F T_F n_f\,, \\ d^{(2,1)} =&\Gamma_1/2\,, \qquad d^{(2,2)} = \Gamma_0\beta_0/4\,. \end{aligned} \tag{2.123}$$

On the other hand, in order to describe the perturbative TMD evolution, we want to analytically solve the integral

$$\int_{\mu_L}^{\mu_U} \frac{d\bar{\mu}}{\bar{\mu}} \left(\gamma^V + \Gamma_{\rm cusp} \ln\frac{\mu_U^2}{\bar{\mu}^2}\right)\,, \tag{2.124}$$

where the coefficients of the perturbative expansions of the anomalous dimensions can be found in the below.

2.6.2 Integration at NLL accuracy

For this order we take γ_0, Γ_0, Γ_1, β_0 and β_1. Thus we have:

$$\begin{aligned} C_{\gamma_0}^{\rm NLL} =& \int_{\mu_L}^{\mu_U} \frac{d\bar{\mu}}{\bar{\mu}} \gamma_0 \frac{\alpha_s(\bar{\mu})}{4\pi} \\ =& \frac{\gamma_0}{2\beta_0} \int_{x_L}^{x_U} dx \left(\frac{1}{x} - \frac{\beta_1}{\beta_0^2}\frac{\ln x}{x^2}\right) \\ =& \frac{\gamma_0}{2\beta_0} \left[\ln x - \frac{\beta_1}{\beta_0^2}\left(\frac{-1-\ln x}{x}\right)\right]\Bigg|_{x_L}^{x_U} \end{aligned} \tag{2.125}$$

$$\begin{aligned} C_{\Gamma_0}^{\rm NLL} =& \int_{\mu_L}^{\mu_U} \frac{d\bar{\mu}}{\bar{\mu}} \Gamma_0 \frac{\alpha_s(\bar{\mu})}{4\pi} \ln\frac{\mu_U^2}{\bar{\mu}^2} \\ =& \frac{\Gamma_0}{2\beta_0} \int_{x_L}^{x_U} dx \left(\frac{1}{x} - \frac{\beta_1}{\beta_0^2}\frac{\ln x}{x^2}\right)(x_U - x) \\ =& \frac{\Gamma_0}{2\beta_0} \left[-x + x_U \ln x - \frac{\beta_1}{\beta_0^2}\left(-\frac{x_U}{x} - \frac{x_U \ln x}{x} - \frac{\ln^2 x}{2}\right)\right]\Bigg|_{x_L}^{x_U} \end{aligned} \tag{2.126}$$

$$\begin{aligned} C_{\Gamma_1}^{\rm NLL} =& \int_{\mu_L}^{\mu_U} \frac{d\bar{\mu}}{\bar{\mu}} \Gamma_1 \left(\frac{\alpha_s(\bar{\mu})}{4\pi}\right)^2 \ln\frac{\mu_U^2}{\bar{\mu}^2} \\ =& \frac{\Gamma_1}{2\beta_0^2} \int_{x_L}^{x_U} dx \left(\frac{1}{x} - \frac{\beta_1}{\beta_0^2}\frac{\ln x}{x^2}\right)^2 (x_U - x) \\ =& \frac{\Gamma_1}{2\beta_0^2} \left[-\frac{x_U}{x} - \ln x - 2\frac{\beta_1}{\beta_0^2}\left(\frac{1}{x} - \frac{x_U}{4x^2} + \frac{\ln x}{x} - \frac{x_U \ln x}{2x^2}\right)\right. \end{aligned} \tag{2.127}$$

$$+\frac{\beta_1^2}{\beta_0^4}\left(\frac{1}{4x^2}-\frac{2x_U}{27x^3}+\frac{\ln x}{2x^2}-\frac{2x_U\ln x}{9x^3}+\frac{\ln^2 x}{2x^2}-\frac{x_U\ln^2 x}{3x^3}\right)\Bigg]\Bigg|_{x_L}^{x_U}$$

The final result is then

$$\int_{\mu_L}^{\mu_U}\frac{d\bar{\mu}}{\bar{\mu}}\left(\gamma^V+\Gamma_{\rm cusp}\ln\frac{\mu_U^2}{\bar{\mu}^2}\right)=C_{\gamma_0}^{\rm NLL}+C_{\Gamma_0}^{\rm NLL}+C_{\Gamma_1}^{\rm NLL}\,. \tag{2.128}$$

Be careful with the number of active flavors. The number of flavors for the x_U that appears inside the integrand is fixed and depends on the value of μ_U. However, depending on the hierarchy between μ_L, μ_U and m_b we might have to split the integral in several pieces, and in that case, when we substitute the limits of the integral, x_L and x_U, they would have different numbers of active flavors (still the x_U that already appeared in the integrand before the substitutions just depends on the value of μ_U).

2.6.3 Integration at NNLL accuracy

For this order we take γ_0, γ_1, Γ_0, Γ_1, Γ_2, β_0, β_1 and β_2. Thus we have:

$$\begin{aligned}
C_{\gamma_0}^{\rm NNLL} &= \int_{\mu_L}^{\mu_U}\frac{d\bar{\mu}}{\bar{\mu}}\,\gamma_0\frac{\alpha_s(\bar{\mu})}{4\pi} \qquad (2.129)\\
&= \frac{\gamma_0}{2\beta_0}\int_{x_L}^{x_U}dx\left(\frac{1}{x}-\frac{\beta_1}{\beta_0^2}\frac{\ln x}{x^2}+\frac{\beta_1^2}{\beta_0^4}\frac{\ln^2 x-\ln x-1}{x^3}+\frac{\beta_2}{\beta_0^3}\frac{1}{x^3}\right)\\
&= \frac{\gamma_0}{2\beta_0}\left[\ln x-\frac{\beta_1}{\beta_0^2}\left(\frac{-1-\ln x}{x}\right)+\frac{\beta_1^2}{\beta_0^4}\left(\frac{1}{2x^2}-\frac{\ln^2 x}{2x^2}\right)+\frac{\beta_2}{\beta_0^3}\left(\frac{-1}{2x^2}\right)\right]\Bigg|_{x_L}^{x_U}\\
C_{\gamma_1}^{\rm NNLL} &= \int_{\mu_L}^{\mu_U}\frac{d\bar{\mu}}{\bar{\mu}}\,\gamma_1\left(\frac{\alpha_s(\bar{\mu})}{4\pi}\right)^2 \qquad (2.130)\\
&= \frac{\gamma_1}{2\beta_0^2}\int_{x_L}^{x_U}dx\left(\frac{1}{x}-\frac{\beta_1}{\beta_0^2}\frac{\ln x}{x^2}+\frac{\beta_1^2}{\beta_0^4}\frac{\ln^2 x-\ln x-1}{x^3}+\frac{\beta_2}{\beta_0^3}\frac{1}{x^3}\right)^2\\
&= \frac{\gamma_1}{2\beta_0^2}\left[-\frac{1}{x}+\frac{\beta_1^2}{\beta_0^4}\left(-\frac{2}{27x^3}-\frac{\ln^2(x)}{3x^3}-\frac{2\ln(x)}{9x^3}\right)\right.\\
&+\frac{\beta_1^4}{\beta_0^8}\left(-\frac{789}{3125x^5}-\frac{\ln^4(x)}{5x^5}+\frac{6\ln^3(x)}{25x^5}+\frac{43\ln^2(x)}{125x^5}-\frac{164\ln(x)}{625x^5}\right)\\
&+\frac{\beta_2^2}{\beta_0^6}\left(-\frac{1}{5x^5}\right)-2\frac{\beta_1}{\beta_0^2}\left(-\frac{1}{4x^2}-\frac{\ln(x)}{2x^2}\right)\\
&\left.+2\frac{\beta_1^2}{\beta_0^4}\left(\frac{10}{27x^3}-\frac{\ln^2(x)}{3x^3}+\frac{\ln(x)}{9x^3}\right)+2\frac{\beta_2}{\beta_0^3}\left(-\frac{1}{3x^3}\right)\right.
\end{aligned}$$

$$
\begin{aligned}
&- 2\frac{\beta_1^3}{\beta_0^6}\left(\frac{9}{128x^4} - \frac{\ln^3(x)}{4x^4} + \frac{\ln^2(x)}{16x^4} + \frac{9\ln(x)}{32x^4}\right) \\
&- 2\frac{\beta_1\beta_2}{\beta_0^5}\left(-\frac{1}{16x^4} - \frac{\ln(x)}{4x^4}\right) \\
&+2\frac{\beta_1^2\beta_2}{\beta_0^7}\left(\frac{28}{125x^5} - \frac{\ln^2(x)}{5x^5} + \frac{3\ln(x)}{25x^5}\right)\Bigg]\Bigg|_{x_L}^{x_U} \\
C_{\Gamma_0}^{\rm NNLL} &= \int_{\mu_L}^{\mu_U}\frac{d\bar{\mu}}{\bar{\mu}}\,\Gamma_0\frac{\alpha_s(\bar{\mu})}{4\pi}\ln\frac{\mu_U^2}{\bar{\mu}^2} \\
&= \frac{\Gamma_0}{2\beta_0}\int_{x_L}^{x_U}dx\,\left(\frac{1}{x} - \frac{\beta_1}{\beta_0^2}\frac{\ln x}{x^2} + \frac{\beta_1^2}{\beta_0^4}\frac{\ln^2 x - \ln x - 1}{x^3} + \frac{\beta_2}{\beta_0^3}\frac{1}{x^3}\right)(x_U - x) \\
&= \frac{\Gamma_0}{2\beta_0}\left[-x + x_U\ln x - \frac{\beta_1}{\beta_0^2}\left(-\frac{x_U}{x} - \frac{x_U\ln x}{x} - \frac{\ln^2 x}{2}\right)\right. \\
&\left.+\frac{\beta_1^2}{\beta_0^4}\left(\frac{(\ln(x)+1)((2x-x_U)\ln(x)+x_U)}{2x^2}\right) + \frac{\beta_2}{\beta_0^3}\left(\frac{1}{x} - \frac{x_U}{2x^2}\right)\right]\Bigg|_{x_L}^{x_U} \qquad (2.131) \\
C_{\Gamma_1}^{\rm NNLL} &= \int_{\mu_L}^{\mu_U}\frac{d\bar{\mu}}{\bar{\mu}}\,\Gamma_1\left(\frac{\alpha_s(\bar{\mu})}{4\pi}\right)^2\ln\frac{\mu_U^2}{\bar{\mu}^2} \\
&= \frac{\Gamma_1}{2\beta_0^2}\int_{x_L}^{x_U}dx\,\left(\frac{1}{x} - \frac{\beta_1}{\beta_0^2}\frac{\ln x}{x^2} + \frac{\beta_1^2}{\beta_0^4}\frac{\ln^2 x - \ln x - 1}{x^3} + \frac{\beta_2}{\beta_0^3}\frac{1}{x^3}\right)^2(x_U - x) \\
&= \frac{\Gamma_1}{2\beta_0^2}\left[-\frac{x_U}{x} - \ln x + \frac{\beta_1^2}{\beta_0^4}\left(\frac{1}{4x^2} - \frac{2x_U}{27x^3} + \frac{\ln x}{2x^2} - \frac{2x_U\ln x}{9x^3} + \frac{\ln^2 x}{2x^2} - \frac{x_U\ln^2 x}{3x^3}\right)\right. \\
&+ \frac{\beta_1^4}{\beta_0^8}\left(\frac{20000(5x-4x_U)\ln^4(x) - 4000(25x-24x_U)\ln^3(x) - 200(875x-688x_U)\ln^2(x)}{400000x^5}\right. \\
&\left.\left.+\frac{20(5625x-5248x_U)\ln(x) + 128125x - 100992x_U}{400000x^5}\right)\right. \\
&+ \frac{\beta_2^2}{\beta_0^6}\left(\frac{1}{4x^4} - \frac{x_U}{5x^5}\right) - 2\frac{\beta_1}{\beta_0^2}\left(\frac{1}{x} - \frac{x_U}{4x^2} + \frac{\ln x}{x} - \frac{x_U\ln x}{2x^2}\right) \\
&+ 2\frac{\beta_1^2}{\beta_0^4}\left(\frac{9(3x-2x_U)\ln^2(x) + 6x_U\ln(x) - 27x + 20x_U}{54x^3}\right) + 2\frac{\beta_2}{\beta_0^3}\left(\frac{1}{2x^2} - \frac{x_U}{3x^3}\right) \\
&- 2\frac{\beta_1^3}{\beta_0^6}\left(\frac{96(4x-3x_U)\ln^3(x) + 72x_U\ln^2(x) + (324x_U - 384x)\ln(x) - 128x + 81x_U}{1152x^4}\right) \\
&- 2\frac{\beta_1\beta_2}{\beta_0^5}\left(-\frac{x_U}{16x^4} - \frac{x_U\ln(x)}{4x^4} + \frac{1}{9x^3} + \frac{\ln(x)}{3x^3}\right) \\
&+2\frac{\beta_1^2\beta_2}{\beta_0^7}\left(\frac{200(5x-4x_U)\ln^2(x) + (480x_U - 500x)\ln(x) - 1125x + 896x_U}{4000x^5}\right)\Bigg]\Bigg|_{x_L}^{x_U} \qquad (2.132) \\
C_{\Gamma_2}^{\rm NNLL} &= \int_{\mu_L}^{\mu_U}\frac{d\bar{\mu}}{\bar{\mu}}\,\Gamma_2\left(\frac{\alpha_s(\bar{\mu})}{4\pi}\right)^3\ln\frac{\mu_U^2}{\bar{\mu}^2}
\end{aligned}
$$

$$= \frac{\Gamma_2}{2\beta_0^3}\int_{x_L}^{x_U} dx\,\left(\frac{1}{x} - \frac{\beta_1}{\beta_0^2}\frac{\ln x}{x^2} + \frac{\beta_1^2}{\beta_0^4}\frac{\ln^2 x - \ln x - 1}{x^3} + \frac{\beta_2}{\beta_0^3}\frac{1}{x^3}\right)^3 (x_U - x)$$
$$= \frac{\Gamma_2}{2\beta_0^3}\left[-\frac{\beta_1^3}{\beta_0^6}\left(-\frac{6x_U}{625x^5} - \frac{x_U\ln^3(x)}{5x^5} - \frac{3x_U\ln^2(x)}{25x^5} - \frac{6x_U\ln(x)}{125x^5} + \frac{3}{128x^4}\right.\right.$$
$$\left.+\frac{\ln^3(x)}{4x^4} + \frac{3\ln^2(x)}{16x^4} + \frac{3\ln(x)}{32x^4}\right)$$
$$+ \frac{\beta_1^6}{\beta_0^{12}}\left(\frac{21703x_U}{131072x^8} - \frac{x_U\ln^6(x)}{8x^8} + \frac{9x_U\ln^5(x)}{32x^8} + \frac{45x_U\ln^4(x)}{256x^8} - \frac{275x_U\ln^3(x)}{512x^8}\right.$$
$$- \frac{825x_U\ln^2(x)}{4096x^8} + \frac{5319x_U\ln(x)}{16384x^8} - \frac{159580}{823543x^7} + \frac{\ln^6(x)}{7x^7} - \frac{15\ln^5(x)}{49x^7}$$
$$\left.-\frac{75\ln^4(x)}{343x^7} + \frac{1415\ln^3(x)}{2401x^7} + \frac{4245\ln^2(x)}{16807x^7} - \frac{41931\ln(x)}{117649x^7}\right)$$
$$+ \frac{\beta_2^3}{\beta_0^9}\left(\frac{1}{7x^7} - \frac{x_U}{8x^8}\right) + \frac{1}{x} - \frac{x_U}{2x^2}$$
$$- 3\frac{\beta_1}{\beta_0^2}\left(-\frac{x_U}{9x^3} - \frac{x_U\ln(x)}{3x^3} + \frac{1}{4x^2} + \frac{\ln(x)}{2x^2}\right)$$
$$+ 3\frac{\beta_1^2}{\beta_0^4}\left(-\frac{x_U}{32x^4} - \frac{x_U\ln^2(x)}{4x^4} - \frac{x_U\ln(x)}{8x^4} + \frac{2}{27x^3} + \frac{\ln^2(x)}{3x^3} + \frac{2\ln(x)}{9x^3}\right)$$
$$+ 3\frac{\beta_1^2}{\beta_0^4}\left(\frac{9x_U}{32x^4} - \frac{x_U\ln^2(x)}{4x^4} + \frac{x_U\ln(x)}{8x^4} - \frac{10}{27x^3} + \frac{\ln^2(x)}{3x^3} - \frac{\ln(x)}{9x^3}\right)$$
$$- 6\frac{\beta_1^3}{\beta_0^6}\left(\frac{29x_U}{625x^5} - \frac{x_U\ln^3(x)}{5x^5} + \frac{2x_U\ln^2(x)}{25x^5} + \frac{29x_U\ln(x)}{125x^5} - \frac{9}{128x^4} + \frac{\ln^3(x)}{4x^4}\right.$$
$$\left.-\frac{\ln^2(x)}{16x^4} - \frac{9\ln(x)}{32x^4}\right)$$
$$+ 3\frac{\beta_1^4}{\beta_0^8}\left(\frac{7x_U}{648x^6} - \frac{x_U\ln^4(x)}{6x^6} + \frac{x_U\ln^3(x)}{18x^6} + \frac{7x_U\ln^2(x)}{36x^6} + \frac{7x_U\ln(x)}{108x^6} - \frac{56}{3125x^5}\right.$$
$$\left.+\frac{\ln^4(x)}{5x^5} - \frac{\ln^3(x)}{25x^5} - \frac{28\ln^2(x)}{125x^5} - \frac{56\ln(x)}{625x^5}\right)$$
$$+ 3\frac{\beta_1^4}{\beta_0^8}\left(-\frac{67x_U}{324x^6} - \frac{x_U\ln^4(x)}{6x^6} + \frac{2x_U\ln^3(x)}{9x^6} + \frac{5x_U\ln^2(x)}{18x^6} - \frac{13x_U\ln(x)}{54x^6}\right.$$
$$\left.+\frac{789}{3125x^5} + \frac{\ln^4(x)}{5x^5} - \frac{6\ln^3(x)}{25x^5} - \frac{43\ln^2(x)}{125x^5} + \frac{164\ln(x)}{625x^5}\right)$$
$$- 3\frac{\beta_1^5}{\beta_0^{10}}\left(-\frac{3263x_U}{117649x^7} - \frac{x_U\ln^5(x)}{7x^7} + \frac{9x_U\ln^4(x)}{49x^7} + \frac{85x_U\ln^3(x)}{343x^7} - \frac{431x_U\ln^2(x)}{2401x^7}\right.$$
$$\left.-\frac{3263x_U\ln(x)}{16807x^7} + \frac{37}{972x^6} + \frac{\ln^5(x)}{6x^6} - \frac{7\ln^4(x)}{36x^6} - \frac{8\ln^3(x)}{27x^6} + \frac{5\ln^2(x)}{27x^6} + \frac{37\ln(x)}{162x^6}\right)$$
$$+ 3\frac{\beta_2}{\beta_0^3}\left(\frac{1}{3x^3} - \frac{x_U}{4x^4}\right) - 6\frac{\beta_1\beta_2}{\beta_0^5}\left(-\frac{x_U}{25x^5} - \frac{x_U\ln(x)}{5x^5} + \frac{1}{16x^4} + \frac{\ln(x)}{4x^4}\right)$$

$$
\begin{aligned}
&+3\frac{\beta_1^2\beta_2}{\beta_0^7}\left(-\frac{x_U}{108x^6}-\frac{x_U\ln^2(x)}{6x^6}-\frac{x_U\ln(x)}{18x^6}+\frac{2}{125x^5}+\frac{\ln^2(x)}{5x^5}+\frac{2\ln(x)}{25x^5}\right)\\
&+6\frac{\beta_1^2\beta_2}{\beta_0^7}\left(\frac{225(6x-5x_U)\ln^2(x)+(750x_U-810x)\ln(x)-1512x+1250x_U}{6750x^6}\right)\\
&-6\frac{\beta_1^3\beta_2}{\beta_0^9}\left(\frac{57x_U}{2401x^7}-\frac{x_U\ln^3(x)}{7x^7}+\frac{4x_U\ln^2(x)}{49x^7}+\frac{57x_U\ln(x)}{343x^7}-\frac{7}{216x^6}+\frac{\ln^3(x)}{6x^6}\right.\\
&\left.-\frac{\ln^2(x)}{12x^6}-\frac{7\ln(x)}{36x^6}\right)\\
&+3\frac{\beta_1^4\beta_2}{\beta_0^{11}}\left(-\frac{615x_U}{4096x^8}-\frac{x_U\ln^4(x)}{8x^8}+\frac{3x_U\ln^3(x)}{16x^8}+\frac{25x_U\ln^2(x)}{128x^8}-\frac{103x_U\ln(x)}{512x^8}\right.\\
&\left.+\frac{2929}{16807x^7}+\frac{\ln^4(x)}{7x^7}-\frac{10\ln^3(x)}{49x^7}-\frac{79\ln^2(x)}{343x^7}+\frac{528\ln(x)}{2401x^7}\right)\\
&+3\frac{\beta_2^2}{\beta_0^6}\left(\frac{1}{5x^5}-\frac{x_U}{6x^6}\right)-3\frac{\beta_1\beta_2^2}{\beta_0^8}\left(-\frac{x_U}{49x^7}-\frac{x_U\ln(x)}{7x^7}+\frac{1}{36x^6}+\frac{\ln(x)}{6x^6}\right)\\
&+3\frac{\beta_1^2\beta_2^2}{\beta_0^{10}}\left(\frac{35x_U}{256x^8}-\frac{x_U\ln^2(x)}{8x^8}+\frac{3x_U\ln(x)}{32x^8}-\frac{54}{343x^7}+\frac{\ln^2(x)}{7x^7}-\frac{5\ln(x)}{49x^7}\right)\Bigg]\Bigg|_{x_L}^{x_U}
\end{aligned}
\tag{2.133}
$$

The final result is then

$$
\int_{\mu_L}^{\mu_U}\frac{d\bar{\mu}}{\bar{\mu}}\left(\gamma^V+\Gamma_{\text{cusp}}\ln\frac{\mu_U^2}{\bar{\mu}^2}\right)=C_{\gamma_0}^{\text{NNLL}}+C_{\gamma_1}^{\text{NNLL}}+C_{\Gamma_0}^{\text{NNLL}}+C_{\Gamma_1}^{\text{NNLL}}+C_{\Gamma_2}^{\text{NNLL}}\,. \tag{2.134}
$$

2.6.4 Evolution of the Hard Matching Coefficient

The evolution of the hard matching coefficient C_V, which is related to the usual hard function as $H=|C_V|^2$, is given by

$$
\frac{d}{d\ln\mu}\ln C_V(Q^2/\mu^2)=\gamma_{C_V}\left(\alpha_s(\mu),\ln\frac{Q^2}{\mu^2}\right)\,, \tag{2.135}
$$

$$
\gamma_{C_V}=\Gamma_{\text{cusp}}(\alpha_s)\ln\frac{Q^2}{\mu^2}+\gamma^V(\alpha_s)\,, \tag{2.136}
$$

where the cusp term is related to the evolution of the Sudakov double logarithms and the remaining term with the evolution of single logarithms. The exact solution of this equation is

$$
\begin{aligned}
C_V(Q^2/\mu_f^2)=&C_V(Q^2/\mu_i^2)\exp\left[\int_{\mu_i}^{\mu_f}\frac{d\bar{\mu}}{\bar{\mu}}\,\gamma_{C_V}\left(\alpha_s(\bar{\mu}),\ln\frac{Q^2}{\bar{\mu}^2}\right)\right]\\
=&C_V(Q^2/\mu_i^2)\exp\left[\int_{\alpha_s(\mu_i)}^{\alpha_s(\mu_f)}\frac{d\bar{\alpha}_s}{\beta(\bar{\alpha}_s)}\,\gamma_{C_V}\left(\bar{\alpha}_s\right)\right]\,,
\end{aligned}
\tag{2.137}
$$

where we have used that $d/d\ln\mu = \beta(\alpha_s)\, d/d\alpha_s$, where $\beta(\alpha_s) = d\alpha_s/d\ln\mu$ is the QCD β-function.

Below we give the expressions for the anomalous dimensions and the QCD β-function, in the $\overline{\rm MS}$ renormalization scheme. We use the following expansions:

$$\Gamma_{\rm cusp} = \sum_{n=1}^{\infty} \Gamma_{n-1} \left(\frac{\alpha_s}{4\pi}\right)^n , \tag{2.138}$$

$$\gamma^V = \sum_{n=1}^{\infty} \gamma^V_{n-1} \left(\frac{\alpha_s}{4\pi}\right)^n , \tag{2.139}$$

$$\beta = -2\alpha_s \sum_{n=1}^{\infty} \beta_{n-1} \left(\frac{\alpha_s}{4\pi}\right)^n . \tag{2.140}$$

The coefficients for the cusp anomalous dimension $\Gamma_{\rm cusp}$ are

$$\begin{aligned}
\Gamma_0 =& 4C_F \,, \\
\Gamma_1 =& 4C_F \left[\left(\frac{67}{9} - \frac{\pi^2}{3}\right) C_A - \frac{20}{9}\, T_F n_f\right] , \\
\Gamma_2 =& 4C_F \left[C_A^2 \left(\frac{245}{6} - \frac{134\pi^2}{27} + \frac{11\pi^4}{45} + \frac{22}{3}\,\zeta_3\right) + C_A T_F n_f \left(-\frac{418}{27} + \frac{40\pi^2}{27} - \frac{56}{3}\,\zeta_3\right)\right. \\
& \left. + C_F T_F n_f \left(-\frac{55}{3} + 16\zeta_3\right) - \frac{16}{27}\, T_F^2 n_f^2\right] .
\end{aligned} \tag{2.141}$$

The anomalous dimension γ^V can be determined up to three-loop order from the partial three-loop expression for the on-shell quark form factor in QCD. We have

$$\begin{aligned}
\gamma_0^V =& -6C_F \,, \\
\gamma_1^V =& C_F^2 \left(-3 + 4\pi^2 - 48\zeta_3\right) + C_F C_A \left(-\frac{961}{27} - \frac{11\pi^2}{3} + 52\zeta_3\right) + C_F T_F n_f \left(\frac{260}{27} + \frac{4\pi^2}{3}\right) .
\end{aligned} \tag{2.142}$$

CHAPTER 3

Global Analyses of the Spin-Dependent Proton

3.1 Introduction

So far I have established a procedure which can be used to perform quantum tomography in an unpolarized hadron. In this Chapter, I will describe in details how we perform a global analysis of the polarized structure of hadrons.

Intuitively you can think about a polarized hadron as containing two seas, one sea consists of particles which are influenced by the introduction of the polarization and the other sea consists of particles which are uncorrelated with the polarization. In experiments which measure the spin-dependent structure of the proton, the aim is to remove the background contributions from the uncorrelated sea. This is accomplished by measuring spin asymmetries, which are the difference between two cross sections with opposite spins. For the past five decades, spin asymmetries have served as the experimental driving force for probing this structure. In these early days, it was thought that spin asymmetries should be driven by perturbative contributions, and as a result these spin asymmetries should be small. However, this contrasted with the experimental measurements which demonstrated large spin asymmetries. To reconcile the spin asymmetries with QCD, it was demonstrated that the relatively large spin asymmetries arise due to correlations between multiple partons, which is naturally addressed in higher twist contributions to the cross section.

By far, the most experimentally and theoretically studied example of such an effect is the Sivers asymmetry, in which an initial-state hadron is transversely polarized. The expression for the cross section for a polarized hadron can be obtained by replacing the unpolarized

TMD with the spin-dependent quark-quark correlation function

$$\Phi^{\text{unsub}}\left(x, \boldsymbol{k}_\perp, \boldsymbol{S}; \mu, \zeta/\nu^2\right) = \left(f - \frac{\epsilon_\perp^{\rho\sigma} k_{\perp\rho} S_{\perp\sigma}}{M} f_{1T}^\perp\right) \frac{\not{\bar{n}}}{4} + \dots \,. \tag{3.1}$$

In this expression, the ellipsis represents other TMDs do not do not contribute to the Sivers asymmetry. The second term contains the contribution of the Sivers function [64, 65], which provides the distribution of unpolarized quarks in a transversely polarized hadron and is the main topic of this chapter. An important aspect of the second term is that the prefactor changes sign under time reversal. This can be readily seen by re-writing this term as

$$\epsilon_\perp^{\rho\sigma} k_{\perp\rho} S_{\perp\sigma} = \left(\hat{\boldsymbol{P}} \times \boldsymbol{k}_\perp\right) \cdot \boldsymbol{S} \,. \tag{3.2}$$

Since QCD is invariant under time reversal, the partonic cross section must also be must then also be time reversal odd. From this logic, in Ref. [66, 67] it was demonstrated that time reversal odd partonic cross sections could be obtained by considering poles originating from three parton correlations functions. For instance in Fig. 3.1, I have provided the partonic processes for the Sivers asymmetry in Drell-Yan and Semi-Inclusive DIS. In a collinear framework, the introduction of another gluon produces Wilson coefficient functions in the OPE which are suppressed by Λ_{QCD}/Q and thus enter at collinear twist-3. This three parton correlation function is known as the Qiu-Sterman function. In a collinear limit, one needs to consider two types of poles. The soft gluon poles occur where the additional gluon has a Bjorken $x_g \to 0$ and the soft gluon attaches to an external parton. The hard gluon poles occur where an internal propagators go on shell and $x_g \neq 0$. In a TMD framework, the tree level hard contribution has no internal lines and as a result, the poles which generate the spin asymmetry only occur in the limit that $x_g \to 0$. Due to this $x_g \to 0$ scaling, the Sivers function can be treated as a two parton correlation function which is related to the limit of the Qiu-Sterman function. This connection between the Sivers function and the Qiu-Sterman function has important consequences for universality. It is important to note that the poles enter into the partonic interaction are simply factors of ig. These factors are commonly absorbed into the definition of the Sivers function to render the partonic contribution time even while making the Sivers function time odd as a result. This absorption

has causes the Sivers functions in Semi-Inclusive DIS and Drell-Yan to be opposite from one another.

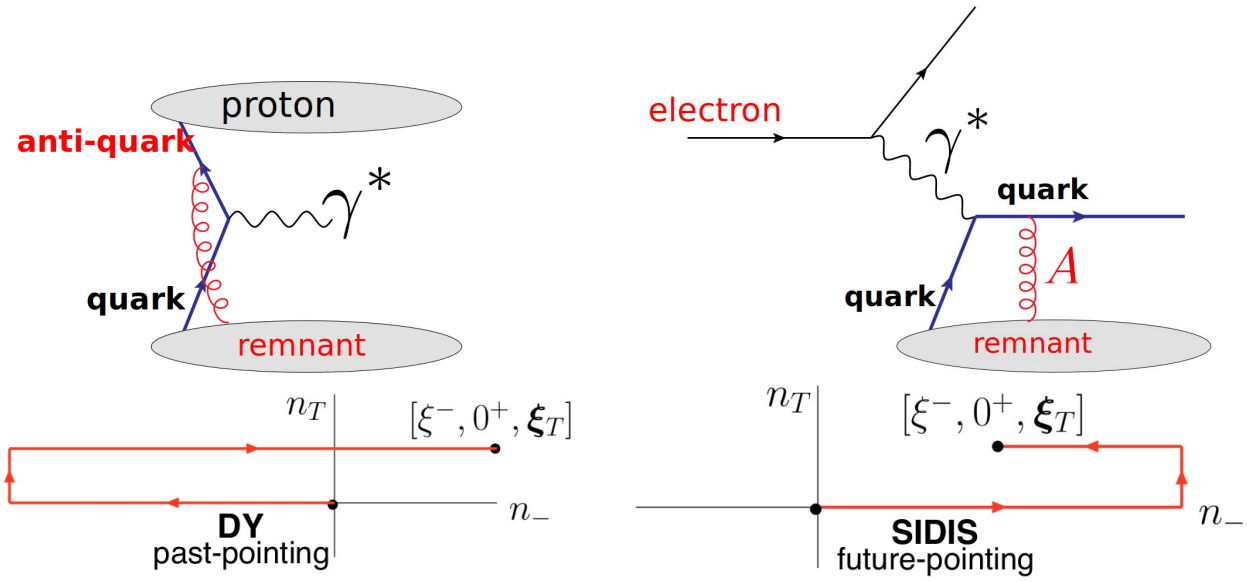

Figure 3.1: Top: Diagrams associated with the soft gluon pole contribution in the hard diagram. Bottom: The Wilson line structure for Drell-Yan and Semi-Inclusive DIS.

A fundamental goal of the future Electron Ion Collider (EIC) [68] will be high precision determination of of the Sivers function. Within the past several years, the field of TMDs has been pushing for increased perturbative accuracy. In [69, 70] global extractions of the unpolarized TMD PDFs and TMD FFs were performed from Semi-Inclusive DIS and Drell-Yan data at leading order (LO) and next-to-leading logarithmic (NLL) accuracy. In [71] the unpolarized TMD PDFs were extracted at next-to-next-to leading order (NNLO) and next-to-next-to leading logarithm (NNLL) accuracy. In [72] the TMD PDFs were extracted at NNLO+N^{3}LL accuracy from Drell-Yan data. In [73] and [74], the TMD PDFs and TMD FFs were extracted simultaneously from Semi-Inclusive DIS and Drell-Yan data at NNLO+N^{3}LL. Progress has also been made in understanding the predictive power of the TMD factorization formalism in different kinematic regions [75, 76], and in matching with the collinear factorization [77, 78, 79].

Prior to my analysis, the highest precision ever extraction of the Sivers function has been

at LO+NLL in [80, 81]. However, I will note that after my analysis an additional work was performed at LO+N^{3}LL accuracy in Refs. [82, 83]. In this chapter, I will discuss my work where I performed the first and only extraction of the quark Sivers function at NLO+NNLL. This analysis took into consideration for the first time the global set of experimental data, which included Semi-Inclusive DIS at HERMES, COMPASS, and JLab, Drell-Yan lepton pair at COMPASS, and W/Z production at RHIC. At HERMES, the Sivers function has been probed by measuring both pion and kaon production in Semi-Inclusive DIS on a proton target [5]. At COMPASS, the Sivers asymmetries have been measured in [84] for unidentified charged hadron production from the proton target, with a re-analysis of this data in [6]. The measurements with a deuteron target are presented in [4]. The Sivers function has also been probed for a neutron target at JLab for pion production in [7]. To test the modified universality prediction, Drell-Yan Sivers asymmetries have been measured at COMPASS [8] for virtual photon (or lepton pair) production at relatively small energy scales of $Q \sim$ a few GeV, as well as RHIC [9] for W and Z production at much large energy scales, $Q \sim M_{W/Z}$. Finally, after our paper was published multi-dimensional binning was performed in [85].

The rest of this chapter is organized as follows. In Sec. 3.2, I will summarize the relevant TMD factorization formalism for Semi-Inclusive DIS and Drell-Yan processes. In Sec. 3.3, I first discuss our non-perturbative parameterizations for the unpolarized TMD PDFs and TMD FFs, and benchmark them with the Semi-Inclusive DIS hadron multiplicity and Drell-Yan cross section data. I then present our non-perturbative parametrization for the Sivers function, and discuss how we performed the DGLAP evolution of the Qiu-Sterman function. In Sec. 3.4, I'll present our fit results, where I'll explore several different ways for performing the fit. In Sec. 3.5 I provide predictions for Sivers asymmetry at the EIC. I conclude this chapter in Sec. 3.6.

3.2 Formalism

In this section, I provide the TMD factorization formalism for the Sivers asymmetry in Semi-Inclusive DIS, Drell-Yan and vector boson production. I'll begin with Semi-Inclusive DIS in

Sec. 3.2.1, while in Sec. 3.2.2 and 3.2.3 I'll present the formalism for Drell-Yan lepton pair and W/Z boson production, respectively.

3.2.1 Sivers Formalism in Semi-Inclusive DIS

The factorized cross section for Semi-Inclusive DIS can be obtained in a similar manner that I demonstrated for Drell-Yan. In the appendix, I provide finer details of this calculation. In this section however, I quote that the factorized cross section [86, 34]. To begin, let's denote the momenta and the spin vectors as $e(\ell) + p\,(P, \mathbf{S}_\perp) \to e\,(\ell') + h\,(P_h) + X$, where $\mathbf{S}_\perp$ is the transverse spin vector of the polarized nucleon. As I discussed previously, when introducing a spin a part of the distribution will be affected while another part will remain unchanged. Therefore, the factorized cross section can be written as

$$\frac{d\sigma}{d\mathcal{PS}} = \sigma_0^{\text{DIS}} \left[F_{UU} + \sin(\phi_h - \phi_s) F_{UT}^{\sin(\phi_h - \phi_s)} \right] . \tag{3.3}$$

In this expression σ_0^{DIS} is the leading order (LO) electromagnetic scattering cross section given by

$$\sigma_0^{\text{DIS}} = \frac{2\pi\alpha_{\text{EM}}^2}{Q^4} \left[1 + (1-y)^2 \right] , \tag{3.4}$$

where α_{EM} is the electromagnetic fine structure constant. The function F_{UU} is the spin-independent structure function and $F_{UT}^{\sin(\phi_h - \phi_s)}$ is the spin-dependent one. We can see from the expression for the spin-dependent structure function that there is a sinusoidal modulation between the angles ϕ_h and ϕ_s, the azimuthal angles of $\boldsymbol{P}_{h\perp}$produced hadron and the spin of the parent hadron. This modulation originates from the prefactor attached to the Sivers function in the quark correlation function.

The interaction between the quark and the electron is moderated through the exchange of a virtual photon with momentum $q = \ell' - \ell$ with invariant mass $-Q^2$ while the electron-proton center of mass energy is denoted S. Using these kinematic variables, the we can define the momentum fraction variables

$$x_B = \frac{Q^2}{2P \cdot q} , \qquad y = \frac{P \cdot q}{P \cdot l} = \frac{Q^2}{x_B S} , \qquad z_h = \frac{P \cdot P_h}{P \cdot q} . \tag{3.5}$$

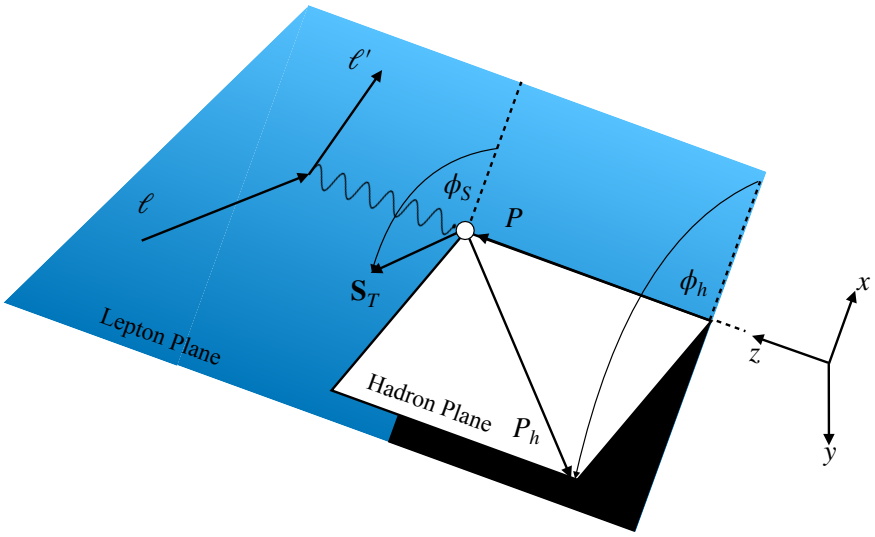

Figure 3.2: The SIDIS cross section in the hadronic Breit frame.

In Eq. 3.3, $d\mathcal{PS} = dx_B\, dQ^2\, dz_h\, d^2P_{h\perp}$ is the phase space element. In this phase space element is the transverse momentum of the observed final-state hadron.

In Fig. 3.2, I have included a plot demonstrating the various angles that enter into the scattering cross section. For the purpose of experiments, it is conventional to take ϕ_s to be $\pi/2$ so that the spin is oriented in the y direction. Experimental measurements also take ϕ_h to be 0 so that the hadron moves in the x direction.

The Sivers asymmetry is the experimentally measured quantity and is given by

$$A_{UT}^{\sin(\phi_h-\phi_s)} = \frac{F_{UT}^{\sin(\phi_h-\phi_s)}}{F_{UU}}\,. \tag{3.6}$$

To obtain the factorized expressions for the structure functions, I'll note that the projection operators for the unpolarized TMD PDF and the Sivers function are the same. Therefore the hard contributions are identical in the two processes. Furthermore, I also note that since unpolarized quarks are produced in both processes, the soft functions must be identical. The structure functions can then be shown to have the form

$$F_{UU}(x_B, z_h, P_{h\perp}, Q) = H^{\rm DIS}(Q;\mu_Q)\,\mathcal{C}^{\rm DIS}\left[fD\right]\,, \tag{3.7}$$

$$F_{UT}^{\sin(\phi_h-\phi_s)}(x_B, z_h, P_{h\perp}, Q) = H^{\rm DIS}(Q;\mu_Q)\,\mathcal{C}^{\rm DIS}\left[-\frac{\hat{\mathbf{h}}\cdot\mathbf{k}_\perp}{M} f_{1T}^\perp D\right]\,. \tag{3.8}$$

To obtain the hard function, I have just performed the calculation in the previous section except that I have taken the virtuality of the photon to be negative. The exact form is given by

$$H^{\rm DIS}(Q;\mu) = H^{\rm DIS}(Q;\mu_Q)\,\exp\left(\int_{\mu_Q}^{\mu}\frac{d\mu'}{\mu'}\Gamma_H\left(Q;\mu'\right)\right)\,. \tag{3.9}$$

$$H^{\rm DIS}(Q;\mu_Q) = 1+\frac{\alpha_s}{\pi}C_F\left[\frac{3}{2}\ln\left(\frac{Q^2}{\mu_Q^2}\right)-\frac{1}{2}\ln^2\left(\frac{Q^2}{\mu_Q^2}\right)-4+\frac{\pi^2}{12}\right]\,, \tag{3.10}$$

which matches the result in [61, 87]. In these expressions, I have used the short-hand notation

$$\begin{aligned}\mathcal{C}^{\rm DIS}\left[wAB\right] =& \sum_q e_q^2\int d^2\mathbf{k}_\perp\,d^2\mathbf{p}_\perp\,\delta^2\left(z_h\mathbf{k}_\perp+\mathbf{p}_\perp-\mathbf{P}_{h\perp}\right)w(\mathbf{k}_\perp,\mathbf{p}_\perp)\\ &\times B_{h/q}(z_h,p_\perp;\mu,\zeta_2)\,A_{q/p}(x_B,k_\perp;\mu,\zeta_1)\,,\end{aligned} \tag{3.11}$$

for the convolution integrals. In these expressions e_q is the fractional electric charge for the quarks. $\mathbf{k}_\perp$ represents the transverse momentum of the quark relative to the nucleon, while $\mathbf{p}_\perp$ is the transverse momentum of the final state hadron relative to the fragmenting quark. $\hat{\mathbf{h}}=\mathbf{P}_{h\perp}/P_{h\perp}$ is the unit vector which points in the direction of the final-state hadron transverse momentum and M is the mass of the struck nucleon. In this expression, I have introduced $f_{1T,q/p}^{\perp}$ is the Sivers function in Semi-Inclusive DIS and $D_{h/q}$ is the unpolarized TMD FF.

Once again, we simplify the convolution integrals by working in b-space and the structure functions become

$$\begin{aligned}F_{UU}(x_B,z_h,P_{h\perp},Q) =& H^{\rm DIS}(Q;\mu)\sum_q e_q^2\int_0^\infty\frac{b\,db}{2\pi}J_0\left(\frac{bP_{h\perp}}{z_h}\right)\\ &\times D_{h/q}(z_h,b;\mu,\zeta_2)\,f_{q/p}(x_B,b;\mu,\zeta_1)\,,\end{aligned} \tag{3.12}$$

$$\begin{aligned}F_{UT}^{\sin(\phi_h-\phi_s)}(x_B,z_h,P_{h\perp},Q) =& H^{\rm DIS}(Q;\mu)\sum_q e_q^2\int_0^\infty\frac{b^2\,db}{4\pi}J_1\left(\frac{bP_{h\perp}}{z_h}\right)\\ &\times D_{h/q}(z_h,b;\mu,\zeta_2)\,f_{1T,q/p}^{\perp}(x_B,b;\mu,\zeta_1)\,.\end{aligned} \tag{3.13}$$

The TMD FF and the b-space Sivers functions are defined in terms of their momentum space counter parts as

$$D_{h/q}(z,b;\mu,\zeta) = \int \frac{d^2\mathbf{p}_\perp}{z^2} e^{-i\mathbf{p}_\perp\cdot\mathbf{b}/z} D_{h/q}(z,p_\perp;\mu,\zeta)\,, \tag{3.14}$$

$$\begin{aligned} f_{1T,q/p}^{\perp\,\alpha\,\mathrm{SIDIS}}(x,b;\mu,\zeta) =& \frac{1}{M}\int d^2\mathbf{k}_\perp\, k_\perp^\alpha\, e^{-i\mathbf{k}_\perp\cdot\mathbf{b}} f_{1T,q/p}^{\perp\,\mathrm{SIDIS}}(x,k_\perp;\mu,\zeta) \\ \equiv& \left(\frac{ib^\alpha}{2}\right) f_{1T,q/p}^{\perp}(x,b;\mu,\zeta)\,. \end{aligned} \tag{3.15}$$

As in the case of the TMD PDF, these TMDs can be expanded in terms of collinear distributions. The TMD FF can naturally be matched onto the collinear FF. Since the Sivers function is related to a limit of the Qiu-Sterman function, it naturally matches onto that function and we have the matching relations

$$D_{h/q}(z,b;\mu,\zeta) = \frac{1}{z^2}\left[\hat{C}_{i\leftarrow q}\otimes D_{h/i}\right](z,b;\mu,\zeta)\,, \tag{3.16}$$

$$f_{1T,q/p}^{\perp}(x,b;\mu,\zeta) = \left[\bar{C}_{q\leftarrow i}\bar{\otimes} T_{F\,i/p}\right](x,b;\mu,\zeta)\,, \tag{3.17}$$

In the case of D, the operator $\otimes$ denotes the convolution that was previously discussed. In these expressions, the sum over the index $i = q, g$ is implicit. The convolution in the case of the Sivers function is more complicated, since it involves two kinematic variables $\hat{x}_1$ and $\hat{x}_2$:

$$\left[\bar{C}_{q\leftarrow i}\bar{\otimes} T_{F\,i/p}\right](x,b;\mu,\zeta) = \int_x^1 \frac{d\hat{x}_1}{\hat{x}_1}\frac{d\hat{x}_2}{\hat{x}_2}\bar{C}_{q\leftarrow i}(x/\hat{x}_1, x/\hat{x}_2, b;\mu,\zeta)\, T_{F\,i/p}(\hat{x}_1,\hat{x}_2;\mu)\,. \tag{3.18}$$

The C functions in the above equations are the Wilson coefficient functions, and their expressions at NLO are given in Appendix. 3.7.

For the cross section, it is typical to take $\mu = Q$, $\zeta = Q^2$, $\mu_c = \mu_s = \mu_b$, and $\zeta_i = \mu_b^2$. The expressions for the cross section become

$$\begin{aligned} F_{UU}(x_B,z_h,P_{h\perp},Q) =& H^{\mathrm{DIS}}(Q;Q)\int_0^\infty \frac{db\,b}{2\pi} J_0\left(\frac{bP_{h\perp}}{z_h}\right)\sum_q e_q^2 \\ &\times\left[C_{q\leftarrow i}\otimes f_{i/p}\right](x_B,b;\mu_b,\mu_b^2)\,\frac{1}{z_h^2}\left[\hat{C}_{j\leftarrow q}\otimes D_{h/j}\right](z_h,b;\mu_b,\mu_b^2) \\ &\times\exp\left[S_{\mathrm{pert}}\left(b;\mu_b,Q,\mu_b^2,Q^2\right) - S_{\mathrm{NP}}^f(b,Q_0,Q) - S_{\mathrm{NP}}^D(z_h,b,Q_0,Q)\right], \end{aligned} \tag{3.19}$$

$$F_{UT}^{\sin(\phi_h-\phi_s)}(x_B,z_h,P_{h\perp},Q) = H^{\mathrm{DIS}}(Q;Q)\int_0^\infty \frac{db\,b^2}{4\pi} J_1\left(\frac{bP_{h\perp}}{z_h}\right)\sum_q e_q^2 \tag{3.20}$$

$$\times \left[\bar{C}_{q\leftarrow i} \otimes T_{F\,i/p}\right](x_B, b; \mu_b, \mu_b^2) \frac{1}{z_h^2} \left[\hat{C}_{j\leftarrow q} \otimes D_{h/j}\right] \left(z_h, b; \mu_b, \mu_b^2\right)$$
$$\times \exp\left[S_{\text{pert}}\left(b; \mu_b, Q, \mu_b^2, Q^2\right) - S_{\text{NP}}^s(b, Q_0, Q) - S_{\text{NP}}^D(z_h, b, Q_0, Q)\right].$$

Note that in principle as b grows large enough, an issue occurs as $1/b \sim \Lambda_{\text{QCD}}$ due to the Landau pole. In Sec. 3.3.1 I will address this issue. In the expression for the structure functions, I have introduced the non-perturbative Sudakov functions for the TMD FF and Sivers function as S_{NP}^D, and S_{NP}^s.

3.2.2 Sivers Formalism in Drell-Yan

Analogous to Semi-Inclusive DIS, the cross section with a transversely polarized initial-state hadron is given by [88, 89, 90, 91]

$$\frac{d\sigma}{d\mathcal{PS}} = \sigma_0^{\text{DY}} \left[W_{UU} + \sin(\phi_q - \phi_s) W_{UT}^{\sin(\phi_q - \phi_s)}\right]. \tag{3.21}$$

In this expression, the point-like scattering cross section for $q\,\bar{q} \to l\,\bar{l}$ is given by

$$\sigma_0^{\text{DY}} = \frac{4\pi\alpha_{\text{EM}}^2}{3SQ^2N_C}, \tag{3.22}$$

while $S = (P_A + P_B)^2$ is the center of mass energy squared and $N_C = 3$ is the number of colors. Furthermore, W_{UU} and $W_{UT}^{\sin(\phi_q - \phi_s)}$ are the spin-independent and spin-dependent structure functions. Once again, the spin-dependent structure function contains a sinusoidal modulation between the azimuthal angles of $\boldsymbol{S}_\perp$ and $\boldsymbol{q}_\perp$. Note that I have deviated from the notation in [89] by writing the Drell-Yan structure functions as W in order to differentiate them from the Semi-Inclusive DIS structure function. The phase space element is given by $d\mathcal{PS} = dQ^2\, dy\, d^2q_\perp$, where y, Q, and y are the rapidity, invariant mass, and transverse momentum of the virtual photon.

We note that in the case of Drell-Yan, there are two asymmetries which are measured in the literature. The first asymmetry is analogous to the one in Semi-Inclusive DIS and is given by

$$A_{UT}^{\sin(\phi_q - \phi_s)} = \frac{W_{UT}^{\sin(\phi_q - \phi_s)}}{W_{UU}}. \tag{3.23}$$

This is the measurement that was performed by COMPASS. However the STAR measurement is A_N, which differs from $A_{UT}^{\sin(\phi_q-\phi_s)}$ by a minus sign.

Using the results from Sec. 2.5, we can write the factorized structure function as

$$W_{UU}(x_a, x_b, q_\perp, Q) = H^{\rm DY}(Q;\mu)\, \mathcal{C}^{\rm DY}\left[f\ f\right], \tag{3.24}$$

$$W_{UT}^{\sin(\phi_q-\phi_s)}(x_a, x_b, q_\perp, Q) = H^{\rm DY}(Q;\mu)\, \mathcal{C}^{\rm DY}\left[\frac{\hat{\mathbf{q}}_\perp\cdot\mathbf{k}_{aT}}{M}\, f_{1T}^\perp\, f\right]. \tag{3.25}$$

For Drell-Yan, the convolutional integrals are given by

$$\begin{aligned}\mathcal{C}^{\rm DY}\left[wAB\right] =& \sum_q e_q^2 \int d^2\mathbf{k}_{aT}\, d^2\mathbf{k}_{bT}\, \delta^2\left(\mathbf{k}_{aT}+\mathbf{k}_{bT}-\mathbf{q}_\perp\right) w(\mathbf{k_{aT}}, \mathbf{k_{bT}}) \\ & \times A_{q/A}(x_a, k_{aT}^2;\mu,\zeta_1)\, B_{\bar{q}/B}(x_b, k_{bT}^2;\mu,\zeta_2)\,,\end{aligned} \tag{3.26}$$

In this expression, $\mathbf{k}_{aT}$ and $\mathbf{k}_{bT}$ are the transverse momenta of the parton relative to their corresponding nucleon.

In the QCD background section, we calculated the hard function to be

$$H^{\rm DY}(Q;\mu) = H^{\rm DY}(Q;\mu_Q)\, \exp\left(\int_{\mu_Q}^{\mu}\frac{d\mu'}{\mu'}\Gamma_H\left(Q;\mu'\right)\right). \tag{3.27}$$

$$H^{\rm DY}(Q;\mu_Q) = 1+\frac{\alpha_s}{\pi}C_F\left[\frac{3}{2}\ln\left(\frac{Q^2}{\mu_Q^2}\right)-\frac{1}{2}\ln^2\left(\frac{Q^2}{\mu_Q^2}\right)-4+\frac{7\pi^2}{12}\right], \tag{3.28}$$

Since the soft pole contributions to the partonic contributions are opposite in Drell-Yan and Semi-Inclusive DIS, the Sivers functions are defined to be opposite in Drell-Yan and Semi-Inclusive DIS so we have in Eq. 3.8:

$$f_{1T}^{\perp\,\rm DY}(x, k_\perp;\mu,\zeta) = -f_{1T}^{\perp\,\rm SIDIS}(x, k_\perp;\mu,\zeta)\,. \tag{3.29}$$

This will lead to slightly different definition for the Sivers function in the b-space:

$$\begin{aligned}f_{1T,q/p}^{\perp\,\alpha\,\rm DY}(x, b;\mu,\zeta) =& \frac{1}{M}\int d^2\mathbf{k}_\perp\, k_\perp^\alpha\, e^{-i\mathbf{k}_\perp\cdot\mathbf{b}} f_{1T,q/p}^{\perp\,\rm DY}(x, k_\perp;\mu,\zeta) \\ \equiv& \left(-\frac{ib^\alpha}{2}\right) f_{1T,q/p}^\perp(x, b;\mu,\zeta)\,.\end{aligned} \tag{3.30}$$

Note the additional minus sign in the second line of the equation, in comparison with the corresponding Semi-Inclusive DIS expression in Eq. 3.15. Performing the OPE, the expressions for the structure functions take the form

$$W_{UU}(x_a, x_b, q_\perp, Q) = H^{\rm DY}(Q;Q) \int \frac{db\, b}{2\pi} J_0(b\, q_\perp) \sum_q e_q^2 \tag{3.31}$$
$$\times \left[C_{q\leftarrow i} \otimes f_{i/A}\right](x_a, b; \mu_b, \mu_b^2) \left[C_{\bar{q}\leftarrow j} \otimes f_{j/B}\right](x_b, b; \mu_b, \mu_b^2)$$
$$\times \exp\left[S_{\rm pert}(b;\mu_b, Q, \mu_b^2, Q^2) - S^f_{\rm NP}(b, Q_0, Q) - S^f_{\rm NP}(b, Q_0, Q)\right],$$
$$W_{UT}^{\sin(\phi_q-\phi_s)}(x_a, x_b, q_\perp, Q) = H^{\rm DY}(Q;Q) \int \frac{db\, b^2}{4\pi} J_1(b\, q_\perp) \sum_q e_q^2 \tag{3.32}$$
$$\times \left[\bar{C}_{q\leftarrow i} \otimes T_{F\, i/p}\right](x_a, b; \mu_b, \mu_b^2) \left[C_{\bar{q}\leftarrow j} \bar{\otimes} f_{j/B}\right](x_b, b; \mu_b, \mu_b^2)$$
$$\times \exp\left[S_{\rm pert}(b;\mu_b, Q, \mu_b^2, Q^2) - S^s_{\rm NP}(b, Q_0, Q) - S^f_{\rm NP}(b, Q_0, Q)\right].$$

Note that in the second expression, I have already taken into account the sign change in the Sivers functions between Drell-Yan and Semi-Inclusive DIS processes in Eq. 3.29.

3.2.3 Sivers formalism for W/Z ,Production

The case for W/Z production very similar to the case for virtual photon production. For this case, the differential cross section can be written as

$$\frac{d\sigma_V}{d\mathcal{PS}} = \sigma_0^{\rm V} \left[W_{UU,V} + \sin(\phi_q - \phi_s) W_{UT,V}^{\sin(\phi_q-\phi_s)}\right], \tag{3.33}$$

where the phase space $d\mathcal{PS} = dy\, d^2q_\perp$ and $V = W, Z$. I'll note that to arrive at this expression, I have taken $Q = M_V$ where M_V is the mass of the vector boson. This is known as the narrow width approximation. This approximation in general affects the normalization of $q_\perp$ distributions at $Q = M_Z$ at a few percent. However, since we will be interested in a ratio, these percent corrections are negligible.

For W/Z production, the point-like cross section can be written as

$$\sigma_0^W = \frac{\sqrt{2}\pi G_F M_W^2}{S N_C}, \qquad \sigma_0^Z = \frac{\sqrt{2}\pi G_F M_Z^2}{S N_C}, \tag{3.34}$$

where G_F is the Fermi weak coupling constant. The expressions for the structure functions are given by

$$W_{UU,V}(x_a, x_b, q_\perp, Q) = H^{\rm DY}(Q;Q) \int \frac{db\, b}{2\pi} J_0(b\, q_\perp) \sum_{q,q'} e^2_{qq',V} \tag{3.35}$$
$$\times \left[C_{q\leftarrow i} \otimes f_{i/A}\right](x_a, b; \mu_b, \mu_b^2) \left[C_{q'\leftarrow j} \otimes f_{j/B}\right](x_b, b; \mu_b, \mu_b^2)$$
$$\times \exp\left[S_{\rm pert}(b;\mu_b, Q, \mu_b^2, Q^2) - S^f_{\rm NP}(b, Q_0, Q) - S^f_{\rm NP}(b, Q_0, Q)\right],$$
$$W^{\sin(\phi_q-\phi_s)}_{UT,V}(x_a, x_b, q_\perp, Q) = H^{\rm DY}(Q;Q) \int \frac{db\, b^2}{4\pi} J_1(b\, q_\perp) \sum_{q,q'} e^2_{qq',V} \tag{3.36}$$
$$\times \left[\bar{C}_{q\leftarrow i} \otimes T_{F\, i/p}\right](x_a, b; \mu_b, \mu_b^2) \left[C_{q'\leftarrow j} \otimes f_{j/B}\right](x_b, b; \mu_b, \mu_b^2)$$
$$\times \exp\left[S_{\rm pert}(b;\mu_b, Q, \mu_b^2, Q^2) - S^s_{\rm NP}(b, Q_0, Q) - S^f_{\rm NP}(b, Q_0, Q)\right],$$

where we have

$$e^2_{qq',W} = |V_{qq'}|^2\,, \qquad e^2_{qq',Z} = \left(V_q^2 + A_q^2\right)\delta_{qq'}\,. \tag{3.37}$$

Here $|V_{qq'}|^2$ is the CKM matrix, while V_q and A_q are the vector and axial couplings of the Z boson to a quark of flavor q. Just like Eq. 3.23 in the last section, the asymmetry can be written as a ratio of these structure functions in the exactly same form.

3.3 Numerical Input

To obtain the non-perturbative contributions of the Sivers function, we need to parameterize all of the non-perturbative physics. In this section, I will discuss the parameterization that was used in our extraction of the Sivers function. This sub-section is organized as follows. In Sec. 3.3.1, I will first introduce our parameterization of the unpolarized TMDs. In Sec. 3.3.2, I will then parameterize the Sivers function.

3.3.1 Unpolarized Non-perturbative Input

To perform a global analysis of the Sivers function, I chose to parameterize the unpolarized TMDs by taking the results of a previous analysis. Within the literature, there have been

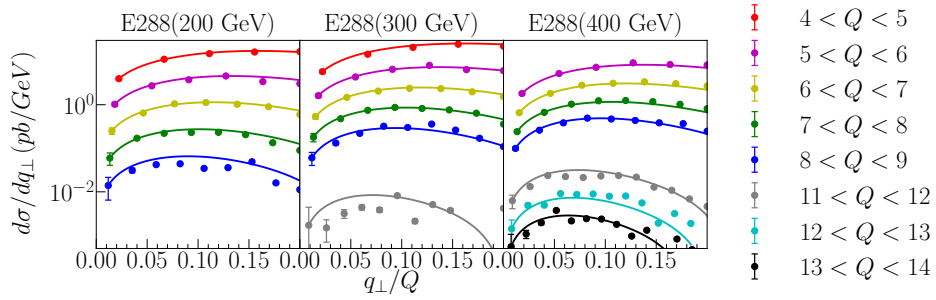

Figure 3.3: The experimental data for Drell-Yan lepton pair production measured by the E288 collaboration [1] plotted as a function of $q_\perp/Q$ are compared with the normalized theoretical curve. Different colors represent different invariant mass of the lepton pair from $4 < Q < 5$, $5 < Q < 6$, $6 < Q < 7$, $7 < Q < 8$, $8 < Q < 9$, $11 < Q < 12$, $12 < Q < 13$, $13 < Q < 14$ GeV, respectively. Three panels correspond to different energies for incident proton beams: 200 GeV (left), 300 GeV (middle), and 400 GeV (right).

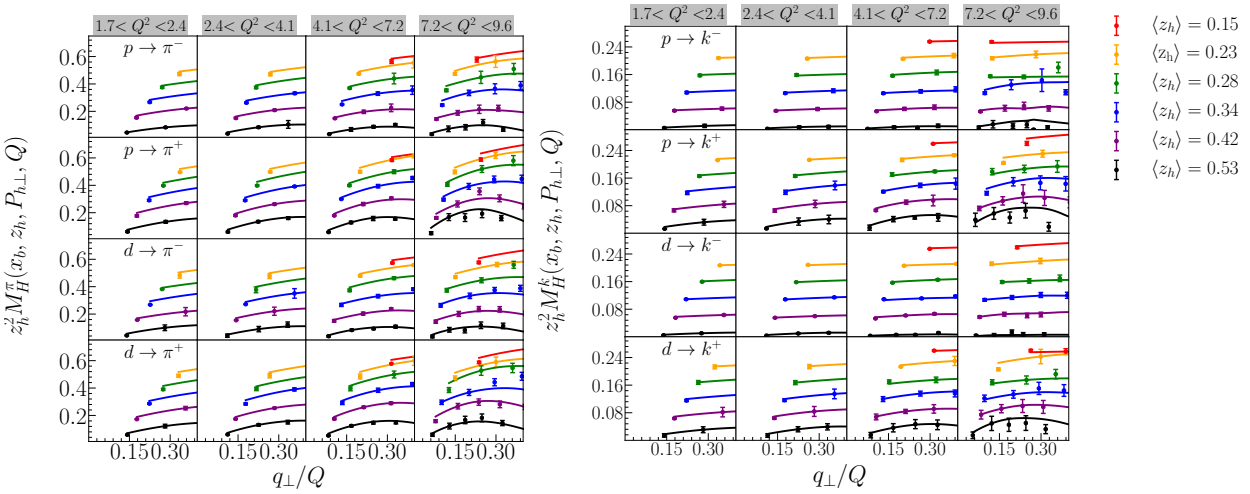

Figure 3.4: Left panel: The HERMES multiplicity data in [2] for pion production from either a proton (denoted as $p \to \pi$) or deuteron (denoted as $d \to \pi$) target. For better presentation, the data is offset by 0.0 for $\langle z_h \rangle = 0.53$, 0.1 for $\langle z_h \rangle = 0.42$, 0.2 for $\langle z_h \rangle = 0.34$, 0.3 for $\langle z_h \rangle = 0.28$, 0.4 for $\langle z_h \rangle = 0.23$, and 0.5 for $\langle z_h \rangle = 0.15$. Right panel: The HERMES multiplicity data for kaon production. The offsets are half of the offsets from the pions.

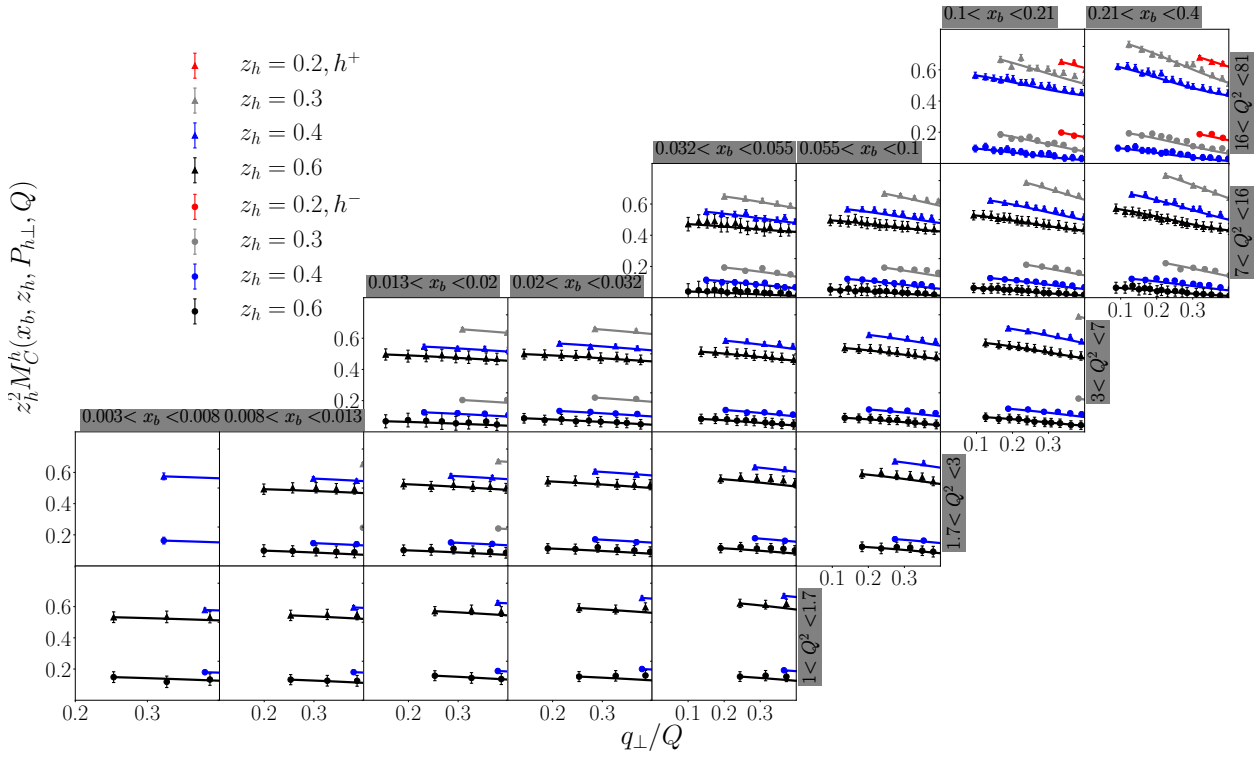

Figure 3.5: The COMPASS multiplicity in [3] for charged hadron production from a deuteron target is compared with the normalized theory curve. The triangular points represent the h^+ data points while the circular data points represent the h^- data points. For better presentation, the h^+ data is offset by a factor of 0.4.

many global analyses of unpolarized TMDs. However, as the goal of this study was to improve upon the extraction of the Sivers function, we must use a parameterization from the literature which was performed at NLO+NNLL. Furthermore, as we are attempting to perform a simultaneous global analysis from data in Semi-Inclusive DIS and Drell-Yan, we must also select a global analysis which simultaneously fit these data. The global analysis which most closely matches these requirements is in [92], in which the unpolarized TMDs were obtained NLO+NLL accuracy from a global analysis. From the analysis in Ref. [92], the non-perturbative factors for the TMD PDF and TMD FF are given by

$$g_q\left(b,Q,Q_0\right) = g_1^f b^2\,, \tag{3.38}$$

$$g_h\left(z,b,Q,Q_0\right) = g_1^D \frac{b^2}{z^2}\,, \tag{3.39}$$

$$g_K(b) = g_2 \ln\left(\frac{b}{b_*}\right)\,, \tag{3.40}$$

such that the non-perturbative contributions to the unpolarized TMD PDF and TMD FF are given by

$$S^f_{\rm NP}(b,Q,Q_0) = -g_q(b,Q,Q_0) - g_K(b)\,, \qquad S^D_{\rm NP}(z,b,Q,Q_0) = -g_h(b,Q,Q_0) - g_K(b)\,. \tag{3.41}$$

The factors which contain g_1^f and g_1^D give the Gaussian width of the TMDs at the scale Q_0. The factor g_2 drives the strength of the non-perturbative rapidity evolution. The values of the parameters that were obtained in this reference are given by

$$g_1^f = 0.106\,, \qquad g_1^D = 0.042\,, \qquad g_2 = 0.84\,. \tag{3.42}$$

Finally, I also note that the COMPASS Drell-Yan data was obtained through the collision of a pion with a polarized proton. In [93] the pion TMD PDF was extracted from the experimental data in [94] and it was found that $g_1^f = 0.082$ for pions. In Eq. 3.40, I have introduced b_*, which is defined as

$$b_* = b/\sqrt{1+b^2/b^2_{\rm max}}\,, \tag{3.43}$$

where $b_{\rm max} = 1.5$. This factor acts to regulate the behavior of the rapidity anomalous dimension in the region where b approaches $1/\Lambda_{\rm QCD}$. Following the work in Ref. [36], we can

replace the scale μ_b with $\mu_{b_*} = 2e^{-\gamma_E}/b_*$ to obtain a cross section that is insensitive to the Landau pole. I'll note that various alternatives to this scheme have been presented in the literature. See for instance Refs. [95, 96, 97].

We will now discuss the parameterization of the collinear physics for the unpolarized TMDs. For the PDF, we used the `HERA_NLO_as_118` parametrization in [98] for the collinear parton distribution functions. To parameterize the collinear pion fragmentation function, we used the DSS14 parameterization [99]. While for the collinear kaon fragmentation function $D_{K/q}(z_h; \mu_{b_*})$, we used the DSS17 parameterization in [100]. For unidentified charged hadrons, we followed the work in [73] to use the approximation $D_{h/q}(z; \mu_{b_*}) = D_{\pi/q}(z; \mu_{b_*}) + D_{K/q}(z; \mu_{b_*})$.

Having parameterized the non-perturbative physics, I will now check this parameterization against experimental data. We start this comparison by examining a sample of Drell-Yan data in order to check the validity of the scheme for the TMD PDF. Note that the Drell-Yan Sivers asymmetry data which enters into our fit from COMPASS and RHIC do not contain so-called fiducial cuts, or cuts on the final state leptonic momentum. In order to avoid complications associated with these cuts on Drell-Yan data, we chose to benchmark our expression for the unpolarized cross section against the E288 data [1], which also does not contain fiducial cuts, see Tab. 2 of [72]. For E288, the target nucleus is Copper. In order to describe the Copper TMD PDF, we used nuclear modification prescription in [101]. In Fig. 3.3, I have plotted the theoretical curve against the experimental data [1], as a function of $q_\perp/Q$. For each bin, we normalized the theory such that the theory and data are equal at the first point. Different colors represent different invariant mass of the lepton pair from $4 < Q < 5$, $5 < Q < 6$, $6 < Q < 7$, $7 < Q < 8$, $8 < Q < 9$, $11 < Q < 12$, $12 < Q < 13$, $13 < Q < 14$ GeV, respectively. Three panels correspond to different energies for incident proton beams: 200 GeV (left), 300 GeV (middle), and 400 GeV (right). We find that the parameterization of [92] is well-suited at describing the shape of the Drell-Yan data.

To check the validity of our scheme for the unpolarized TMD FFs, we now examine the

HERMES multiplicity defined as

$$M_{\rm H}^{h}(x_B, z_h, P_{h\perp}, Q^2) = \frac{(d\sigma/dx_B dz_h dQ^2 dP_{h\perp})}{(d\sigma_{\rm DIS}/dx_B dQ^2)}\,, \tag{3.44}$$

where the superscript h denotes the species of the final state observed hadron, and the subscript "H" represents the HERMES data. We also study the COMPASS multiplicity data, which has a slightly different convention and is given by

$$M_{\rm C}^{h} = 2P_{h\perp} M_{\rm H}^{h}\,, \tag{3.45}$$

where the subscript "C" denotes the COMPASS data and $M_{\rm H}^{h}$ is defined in Eq. 3.44. On the other hand, the denominator in Eq. 3.44 is the inclusive DIS cross section and is given by

$$\frac{d\sigma_{\rm DIS}}{dx_B dQ^2} = \frac{\sigma_0^{\rm DIS}}{x_B}\left[F_2(x_B, Q^2) - \frac{y^2}{1+(1-y)^2} F_L(x_B, Q^2)\right]\,, \tag{3.46}$$

where F_2 is the usual DIS structure function while F_L is the longitudinal structure function. For their precise definitions see [102]. We compute the denominator at the NLO by using the APFEL library [103].

In the left panel of Fig. 3.4 we plot the HERMES pion multiplicity data [2] as a function of $q_\perp/Q$ along with the numerical results for the theory. In the right panel of this figure we plot kaon multiplicity data and theory. As shown in the figure, different colors represent different average z_h values from $\langle z_h \rangle = 0.15$, 0.23, 0.28, 0.34, 0.34, 0.42, 0.53, respectively. In these plots, we have normalized the theory so that data is equal to the theory at the second point of each data set [1]. In Fig. 3.5, we plot the COMPASS multiplicity data [3] for charged hadron production from a deuteron target along with the numerical results of our scheme. The triangular points represent the h^+ data points while the circular data points represent the h^- data points. Here again, different colors represent different $z_h = 0.2$, 0.3, 0.4, 0.6, respectively. From these plots, we find that the presented parameterization work very well at describing the shape of the multiplicity data for both HERMES and COMPASS data, indicating that the scheme for the TMD FFs are valid.

[1] Without normalizing to the second point of the data, we find that the overall normalization factor is around 2 for each data set, which is consistent with the results of [92].

3.3.2 Numerical Scheme for Sivers Function

To parameterize the non-perturbative Sudakov for the Sivers function, we take the parameterization

$$S^s_{\rm NP}(b, Q_0, Q) = \frac{g_2}{2} \ln\frac{Q}{Q_0} \ln\frac{b}{b_*} + g_1^T b^2 \,. \tag{3.47}$$

In the first term, we have used the same non-perturbative contribution for the rapidity anomalous dimension. In the second term, we have introduced the Gaussian width of the Sivers function.

To parameterize the collinear dependence of the Sivers function, we must parameterize the Qiu-Sterman function. Through trial and error, we found that the optimal parameterization which provides a stable fit is given by

$$T_{F\,q/p}(x, x, \mu_0) = \mathcal{N}_q(x) f_{q/p}(x, \mu_0) \,, \tag{3.48}$$

where $T_{F\,q/p}$ is the Qiu-Sterman function and $\mathcal{N}_q(x)$ is a collinear correction given by

$$\mathcal{N}_q(x) = N_q \frac{(\alpha_q + \beta_q)^{(\alpha_q+\beta_q)}}{\alpha_q^{\alpha_q} \beta_q^{\beta_q}} x^{\alpha_q} (1-x)^{\beta_q} \,. \tag{3.49}$$

Here we have introduced the initial collinear scale $\mu_0 = \sqrt{1.9}$ GeV. In the parameterization for the collinear modulation, we introduce non-perturbative parameters α_u and N_u are used to fit the up quarks. α_d and N_d are the fit parameters for the down quarks and $N_{\bar{u}}$, $N_{\bar{d}}$, N_s, $N_{\bar{s}}$, α_{sea} are for sea quarks and $\beta_q = \beta$ is the same for all flavors. This parameterization enforces that the form of the sea quarks is the same while the normalization of each sea quark can vary. Overall we use 11 parameters in total to perform the fit, including g_1^T.

To describe the cross section, we must evolve the Qiu-Sterman function from its initial scale to the scale μ_{b_*}. The DGLAP evolution of the Sivers function has been studied extensively in the literature, see for instance [104, 105, 106, 107, 108, 109, 110, 111, 112]. However, performing the full evolution of the Qiu-Sterman function is highly nontrivial due to its dependence on two momentum fractions x_1, x_2 in general [104, 113]. Thus in the TMD global analysis, the evolution of the Qiu-Sterman function has been implemented under certain

approximations. In this paper, we use the approximate evolution which is given by

$$\frac{\partial T_{F\,q/p}(x,x;\mu)}{\partial \ln \mu^2} = \frac{\alpha_s(\mu^2)}{2\pi}\left[P^{\mathrm{T}}_{q\leftarrow q}\otimes T_{F\,q/p}\right](x;\mu)\ . \tag{3.50}$$

In the first scheme that we consider, from [108], the authors show that at large x, the transverse spin dynamics leads to a modification to the quark to quark splitting kernel, $P^{\mathrm{T}}_{q\leftarrow q}$, with

$$P^{\mathrm{T}}_{q\leftarrow q}(x) = P_{q\leftarrow q}(x) - N_C\,\delta(1-x)\,, \tag{3.51}$$

where $P_{q\leftarrow q}(x)$ is the standard quark to quark splitting kernel for unpolarized PDFs,

$$P_{q\leftarrow q}(x) = C_F\left[\frac{1+x^2}{(1-x)_+} + \frac{3}{2}\delta(1-x)\right]\ . \tag{3.52}$$

This scheme has been used for instance in [114].

To solve this evolution equation, it is useful to take the Mellin transform of this expression; for details on Mellin-space evolution, see Sec. 3 in [115]. After performing the Mellin transform of this expression, the evolution equation becomes

$$\frac{\partial}{\partial \ln \mu^2} T_{F\,q/p}(N,\mu) = \frac{\alpha_s(\mu^2)}{2\pi}\,\gamma(N)\,T_{F\,q/p}(N,\mu)\,. \tag{3.53}$$

In this expression, $T_{F\,q/p}(N,\mu)$ is the Mellin transforms of the Qiu-Sterman function, i.e.

$$T_{F\,q/p}(N,\mu) = \int_0^1 dx\,x^{N-1}\,T_{F\,q/p}(x,x,\mu)\,. \tag{3.54}$$

Similarly $\gamma(N)$ is the Mellin transform of $P^{\mathrm{T}}_{q\leftarrow q}(x)$ which can be written as

$$\gamma(N) = \gamma_u(N) - N_C\,. \tag{3.55}$$

Here $\gamma_u(N)$ is the Mellin transform of the unpolarized splitting function $P_{q\leftarrow q}(x)$ and is given by

$$\gamma_u(N) = C_F\left(\frac{3}{2} + \frac{1}{N(N+1)} - 2S_1(N)\right)\ , \tag{3.56}$$

with $S_1(N)$ the harmonic sum function.

In the region where $\mu_{b_*} < m_b$, the mass of the b quark, the solution of the evolution equation is given by

$$T_{F\,q/p}\left(N,\mu_{b_*}\right) = T_{F\,q/p}\left(N,\mu_0\right)\left(\frac{\alpha_s\left(\mu_{b_*}^2\right)}{\alpha_s\left(\mu_0^2\right)}\right)^{-\gamma(N)/\beta_0(\mu_0)} . \tag{3.57}$$

Here $\beta_0(\mu_0) = 11 - 2/3\, n_f(\mu_0)$, where $n_f(\mu_0)$ is the number of active flavors at the scale μ_0. In the region where $\mu_{b_*} > m_b$, the solution of the evolution equation is given by

$$T_{F\,q/p}\left(N,\mu_{b_*}\right) = T_{F\,q/p}\left(N,m_b\right)\left(\frac{\alpha_s\left(\mu_{b_*}^2\right)}{\alpha_s\left(m_b^2\right)}\right)^{-\gamma(N)/\beta_0(\mu_{b_*})} , \tag{3.58}$$

where $T_{F\,q/p}\left(N,m_b\right)$ is given by

$$T_{F\,q/p}\left(N,m_b\right) = T_{F\,q/p}\left(N,\mu_0\right)\left(\frac{\alpha_s\left(m_b^2\right)}{\alpha_s\left(\mu_0^2\right)}\right)^{-\gamma(N)/\beta_0(\mu_0)} , \tag{3.59}$$

and $n_f(\mu_{b_*})$ is the number of active flavors at the scale μ_{b_*}.

In order to construct the Sivers function in Eq. 3.17 at NLO, there is an additional convolution of the coefficient C function and the Qiu-Sterman function. We find that it is useful to first take its Mellin transform and thus the convolution over the momentum fraction becomes a simple product in Mellin space:

$$f_{1T,q/p}^{\perp q}\left(N,b;\mu,\zeta\right) = \bar{C}_{q\leftarrow i}(N;\mu,\zeta) T_{F\,i/p}\left(N,\mu\right) , \tag{3.60}$$

where $\bar{C}_{q\leftarrow q'}(N,b;\mu,\zeta)$ is the Mellin transform of the Sivers Wilson coefficient function. The NLO Sivers function can then be obtained by numerically taking the inverse Mellin transform of this function,

$$f_{1T,q/p}^{\perp q}(x,b;\mu,\zeta) = \frac{1}{\pi}\int_0^\infty dz \mathrm{Im}\left[e^{i\phi}x^{-c-ze^{i\phi}} f_{1T,q/p}^{\perp q}\left(c+ze^{i\phi},b;\mu,\zeta\right)\right] , \tag{3.61}$$

where the parameter c must be taken such that all of the singularities in the function $f_{1T,q/p}^{\perp q}\left(c+ze^{i\phi},b;\mu,\zeta\right)$ lie to the left of the line $x = c$ in the imaginary plane. In our code, we use $c = 2$ which satisfies this criteria. We also take $\phi = \pi/4$ to optimize the numerical integration.

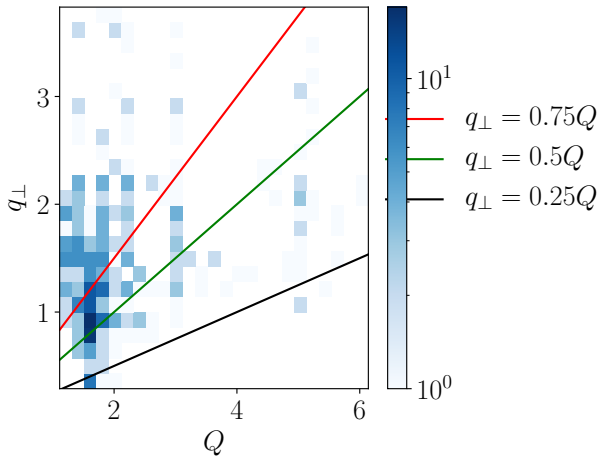

Figure 3.6: Histogram of the Semi-Inclusive DIS data in $q_\perp$ and Q. To obtain this plot, we bin the Semi-Inclusive DIS data sets in $q_\perp$ and Q. The dark spots indicate a large number of experimental data while the white spots indicate that there are no experimental data. We also plot the line $q_\perp = 0.75\,Q$ in red, $0.5\,Q$ in green, and $0.25\,Q$ in black.

3.4 Fit Results

This section is organized as follows. In Subsec. 3.4.1, I will present the results of a fit to Semi-Inclusive DIS and low energy Drell-Yan data. In Subsec. 3.4.2, I present discussion on the RHIC data.

3.4.1 Simultaneous Fit to Semi-Inclusive DIS and Drell-Yan

The fit to the data from Semi-Inclusive DIS and Drell-Yan took into consideration Semi-Inclusive DIS data from JLAB in [7], HERMES in [5], COMPASS in [6, 4] and the COMPASS Drell-Yan data in [8]. I'll note that there are also data points from COMPASS in [84]. However, this data is re-binned from the same events as the in [6]. These two data sets are then correlated and including both data sets would lead to double counting of the events. Therefore, we only take into consideration the data from [6]. Furthermore, I'll also note that the data set in [6] was projected into two sets of data $z_h > 0.1$ and $z_h > 0.2$. To avoid fitting correlated data sets, we choose to fit only the $z_h > 0.1$ data set. Using the extracted Sivers

function, we then compare with the RHIC data.

Before beginning to fit the Sivers data, we need to remove the experimental data that are outside the TMD region. Typical kinematic cuts from unpolarized Semi-Inclusive DIS fits are given for instance in [73] and use the cut $q_\perp/Q < 0.25$. However, we find that this selection process leaves very few data points for the available Sivers data. In Fig. 3.6 we plot a histogram of the selected data Semi-Inclusive DIS data as a function of $q_\perp$ and Q. We find that the cut $q_\perp/Q < 0.25$ leaves only 12 Semi-Inclusive DIS data points, while the cut $q_\perp/Q < 0.5$ leaves 97 data points. In fact, we find that the majority of the data has $q_\perp/Q > 0.5$. In order to retain a large enough data set to perform a meaningful fit we perform the cut $q_\perp/Q < 0.75$. Furthermore to restrict the selected data set to the TMD region, we also enforce that the Semi-Inclusive DIS data must have $P_{h\perp} < 1$ GeV. At the same time in order to avoid the threshold resummation region, we also enforce that $z_h < 0.7$. These cuts are similar to those used in Ref. [81].

The χ^2 is defined as

$$\chi^2\left(\{a\}\right) = \sum_{i=1}^{N} \frac{\left(T_i\left(\{a\}\right) - E_i\right)}{\Delta E_i^2}\,. \tag{3.62}$$

The fundamental idea behind a global fitting procedure is to first parameterize the non-perturbative contributions to the cross section. The χ^2 distribution can then be interpreted as a surface in the parameter space. The properties of the χ^2 surface are then obtained through a sampling procedure. The sampling of the χ^2 is performed through the `MINUIT` package [116, 117]. In the expression for the χ^2, E_i are the central values of the experimental measurements, ΔE_i are the total experimental errors, $T_i\left(\{a\}\right)$ is the theoretical value at the experimental kinematics, and $\{a\}$ is a vector containing the fit parameters.

To generate the uncertainty band, we use the 'replica method' in Refs. [70, 12]. In this method, we generate replicate possible effects due to experimental uncertainties in the measurements by shifting the central value of each data point by a Gaussian noise. The width of the Gaussian noise is determined by the experimental errors. We inject this noise to all data point and copy this data into a 'replica'. Overall we generate 200 noisy replicas. We

then fit all of the 200 replicas and the noiseless fit. From the fitting of the replicas, we obtain 201 sets of parameters. We then generate predictions for each experimental data point. We take the noiseless fit to give the central prediction while we use the remaining predictions to generate the uncertainty band by examining the middle 68% of the replicas. In Table. 3.1, we present the results for the parameter values along with the $\chi^2/d.o.f$ and the parameter uncertainties. In terms of the quality of the fit, we find an excellent agreement between our fitted theoretical result and the experimental data with a global $\chi^2/d.o.f = 1.032$. In Tab. 3.2, we give the value of the $\chi^2/d.o.f$ for each of the sets of data.

$\chi^2/d.o.f. = 1.032$			
$N_u =$	$0.077^{+0.004}_{-0.005}$ GeV	$\alpha_u =$	$0.967^{+0.028}_{-0.045}$
$N_d =$	$-0.152^{+0.017}_{-0.016}$ GeV	$\alpha_d =$	$1.188^{+0.056}_{-0.023}$
$N_s =$	$0.167^{+0.053}_{-0.051}$ GeV	$\alpha_{sea} =$	$0.936^{+0.069}_{-0.026}$
$N_{\bar{u}} =$	$-0.033^{+0.016}_{-0.017}$ GeV	$\beta =$	$5.129^{+0.017}_{-0.034}$
$N_{\bar{d}} =$	$-0.069^{+0.019}_{-0.026}$ GeV	$g_1^T =$	$0.045^{+0.009}_{-0.015}$ GeV^2
$N_{\bar{s}} =$	$-0.002^{+0.047}_{-0.040}$ GeV		

Table 3.1: Fit parameters. The presented values is the parameter value of the fit with no Gaussian noise. The uncertainties for the replicas are generated from the parameter values which lie on the boundary of 68% confidence.

In Fig. 3.12, we plot the extracted first transverse moment of the proton Semi-Inclusive DIS Sivers function at the initial PDF scale, $f_{1T}^{\perp\,(1)}(x, \mu_0)$ with $\mu_0 = \sqrt{1.9}$ GeV which is defined in terms of the Qiu-Sterman function as

$$f_{1T\,q/p}^{\perp\,(1)}(x; Q) = -\frac{1}{2M} T_{F\,q/p}(x, x; Q)\,. \tag{3.63}$$

In this figure, I plotted all 200 replicas for each of the extracted quark flavors. The uncertainty band is generated by consider the middle 68% of the obtained distribution at each point in x. We find that the size of the first moment of the Sivers function is roughly equal

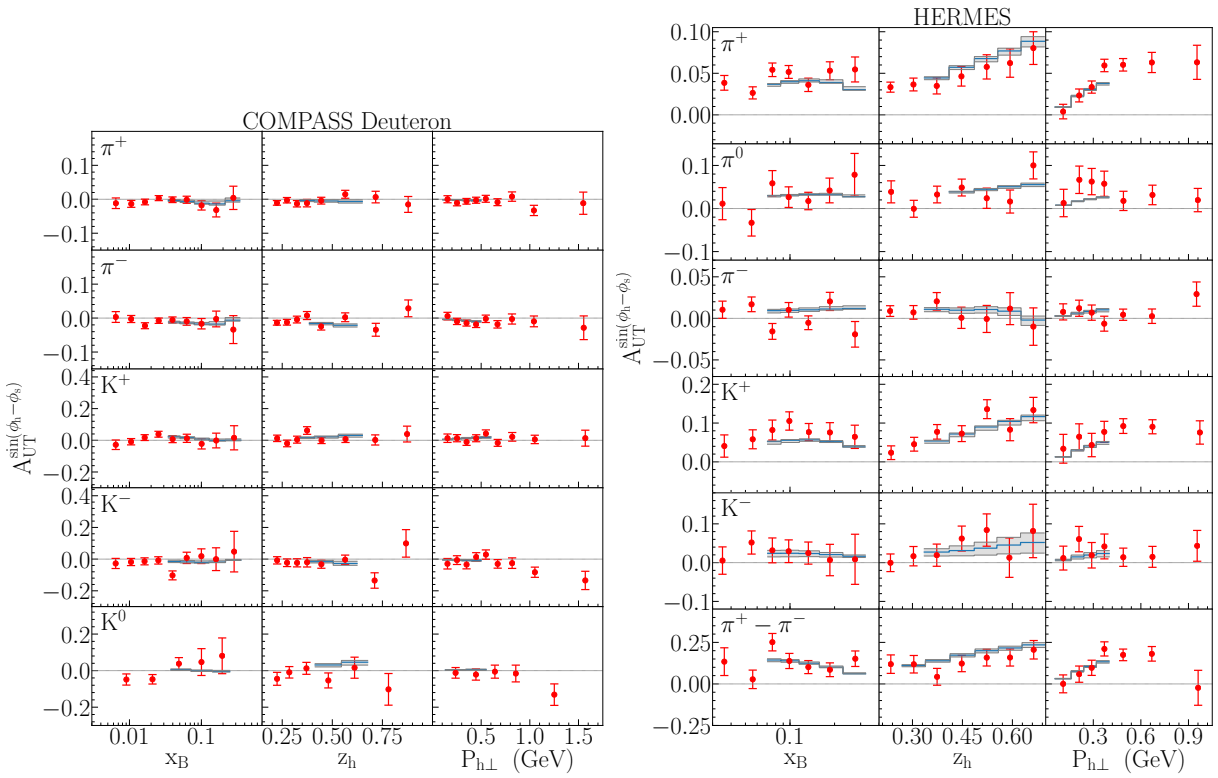

Figure 3.7: Left: The COMPASS deuteron target measurement [4] for π^+, π^-, K^+, K^-, and K^0 from top to bottom, and as a function of x_B (left), z_h (middle), and $P_{h\perp}$ (right). Right: HERMES proton target measurement [5] π^+, π^0, π^-, K^+, K^-, and $(\pi^+ - \pi^-)$ from top to bottom, and as a function of x_B (left), z_h (middle), and $P_{h\perp}$ (right). The data is plotted in red along with the total experimental error.

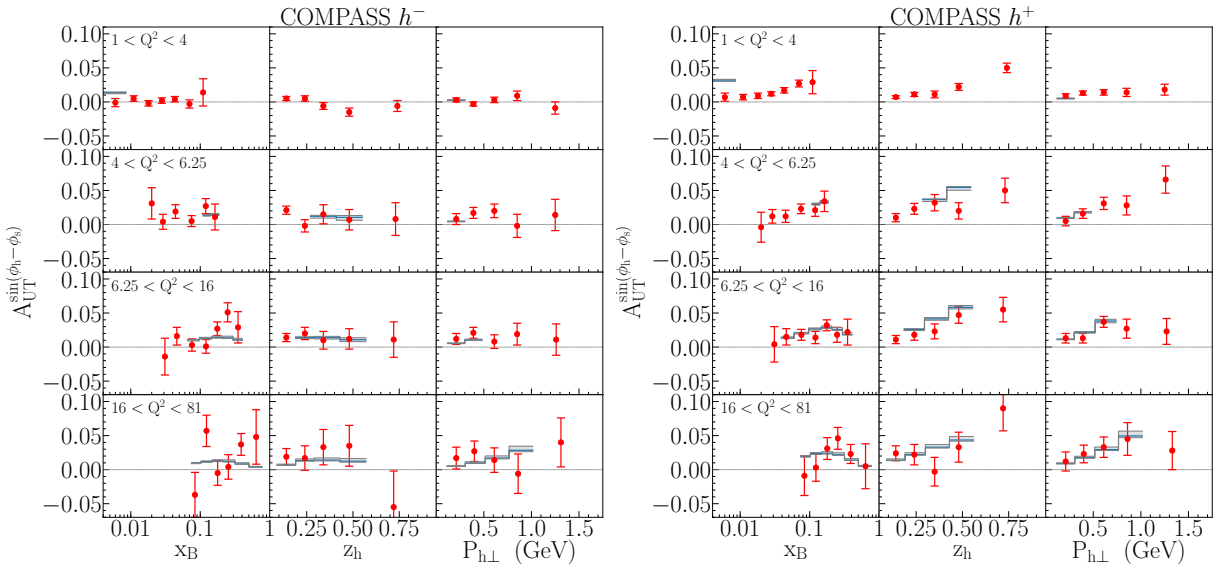

Figure 3.8: Left: The COMPASS proton target measurement for h^- for 1 GeV^2 $< Q^2 <$ 4 GeV^2, 4 GeV^2 $< Q^2 <$ 6.25 GeV^2, 6.25 GeV^2 $< Q^2 <$ 16 GeV^2, 16 GeV^2 $< Q^2 <$ 81 GeV^2 from top to bottom [6]. Right: Same as the left except for h^+ production.

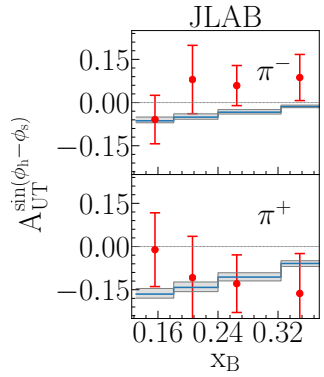

Figure 3.9: JLab measurement of the Sivers asymmetry for a neutron target [7] as a function of x_B.

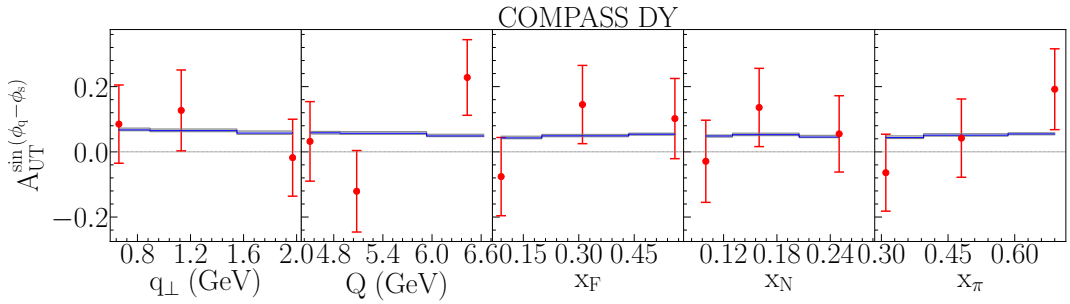

Figure 3.10: COMPASS Drell-Yan measurement for π^--p collision [8] as a function of $q_\perp$, Q, x_F, x_N, and x_π from left to right.

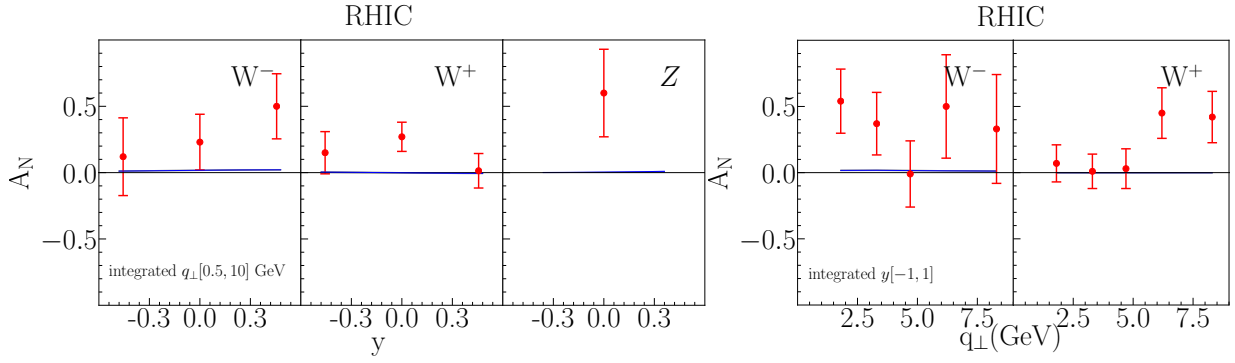

Figure 3.11: Top: Prediction for the Sivers asymmetry for $p + p \to W/Z$ at $\sqrt{S} = 500$ GeV [9]. We plot only the central curve of the fit here since the size of the uncertainty band is small for this prediction. Left: The y dependent data integrated in $q_\perp$ from 0.5 to 10 GeV. Right: The $q_\perp$ dependent data integrated in y from -1 to 1.

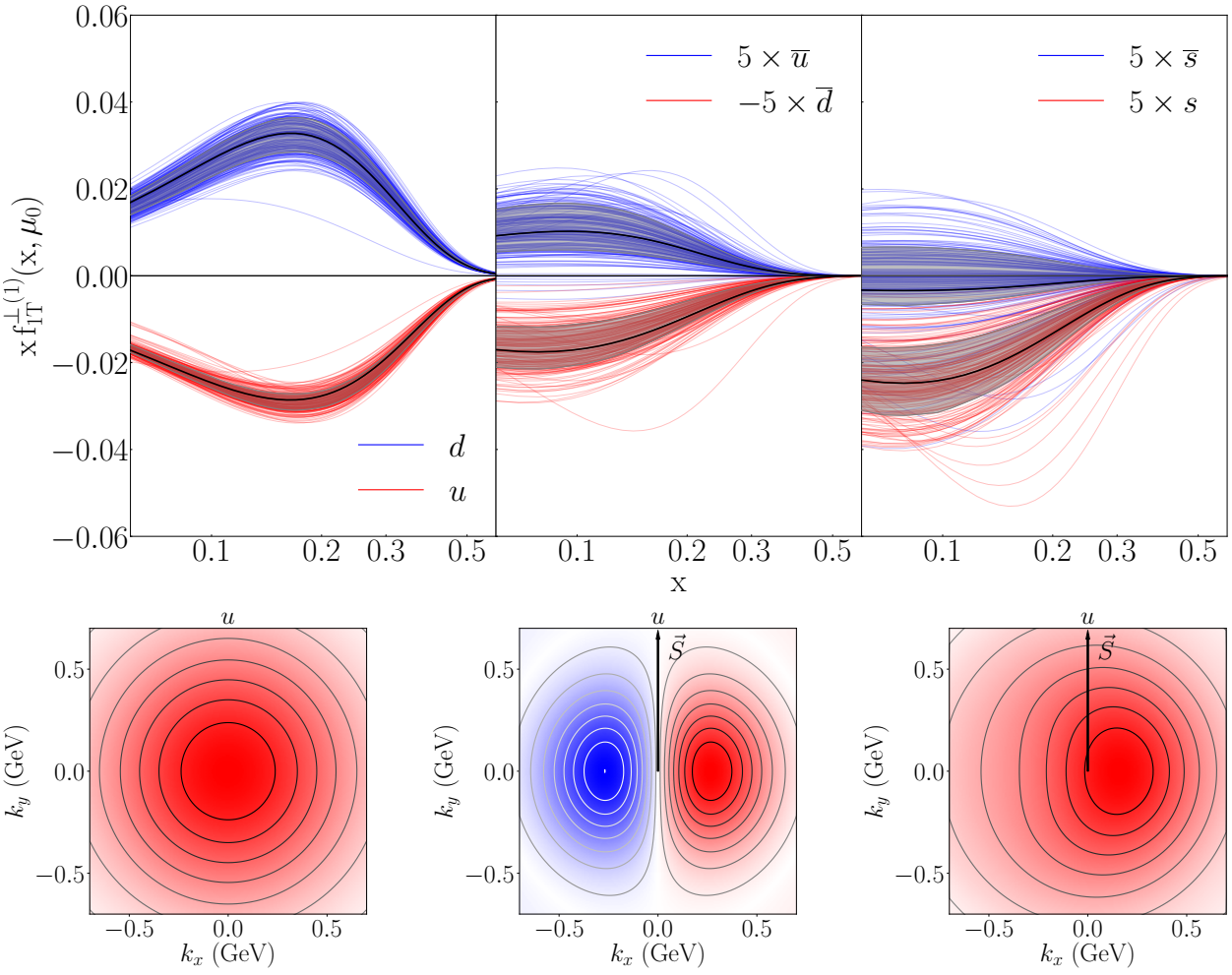

Figure 3.12: Top: The extracted transverse moment of the Sivers function at $\mu_0 = \sqrt{1.9}$ GeV. The black curve is the fit to the experimental data with no Gaussian noise. Bottom left: The distribution of unpolarized quarks in an unpolarized proton at μ_0 and $x = 0.2$. Bottom middle: The extracted Sivers function from the fit with no noise. Bottom right: The number density which is obtained by the sum of the two contribution.

Collab	Ref	Process	Q_{avg}	N_{data}	χ^2/N_{data}
COMPASS	[4]	$ld \to lK^0X$	2.52	7	0.770
		$ld \to lK^-X$	2.80	11	1.325
		$ld \to lK^+X$	1.73	13	0.749
		$ld \to l\pi^-X$	2.50	11	0.719
		$ld \to l\pi^+X$	1.69	12	0.578
	[6]	$lp \to lh^-X$	4.02	31	1.055
		$lp \to lh^+X$	3.93	34	0.898
	[8]	$\pi^-p \to \gamma^*X$	5.34	15	0.658
HERMES	[5]	$lp \to lK^-X$	1.70	14	0.376
		$lp \to lK^+X$	1.73	14	1.339
		$lp \to l\pi^0X$	1.76	13	0.997
		$lp \to l(\pi^+ - \pi^-)X$	1.73	15	1.252
		$lp \to l\pi^-X$	1.67	14	1.498
		$lp \to l\pi^+X$	1.69	14	1.697
JLAB	[7]	$lN \to l\pi^+X$	1.41	4	0.508
		$lN \to l\pi^-X$	1.69	4	1.048
RHIC	[9]	$pp \to W^+X$	M_W	8	2.189
		$pp \to W^-X$	M_W	8	1.684
		$pp \to Z^0X$	M_Z	1	3.270
Total				226	0.989

Table 3.2: The distribution of experimental after taking the kinematic cuts $q_\perp/Q < 0.75$, $P_{h\perp} < 1$ GeV, and $z < 0.7$. The column Q_{avg} gives the average hard scale for the measured data set. On the right column, we have included the χ^2/N_{data} for each set. The RHIC data was not included into the fit. Here we give the χ^2/N_{data} for the prediction.

and opposite for the u and d quarks while the first moment for the sea quarks is much smaller. For the $\bar{u}$, s and $\bar{s}$-quarks, the Sivers moment have been multiplied by a factor of 5 while

for $\bar{d}$, we have multiplied by a factor of -5. We find that the Sivers d function is the largest in magnitude and is positive; while the Sivers u function is nearly as large but is negative. Furthermore we find that the $\bar{u}$ and $\bar{d}$-quark functions are nearly equal to one another in magnitude, both are more than 5 times smaller in magnitude than the valence quarks, and are both positive. For the s-quark, we find that the magnitude is approximately 5 times smaller than the valence quarks in magnitude and is negative. Finally for the $\bar{s}$-quark, we find that the magnitude is very small and that the sign is not well determined in this fit. In the bottom half of that figure on the left, I also plot on the left the unpolarized TMD PDF at $x = 0.2$ and $Q = \mu_0$ as a function of $\hat{x} \cdot \boldsymbol{k}_\perp$ and $\hat{y} \cdot \boldsymbol{k}_\perp$. In the middle, I plot the extracted Sivers function at the same x and Q and on the right, I plot the number density which is obtained by combining these two contributions.

In Figs. 3.7, 3.8, and 3.9, we plot our theoretical curves against the Semi-Inclusive DIS data. Fig. 3.7 is for COMPASS deuteron target (left panel) and for HERMES proton target (right panel), and for both pions and kaons. Fig. 3.8 is for charged hadrons from COMPASS proton target. Fig. 3.9 is for pion production on a neutron target from JLab. Finally in Fig. 3.10 we plot theoretical curves against the COMPASS Drell-Yan lepton pair data in $\pi^- + p$ collisions. We plot the asymmetry $A_{UT}^{\sin(\phi_q - \phi_s)}$ as a function of transverse momentum $q_\perp$, invariant mass Q, Feynman $x_F = x_\pi - x_N$, momentum fraction x_N in the proton target, and momentum fraction x_π in the pion target, respectively. The experimental data along with the total experimental uncertainties are plotted in red. The blue curves are the theory curves from the fit with no noise. The uncertainty band in grey is generated from the stored values of the asymmetry for each of the replicas. For each data point, the maximum and minimum value of the asymmetry within the middles 68% are used to generate these error bars. As it is indicated already in Tab. 3.2 and as it is evident from the figures, the agreement between our theory and Semi-Inclusive DIS and Drell-Yan data is very good, although to a less degree with the Drell-Yan data because of the much larger experimental uncertainty. I would like to note at this point that very shortly after finishing our paper, the HERMES collaboration posted additional data in Ref. [118]. We found in an analysis of this data after

publication that there was great agreement between our fit results and this data.

In Fig. 3.11, we plot the prediction for the RHIC data in $p+p$ collisions at $\sqrt{S} = 500$ GeV using the extracted Sivers function from this fit. In the left panel, we plot the Sivers asymmetry A_N as a function of rapidity for W^- (left), W^+ (middle), and Z^0 (right), respectively. We integrate vector boson transverse momentum over $0.5 < q_\perp < 10$ GeV. On the right panel, we plot A_N as a function of $q_\perp$ while we integrate over the rapidity $|y| < 1$. We find that the asymmetry for W/Z for the central fit is at most 2%, which is more than an order of magnitude smaller than the central values recorded at RHIC. This leads to a $\chi^2/N_{\rm data}$ of 2.015 for the prediction for RHIC, as shown in Tab. 3.2. Even if one considers the very large error bars in the RHIC data, this comparison seems to indicate some tension between our theory and the RHIC data.

3.4.2 Discussion on the RHIC data

In this section, I will discuss the implications of the RHIC data and the developments in this direction since our paper was published.

In order to access which one of our theoretical assumptions is responsible for the large χ^2 of the RHIC data, we performed several tests. Firstly, we have checked whether the quality of the description of the RHIC data was due to the cut on $q_\perp/Q$. In order to check if quality of the fit is due to the value of this cut, we have performed an additional fit with the cut $q_\perp/Q < 0.5$. We find that this change leads to a $\chi^2/N_{\rm data}$ is 1.885 for the RHIC data. While it would be preferable to perform an fit with $q_\perp/Q < 0.25$, we note that there is not enough data in this region to constrain the parameters of the fit. Because there is no strong improvement in the description of the RHIC data after applying the $q_\perp/Q < 0.5$, we conclude that this cut is not responsible for the disagreement between the data sets.

Another possible assumption that could be causing the large χ^2 of the RHIC data is the assumption that the sea quarks have the same α and β parameter. To check this, we have performed a 13 parameter fit with the chosen parameter with the parameters α_u, N_u, $\beta_{\rm val}$, α_d, N_d, $N_{\bar{u}}$, $N_{\bar{d}}$, N_s, $N_{\bar{s}}$, α_+, α_-, and $\beta_{\rm sea}$. Here $\alpha_{\bar{d}} = \alpha_{\bar{s}} = \alpha_+$ and $\alpha_s = \alpha_{\bar{u}} = \alpha_-$.

The introduction of the α_+ and α_- parameterization decouples the positive and negative sea quarks from one another while the introduction of the parameters $\beta_{\rm val}$ and $\beta_{\rm sea}$ decouples the valance and sea quarks. However, we find that the addition of these parameters lead to a $\chi^2/N_{\rm data}$ is 1.885. This implies that this assumption on the function form is not the issue.

To discuss the origin of the disagreement with the RHIC data, it is useful to examine Fig. 3.13, where I have plotted profiles in the $\chi^2/N_{\rm data}$ distributions. In each plot, we set all but one of the parameters equal to the values which are determined by the fit and we vary the remaining parameter about its best value. The best value determined by the fit is given by a vertical gray line. In this plot, we see that the curves for the RHIC χ^2 do not change much as the α, β, and g_1^T parameters are varied. This indicates that the RHIC data is insensitive to these parameters. On the other hand, we see that when N_q parameters are varied that there are large modifications to the RHIC χ^2. Thus, the RHIC data is sensitive to these parameters. We see that the RHIC data in general demands a much larger value for the Sivers function N parameters, which control the magnitude. Nevertheless, these parameters are well-constrained by the data from Semi-Inclusive DIS and the COMPASS Drell-Yan measurement. Since the Semi-Inclusive DIS and COMPASS Drell-Yan data were gathered at much lower energy scales that the RHIC data, this tension between the sets indicates that the size of the Sivers asymmetry grows as a function of the hard energy scale. At the time that we had published this paper, we interpreted this result to indicate that either the RHIC data was flawed or that there were missing evolution effects entering into the DGLAP evolution of the Qiu-Sterman function. However, since this time, a re-analysis of this measurement has been made. In Fig. 3.14 I have plotted our theoretical prediction for the RHIC asymmetry. We see that the updated RHIC measurement is now consistent with our extraction. This likely indicates that there is no inconsistency in our analysis. Rather, it appears to indicate that the limited statistics for the RHIC measurement were to blame for this disagreement.

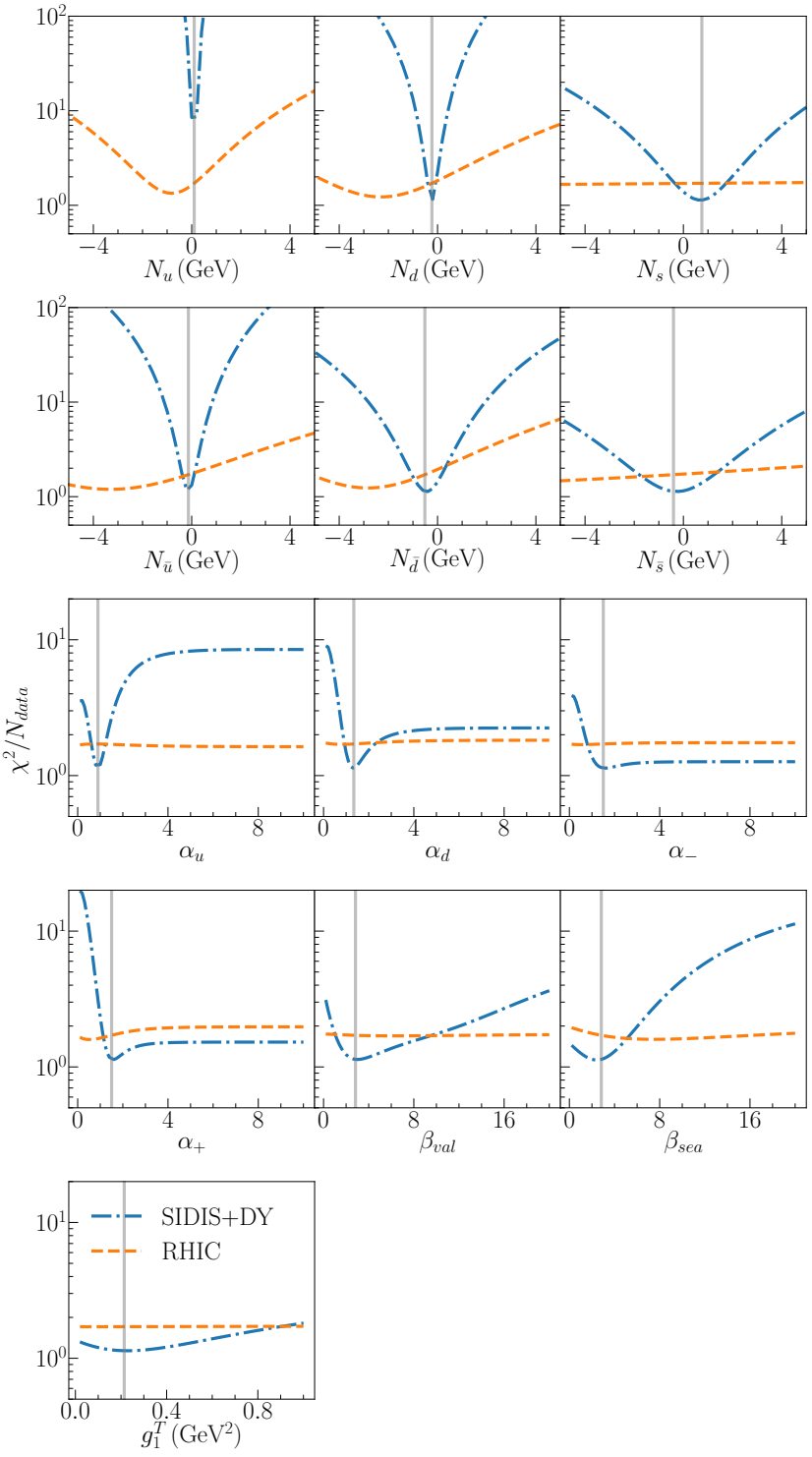

Figure 3.13: The distribution of χ^2/N_{data} for each parameter. In each subplot, we vary each parameter about the central value while keeping all other parameters fixed to the optimal values determined by the fit. The gray line is the central value determined from the fit.

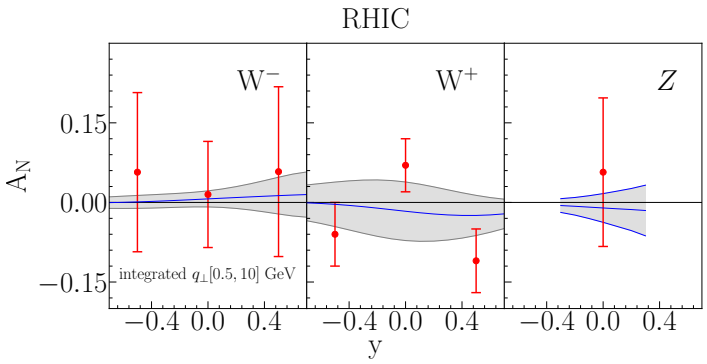

Figure 3.14: Comparison with theoretical uncertainties for the re-analysis of the RHIC measurement.

3.5 Predictions for the EIC

In the previous section, I have performed the first global extraction of the Sivers function and clarified the inconsistency with the RHIC data. In this section, we provide predictions for the Sivers asymmetry at the future EIC. On the left side of Fig. 3.15, we plot our prediction

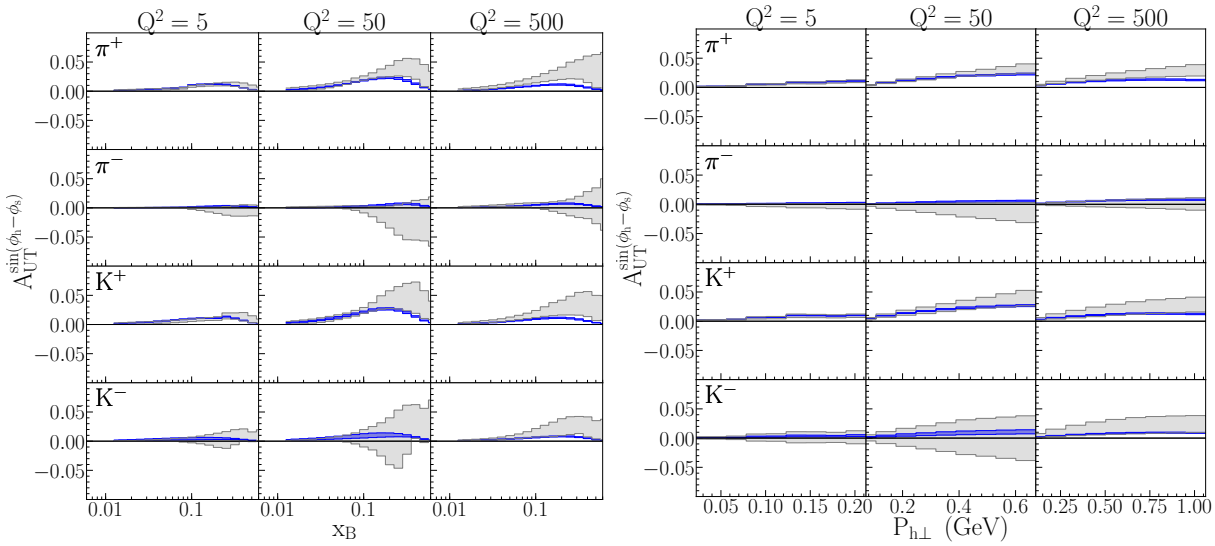

Figure 3.15: The prediction for the EIC at $\sqrt{S} = 105$ GeV. Left: The x_B dependent prediction at $z_h = 0.5$ and $q_\perp/Q = 0.2$. Right: The $P_{h\perp}$ dependent prediction at $x_B = 0.2$ and $z_h = 0.25$. The blue band represents the prediction from the low energy extraction while the grey band represents the prediction when one includes the RHIC data into the analysis.

for the Sivers asymmetry in Semi-Inclusive DIS on a proton target as a function of x_B at $\sqrt{S} = 105$ GeV, $z_h = 0.25$, $q_\perp/Q = 0.2$ at $Q^2 = 5$, 50, 500 GeV^2 for π^+, π^-, K^+, and K^- production. In this figure, we have plotted our prediction for the fit in blue. In gray, we have plotted our prediction which is obtained through heavily weighting the RHIC data, not discussed in this dissertation. While this prediction demonstrates the x-dependence of our fits, in order to demonstrate the $k_\perp$-dependence of our fitted Sivers function, we also make a prediction as a function of $P_{h\perp}$ on the right side of Fig. 3.15. In this figure, we have used the same kinematics as the left side except that we take $x_B = 0.2$. We see from these curves that the predicted asymmetry for π^- and K^- production is small. This behavior is expected because of the suppression by the fractional charge e_d^2 for the d-quark Sivers function, as well as the cancellation that occurs between the u and d-quarks. On the other hand, we predict an asymmetry of a few percent for π^+ and K^+ production in this kinematic region.

3.6 Conclusions

In this chapter, I have outlined our extraction of the Sivers function for the first time at the NLO+NNLL order. We first perform an extraction from the Sivers asymmetry data measured in Semi-Inclusive DIS at HERMES, COMPASS and JLab, and in Drell-Yan lepton pair production at COMPASS. Using this first extraction, we generate a prediction for the Sivers asymmetry of W/Z boson at RHIC kinematics and compare with the experimental data. We find that while the Semi-Inclusive DIS and COMPASS Drell-Yan lepton pair production data is very well described by our extraction, that our theoretical curve is much smaller than the RHIC data. We studied in great detail the impact of the RHIC data and their implications. We found that the RHIC data was inconsistent with our extraction. However, the preliminary re-analysis of the RHIC measurement is consistent with our current extraction. Finally, we have provided projections at the future EIC.

3.7 Appendix I: Wilson Coefficient Functions

The scale dependent TMD PDF quark to quark and gluon to quark Wilson coefficient function is given by [119, 120, 121]

$$\begin{aligned} C_{q\leftarrow q'}(x,b;\mu,\zeta) =& \delta_{qq'}\delta(1-x) + \delta_{qq'}\frac{\alpha_s}{4\pi}\Big[2C_F(1-x) - 2P_{q\leftarrow q}(x)L \\ & - L\left(-3 + C_F\left(L + 2L_\zeta\right)\right)\delta(1-x) - C_F\frac{\pi^2}{6}\delta(1-x)\Big], \\ C_{q\leftarrow g}(x,b;\mu,\zeta) =& \frac{\alpha_s}{\pi}\left[x(1-x)T_F - \frac{1}{2}P_{q\leftarrow g}(x)L\right]. \end{aligned} \tag{3.64}$$

The quark to quark coefficient function for the TMD FF is given by the relation

$$\hat{C}_{q\leftarrow q'}(z,b;\mu,\zeta) = C_{q\leftarrow q'}(z,b;\mu,\zeta)|_{L\to L-\ln(z^2)}, \tag{3.65}$$

while the quark to gluon Wilson coefficient function for the TMD FF is given by

$$\hat{C}_{g\leftarrow q'}(z,b;\mu,\zeta) = \frac{\alpha_s}{2\pi}\left[C_F z + 2P_{g\leftarrow q}(z)\left(\ln(z) - \frac{1}{2}L\right)\right]. \tag{3.66}$$

In these expressions, we have introduced the standard collinear splitting kernels

$$P_{q\leftarrow q}(x) = C_F\left[\frac{1+x^2}{(1-x)_+} + \frac{3}{2}\delta(1-x)\right] \tag{3.67}$$

$$P_{g\leftarrow q}(x) = C_F\frac{1+(1-z)^2}{z} \tag{3.68}$$

$$P_{q\leftarrow g}(x) = T_F\left[z^2 + (1-z)^2\right]. \tag{3.69}$$

Finally, the coefficient function for the quark-Sivers function is given by [122, 114, 112, 123, 124]

$$\begin{aligned} \bar{C}_{q\leftarrow q'}(x_1,x_2,b;\mu,\zeta) =& \delta_{qq'}\,\delta(1-x_1)\,\delta(1-x_2) \\ & - \frac{\alpha_s}{2\pi}\delta_{qq'}\Bigg\{ - L\Bigg[\delta(1-x_2/x_1)\left(C_F\left(\frac{1+x_1^2}{1-x_1}\right)_+ \right. \\ & \left. - C_A\delta(1-x_1)\right) + \frac{C_A}{2}\left(\delta(1-x_2)\frac{1+x_1}{1-x_1} - \delta(1-x_2/x_1)\frac{1+x_1^2}{1-x_1}\right)\Bigg] \\ & - \frac{1}{2N_C}\delta(1-x_2/x_1)(1-x_1) \end{aligned}$$

$$+ C_F\delta(1-x_1)\delta(1-x_2)\left[\frac{3}{2}L - L_\zeta L - \frac{1}{2}L^2 - \frac{\pi^2}{12}\right]\Bigg\}, \tag{3.70}$$

which for $\mu^2 = \zeta = \mu_{b_*}^2$ reduces to

$$\begin{aligned}\bar{C}_{q\leftarrow q'}(x_1,x_2,b;\mu_{b_*},\mu_{b_*}^2) =& \delta_{qq'}\delta(1-x_1)\delta(1-x_2) - \frac{\alpha_s}{2\pi}\frac{\delta_{qq'}}{2N_C}\delta(1-x_2/x_1)(1-x_1) \\ & - \frac{\alpha_s}{2\pi}\delta_{qq'}C_F\frac{\pi^2}{12}\delta(1-x_1)\delta(1-x_2).\end{aligned} \tag{3.71}$$

3.8 Appendix II: Factorization for Semi-Inclusive DIS

3.8.1 Kinematics

The differential cross section for Semi-Inclusive DIS is given by

$$E'_\ell E_h \frac{d\sigma}{d^3\ell'\, d^3P_h} = \frac{\alpha_{\rm em}^2}{\ell\cdot P}\frac{1}{4Q^4}L_{\mu\nu}W^{\mu\nu}\,, \tag{3.72}$$

see for instance Ref. [86]. In this expression, $W^{\mu\nu}$ and $L_{\mu\nu}$ are the hadronic and leptonic tensors. It's conventional to write the phase space element in terms of the parton fraction z by making the change of variables

$$\frac{d^3P_h}{2E_h} = \frac{dz}{z}\, d^2P_{h\perp}\,. \tag{3.73}$$

After which, the cross section can be written in the form

$$\frac{d\sigma}{dx\, dy\, d\psi\, dz\, d^2P_{h\perp}} = \frac{\alpha_{\rm em}^2}{4Q^4}\frac{y}{z}L_{\mu\nu}W^{\mu\nu}\,, \tag{3.74}$$

where ψ is the azimuthal angle of the final-state lepton.

The leptonic tensor which is defined in terms of the leptonic momenta as

$$L^{\mu\nu} = \langle\ell|J^\mu(0)|\ell'\rangle\langle\ell'|J^{\nu\dagger}(0)|\ell\rangle \tag{3.75}$$

$$= 2\left(\ell^\mu\,\ell'^\nu + \ell^\nu\,\ell'^\mu - \ell\cdot\ell' g^{\mu\nu} + i\lambda_l\epsilon^{\mu\nu\rho\sigma}\ell_\rho\ell'_\sigma\right) \tag{3.76}$$

where the factor of 2 in the leptonic tensor enters from the final state spin configurations. Analogous to the work that we performed for Drell-Yan, in the Breit frame, it is useful to

define a complete set of coordinates as

$$\hat{t}^\mu = \frac{2x}{Q} P^\mu + \frac{q^\mu}{Q}\,, \qquad \hat{x}^\mu = \frac{P_{h\,T}^\mu}{P_{h\,T}}\,, \qquad \hat{z}^\mu = -\frac{q^\mu}{Q}\,, \tag{3.77}$$

$$\hat{y}^\mu = \epsilon^{\mu\nu\rho\sigma} \hat{t}_\nu \hat{x}_\rho \hat{z}_\sigma\,. \tag{3.78}$$

Using this coordinate system, the the leptonic momenta can be parameterized as

$$\ell^\mu = \frac{Q}{2}\left[\cosh\varphi\,\hat{t}^\mu + \sinh\varphi\cos\theta\,\hat{x}^\mu + \sinh\varphi\sin\theta\,\hat{y}^\mu - \hat{z}^\mu\right]\,, \tag{3.79}$$

$$\ell'^\mu = \frac{Q}{2}\left[\cosh\varphi\,\hat{t}^\mu + \sinh\varphi\cos\theta\,\hat{x}^\mu + \sinh\varphi\sin\theta\,\hat{y}^\mu + \hat{z}^\mu\right]\,, \tag{3.80}$$

where we define the parameter

$$\cosh\varphi = \left(\frac{2}{y} - 1\right)\,, \tag{3.81}$$

To obtain the azimuthal asymmetries for the cross section originating from the leptonic tensor, we once again define the operators

$$\begin{aligned}
\mathcal{V}_1^{\mu\nu} &= \hat{x}^\mu\hat{x}^\nu + \hat{y}^\mu\hat{y}^\nu, & \mathcal{V}_2^{\mu\nu} &= \hat{z}^\mu\hat{z}^\nu, \\
\mathcal{V}_3^{\mu\nu} &= \hat{t}^\mu\hat{x}^\nu + \hat{x}^\mu\hat{t}^\nu, & \mathcal{V}_4^{\mu\nu} &= \hat{x}^\mu\hat{x}^\nu - \hat{y}^\mu\hat{y}^\nu, \\
\mathcal{V}_5^{\mu\nu} &= \hat{t}^\mu\hat{x}^\nu - \hat{x}^\mu\hat{t}^\nu, & \mathcal{V}_6^{\mu\nu} &= \hat{x}^\mu\hat{y}^\nu - \hat{y}^\mu\hat{x}^\nu, \\
\mathcal{V}_7^{\mu\nu} &= \hat{t}^\mu\hat{y}^\nu - \hat{y}^\mu\hat{t}^\nu, & \mathcal{V}_8^{\mu\nu} &= \hat{t}^\mu\hat{y}^\nu + \hat{y}^\mu\hat{t}^\nu, \\
\mathcal{V}_9^{\mu\nu} &= \hat{x}^\mu\hat{y}^\nu + \hat{y}^\mu\hat{x}^\nu\,,
\end{aligned} \tag{3.82}$$

where we note that the role of $\hat{t}$ and $\hat{z}$ are opposite of those in the case for Drell-Yan. We once again perform the decomposition of the leptonic tensor as

$$L^{\mu\nu} = \sum_i L_i\left(\phi,\theta\right)\,\mathcal{V}_i^{\mu\nu}\,, \tag{3.83}$$

where $L_i(\phi,\theta)$ are angular coefficients.

$$\begin{aligned}
L_1\left(\phi,\theta\right) &= \frac{Q^2\left(y^2-2y+2\right)}{y^2}\mathcal{V}_1^{\mu\nu}, & L_2\left(\phi,\theta\right) &= 0, \\
L_3\left(\phi,\theta\right) &= -\frac{2Q^2\sqrt{1-y}(y-2)\cos(\psi)}{y^2}\mathcal{V}_3^{\mu\nu}, & L_4\left(\phi,\theta\right) &= -\frac{2Q^2(y-1)\cos(2\psi)}{y^2}\mathcal{V}_4^{\mu\nu},
\end{aligned} \tag{3.84}$$

$$L_5(\phi,\theta) = \frac{2i\lambda Q^2\sqrt{1-y}\sin(\psi)}{y}\mathcal{V}_5^{\mu\nu}), \qquad L_6(\phi,\theta) = \frac{i\lambda Q^2(y-2)}{y}\mathcal{V}_6^{\mu\nu},$$
$$L_7(\phi,\theta) = -\frac{2i\lambda Q^2\sqrt{1-y}\cos(\psi)}{y}\mathcal{V}_7^{\mu\nu}, \qquad L_8(\phi,\theta) = -\frac{2Q^2\sqrt{1-y}(y-2)\sin(\psi)}{y^2}\mathcal{V}_8^{\mu\nu},$$
$$L_9(\phi,\theta) = -\frac{2Q^2(y-1)\sin(2\psi)}{y^2}\mathcal{V}_9^{\mu\nu},$$

In this expression $W^{\mu\nu}$ is the hadronic tensor which is given by the expression

$$W_{\mu\nu} = \frac{1}{(2\pi)^4}\sum_X \int d^4x\, e^{-iqx} \left\langle P \left| J_\mu^\dagger(x) \right| h, X \right\rangle \left\langle h, X \left| J_\nu(0) \right| P_1 \right\rangle , \tag{3.85}$$

where $J_\mu(x)$ once again represents the current operator.

3.8.2 Factorization

The hadronic terms can be written in terms of the quark correlation functions for the TMD PDF and TMD FF as

$$\begin{aligned} W_{\mu\nu} =& \frac{1}{N_c}\sum_q e_q^2 \int d^2\boldsymbol{k}_{1\perp}\, d^2\boldsymbol{k}_{2\perp}\, \delta^{(2)}\left(\boldsymbol{q}_\perp + \boldsymbol{k}_\perp + \boldsymbol{p}_\perp/z\right) \\ & \times \mathrm{Tr}\left[\Phi_q\left(x, \boldsymbol{k}_\perp, \boldsymbol{S}; \mu, \zeta_1/\nu^2\right)\gamma^\mu \Delta_q\left(z, \boldsymbol{p}_\perp, \boldsymbol{S}_h; \mu, \zeta_2/\nu^2\right)\gamma^\nu\right] . \end{aligned} \tag{3.86}$$

$$\tag{3.87}$$

In this expression, I have introduced the quark correlation function for the TMD FF. The explicit expression for this function is

$$\Delta_{jj'}\left(z, \boldsymbol{p}_\perp, \boldsymbol{S}_h; \mu, \zeta_2/\nu^2\right) = \frac{1}{2z}\sum_X \int \frac{d^4\xi}{(2\pi)^4}\, e^{ip\cdot\xi}\, \delta\left(\xi^-\right) \tag{3.88}$$
$$\times \left\langle 0 \left| W^n(+\infty, \xi^+; \boldsymbol{\xi}_\perp)\, \psi_{j'}^{\bar{c}}(\xi) \right| h, \boldsymbol{S}_h, X \right\rangle \left\langle h, \boldsymbol{S}_h, X \left| \bar{\psi}_j^{\bar{c}}(0)\, W^n(0, +\infty, \boldsymbol{0}_\perp)\, W^T(\boldsymbol{0}, \boldsymbol{\xi}_\perp; +\infty) \right| 0 \right\rangle .$$

Retaining only leading power distributions in m/Q and $p_\perp/Q$, this correlation function can be written as

$$\begin{aligned} \Delta(z, \boldsymbol{p}_\perp, \boldsymbol{S}_h) =& \left(D - \frac{\epsilon_\perp^{\rho\sigma} p_{\perp\rho} S_{h\perp\sigma}}{zM} D_{1T}^\perp\right)\frac{\not{n}}{4} + \left(\Lambda_h G_{1L} - \frac{\boldsymbol{p}_\perp \cdot \boldsymbol{S}_{h\perp}}{zM} G_{1T}\right)\frac{\gamma^5 \not{n}}{4} \\ & + \left(S_{h\perp}^k H_{1T} + \frac{\lambda p_\perp^k}{zM} H_1^\perp - \frac{\epsilon_\perp^{kj} p_{\perp j}}{zM} H_1^\perp - \frac{p_\perp^k p_\perp^j - \frac{1}{2} p_\perp^2 g_\perp^{kj}}{z^2 M^2} S_{h\perp j} H_{1T}^\perp\right)\frac{i\gamma^5 \sigma_{+k}}{4} . \end{aligned} \tag{3.89}$$

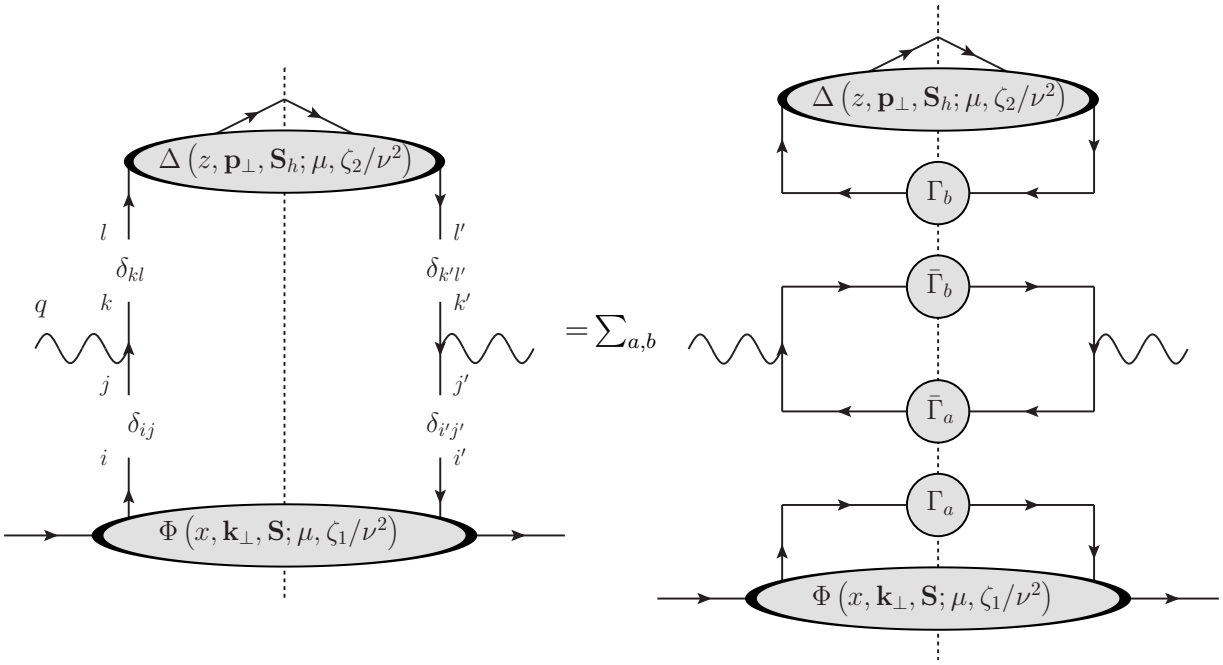

Figure 3.16: Diagrammatic representation of the Fierz decomposition of the hadronic tensor. Left: The broken lines are used to separate the hard interaction from the definition of the quark-quark correlation function. Right: The Fierz decomposition where Γ_i represent the operators which give rise to the parton densities while $\bar{\Gamma}_i$ represent the operators which enter into the hard function.

Making this replacement, the hadronic tensor can be simplified as

$$W_{\mu\nu} = \frac{1}{N_c}\sum_{a,b}\sum_{q} e_q^2 \int d^2\boldsymbol{k}_{1\perp}\, d^2\boldsymbol{k}_{2\perp}\, \delta^{(2)}\left(\boldsymbol{q}_\perp + \boldsymbol{k}_\perp + \boldsymbol{p}_\perp/z\right) \tag{3.90}$$

$$\times \mathrm{Tr}\left[\gamma^\mu\, \bar{\Gamma}_1^a\, \gamma^\nu\, \bar{\Gamma}_1^b\right]\, \Phi^{[\Gamma^a]}\left(x, \boldsymbol{k}_\perp, \boldsymbol{S}; \mu, \zeta_1/\nu^2\right)\, \Delta^{\left[\Gamma^b\right]}\left(z, \boldsymbol{p}_\perp, \boldsymbol{S}_h; \mu, \zeta_2/\nu^2\right)\,.$$

Where in this expression

$$\Delta^{\left[\Gamma^b\right]}\left(x_1, \boldsymbol{p}_\perp, \boldsymbol{S}_h; \mu, \zeta_2/\nu^2\right) = \mathrm{Tr}\left[\Delta\left(z, \boldsymbol{p}_\perp, \boldsymbol{S}_h; \mu, \zeta_2/\nu^2\right)\Gamma^b\right]\,. \tag{3.91}$$

Therefore hadronic tensor for the unpolarized cross section is given by

$$W_{\mu\nu} = -g_\perp^{\mu\nu}\frac{1}{N_c}\sum_{a,b}\sum_{q} e_q^2 \int \frac{db\, b}{2\pi} J_0\left(bq_\perp\right)\, D_{h/q}(z, b; \mu, \zeta_2)\, f_{q/P}(x, b; \mu, \zeta_1) \tag{3.92}$$

.

Upon contracting with the leptonic tensor, we arrive at the expression for the differential cross section

$$\frac{d\sigma}{dx_B\, dQ^2\, dz_h\, d^2P_{h\perp}} = \frac{Q^2\left(y^2 - 2y + 2\right)}{y^2}\frac{1}{N_c}\sum_{a,b}\sum_{q} e_q^2 \tag{3.93}$$

$$\times \int \frac{db\, b}{2\pi} J_0\left(bq_\perp\right)\, D_{h/q}(z, b; \mu, \zeta_2)\, f_{q/P}(x, b; \mu, \zeta_1)\,, \tag{3.94}$$

which matches the expression in the previous section upon a change of variables from Q^2 to y.

CHAPTER 4

Jets for Tomography

4.1 Introduction

Since the asymptotic contributions of QCD amplitudes originates from the soft and collinear regions, sufficiently high energy partons generate jets [125]. These objects are defined by three relevant parameters, the jet axis, the jet radius, and the jet p_T^{cut}, which provide information for the direction of the jet, its width, and the required energy which is used to define the jet. Because of the enhancement of radiation in the collinear and soft directions, jets axes are a powerful tool for estimating the direction of the parent parton. This property is particularly useful for QCD tomography, where the direction of the parton provides information about the momentum of the parton that originated in the beam hadrons. In the case of Semi-Inclusive DIS as an example, we saw that the transverse momentum of the initial quark is convoluted with the transverse momentum generated through hadronization in the TMD FF. Furthermore, jets are predominantly perturbative objects and therefore offer limited non-perturbative input as opposed to fragmentation function. Over the past few years, many studies have featured using jets to measure TMD PDFs, see for instance Refs. [126, 127, 128, 129, 130, 131, 132, 133, 134, 135]. Furthermore, as radiative emission and hadronization occurs within the jet, the final-state hadrons of the jet pick up transverse momentum with respect to the jet axis. Thus by measuring the distribution of hadrons within the jet, we gain sensitivity to the non-perturbative contributions associated with fragmentation. In principle since these measurements are sensitive to both perturbative and non-perturbative contributions, a detailed proof of factorization is required. In Ref. [136] this separation was performed in an effective field theory approach. Since this time, a large num-

ber of measurements have been presented in which the distribution of hadrons within the jets can be used to measure the TMD FFs, see for instance Refs. [137, 138, 139, 140, 141, 142].

In this chapter, I will focus on the work that I have performed in which we used jets to probe TMDs. In Sec. 4.2, I will discuss the use of heavy-flavor di-jets at the EIC to probe the gluon Sivers function. In Sec. 4.3, I will discuss the use of back-to-back di-jets to probe quark Sivers function in hadron-hadron collisions. In Sec. 4.4, I will discuss the use of Z-tagged jets to probe fragmentation functions in hadron-hadron collisions.

4.2 QCD evolution of the gluon Sivers function in heavy flavor dijet production at the Electron-Ion Collider

4.2.1 Introduction

To explore quark TMDs, Semi-Inclusive DIS, Drell-Yan and DIA have served as the primary processes. The shortcoming of these processes are that the virtual bosons in each process probe only the non-perturbative quark TMDs. While the high center of mass energies and the electro-magnetic background at the EIC offers the possibility of isolating gluon distributions. As the fundamental goals of the EIC are to understand the gluon and spin content of the hadrons, the gluon Sivers function is regarded as one of the "golden measurements" at the future EIC [68]. Within the literature, several processes have been presented as a possible probe of these distributions at the future EIC such as heavy quark pair production [143], heavy quarkonium production [144, 145, 146, 147, 148], and quarkonium-jet production [149], as well as back-to-back dihadron and dijet production [150]. In [151], the authors used a PYTHIA event generator [152] and the reweighting method of [153] to investigate the experimental uncertainties associated with these processes. The authors concluded that because jets can be used as a reliable proxy for the parton-level asymmetry, the optimal process for probing the gluon Sivers function at the future EIC is dijet production. In their analysis however, the contribution of the quark Sivers function contaminated their analysis. In our analysis in this section, we discuss the Sivers spin asymmetry for heavy flavor (HF)

dijet production, where the contribution of the quark Sivers function is further suppressed compared to that of the light flavor dijet case.

As we demonstrated in the previous section, the Sivers function is related to the limit of the Qiu-Sterman function and thus exhibits modified universality between Semi-Inclusive DIS and Drell-Yan [154, 155, 156]. Similarly, it has been demonstrated that the gluon Sivers function for the process of back-to-back diphoton production in $p+p$ collisions, $p^\uparrow p \to \gamma\gamma X$, carries a sign opposite to that of dijet production in $e+p$ collisions, $ep^\uparrow \to e'jjX$: $f_{1T,g}^{\perp\left[ep^\uparrow \to e'jjX\right]}(x,k_T) = -f_{1T,g}^{\perp\left[p^\uparrow p\to\gamma\gamma X\right]}(x,k_T)$ [143]. In [157], it was demonstrated that the gluon Sivers function in any process can be expressed in terms of two "universal" functions with calculable color coefficients for each partonic subprocess. We briefly discuss such a process-dependence for HF dijet production below. For a comprehensive review on gluon TMD PDFs, see [158, 159].

So far, studies of the gluon Sivers function at the EIC are mostly performed within the leading-order (LO) parton model, without considering the impact of QCD evolution. The effects of resummation for back-to-back light flavor dijet production in the unpolarized DIS process have been investigated in [160], where the authors apply the p_T-weighted recombination scheme [161] in defining the jet axis to avoid the theoretical complexity arising from non-global logarithm (NGL) resummation [162]. A similar idea is used to study single inclusive jet production in the Breit frame at the EIC in [128, 129]. Recently, following the same Soft-Collinear Effective Theory (SCET) framework utilized in [135, 130, 163, 164, 165], the TMD factorization formula for light flavor dijet production at the EIC has been derived [166], where the azimuthal-angle-dependent soft function, describing the interaction between two final-state jets through the exchange of low-energy gluons, is analytically calculated at one-loop order. For HF jet production in the kinematic region of comparable jet and heavy quark masses, a new effective theory framework is needed. In this work, we provide such a framework and derive the TMD factorization formula.

The remainder of this section is organized as follows. In Sec. 4.2.2, I provide details the factorization framework required to carry out resummation in the back-to-back region where

the transverse momentum imbalance of the HF dijet is small. In Sec. 4.2.3, I present numerical results for charm and bottom dijet production in both unpolarized and transversely-polarized-proton-electron scattering. I summarize our findings and give an outlook for future investigations in Sec. 4.2.4.

4.2.2 Factorization and resummation formula

In this section, I start with the kinematics for HF dijet production in $e + p$ collisions. We then provide the TMD factorization formalism with explicit expressions for all the relevant factorized ingredients.

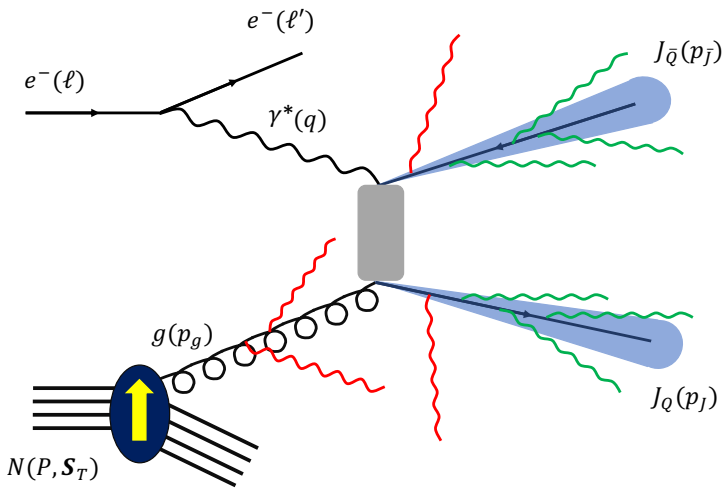

Figure 4.1: HF dijet production in electron-proton collisions, as stated in Eq. (4.1).

4.2.2.1 Kinematics

As shown in Fig. 4.1, we consider HF dijet production in the polarized-proton-electron scattering process

$$e(\ell) + N(P, \boldsymbol{S}_T) \to e(\ell') + J_{\mathcal{Q}}(p_J) + J_{\bar{\mathcal{Q}}}(p_{\bar{J}}) + X\,, \tag{4.1}$$

where $\boldsymbol{S}_T$ [1] is the transverse spin of the polarized proton with momentum P and ℓ (ℓ') is the momentum of the incoming (outgoing) electron. At LO, HF dijets are produced via the $\gamma^* g \to \mathcal{Q}\bar{\mathcal{Q}}$ process. The HF quark $\mathcal{Q}$ and antiquark $\bar{\mathcal{Q}}$ initiate the observed HF jets $J_{\mathcal{Q}}$ and $J_{\bar{\mathcal{Q}}}$ with momentum p_J and $p_{\overline{J}}$, respectively. In this section, we choose to work in the Breit frame so that both the virtual photon (with momentum $q = \ell - \ell'$) and the beam proton scatter along the z-axis. For convenience, we define the following variables commonly used in DIS,

$$Q^2 = -q^2\,, \quad x_B = \frac{Q^2}{2P\cdot q}\,, \quad y = \frac{P\cdot q}{P\cdot \ell}\,. \tag{4.2}$$

We may further note that $Q^2 = x_B\, y\, S_{\ell P}$, where $S_{\ell P} = (\ell + P)^2$ denotes the electron-proton center-of-mass energy. In a fashion analogous to SIDIS, we also define the kinematic variable $z = P\cdot p_J / P\cdot q$, which gives the momentum fraction of the photon carried by the jet $J_{\mathcal{Q}}$. At LO, the four-momenta of the incoming and outgoing particles are expressed as

$$\begin{aligned}
q^\mu &= \frac{Q}{2}(n^\mu - \bar{n}^\mu)\,, \quad P^\mu = \frac{Q}{x_B}\frac{\bar{n}^\mu}{2}\,,\\
\ell^\mu &= \frac{Q}{y}\frac{n^\mu}{2} + Q\frac{1-y}{y}\frac{\bar{n}^\mu}{2} + \ell_t^\mu\,, \quad \ell'^\mu = Q\frac{1-y}{y}\frac{n^\mu}{2} + \frac{Q}{y}\frac{\bar{n}^\mu}{2} + \ell_t^\mu\,,\\
p_J^\mu &= zQ\frac{n^\mu}{2} + \frac{p_T^2}{zQ}\frac{\bar{n}^\mu}{2} + p_t^\mu\,, \quad p_{\overline{J}}^\mu = (1-z)Q\frac{n^\mu}{2} + \frac{p_T^2}{(1-z)Q}\frac{\bar{n}^\mu}{2} - p_t^\mu\,,
\end{aligned} \tag{4.3}$$

where we have defined p_t^μ such that $p_t^\mu p_{t_\mu} = -p_T^2$ with $\boldsymbol{p}_T = p_T(\cos\phi_J, \sin\phi_J)$. Here, we assume $p_T^2 \gg m_{\mathcal{Q}}^2$ and take $p_J^2 = p_{\overline{J}}^2 = 0$. This allows us to derive the factorized cross section in the following section. Lastly, the parton-level Mandelstam variables can be defined as

$$\hat{s} \equiv (p_g + q)^2 = (p_J + p_{\overline{J}})^2 = \frac{p_T^2}{z(1-z)}\,, \tag{4.4}$$

$$\hat{t} \equiv (p_g - p_J)^2 = (q - p_{\overline{J}})^2 = -\frac{Q^2 x\, z}{x_B}\,, \tag{4.5}$$

$$\hat{u} \equiv (p_g - p_{\overline{J}})^2 = (q - p_J)^2 = -\frac{Q^2 x\,(1-z)}{x_B}\,, \tag{4.6}$$

where x is the momentum fraction of the proton carried by the gluon, and is given by

$$x = \frac{x_B D}{Q^2 z(1-z)}, \quad \text{with} \quad D = Q^2 z(1-z) + p_T^2\,. \tag{4.7}$$

[1] In this chapter, I use T to denote transverse to the proton-photon while I use $\perp$ to mean transverse to the jet

4.2.2.2 Factorization formula

As we saw for Semi-Inclusive DIS and Drell-Yan, the TMD region is valid where we have two scales with the hierarchy $q_\perp \ll Q_h$ where $q_\perp$ is some transverse momentum scale and Q_h is some hard scale. In the case of back-to-back jet production, we can define the small scale as the imbalance of the jets $\boldsymbol{q}_T = \boldsymbol{p}_{JT} + \boldsymbol{p}_{\bar{J}T}$ where $q_T \ll p_{\bar{J}T} \sim p_{JT} \equiv p_T$. When considering HF dijet production, we also need to consider the additional scale which is associated with the mass of the HF quark.

Furthermore, we work in the kinematic regime where $m_{\mathcal{Q}} \lesssim p_T R \ll p_T$, with R denoting the jet radius. Overall, in the region with the scale hierarchy as $q_T R \ll q_T \lesssim m_Q \lesssim p_T R \ll p_T$. Using SCET, we can decompose the fields entering into the cross sections as

$$A^\mu(x) = A^\mu_J(x) + A^\mu_{\bar{J}}(x) + A^\mu_c(x) + A^\mu_s(x) + A^\mu_{\rm cs}(x) + A^\mu_{\bar{c}\bar{s}}(x) \tag{4.8}$$

$$\psi(x) = \psi_J(x) + \psi_{\bar{J}}(x) + \psi_c(x) + \psi_s(x) + \psi_{cs}(x) + \psi_{\bar{c}\bar{s}}(x)\,. \tag{4.9}$$

In this expression, $\psi_{J/\bar{J}}$ and $A_{J/\bar{J}}$ are the quark and gluon fields associated with collinear emissions within the jet while ψ_{cs} and A_{cs} are known as collinear-soft modes which provide information on soft radiation leaving the jet. The momentum of the collinear jet modes scales as $p_{JT}\,(1, R^2, R)$ while the momentum of the collinear-soft modes scale as $q_\perp\,(1, R^2, R)$.

The factorized expression for the proton-spin-independent cross section is given by

$$\begin{aligned}\frac{d\sigma^{UU}}{dQ^2 dy d^2\boldsymbol{p}_T dy_J d^2\boldsymbol{q}_T} =& H(Q, y, p_T, y_J; \mu) \int d^2\lambda_T\, d^2k_T\, d^2l_{\mathcal{Q}T}\, d^2l_{\bar{\mathcal{Q}}T} S(\boldsymbol{\lambda}_T; \mu, \nu) \\ &\times \delta^{(2)}(\boldsymbol{\lambda}_T + \boldsymbol{k}_T + \boldsymbol{l}_{\mathcal{Q}T} + \boldsymbol{l}_{\bar{\mathcal{Q}}T} - \boldsymbol{q}_T)\, f^{\rm unsub}_{g/N}\left(x, k_T; \mu, \zeta/\nu^2\right) \\ &\times J_{\mathcal{Q}}(p_T R, m_{\mathcal{Q}}; \mu)\, S^c_{\mathcal{Q}}(\boldsymbol{l}_{\mathcal{Q}T}, R, m_{\mathcal{Q}}; \mu)\, J_{\bar{\mathcal{Q}}}(p_T R, m_{\mathcal{Q}}; \mu)\, S^c_{\bar{\mathcal{Q}}}(\boldsymbol{l}_{\bar{\mathcal{Q}}T}, R, m_{\mathcal{Q}}; \mu)\,.\end{aligned} \tag{4.10}$$

Above, y_J is the rapidity of the HF jet $J_{\mathcal{Q}}$ and is related to the kinematic variable z through the relation $z = e^{y_J} p_T/Q$. In the factorization formula Eq. (4.10), S denotes the soft function while $f_{g/N}$ is the unpolarized gluon TMD PDF. Their perturbative one-loop expressions can be found in Sec. 4.2.2.4. In the third line of Eq. (4.10), $J_{\mathcal{Q}}$ and $S^c_{\mathcal{Q}}$ are the massive quark jet and collinear-soft functions, which differ from the corresponding functions utilized in light jet production [135, 130, 163, 164, 165]. In Secs. 4.2.2.5 and 4.2.2.6, we present their

explicit calculations at next-to-leading order (NLO). The variables $\boldsymbol{k}_T$, $\boldsymbol{\lambda}_T$, and $\boldsymbol{l}_T$ label the transverse momenta associated with the collinear, soft, and collinear-soft modes. Finally, μ and ν are the factorization and rapidity scales, respectively, while ζ is the Collins-Soper parameter [36, 167]. In the derivation of the above factorization formula we apply the narrow jet approximation with $R \ll 1$. However, as shown in [168, 169, 170, 171] this approximation works well even for fat jets with radius $R \sim \mathcal{O}(1)$, and the power corrections of $\mathcal{O}(R^{2n})$ with $n > 0$ can be obtained from the perturbative matching calculation.

Fourier transforming to b-space, the factorized cross section becomes

$$\begin{aligned}\frac{d\sigma^{UU}}{dQ^2 dy d^2\boldsymbol{p}_T dy_J d^2\boldsymbol{q}_T} =& H(Q, y, p_T, y_J; \mu) \int \frac{d^2b}{(2\pi)^2} e^{i\boldsymbol{b}\cdot\boldsymbol{q}_T} S(\boldsymbol{b}; \mu, \nu)\, f_{g/N}^{\text{unsub}}\left(x, b; \mu, \zeta/\nu^2\right) \\ & \times J_{\mathcal{Q}}(p_T R, m_{\mathcal{Q}}; \mu)\, S^{\text{c}}_{\mathcal{Q}}(\boldsymbol{b}, R, m_{\mathcal{Q}}; \mu)\, J_{\bar{\mathcal{Q}}}(p_T R, m_{\mathcal{Q}}; \mu)\, S^{\text{c}}_{\bar{\mathcal{Q}}}(\boldsymbol{b}, R, m_{\mathcal{Q}}; \mu)\,, \end{aligned} \tag{4.11}$$

where soft function S and the gluon TMD PDF $f_{g/N}$ both depend on the rapidity scale ν. However, the soft function can be written as

$$S(\boldsymbol{b}; \mu, \nu) = \sqrt{S_{n\bar{n}}(b; \mu, \nu)} S(\boldsymbol{b}; \mu)\,, \tag{4.12}$$

where $S_{n\bar{n}}(b, \mu, \nu)$ is the soft function for Higgs production in $p + p$ collisions [62, 172], and the function $S(\boldsymbol{b}, \mu)$ on the right-hand side no longer depends on the rapidity scale ν. Upon making this replacement, the factorized expression for the cross section can be written in terms of the properly-defined TMD gluon distribution [36] by noting that

$$f_{g/N}^{\text{unsub}}\left(x, b; \mu, \zeta/\nu^2\right) S(\boldsymbol{b}; \mu, \nu) = f_{g/N}(x, b; \mu, \zeta) S(\boldsymbol{b}; \mu)\,. \tag{4.13}$$

Here, $f_{g/N}(x, b; \mu, \zeta)$ on the right-hand side is defined as

$$f_{g/N}(x, b; \mu, \zeta) = f_{g/N}^{\text{unsub}}\left(x, b; \mu, \zeta/\nu^2\right) \sqrt{S_{n\bar{n}}(b; \mu, \nu)}\,. \tag{4.14}$$

This is the properly-defined gluon TMD PDF probed in Higgs production in $p + p$ collisions [172] and is thus the counterpart of the quark TMD PDF as probed in Drell-Yan lepton pair production. Finally, Eq. (4.11) can be expressed in the following form

$$\frac{d\sigma^{UU}}{dQ^2 dy d^2\boldsymbol{p}_T dy_J d^2\boldsymbol{q}_T} = H(Q, y, p_T, y_J; \mu) \int \frac{d^2b}{(2\pi)^2} e^{i\boldsymbol{b}\cdot\boldsymbol{q}_T} S(\boldsymbol{b}; \mu)\, f_{g/N}(x, b; \mu, \zeta) \tag{4.15}$$

$$\times\, J_{\mathcal{Q}}(p_T R, m_{\mathcal{Q}};\mu)\, S^c_{\mathcal{Q}}(\boldsymbol{b}, R, m_{\mathcal{Q}};\mu)\, J_{\bar{\mathcal{Q}}}(p_T R, m_{\mathcal{Q}};\mu)\, S^c_{\bar{\mathcal{Q}}}(\boldsymbol{b}, R, m_{\mathcal{Q}};\mu)\,.$$

In the following sections we calculate the one-loop expressions for all the above functions. An important physical requirement is that the factorized cross section must be independent of the scale μ–we verify this factorization-scale-independence in Sec. 4.2.2.7.

Next, if one considers the scattering of an electron with a transversely-polarized proton with spin $\boldsymbol{S}_T$, Eq. (4.10) can be generalized. In this case, the spin-dependent cross section once again contains two terms, the spin-independent contribution and the spin-dependent contribution

$$d\sigma(\boldsymbol{S}_T) = d\sigma^{UU} + d\sigma^{UT}(\boldsymbol{S}_T)\,, \tag{4.16}$$

where $d\sigma^{UT}$ depends on the gluon Sivers function. The full expressions for the leading twist gluon distributions are given in [173]. Using these results, we can obtain the expression for the polarized cross section by simply replacing the unpolarized gluon TMD PDF in Eq. (4.10) with the gluon Sivers function, namely

$$f^{\text{unsub}}_{g/N}\left(x, k_T;\mu,\zeta/\nu^2\right) \to \frac{1}{M}\epsilon_{\alpha\beta}\, S_T^\alpha\, k_T^\beta\, f^{\perp,f\,\text{unsub}}_{1T,g/N}\left(x, k_T;\mu,\zeta/\nu^2\right). \tag{4.17}$$

Here, it is important to note that there exist both f- and d-type gluon Sivers functions, which are associated with different color configurations in the three-gluon correlator, i.e., involving the antisymmetric f^{abc} and symmetric d^{abc} structure constants of $SU(3)$, respectively. For details, see for instance [157, 174]. In Eq. (4.17), we have denoted the gluon Sivers function with the superscript f, which is used to indicate that it is f-type. We note that at LO, this process is only sensitive to the f-type function. Further details on this matter are provided in Sec. 4.2.2.3. After making this substitution, the factorized cross section then reads

$$\begin{aligned}\frac{d\sigma^{UT}(\boldsymbol{S}_T)}{dQ^2 dy d^2\boldsymbol{p}_T dy_J d^2\boldsymbol{q}_T} =& H^{\text{Sivers}}(Q, y, p_T, y_J;\mu)\int d^2\lambda_T\, d^2k_T\, d^2l_{\mathcal{Q}T}\, d^2l_{\bar{\mathcal{Q}}T} S(\boldsymbol{\lambda}_T;\mu,\nu) \\ &\times \delta^{(2)}(\boldsymbol{\lambda}_T + \boldsymbol{k}_T + \boldsymbol{l}_{\mathcal{Q}T} + \boldsymbol{l}_{\bar{\mathcal{Q}}T} - \boldsymbol{q}_T)\,\frac{1}{M}\epsilon_{\alpha\beta}\, S_T^\alpha\, k_T^\beta\, f^{\perp,f\,\text{unsub}}_{1T,g/N}\left(x, k_T;\mu,\zeta/\nu^2\right) \\ &\times J_{\mathcal{Q}}(p_T R, m_{\mathcal{Q}};\mu)\, S^c_{\mathcal{Q}}(\boldsymbol{l}_{\mathcal{Q}T}, R, m_{\mathcal{Q}};\mu)\, J_{\bar{\mathcal{Q}}}(p_T R, m_{\mathcal{Q}};\mu)\, S^c_{\bar{\mathcal{Q}}}(\boldsymbol{l}_{\bar{\mathcal{Q}}T}, R, m_{\mathcal{Q}};\mu)\,,\end{aligned} \tag{4.18}$$

where H^{Sivers} denotes the hard function for the polarized process, and this expression can once again be written as a Fourier transform by defining

$$\frac{ib^\beta}{2} f_{1T,g/N}^{\perp,f\,\text{unsub}}(x,b;\mu,\zeta/\nu^2) = \int d^2k_T e^{-i\boldsymbol{b}\cdot\boldsymbol{k}_T} \frac{k_T^\beta}{M} f_{1T,g/N}^{\perp,f\,\text{unsub}}(x,k_T;\mu,\zeta/\nu^2)\,. \tag{4.19}$$

Finally, the factorization formula for the polarized differential cross section becomes

$$\begin{aligned}\frac{d\sigma^{UT}(\boldsymbol{S}_T)}{dQ^2dyd^2\boldsymbol{p}_T dy_J d^2\boldsymbol{q}_T} =& H^{\text{Sivers}}(Q,y,p_T,y_J;\mu) \int \frac{d^2b}{(2\pi)^2} e^{i\boldsymbol{b}\cdot\boldsymbol{q}_T} S(\boldsymbol{b};\mu) \\ &\times \frac{i}{2}(\epsilon_{\alpha\beta}\, S_T^\alpha\, b^\beta) f_{1T,g/N}^{\perp,f}(x,b;\mu,\zeta) \\ &\times J_{\mathcal{Q}}(p_T R, m_{\mathcal{Q}};\mu)\, S_{\mathcal{Q}}^c(\boldsymbol{b},R,m_{\mathcal{Q}};\mu)\, J_{\bar{\mathcal{Q}}}(p_T R, m_{\mathcal{Q}};\mu)\, S_{\bar{\mathcal{Q}}}^c(\boldsymbol{b},R,m_{\mathcal{Q}};\mu)\,.\end{aligned} \tag{4.20}$$

Here, we have applied the redefinition Eq. (4.12) to obtain the rapidity-scale-independent gluon Sivers function

$$f_{1T,g/N}^{\perp,f}(x,b;\mu,\zeta) \equiv f_{1T,g/N}^{\perp,f\,\text{unsub}}(x,b;\mu,\zeta/\nu^2)\sqrt{S_{n\bar{n}}(b;\mu,\nu)}\,. \tag{4.21}$$

4.2.2.3 Hard function

In the unpolarized process, the LO hard function is determined by the tree-level cross section for dijet production in DIS, which is expressed as [175, 176]

$$\begin{aligned}H(Q,y,p_T,y_J;\mu) =& \frac{\alpha_{\text{em}}^2 \alpha_s Q_f^2 C_F C_A}{4\pi Q^2 y^2 S_{\ell P}} \Big\{ \left[1+(1-y)^2\right] H^{U,U+L} - y^2\, H^{U,L} \\ &- (2-y)\sqrt{1-y}\, H^{U,I} + 2(1-y)\, H^{U,T} \Big\}\,,\end{aligned} \tag{4.22}$$

where α_{em} is the fine structure constant and Q_f denotes the fractional charge of the HF quark. On the right-hand side, the first superscript U indicates that the incoming gluon is unpolarized, while the second superscripts $\{U+L, L, I, T\}$ correspond to the different helicity states of the off-shell photon. Explicitly, the functions $H^{U,i}$ are expressed as

$$\begin{aligned}&H^{U,I} = \cos(\phi_J) H_{\cos(\phi_J)}^{U,I}, \quad H^{U,T} = \cos(2\phi_J) H_{\cos(2\phi_J)}^{U,T}, \\ &H_{\cos(\phi_J)}^{U,I} = \frac{2z(1-2z)p_T Q}{D^2}\left(-1+\frac{2p_T^2}{D}\right), \quad H_{\cos(2\phi_J)}^{U,T} = \frac{2z\,p_T^2}{D^2}\left(1-\frac{p_T^2}{D}\right), \\ &H^{U,U+L} = \frac{1}{D}\left(\frac{1}{2-2z}-z\right) + \frac{2zp_T^2}{D^2} - \frac{zp_T^2}{D^3}\left(2p_T^2+Q^2(1-2z)^2\right),\end{aligned}$$

$$H^{U,L} = \frac{4zp_T^2}{D^2}\left(1 - \frac{p_T^2}{D}\right) . \tag{4.23}$$

One immediately sees that the functions $H^{U,I}$ and $H^{U,T}$ vanish upon integrating out the azimuthal angle ϕ_J of the jet. As such, these contributions do not play a role in our numerical calculations.

The expression for the hard anomalous dimension can be obtained from the calculation of the 3-jet process $\gamma^* \to q\bar{q}g$ at lepton collisions [177, 178]. The hard anomalous dimension can also be read from the general structures in [179, 180] and is given as

$$\Gamma^h_\mu(\alpha_s) = C_A\Gamma^{\rm cusp}(\alpha_s)\ln\left(\frac{\hat{u}\,\hat{t}}{\hat{s}\,\mu^2}\right) - 2C_F\Gamma^{\rm cusp}(\alpha_s)\ln\left(\frac{\mu^2}{\hat{s}}\right) + 4\gamma^q(\alpha_s) + 2\gamma^g(\alpha_s)\,, \tag{4.24}$$

where $\Gamma^{\rm cusp}$ is the cusp anomalous dimension, while γ^q and γ^g represent the single logarithmic anomalous dimensions for the quark and gluon, respectively. With this anomalous dimension, one can then perform resummation by solving the following renormalization group (RG) equation for the hard function

$$\frac{d}{d\ln\mu}\ln H(\mu) = \Gamma^h_\mu(\alpha_s)\,, \tag{4.25}$$

where, for brevity, we maintain only the scale μ-dependence in the hard function. We note that in order to perform the evolution at next-to-leading logarithmic (NLL) accuracy, the cusp anomalous dimension is needed at two-loop order and the single logarithmic anomalous dimensions are needed at one-loop order. The values of these expressions are

$$\begin{aligned} &\gamma_0^{\rm cusp} = 4\,, \quad \gamma_1^{\rm cusp} = \left(\frac{268}{9} - \frac{4\pi^2}{3}\right)C_A - \frac{40}{9}C_F n_f\,, \\ &\gamma_0^q = -3C_F\,, \quad \gamma_0^g = -\beta_0, \quad \beta_0 = \frac{11}{3}C_A - \frac{4}{3}T_F n_f\,, \end{aligned} \tag{4.26}$$

where we have organized the perturbative expansion of each anomalous dimension as

$$\gamma(\alpha_s) = \frac{\alpha_s}{4\pi}\gamma_0 + \left(\frac{\alpha_s}{4\pi}\right)^2\gamma_1 + \mathcal{O}(\alpha_s^3)\,. \tag{4.27}$$

For the polarized process, we must consider the process-dependence of the corresponding gluon Sivers functions [157]. Such process-dependence can be computed via the attachment

of an additional gluon originating from the gauge link in the definition of the Sivers function. This additional gluon is responsible for the soft pole that generates Sivers asymmetry. This method is widely used in computing the process-dependence of the quark Sivers function, see e.g. [133], which gives the same results as shown in [157, 181]. In Fig. 4.2, the soft poles are represented by red lines. We note that for both the polarized and unpolarized cases, the hard functions can be expressed as matrices in color space [165]. For more complicated processes, the relationship between the polarized and unpolarized hard matrices is non-trivial. However, for the $\gamma^* q \to \mathcal{Q}\bar{\mathcal{Q}}$ process, the color space is one-dimensional and, therefore, the polarized hard function can be simply written as

$$H^{\text{Sivers}}(Q, y, p_T, y_J; \mu) = (C_1 + C_2)\ h(Q, y, p_T, y_J; \mu)\,. \tag{4.28}$$

Here, C_1 and C_2 are the color factors for the polarized hard process associated with the attachment of the additional gluon to the HF quark and anti-quark [144, 182, 183], respectively. The function $h(Q, y, p_T, y_J, \mu)$ is the kinematic part of the hard function. For the unpolarized case, the hard function can be written as

$$H(Q, y, p_T, y_J; \mu) = C_u\, h(Q, y, p_T, y_J; \mu)\,, \tag{4.29}$$

where factor C_u is the color factor associated with the unpolarized hard process. We find that at LO for this process, the attachment of this additional gluon originating from the gauge link in the definition of the Sivers function produces color configurations which are proportional to $(-if^{abc})$. This analysis indicates that while there are both d- and f-type gluon Sivers functions [157], this process at LO is only sensitive to the f-type gluon Sivers function. In addition to this, while the term $(-if^{abc})$ in Fig. 4.2 appears in the hard function, this term should be absorbed into the definition of the gluon Sivers function as it originates from the Wilson line in the adjoint representation. Similarly, the term δ^{ac} in that figure should be absorbed into the definition of the unpolarized TMD PDF. For this process, we find that $(C_1 + C_2) = C_u$. As a result, the polarized and unpolarized hard functions are equal and the hard anomalous dimension is unchanged for the polarized case.

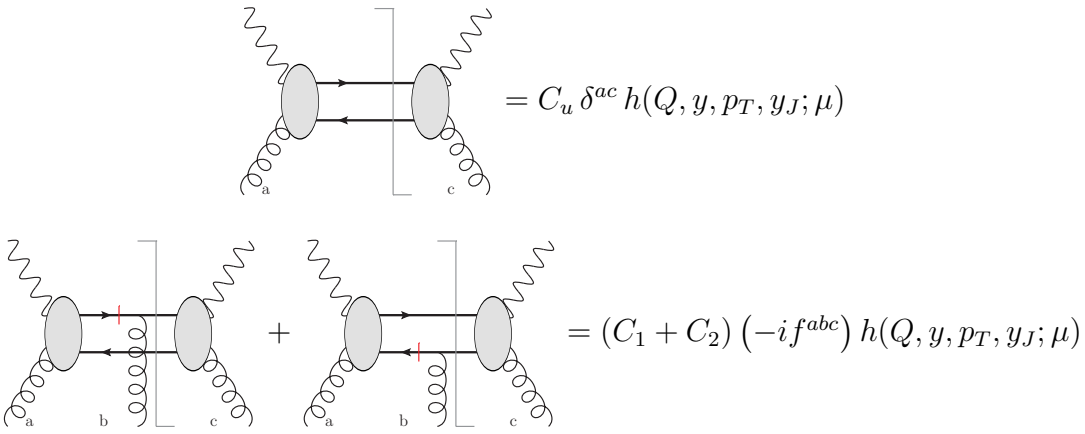

Figure 4.2: Top: Unpolarized hard Feynman diagram for HF dijet production. Bottom: Polarized hard diagram for HF dijet production. The red lines in the polarized case indicate the location of a soft pole.

4.2.2.4 TMD PDFs and the global soft function

In order to regulate the rapidity divergences in the TMD PDFs and the global soft function, we use the η regulator of [62]. The expression for the unsubtracted gluon TMD in this regularization scheme can be obtained from [136], and is given by

$$\begin{aligned} f_{g/g}^{\text{NLO unsub}}(x, b; \mu, \zeta/\nu^2) &= \delta(1-x) \\ &+ \frac{\alpha_s}{4\pi} C_A \left[\frac{4}{\eta}\left(\frac{1}{\epsilon} + L\right) + \frac{2}{\epsilon}\left(L_\zeta + \frac{\beta_0}{C_A}\right)\right]\delta(1-x) \\ &- \frac{\alpha_s}{4\pi}\left[\frac{2}{\epsilon} + 2L\right] P_{gg}(x) \\ &+ \frac{\alpha_s}{4\pi} C_A \left[L\left(L_\zeta + \frac{\beta_0}{C_A}\right)\delta(1-x)\right], \end{aligned} \tag{4.30}$$

$$f_{g/q}^{\text{NLO unsub}}(x, b; \mu, \zeta/\nu^2) = -\frac{\alpha_s}{4\pi}\left[\frac{2}{\epsilon} + 2L\right] P_{qg}(x) + \frac{\alpha_s}{4\pi} C_F\,(2x)\,, \tag{4.31}$$

where b is the magnitude of the two-dimensional vector transverse to the beam direction $\boldsymbol{b} = b\,(\cos\phi_b, \sin\phi_b)$, and the splitting kernels are defined as

$$P_{gg}(x) = 2C_A\left[\frac{x}{(1-x)_+} + \frac{1-x}{x} + x(1-x)\right] + \frac{\beta_0}{2}\delta(1-x)\,, \tag{4.32}$$

$$P_{gq}(x) = C_F \frac{1 + (1-x)^2}{x}\,, \tag{4.33}$$

are the collinear splitting kernels. The term in the third line of Eq. (4.30) and the analogous term in Eq. (4.31) contain the infrared divergences which are to be matched to the collinear PDF. The RG equations for the gluon TMD PDF are then

$$\frac{d}{d\ln\mu}\ln f_{g/N}^{\rm unsub}(x,b;\mu,\zeta/\nu^2) = \Gamma_\mu^{f_g}(\alpha_s)\,, \tag{4.34}$$

$$\frac{d}{d\ln\nu}\ln f_{g/N}^{\rm unsub}(x,b;\mu,\zeta/\nu^2) = \Gamma_\nu^{f_g}(\alpha_s)\,. \tag{4.35}$$

Here the anomalous dimensions are given by

$$\Gamma_\mu^{f_g}(\alpha_s) = C_A\gamma^{\rm cusp}(\alpha_s)L_\zeta - 2\gamma_\mu^{f_g}(\alpha_s)\,, \quad \Gamma_\nu^{f_g}(\alpha_s) = \frac{\alpha_s}{\pi}C_A L + \mathcal{O}(\alpha_s^2)\,, \tag{4.36}$$

with $\gamma_0^{f_g} = \gamma_0^g$, which is given in Eq. (4.26).

To obtain the soft function, we need to consider all the different configuration in which soft gluons can scatter in the cross section. The soft function at LO and NLO are given by

$$S^{\rm LO}(b;\mu,\nu) = 1\,, \tag{4.37}$$

$$S^{\rm NLO}(\boldsymbol{b};\mu,\nu) = -\frac{C_A}{2}\,\mathcal{I}_{BJ} - \frac{C_A}{2}\,\mathcal{I}_{B\bar{J}} + \left(\frac{C_A}{2} - C_F\right)\mathcal{I}_{J\bar{J}}\,, \tag{4.38}$$

where the soft integrals $\mathcal{I}_{ij}$ are given by

$$\mathcal{I}_{ij} = \frac{\alpha_s\mu^{2\epsilon}\pi^\epsilon e^{\epsilon\gamma_E}}{\pi^2}\int d^dk\,\delta^+(k^2)e^{-i\,k\cdot b}\frac{n_i\cdot n_j}{(n_i\cdot k)(n_j\cdot k)}\frac{\nu^\eta}{|k^+-k^-|^\eta}\,. \tag{4.39}$$

To obtain this expression, I have considered all possible appearances of virtual soft gluon emissions. In this expression, the measurement function is the usual one for the soft function, which is given by $\delta(\boldsymbol{k}_\perp - \boldsymbol{l}_\perp)$ and gives rise to the phase factor $e^{-ik\cdot b}$ after performing the Fourier transform. In this expression, i and j are either B, J, or $\bar{J}$, where B denotes the beam direction while J and $\bar{J}$ denote the directions of the jet initiated by the HF quark and anti-quark, respectively. Therefore, the $\mathcal{I}_{J\bar{J}}$ provides the information for the scattering of a soft gluon from one jet to another and analogous soft contributions can be defined for the other $\mathcal{I}$ terms. The expressions for the ϕ_b-dependent beam-jet soft function integrals are given in [135] as

$$\mathcal{I}_{BJ} = \frac{\alpha_s}{4\pi}\left[\frac{4}{\eta}\left(\frac{1}{\epsilon}+L\right) - \frac{4}{\epsilon^2} - \frac{2}{\epsilon}\left(-2y_J + L_\nu + 2\ln\frac{2i\mu\,c_{bJ}}{\mu_b}\right)\right] + \mathcal{I}_{BJ}^{\rm fin}, \tag{4.40}$$

$$\mathcal{I}_{B\bar{J}} = \frac{\alpha_s}{4\pi}\left[\frac{4}{\eta}\left(\frac{1}{\epsilon}+L\right) - \frac{4}{\epsilon^2} - \frac{2}{\epsilon}\left(-2y_{\bar{J}} + L_\nu + 2\ln\frac{-2i\mu\, c_{bJ}}{\mu_b}\right)\right] + \mathcal{I}^{\text{fin}}_{B\bar{J}}, \tag{4.41}$$

with $c_{bJ} = \cos(\phi_b - \phi_J)$ and where the rapidity of jets are

$$y_J = \ln\frac{zQ}{p_T}, \qquad y_{\bar{J}} = \ln\frac{(1-z)Q}{p_T}\,. \tag{4.42}$$

Here, the terms marked by "fin" in their superscripts denote the finite contributions of their respective functions. While the divergent pieces are required for the purposes of resummation, the finite pieces are only needed at NLO. Since we perform our analysis at NLL accuracy, these terms are not needed for this study. Recently in [166], the authors derive the following the jet-jet soft function integral which contains no rapidity divergence. This integral can be written as

$$\mathcal{I}_{J\bar{J}} = \frac{\alpha_s}{4\pi}\left[-\frac{4}{\epsilon^2} + \frac{4}{\epsilon}\left(\ln\frac{\hat{s}}{p_T^2} - L - \ln\left(4c_{bJ}^2\right)\right)\right] + \mathcal{I}^{\text{fin}}_{J\bar{J}}. \tag{4.43}$$

From Eqs. (4.40), (4.41), and (4.43), we obtain the following expressions for the soft anomalous dimensions

$$\Gamma^s_\mu(\alpha_s) = 2C_F\,\Gamma^{\text{cusp}}(\alpha_s)L + C_A\,\Gamma^{\text{cusp}}(\alpha_s)L_\nu + \gamma^s(\alpha_s)\,, \tag{4.44}$$

$$\Gamma^s_\nu(\alpha_s) = -\frac{\alpha_s}{\pi}C_A L + \mathcal{O}(\alpha_s^2)\,, \tag{4.45}$$

with the one-loop single logarithmic anomalous dimension

$$\gamma^s_0 = 8C_F\ln\left(4c_{bJ}^2\right) + 4(C_A - 2C_F)\ln\frac{\hat{s}}{p_T^2} + 4\,C_A\ln\frac{\hat{s}}{Q^2}\,. \tag{4.46}$$

As expected, we see that the one-loop rapidity anomalous dimensions of the TMD PDF and the soft function fulfill the condition

$$\Gamma^{f_g}_{\nu,0} + \Gamma^s_{\nu,0} = 0\,. \tag{4.47}$$

Thus, the product of $f^{\text{unsub}}_{g/N}(x,b;\mu,\zeta/\nu^2)$ and $S(\boldsymbol{b},\mu,\nu)$ is ν-independent, and we can construct the properly-defined gluon TMD PDF as in Eq. (4.13).

Here we find that the soft function depends not only the magnitude but also the direction of the vector $\boldsymbol{b}$. As shown in Sec. 4.2.2.6 a similar structure also shows up in the collinear-soft function, and the ϕ_b dependence in the anomalous dimensions will cancel out between

these two functions. However, after taking into account the evolution between the soft and collinear-soft function, one finds that the ϕ_b integral is divergent in some phase space region. In order to avoid such divergences we apply methods in [135, 165] where one first performs an averaging over the ϕ_b angle in both soft and collinear-soft function. We note that this method does not change the RG invariance as shown in Eqs. (4.75) and (4.76). In addition, as discussed in [164] no significant numerical effects between different methods are observed in the NLL resummation calculation.

The ϕ_b-averaged soft function can be constructed from Eqs. (4.37) and (4.38) by replacing the soft integrals with

$$\bar{\mathcal{I}}_{BJ} = \frac{\alpha_s}{4\pi}\left[2\left(\frac{2}{\eta} - L_\nu + 2y_J\right)\left(\frac{1}{\epsilon} + L\right) - \frac{4}{\epsilon^2} - \frac{2}{\epsilon}L + \frac{\pi^2}{3}\right], \tag{4.48}$$

$$\bar{\mathcal{I}}_{B\bar{J}} = \frac{\alpha_s}{4\pi}\left[2\left(\frac{2}{\eta} - L_\nu + 2y_{\bar{J}}\right)\left(\frac{1}{\epsilon} + L\right) - \frac{4}{\epsilon^2} - \frac{2}{\epsilon}L + \frac{\pi^2}{3}\right], \tag{4.49}$$

$$\begin{aligned}\bar{\mathcal{I}}_{J\bar{J}} = \frac{\alpha_s}{2\pi}\Bigg[&4\left(\frac{1}{\epsilon} + L\right)\ln\big(2\cosh(\Delta y/2)\big) - \frac{2}{\epsilon^2} - \frac{2}{\epsilon}L - L^2 + \Delta y^2 \\ &- 4\ln^2\big(2\cosh(\Delta y/2)\big) + \frac{\pi^2}{6}\Bigg],\end{aligned} \tag{4.50}$$

where we have placed a bar over these integrals in order to distinguish them from the ϕ_b-dependent ones and have defined $\Delta y = y_J - y_{\bar{J}}$. These results are the same as the soft function calculated in [184]. Therefore, the anomalous dimensions for the averaged case are

$$\bar{\Gamma}^s_\mu(\alpha_s) = 2C_F\,\Gamma^{\rm cusp}(\alpha_s)L + C_A\,\Gamma^{\rm cusp}(\alpha_s)L_\nu + \bar{\gamma}^s(\alpha_s)\,, \tag{4.51}$$

$$\bar{\Gamma}^s_\mu(\alpha_s) = -\frac{\alpha_s}{\pi}C_A L + \mathcal{O}(\alpha_s^2)\,, \tag{4.52}$$

where the one-loop single logarithmic anomalous dimensions is

$$\bar{\gamma}^s_0 = 4(C_A - 2C_F)\ln\frac{\hat{s}}{p_T^2} + 4C_A\ln\frac{\hat{s}}{Q^2}\,. \tag{4.53}$$

By comparing Eqs. (4.45) and (4.52), one can see the rapidity anomalous dimension is unchanged. Therefore in the ϕ_b-averaged case, we can once again write the factorized expression in terms of the properly defined TMD PDFs.

4.2.2.5 Massive quark jet function

In this section, we discuss the calculation of the massive quark jet function at NLO. The massive quark jet function has been investigated in detail for various observables. For example, the factorization formula for the massive event shape distribution involves such a jet function, as the jet and heavy quark masses are of similar magnitude [185, 186, 187, 188]. The corresponding jet function has been calculated to two-loop order [189]. Furthermore, the semi-inclusive massive quark jet fragmentation function has been calculated at NLO and applied to inclusive jet production [190, 191]. Recently, the one-loop expression for the so-called unmeasured massive quark jet function has been presented in [192].

The global jet anomalous dimension can be obtained from the divergent terms of the unmeasured massive quark jet function. As shown in Fig. 4.3, the one-loop calculation involves two types of diagrams: $J_{\mathcal{Q}}^{\mathrm{NLO,V}}$ and $J_{\mathcal{Q}}^{\mathrm{NLO,R}}$, where $J_{\mathcal{Q}}^{\mathrm{NLO,V}}$ contains only single cut propagators and is thereby unconstrained by the jet algorithm. Explicitly, it is written as

$$J_{\mathcal{Q}}^{\mathrm{NLO,V}} = \frac{\alpha_s}{4\pi} C_F \left[\frac{2}{\epsilon^2} + \frac{1}{\epsilon} \left(1 + 2\ln\frac{\mu^2}{m_{\mathcal{Q}}^2} \right) + \left(1 + \ln\frac{\mu^2}{m_{\mathcal{Q}}^2} \right) \ln\frac{\mu^2}{m_{\mathcal{Q}}^2} + 4 + \frac{\pi^2}{6} \right] , \tag{4.54}$$

where the heavy quark mass $m_{\mathcal{Q}}$ is the only physical scale involved. Since the real contribution $J_{\mathcal{Q}}^{\mathrm{NLO,R}}$ is constrained by the jet algorithm, it will depend on the jet scale $p_T R$ in addition to $m_{\mathcal{Q}}$. In this work, we define the HF quark four-momentum q^μ with $q^2 = m_{\mathcal{Q}}^2$, which is known as the M-scheme [188]. We note that in the hierarchy of scales we are considering, the constraint of the anti-k_T algorithm [193] is independent of the HF quark mass $m_{\mathcal{Q}}$ and is in fact identical to that for massless partons [190], namely

$$\Theta_{\text{anti-}k_T} = \theta \left[\left(\frac{q^- (\omega_J - q^-)}{\omega_J} \right)^2 \left(\frac{R}{2\cosh y_J} \right)^2 - \boldsymbol{q}_\perp^2 \right] , \tag{4.55}$$

where $q^\mu = (q^+, q^-, \boldsymbol{q}_\perp)$ is the four-momentum of the HF quark and ω_J is the large component of the jet four-momentum. The jet scale $p_T R$ emerges in Eq. (4.55) upon noting $\omega_J = 2\, p_T \cosh y_J$. In the phase space integral, we expand the integrated momentum q along the jet direction with $q^+ = (m_{\mathcal{Q}}^2 + \boldsymbol{q}_\perp^2)/q^-$ given by the power counting requirement $p_T R \sim m_{\mathcal{Q}}$.

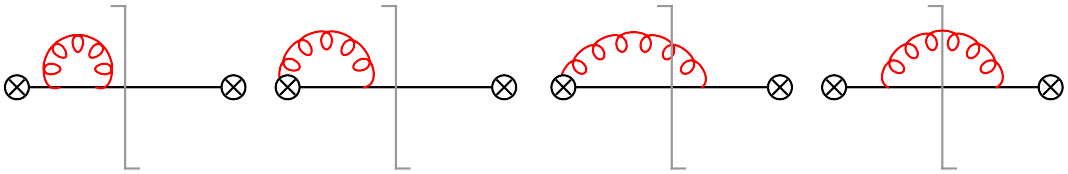

Figure 4.3: Sample Feynman diagrams contributing to the massive quark jet function $J_{\mathcal{Q}}$ at one-loop order in perturbation theory. The virtual corrections $J_{\mathcal{Q}}^{\text{NLO,V}}$ are displayed in the first two diagrams, where each contain only a single cut propagator. The remaining diagrams involving two cut propagators represent the real corrections $J_{\mathcal{Q}}^{\text{NLO,R}}$.

Explicitly, we have

$$\begin{aligned} J_{\mathcal{Q}}^{\text{NLO,R}}(p_T R, m_{\mathcal{Q}}, \epsilon) &= \frac{\alpha_s C_F e^{\epsilon\gamma_E}\mu^{2\epsilon}}{2\pi\Gamma(1-\epsilon)} \int \frac{dq^-}{\omega_J} \frac{d\boldsymbol{q}_\perp^2}{\boldsymbol{q}_\perp^{2\epsilon}} \left[\frac{q^-}{\omega_J - q^-} \frac{2\boldsymbol{q}_\perp^2 \omega_J^4}{[\boldsymbol{q}_\perp^2 \omega_J^2 + m_{\mathcal{Q}}^2(\omega_J - q^-)^2]^2} \right. \\ &\quad \left. + (1-\epsilon) \frac{\omega_J(\omega_J - q^-)}{\boldsymbol{q}_\perp^2 \omega_J^2 + m_{\mathcal{Q}}^2(\omega_J - q^-)^2} \right] \theta(\omega_J - q^-)\Theta_{\text{anti-}k_T} \\ &= \frac{\alpha_s}{4\pi} C_F \left[-2\ln\left(\frac{m_{\mathcal{Q}}^2 + p_T^2 R^2}{m_{\mathcal{Q}}^2} \right) + 2 - \frac{2m_{\mathcal{Q}}^2}{m_{\mathcal{Q}}^2 + p_T^2 R^2} \right] \frac{1}{\epsilon} + J_{\mathcal{Q}}^{\text{R,fin}} \,, \end{aligned} \tag{4.56}$$

where only a single divergence is exhibited, as the heavy quark mass $m_{\mathcal{Q}}$ acts as a regulator of the overlapping soft and collinear regions of phase space. After combining the real and virtual contributions, the logarithmic dependence on the quark mass $m_{\mathcal{Q}}$ cancels out.

The one-loop global jet renormalization constant then reads

$$Z^{J_{\mathcal{Q}}} = 1 + \frac{\alpha_s}{4\pi} C_F \left[\frac{2}{\epsilon^2} + \frac{1}{\epsilon} \left(2\ln \frac{\mu^2}{m_{\mathcal{Q}}^2 + p_T^2 R^2} + 3 - \frac{2m_{\mathcal{Q}}^2}{m_{\mathcal{Q}}^2 + p_T^2 R^2} \right) \right] , \tag{4.57}$$

where, again, we observe that the heavy quark mass $m_{\mathcal{Q}}$ only affects the single pole structure. We further note that as $m_{\mathcal{Q}} \to 0$, the massive quark jet renormalization constant reduces to that of the massless jet, $Z^{J_{\mathcal{Q}}} \to Z^{J_q}$. This gives us the following expression for the global jet anomalous dimension

$$\Gamma_\mu^{j_{\mathcal{Q}}}(\alpha_s) = -C_F \Gamma^{\text{cusp}}(\alpha_s) \ln \frac{m_{\mathcal{Q}}^2 + p_T^2 R^2}{\mu^2} + \gamma^{j_{\mathcal{Q}}}(\alpha_s) \,, \tag{4.58}$$

with the one-loop single logarithmic anomalous dimension as

$$\gamma_0^{j_{\mathcal{Q}}} = 2C_F \left(3 - \frac{2m_{\mathcal{Q}}^2}{m_{\mathcal{Q}}^2 + p_T^2 R^2} \right) , \tag{4.59}$$

where the first term in the brackets is shared by the massless quark jet function and the second term constitutes the finite quark mass correction. Finally, the renormalized HF jet function is given by the following

$$J^{\text{ren.}}_{\mathcal{Q},\text{NLO}}(p_T R, m_{\mathcal{Q}};\mu) = \frac{\alpha_s}{4\pi} C_F \Bigg[\left(3 - \frac{2m_{\mathcal{Q}}^2}{m_{\mathcal{Q}}^2 + p_T^2 R^2}\right) \ln \frac{\mu^2}{m_{\mathcal{Q}}^2 + p_T^2 R^2} + \ln^2 \frac{\mu^2}{m_{\mathcal{Q}}^2 + p_T^2 R^2} + 13 - \frac{3\pi^2}{2} + \mathcal{F}(p_T R, m_{\mathcal{Q}}) \Bigg], \tag{4.60}$$

where the function $\mathcal{F}(p_T R, m_{\mathcal{Q}})$ can be expressed as

$$\begin{aligned}\mathcal{F}(p_T R, m_{\mathcal{Q}}) = {} & \pi^2 - 4\,\text{Li}_2\left(-\frac{m_{\mathcal{Q}}^2}{p_T^2 R^2}\right) + 2\left(1 - \ln\frac{m_{\mathcal{Q}}^2}{p_T^2 R^2}\right)\ln\frac{m_{\mathcal{Q}}^2 + p_T^2 R^2}{p_T^2 R^2} \\ & - \frac{2m_{\mathcal{Q}}^2}{m_{\mathcal{Q}}^2 + p_T^2 R^2}\ln\frac{m_{\mathcal{Q}}^2}{p_T^2 R^2} - \frac{m_{\mathcal{Q}}^2}{p_T^2 R^2}\ln\frac{m_{\mathcal{Q}}^2 + p_T^2 R^2}{m_{\mathcal{Q}}^2} \\ & - 4\left[\frac{m_{\mathcal{Q}}}{p_T R}\left(1 + \frac{m_{\mathcal{Q}}^2}{m_{\mathcal{Q}}^2 + p_T^2 R^2}\right) + \text{Cot}^{-1}\left(\frac{m_{\mathcal{Q}}}{p_T R}\right)\right]\text{Cot}^{-1}\left(\frac{m_{\mathcal{Q}}}{p_T R}\right).\end{aligned} \tag{4.61}$$

This expression for the HF jet function is equivalent to the semi-analytic form presented in [192], and one can see that as $m_{\mathcal{Q}} \to 0$, we have $\mathcal{F} \to 0$ and, therefore, $J_{\mathcal{Q}} \to J_q$. Hence, the massive quark jet function behaves as expected in the massless limit.

4.2.2.6 Collinear-soft function

We saw in the previous chapters of this dissertation that the soft function is responsible for enforcing gauge invariance of the cross section under soft gauge transformations. In our definition of the IR QCD modes, we introduced an additional soft mode, known as the collinear soft mode, and we discussed how this mode is accounts for soft radiation which leaves the jet. In this section, we calculate the one-loop perturbative expression for the collinear-soft function $S^c_{\mathcal{Q}}(\boldsymbol{b}, R, m_{\mathcal{Q}};\mu)$. The corresponding Feynman diagrams are shown in Fig. 4.4, where the blue and black lines represent Wilson lines along v_J^μ and $\bar{n}_J^\mu$ directions, respectively. At this point, I would like to note a rather subtle point. In our calculation of the global soft function, we took the jet to be light-like. However, in our definition of the jet function, we took the parton to have some mass. Thus the relevant Wilson lines which enter into our calculation of the collinear soft function point in the directions n_J and v_J, where

the massive quark velocity v_J^μ is defined by

$$v_J^\mu = \frac{\omega_J}{m_\mathcal{Q}} \frac{n_J^\mu}{2} + \frac{m_\mathcal{Q}}{\omega_J} \frac{\bar{n}_J^\mu}{2}\,, \qquad \text{with } v_J^2 = 1\,. \tag{4.62}$$

Alternatively, we could have treated the jet to point in the v_J direction. The introduction of this direction would add additional mass to both the global soft and collinear-soft function. In our paper, we did not perform this second calculation but we could consider it in another work.

Treating the calculation using the v_J and n_J direction, the explicit expression for the bare NLO collinear-soft function is given by

$$S^c_{\mathcal{Q},\mathrm{NLO}}(\boldsymbol{b}, R, m_\mathcal{Q}, \epsilon) = 2C_F\, w_{\bar{n}_J v_J} - C_F\, w_{v_J v_J}\,, \tag{4.63}$$

where the collinear-soft integrals $w_{\alpha\beta}$ are defined in b-space as

$$\begin{aligned} w_{\alpha\beta} = \frac{\alpha_s \mu^{2\epsilon} \pi^\epsilon e^{\epsilon\gamma_E}}{2\pi^2} \int d^d k\, \delta^+(k^2) e^{-i\,\bar{n}_J\cdot k\, n_J\cdot b/2} \\ \frac{\alpha\cdot\beta}{(\alpha\cdot k)\,(\beta\cdot k)}\, \theta\left[\frac{n_J\cdot k}{\bar{n}_J\cdot k} - \left(\frac{R}{2\cosh y_J}\right)^2\right]\,. \end{aligned} \tag{4.64}$$

Notice at this point that the phase factor for the collinear-soft function is different than that for the soft function. This is a result of the fact that the power counting of the soft function goes as $q_\perp\,(1,1,1)$ while the power counting of the collinear-soft function goes as $q_\perp\,(1,R^2,R)$. As a result, only the plus component of the collinear-soft function can contribute to the observable. Additionally, note that in this calculation, the θ function is associated with enforcing that the collinear-soft radiation leaves the jet and thus produces transverse momentum in the final-state.

Upon performing the k-integration, we obtain the following expressions for $w_{\alpha\beta}$

$$w_{\bar{n}_J v_J} = \frac{\alpha_s}{4\pi}\left[-\frac{1}{\epsilon^2} - \frac{1}{\epsilon}\left(L + 2\ln\frac{-2ic_{bJ}}{R} - \ln\frac{m_\mathcal{Q}^2 + p_T^2 R^2}{p_T^2 R^2}\right)\right] + w^{\mathrm{fin}}_{\bar{n}_J v_J}\,, \tag{4.65}$$

$$w_{v_J v_J} = \frac{\alpha_s}{4\pi}\left[-\frac{1}{\epsilon}\left(\frac{2m_\mathcal{Q}^2}{m_\mathcal{Q}^2 + p_T^2 R^2}\right)\right] + w^{\mathrm{fin}}_{v_J v_J}\,. \tag{4.66}$$

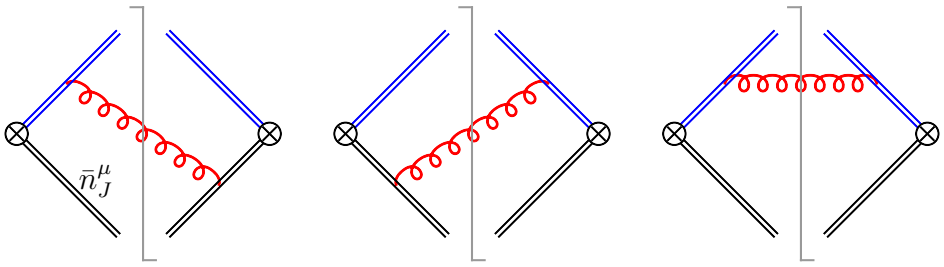

Figure 4.4: One-loop Feynman diagrams of the collinear-soft function $S_{\mathcal{Q}}^c$. The blue and black lines indicate the Wilson lines along v_J^μ and $\bar{n}_J^\mu$ directions, respectively.

We see that the finite quark mass corrections only enter into the single pole structure of the collinear-soft function. This is analogous to the observation made in Sec. 4.2.2.5 in analyzing the massive quark jet function, and can be understood through the same physical reasoning. The finite terms are given by

$$w_{\bar{n}_J v_J}^{\text{fin}} = \frac{\alpha_s}{4\pi}\left[2\left(\ln\frac{m_{\mathcal{Q}}^2+p_T^2R^2}{p_T^2R^2}-\ln\frac{-2i\,c_{bJ}}{R}\right)\ln\frac{-2i\,c_{bJ}}{R}\right. \tag{4.67}$$
$$\left.+\left(\ln\frac{m_{\mathcal{Q}}^2+p_T^2R^2}{p_T^2R^2}-2\ln\frac{-2i\,c_{bJ}}{R}-\frac{1}{2}L\right)L+\text{Li}_2\left(-\frac{m_{\mathcal{Q}}^2}{p_T^2R^2}\right)-\frac{\pi^2}{4}\right],$$
$$w_{v_J v_J}^{\text{fin}} = \frac{\alpha_s}{4\pi}\left[2\ln\frac{m_{\mathcal{Q}}^2+p_T^2R^2}{p_T^2R^2}-\frac{2m_{\mathcal{Q}}^2}{m_{\mathcal{Q}}^2+p_T^2R^2}\left(2\ln\frac{-2i\,c_{bJ}}{R}+L\right)\right]. \tag{4.68}$$

Here, we note that $w_{\bar{n}_J v_J}$ reduces to the massless $w_{\bar{n}_J n_J}$ function [135, 164] as $m_{\mathcal{Q}} \to 0$, while $w_{v_J v_J}$ vanishes. Given the expression for $S_{\mathcal{Q}}^c$, we can calculate the renormalization constant $Z^{S_{\mathcal{Q}}^c}$, which is given by

$$Z^{S_{\mathcal{Q}}^c} = 1 \tag{4.69}$$
$$+\frac{\alpha_s}{4\pi}C_F\left[-\frac{2}{\epsilon^2}-\frac{2}{\epsilon}\left(L+2\ln\frac{-2ic_{bJ}}{R}-\frac{m_{\mathcal{Q}}^2}{m_{\mathcal{Q}}^2+p_T^2R^2}-\ln\frac{m_{\mathcal{Q}}^2+p_T^2R^2}{p_T^2R^2}\right)\right].$$

This renormalization constant leads to the following formula for global collinear-soft anomalous dimension

$$\Gamma_\mu^{cs_{\mathcal{Q}}}(\alpha_s) = C_F\gamma^{\text{cusp}}(\alpha_s)\ln\frac{R^2\mu_b^2}{\mu^2}+\gamma^{cs_{\mathcal{Q}}}(\alpha_s), \tag{4.70}$$

where the one-loop single logarithmic anomalous dimension is

$$\gamma_0^{cs_{\mathcal{Q}}} = -4C_F\left[2\ln\left(-2ic_{bJ}\right)-\frac{m_{\mathcal{Q}}^2}{m_{\mathcal{Q}}^2+p_T^2R^2}-\ln\frac{m_{\mathcal{Q}}^2+p_T^2R^2}{p_T^2R^2}\right]. \tag{4.71}$$

The anomalous dimension for the collinear-soft function associated with the anti-quark is given by

$$\Gamma_\mu^{cs\bar{\mathcal{Q}}}(\alpha_s) = \Gamma_\mu^{cs\mathcal{Q}}(\alpha_s)|_{\phi_J \to \phi_J + \pi}\,. \tag{4.72}$$

For phenomenological purposes, we utilize the ϕ_b-averaged collinear-soft function, which can be obtained through Eq. (4.65) by making use of the following integrals

$$\int_0^{2\pi} \frac{d\phi_b}{2\pi} \ln\left(-2ic_{bJ}\right) = 0\,, \qquad \int_0^{2\pi} \frac{d\phi_b}{2\pi} \ln^2\left(-2ic_{bJ}\right) = -\frac{\pi^2}{6}\,. \tag{4.73}$$

The resulting anomalous dimension for the ϕ_b-averaged collinear-soft function is denoted by $\bar{\Gamma}^{cs\mathcal{Q}}$ with

$$\bar{\gamma}_0^{cs\mathcal{Q}} = 4C_F \left(\frac{m_{\mathcal{Q}}^2}{m_{\mathcal{Q}}^2 + p_T^2 R^2} + \ln \frac{m_{\mathcal{Q}}^2 + p_T^2 R^2}{p_T^2 R^2} \right)\,. \tag{4.74}$$

Upon integrating over ϕ_b, we find that $\bar{\Gamma}^{cs\bar{\mathcal{Q}}}(\alpha_s) = \bar{\Gamma}^{cs\mathcal{Q}}(\alpha_s)$ and, therefore, the two averaged collinear-soft functions $\bar{S}_{\mathcal{Q}}^c$ and $\bar{S}_{\bar{\mathcal{Q}}}^c$ behave identically under QCD evolution.

4.2.2.7 Renormalization group consistency

Armed with the anomalous dimensions of each component, we are now positioned to demonstrate the RG consistency of our factorization framework.

Inspection of Eqs. (4.58) and (4.70) reveals that all mass corrections cancel exactly in the sum $\Gamma_\mu^{j\mathcal{Q}} + \Gamma_\mu^{cs\mathcal{Q}}$, making the RG consistency of our formalism identical to the massless case. A similar observation is made in [192]. This general physical behavior has also been observed in the context of inclusive HF jet production [190], where the authors offer the intuitive argument that as the heavy quark mass $m_{\mathcal{Q}}$ constitutes IR information, it thus does not affect the UV behavior of the semi-inclusive jet function. In the present context, we see that the UV evolution behavior of the product of the jet and collinear-soft functions is insensitive to the IR scale introduced by the heavy quark mass. However, in Sec. 4.2.2.8, we will see how the heavy quark mass enters non-trivially and crucially into the evaluation of the differential cross section.

Therefore, upon combining Eqs. (4.24), (4.36), (4.44), (4.57) and (4.70), the RG consistency of our formalism is established:

$$\Gamma^h_\mu + \Gamma^s_\mu + \Gamma^{f_g}_\mu + 2\Gamma^{j\mathcal{Q}}_\mu + \Gamma^{cs\mathcal{Q}}_\mu + \Gamma^{cs\bar{\mathcal{Q}}}_\mu = 0\,. \tag{4.75}$$

Furthermore, we note that this consistency is preserved under the operation of ϕ_b-averaging

$$\Gamma^h_\mu + \bar{\Gamma}^s_\mu + \Gamma^{f_g}_\mu + 2\Gamma^{j\mathcal{Q}}_\mu + \bar{\Gamma}^{cs\mathcal{Q}}_\mu + \bar{\Gamma}^{cs\bar{\mathcal{Q}}}_\mu = 0\,. \tag{4.76}$$

4.2.2.8 Resummation formula

Utilizing our EFT framework, all-order resummation is achieved through RG evolution. The resulting all-order expression for the HF dijet production cross section is given at NLL[2] by

$$\begin{aligned}\frac{d\sigma^{UU}}{dQ^2 dy d^2\boldsymbol{q}_T dy_J d^2\boldsymbol{p}_T} &= H(Q,y,p_T,y_J;\mu_h)\int_0^\infty \frac{bdb}{2\pi} J_0(b\,q_T) f_{g/N}(x;\mu_{b*}) \\ &\times \exp\left[-\int_{\mu_{b*}}^{\mu_h}\frac{d\mu}{\mu}\Gamma^h_\mu(\alpha_s) - 2\int_{\mu_{b*}}^{\mu_j}\frac{d\mu}{\mu}\Gamma^{j\mathcal{Q}}_\mu(\alpha_s) - \int_{\mu_{b*}}^{\mu_{cs}}\frac{d\mu}{\mu}\left(\bar{\Gamma}^{cs\mathcal{Q}}_\mu(\alpha_s) + \bar{\Gamma}^{cs\bar{\mathcal{Q}}}_\mu(\alpha_s)\right)\right] \\ &\times \exp\left[-S_{\rm NP}(b,Q_0,n\cdot p_g)\right]\,,\end{aligned} \tag{4.77}$$

where J_0 is the zeroth order Bessel function of the first kind. In this expression, μ_h, μ_j, and μ_{cs} are the hard, jet, and collinear-soft scales, respectively. We have also performed the usual operator product expansion (OPE) of the unpolarized gluon TMD PDF $f_{g/N}(x,b;\mu,\zeta)$ in terms of the collinear gluon PDF $f_{g/N}(x;\mu)$ at the initial scales $\zeta_i = \mu_i^2 = \mu_{b*}^2$, and have kept the coefficient at LO to be consistent with NLL accuracy. The matching coefficient at higher-orders can be found in e.g. [172, 195, 196, 197, 198, 199, 200]. The function $S_{\rm NP}$ parameterizes the contribution from non-perturbative power corrections which are enhanced for $q_T \sim \Lambda_{\rm QCD}$. Explicitly, we apply the formula given in [92], which reads

$$S_{\rm NP}(b,Q_0,n\cdot p_g) = g_1 b^2 + \frac{g_2}{2}\frac{C_A}{C_F}\ln\frac{n\cdot p_g}{Q_0}\ln\frac{b}{b_*}\,. \tag{4.78}$$

[2]In our framework, we ignore contributions from NGL resummation. Such resummation could be included multiplicatively by using the parton shower algorithm developed recently for massive particles [194]. Note that the fitting function used in [164, 165] to capture the effects of NGLs is only an approximation for HF jet production, as finite heavy quark mass corrections are not included.

We assign the following values to the parameters: $g_1 = 0.106\,\mathrm{GeV}^2$, $g_2 = 0.84$ and $Q_0^2 = 2.4\,\mathrm{GeV}^2$.

Moreover, the spin-dependent cross section is expressed as

$$\begin{aligned}\frac{d\sigma^{UT}(\boldsymbol{S}_T)}{dQ^2 dy d^2\boldsymbol{q}_T dy_J d^2\boldsymbol{p}_T} &= \sin(\phi_q - \phi_s)\, H(Q, y, p_T, y_J; \mu_h) \int_0^\infty \frac{b^2 db}{4\pi} J_1(b\, q_T) f^{\perp,f}_{1T,g/N}(x; \mu_{b*}) \\ &\times \exp\left[-\int_{\mu_{b*}}^{\mu_h} \frac{d\mu}{\mu} \Gamma^h_\mu(\alpha_s) - 2\int_{\mu_{b*}}^{\mu_j} \frac{d\mu}{\mu} \Gamma^{j_{\mathcal{Q}}}_\mu(\alpha_s) - \int_{\mu_{b*}}^{\mu_{cs}} \frac{d\mu}{\mu} \left(\bar{\Gamma}^{cs_{\mathcal{Q}}}_\mu(\alpha_s) + \bar{\Gamma}^{cs_{\bar{\mathcal{Q}}}}_\mu(\alpha_s) \right) \right] \\ &\times \exp\left[-S^\perp_{\mathrm{NP}}(b, Q_0, n\cdot p_g) \right] . \end{aligned} \tag{4.79}$$

Here, we have expected a similar OPE for the gluon Sivers function $f^\perp_{1T,g/N}(x, b; \mu, \zeta)$ at the initial scales $\zeta_i = \mu_i^2 = \mu_{b*}^2$ and simply expressed the corresponding collinear function at LO as $f^{\perp,f}_{1T,g/N}(x; \mu_{b*})$ for simplicity. In principle, the corresponding collinear functions in the OPE expansion would be the twist-3 three-gluon correlation functions defined in [201, 202]. To the best of our knowledge, detailed OPE calculations for the corresponding coefficient functions are not available in the literature. An expansion of the gluon Sivers function in terms of the collinear twist-3 quark-gluon-quark correlator, or the so-called Qiu-Sterman function [66, 67], in transverse momentum space is performed in [144]. On the other hand, the coefficient functions for the expansion of the quark Sivers function in terms of the three-gluon correlation functions are provided in [112, 123]. The computation of the coefficient functions for expanding the gluon Sivers function in terms of the three-gluon correlation functions is essential for a full understanding of the QCD evolution of the gluon Sivers function. We leave this to future work.

Our knowledge about gluon Sivers functions, especially in the proper TMD factorization formalism, is rather limited. At the present moment, the only experimental constraint on the gluon Sivers function, in the TMD framework, comes from the SIDIS measurement of back-to-back hadron pairs off transversely-polarized deuterons and protons at COMPASS [203]. However, as of yet, there has been no theoretical extraction of the gluon Sivers function from such data. On the other hand, an important theoretical constraint on the gluon Sivers function comes from the Burkardt sum rule [204]. For the phenomenological purposes of

the next section, we adopt the non-perturbative parameterization utilized by [205, 206] [3]. Specifically, for the non-perturbative Sudakov, we take

$$S_{\rm NP}^{\perp}\left(b, Q_0, n\cdot p_g\right) = g_1\rho\, b^2 + \frac{g_2}{2}\frac{C_A}{C_F}\ln\frac{n\cdot p_g}{Q_0}\ln\frac{b}{b_*}\,, \tag{4.80}$$

where the g_2-dependent term is spin-independent and is, therefore, the same term occurring in Eq. (4.78), while the term $\propto g_1\rho$ can be connected to the Gaussian width in transverse momentum space [80] for the gluon Sivers function. For the collinear part of the gluon Sivers function, $f_{1T,g/p}^{\perp,f}(x;\mu)$ in Eq. (4.79), we take

$$f_{1T,g/N}^{\perp f}(x;\mu) = N_g\frac{4\rho\sqrt{2e\rho(1-\rho)g_1}}{M_{\rm proton}}x^{\alpha_g}(1-x)^{\beta_g}\frac{(\alpha_g+\beta_g)^{\alpha_g+\beta_g}}{\alpha_g^{\alpha_g}\beta_g^{\beta_g}}f_{g/N}(x;\mu)\,, \tag{4.81}$$

with the parameters given by

$$N_g = 0.65,\quad \alpha_g = 2.8,\quad \beta_g = 2.8,\quad \rho = 0.5,\quad M_{\rm proton} = 1\,{\rm GeV}\,, \tag{4.82}$$

and $f_{g/N}(x;\mu)$ denoting the unpolarized collinear gluon PDF. For $f_{g/N}(x;\mu)$, we use CT14nlo [208]–specifically, CT14nlo_NF3 (CT14nlo_NF4) for charm (bottom) jet-pair production with 3 (4) active parton flavors.

At this point, it is important to note that while the mass corrections in sum of the anomalous dimensions for the collinear-soft and massive jet functions cancel, the mass-dependence of $\Gamma_\mu^{j\varrho}$ contributes to the differential cross section. By examining Eqs. (4.77) and (4.79), we see that the mass corrections enter into the evolution between the scales μ_j and μ_{cs}. We will see in the following section that this can significantly affect both the q_T-distributions and spin asymmetries for HF dijet production at the EIC.

4.2.3 Numerical results

In this section, we present numerical results for HF dijet production in unpolarized and transversely-polarized-proton-electron collisions at the future EIC. We set the energies of

[3] Note that the gluon Sivers function in [205], and its updated version [207], is constrained to their study of the $p^\uparrow p \to \pi X$ process. Technically, this is not subject to a TMD factorization framework, but it serves as a starting point for our numerical study, following [151].

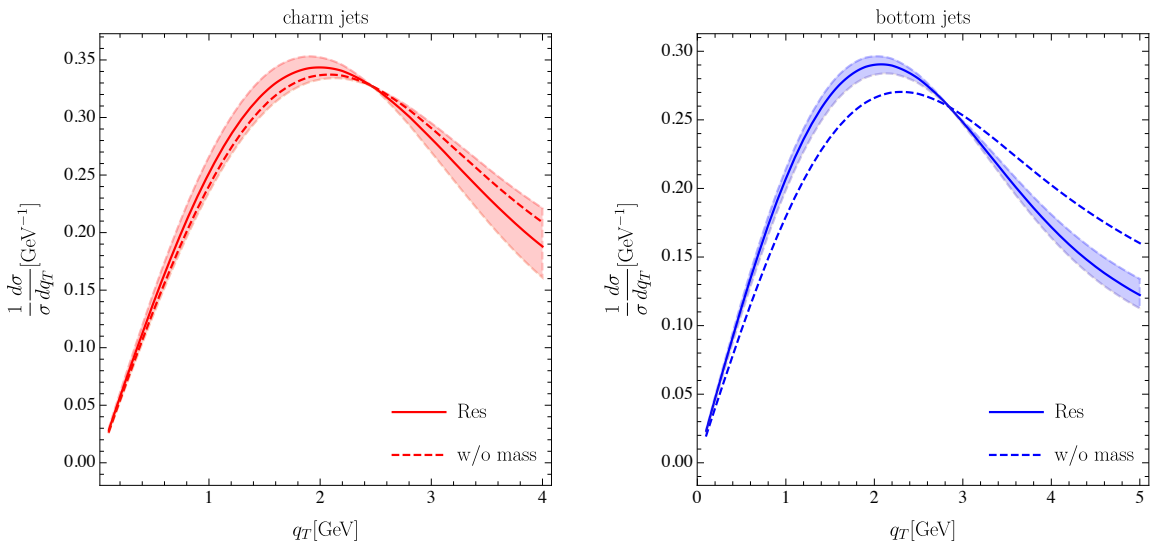

Figure 4.5: The normalized q_T-distribution for the unpolarized cross section of charm (left plot) and bottom (right plot) dijet production at the EIC. The solid curves are the results from using the resummation formula Eq. (4.77), while the dashed curves represent the resummation prediction using the evolution kernel without finite quark mass corrections. The red and blue bands indicate theoretical uncertainties from the variation of hard and jet scales as discussed in the text.

the electron and proton beam to be 20 GeV and 250 GeV, respectively. These beam-energy values yield a electron-proton center-of-mass energy of $\sqrt{S_{\ell P}} = 141$ GeV. For the all-order resummation formulae in Eqs. (4.77) and (4.79), the renormalization scales for each function are chosen to be

$$\mu_h = \sqrt{Q^2 + p_T^2}, \quad \mu_j = p_T R, \quad \mu_{cs} = \mu_{b_*} R\,. \tag{4.83}$$

Here, note that the Landau singularity associated with the collinear-soft scale is also regularized by the b_*-prescription.

As given in the calculation of the jet function, we consider HF jets constructed using the anti-k_T algorithm with radius $R = 0.6$. The corresponding kinematic cuts for charm and bottom jets in the Breit frame are

$$\text{charm jets}: \;\; 5\,\text{GeV} < p_T < 10\,\text{GeV}, \quad |y_J| < 4.5\,,$$

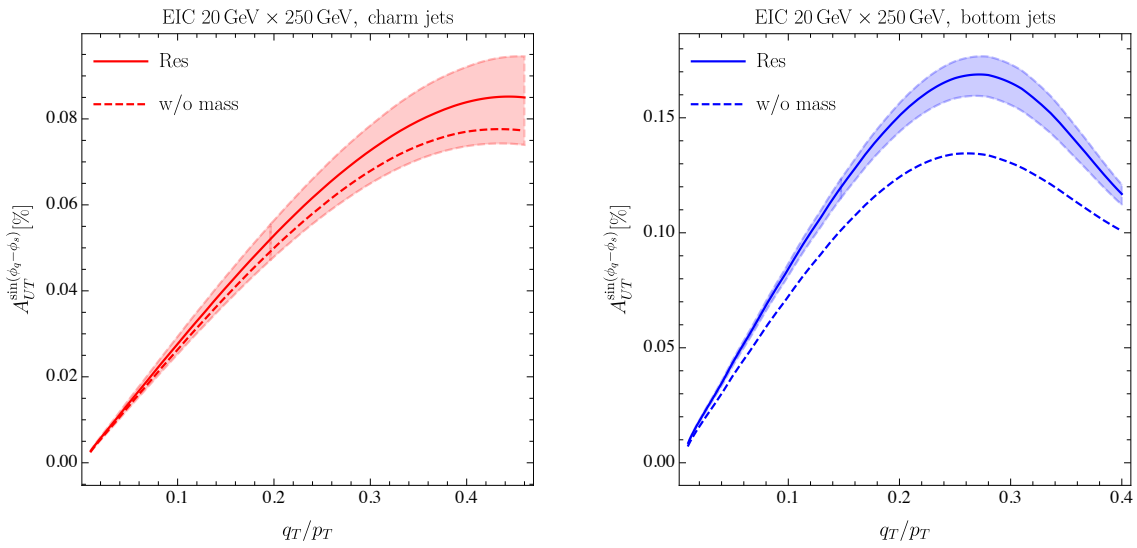

Figure 4.6: The Sivers spin asymmetry for charm (left plot) and bottom (right plot) dijet production at the EIC is plotted as a function of q_T/p_T. The solid curves are the results from using the resummation formula, while the dashed curves represent the resummation prediction using the evolution kernel without finite quark mass corrections. The red and blue bands indicate theoretical uncertainties from the variation of hard and jet scales.

$$\text{bottom jets}: \;\; 10\,\text{GeV} < p_T < 15\,\text{GeV}, \quad |y_J| < 4.5\,, \tag{4.84}$$

respectively. The charm and bottom quark masses are chosen as $m_c = 1.5\,\text{GeV}$ and $m_b = 5\,\text{GeV}$. The spin asymmetry from the gluon Sivers function is defined as

$$A_{UT}^{\sin(\phi_q-\phi_s)} = 2\frac{\int d\phi_s d\phi_q \sin(\phi_q-\phi_s)\, d\sigma^{UT}(\boldsymbol{S}_T)}{\int d\phi_s d\phi_q\, d\sigma^{UU}}\,. \tag{4.85}$$

In Fig. 4.5, we display the normalized unpolarized cross section, $1/\sigma\, d\sigma/dq_T$, as a function of the imbalance q_T. In Fig. 4.6, the Sivers spin asymmetry $A_{UT}^{\sin(\phi_q-\phi_s)}$ is presented as a function of q_T/p_T following [142], for both charm (left panel) and bottom (right panel) jets, respectively. For both plots, the solid curves are the results obtained using the resummation formula, while the dashed curves represent the resummation prediction using the evolution kernel without finite quark mass corrections. For both the unpolarized q_T and $A_{UT}^{\sin(\phi_q-\phi_s)}$ distributions, we find that the effects of the finite quark masses are modest for charm jets

and quite sizable for bottom jets. This can be attributed to the sizes of the charm and bottom masses relative to their associated jet scales $p_T R$. As discussed in Secs. 4.2.2.5 and 4.2.2.6, we have that $J_{\mathcal{Q}} \to J_q$ and $S^c_{\mathcal{Q}} \to S^c_q$ as $m_{\mathcal{Q}} \to 0$, making them analytic functions of $m_{\mathcal{Q}}$ in the neighborhood of zero mass. Since Eqs. (4.77) and (4.79) carry their mass-dependence through the anomalous dimensions for the jet and collinear-soft functions, Eqs. (4.58) and (4.70), one sees that the massive versions of these functions are connected to the massless versions by the ratio $m_{\mathcal{Q}}/(p_T R)$–it is in fact this dimensionless parameter that controls the physical size of the mass corrections. With this in mind, one sees that Eq. (4.84) naturally positions bottom dijets further (in terms of the parameter $m_{\mathcal{Q}}/(p_T R)$) from light flavor jet-pairs than it does charm dijets. This relative positioning is then clearly displayed in Figs. 4.5 and 4.6.

In order to estimate the theoretical uncertainties, in both Figs. 4.5 and 4.6 we also show the uncertainties from scale variations, which are given by the red and blue bands. Here we vary the hard and jet scales by a factor of two around their default values as defined in (4.83), and the total uncertainty bands are obtained by the envelope of all the variations. Since the non-perturbative Sudakov factor in Eq. (4.80) is fitted at the canonical scale μ_{b_*}, we do not include theory uncertainties from μ_{b_*} and μ_{cs} variations. We find that the scale uncertainty is compatible with the finite quark mass corrections in charm dijet process, while its impact on the bottom dijet process is smaller than the mass correction. Therefore in order to identify the finite quark mass effects in the charm dijet process it is essential to reduce the scale uncertainties. Our factorization and resummation formula provides a clear structure to improve the perturbative accuracy, which makes scale uncertainty further reduction possible. We leave the higher-order perturbative calculations in future work.

4.2.4 Conclusion

A major priority of the future EIC is to explore the gluon TMD PDFs. In this section, we have investigated the use of back-to-back HF dijet production in transversely-polarized target DIS as a means of probing spin-dependent gluon TMD PDFs. We have calculated

the expressions for the mass-dependent jet and collinear-soft functions at next-to-leading order. Using these expressions, as well as Soft-Collinear Effective Theory, we resum the large logarithms associated with these expressions at next-to-leading logarithmic accuracy. We then provide a factorization theorem for this process with QCD evolution in the kinematic region where heavy quark mass $m_{\mathcal{Q}} \lesssim p_T R \ll p_T$, with p_T and R being the transverse momentum and the radius of the jet, respectively. Furthermore, we generate a prediction for the Sivers asymmetry for charm and bottom dijets at the EIC, which can be used to probe the gluon Sivers function. We carefully study the effects of the HF masses by comparing our mass-dependent predicted asymmetry against the asymmetry in the massless limit. We find that, in the kinematic region we consider, the HF masses generate modest corrections to the predicted asymmetry for charm dijet production but sizable corrections for the bottom dijet process. Furthermore, we also consider the theoretical uncertainties from the scale variation. We find that the scale uncertainty can be compatible with the corrections from finite quark mass effects, especially for charm dijets production. In order to identify the mass effects and reduce the scale uncertainties one has to include higher-order corrections in the matching coefficients and the corresponding anomalous dimensions in Eqs. (4.77) and (4.79), and we leave the detailed perturbative calculations in future work.

4.3 The Sivers Asymmetry in Hadronic Dijet Production

4.3.1 Introduction

We saw in the previous sections that the Sivers function exhibits modified universality due to the presence of the additional gluon entering into the collinear correlation function. In the previous section, we had the partonic interaction $g\,\gamma \to q\,\bar{q}$ but an interesting question to address which could prove important for EIC physics is: how does the establishment of QCD factorization theorems change as the number of partons in the hard process increases. To study the factorization theorems, I now turn our attention to the Sivers asymmetry in hadronic dijet production.

The Sivers effect has been continuously studied in proton-proton collisions at the RHIC see for instance [209, 210, 211, 212, 213, 214] for experimental measurements and [215, 66, 216, 217, 218, 219, 220, 221, 222, 223, 224, 225] for theoretical developments community. A major difficulty in understanding transverse spin asymmetries with hadronic final-states is that the fragmentation process can introduce a large number of additional spin asymmetries, see for instance [217, 219, 226, 221, 222]. To eliminate these contributions from the spin correlations in the fragmentation process, the Sivers asymmetry for jet production processes has been explored in the experiment [227, 214, 228]. In particular, back-to-back dijet production in transversely polarized proton-proton collisions was proposed by Boer and Vogelsang in 2003 as a unique opportunity at the RHIC [131]. Active investigation has been performed both experimentally [228] and theoretically [134, 229, 230]. On the experimental side, the Sivers asymmetry for dijet production was found to be quite small. This effect can largely be attributed to the fact that the u- and d-quark have similar size but opposite sign [80, 81, 79]. On the theoretical side, dijet production in proton-proton collisions is also subject to TMD factorization breaking [223, 224]. These have slowed down the efforts in the detailed study of the Sivers effect in the dijet production.

Recently, there have been renewed experimental and theoretical interests for jet production processes. Experimentally, the STAR collaboration at the RHIC is analyzing the new data for dijet Sivers asymmetry, and is exploring a novel method based on a charge weighting method in separating the contributions from individual u and d-quark Sivers functions [231]. The PHENIX collaboration at the RHIC is exploring the TMD factorization breaking effects via back-to-back dihadron and photon-hadron production in proton-proton collisions [232, 233]. Theoretically, there have been efforts in performing QCD resummation in back-to-back dijet [234, 235] and vector boson-jet production [135, 164, 236]. At the same time, a theoretical framework has been developed to study spin asymmetries in specific jet charge bin [237], which would facilitate the analysis of the dijet spin asymmetries by the STAR collaboration. In light of all these activities, we set out to develop a resummation formalism for studying the Sivers asymmetry in back-to-back dijet production in transversely

polarized proton-proton collisions. We make predictions for the dijet Sivers asymmetry in the kinematics relevant to the RHIC energy, to be compared with the experimental measurement in the near future.

The rest of this section is organized as follows. In Section 4.3.2, we summarized the QCD formalism for dijet production in both unpolarized and polarized scatterings, and we provide a few remarks about our formalism. In Section 4.3.3, we provide a procedure and demonstrate how to compute the process-dependent polarized hard functions in the color matrix form. In Section 4.3.4, we present the renormalization group evolution of all the relevant functions in our formalism, and we provide the final resummation formula. Section 4.3.5 is devoted to the phenomenological studies, where we make predictions for dijet Sivers asymmetry in the kinematic region relevant to the experiment at the RHIC. Since we are mainly interested in the Sivers asymmetry in the forward rapidity region where quark contributions dominate, we consider only the quark Sivers contribution and neglect the gluon Sivers contribution. We summarize this study in Section 4.3.6.

4.3.2 QCD formalism for dijet production

In this section, we study back-to-back dijet production in transversely polarized proton-proton collisions in the center-of mass frame,

$$p(P_A, \boldsymbol{S}_\perp) + p(P_B) \to J_1(y_c, \boldsymbol{P}_{1\perp}) + J_2(y_d, \boldsymbol{P}_{2\perp}) + X\,, \tag{4.86}$$

where the polarized proton with the momentum P_A and the transverse spin $\boldsymbol{S}_\perp$ is moving in the $+z$-direction, while the unpolarized proton with the momentum P_B is moving in the $-z$-direction, and we have the center-of-mass energy $s = (P_A + P_B)^2$. The produced two jets J_1 and J_2 have rapidities $y_{c,d}$ and transverse momenta $\boldsymbol{P}_{1\perp}$ and $\boldsymbol{P}_{2\perp}$, respectively. These jets will be reconstructed via a suitable jet algorithm [238] and in the rest of this section, we consider both of them to be anti-k_T jets with jet radii R. In order to access the transverse motion of the partons inside the protons, we concentrate in the back-to-back region where the transverse momentum imbalance $q_\perp$ is small. Here we define the average transverse

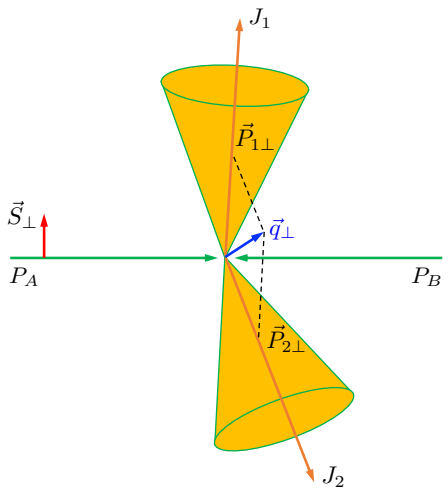

Figure 4.7: Illustration of back-to-back dijet production in transversely polarized proton-proton collisions: $p(P_A, \boldsymbol{S}_\perp) + p(P_B) \to J_1(y_c, \boldsymbol{P}_{1\perp}) + J_2(y_d, \boldsymbol{P}_{2\perp}) + X$. The polarized proton with momentum P_A and transverse spin $\boldsymbol{S}_\perp$ is moving in $+z$-direction, while the unpolarized proton with momentum P_B is moving in $-z$-direction. We have jet rapidities $y_{c,d}$ and transverse momenta $\boldsymbol{P}_{1\perp}$ and $\boldsymbol{P}_{2\perp}$, respectively. The dijet transverse momentum imbalance is defined as $\boldsymbol{q}_\perp = \boldsymbol{P}_{1\perp} + \boldsymbol{P}_{2\perp}$. Sivers asymmetry is generated due to the correlation between $\boldsymbol{S}_\perp$ and $\boldsymbol{q}_\perp$.

momentum $P_\perp$ of the two jets and the transverse momentum imbalance $\boldsymbol{q}_\perp$ as follows

$$P_\perp = |\boldsymbol{P}_{1\perp} - \boldsymbol{P}_{2\perp}|/2\,, \qquad \boldsymbol{q}_\perp = \boldsymbol{P}_{1\perp} + \boldsymbol{P}_{2\perp}\,, \tag{4.87}$$

where one has $q_\perp \ll P_\perp$ in the back-to-back region. The production of such back-to-back dijets is illustrated in Fig. 4.7. In the transversely polarized proton-proton collisions, the transverse spin vector $\boldsymbol{S}_\perp$ of the incoming proton and the transverse momentum imbalance $\boldsymbol{q}_\perp$ of the two jets will be correlated, as advocated in [131]. This correlation is accounted for in the Sivers function, which leads to a $\sin(\phi_q - \phi_S)$-azimuthal modulation in the cross section between ϕ_q and ϕ_S, the azimuthal angles of $\boldsymbol{q}_\perp$ and $\boldsymbol{S}_\perp$, respectively. Below we summarize the factorized formalisms for dijet production in both unpolarized and polarized proton-proton collisions, and we provide more details for the relevant ingredients in the next section.

4.3.2.1 Dijet unpolarized cross section

In the back-to-back region where $q_\perp \ll P_\perp$, within the framework of soft-collinear effective theory (SCET) [54, 55, 53, 56, 239], we consider the following QCD modes

$$A^\mu(x) = A^\mu_{J_c}(x) + A^\mu_{J_d}(x) + A^\mu_c(x) + A^\mu_{\bar{c}}(x) + A^\mu_s(x) + A^\mu_{cs_c}(x) + A^\mu_{cs_d}(x) \tag{4.88}$$

$$\psi(x) = \psi_{J_c}(x) + \psi_{J_d}(x) + \psi_c(x) + \psi_{\bar{c}}(x) + \psi_s(x) + \psi_{cs_c}(x) + \psi_{cs_d}(x)\,, \tag{4.89}$$

where $J_{c/d}$ denote the jet modes, and $cs_{c/d}$ denote the collinear-soft modes. Using this mode analysis, the factorization theorem becomes

$$\begin{aligned}\frac{d\sigma}{dy_c dy_d dP_\perp^2 d^2q_\perp} =& \sum_{abcd} \frac{1}{16\pi^2\hat{s}^2}\frac{1}{N_{\rm init}}\frac{1}{1+\delta_{cd}}\int_\perp x_a f^{\rm unsub}_{a/P_A}(x_a, k_{a\perp};\mu,\zeta_1/\nu^2)\, x_b f^{\rm unsub}_{b/P_B}(x_b, k_{a\perp};\mu,\zeta_2/\nu^2) \\ &\times {\rm Tr}\left[\boldsymbol{S}_{ab\to cd}(\lambda_\perp;\mu,\nu)\cdot\boldsymbol{H}_{ab\to cd}(P_\perp;\mu)\right] J_c(P_\perp R;\mu) S_c^{\rm cs}(k_{c\perp},R;\mu) \\ &\times J_d(P_\perp R;\mu) S_d^{\rm cs}(k_{d\perp},R;\mu)\,,\end{aligned} \tag{4.90}$$

where $\hat{s} = x_a x_b s$ is the partonic center-of-mass energy, $N_{\rm init}$ is the corresponding spin- and color-averaged factor for each channel, while $1/(1+\delta_{cd})$ arises from the symmetry factor due to identical partons in the final state. We have used the following short-hand notation

$$\int_\perp = \int d^2\boldsymbol{k}_{a\perp} d^2\boldsymbol{k}_{b\perp} d^2\boldsymbol{k}_{c\perp} d^2\boldsymbol{k}_{d\perp} d^2\boldsymbol{\lambda}_\perp \delta^{(2)}(\boldsymbol{k}_{a\perp}+\boldsymbol{k}_{b\perp}+\boldsymbol{k}_{c\perp}+\boldsymbol{k}_{d\perp}+\boldsymbol{\lambda}_\perp-\boldsymbol{q}_\perp)\,, \tag{4.91}$$

and the parton fractions are defined as

$$x_a = \frac{P_\perp}{\sqrt{s}}\left(e^{y_c}+e^{y_d}\right)\,, \qquad x_b = \frac{P_\perp}{\sqrt{s}}\left(e^{-y_c}+e^{-y_d}\right)\,, \tag{4.92}$$

where y_c, y_d are the rapidities of the two leading jets.

After performing Fourier transform for Eq. (4.90), we obtain the factorized formula in the coordinate b-space as follows

$$\begin{aligned}\frac{d\sigma}{dy_c dy_d dP_\perp^2 d^2q_\perp} =& \sum_{abcd} \frac{1}{16\pi^2\hat{s}^2}\frac{1}{N_{\rm init}}\frac{1}{1+\delta_{cd}}\int \frac{d^2\boldsymbol{b}}{(2\pi)^2} e^{i\boldsymbol{q}_\perp\cdot\boldsymbol{b}}\, x_a f^{\rm unsub}_{a/P_A}(x_a, b;\mu,\zeta_1/\nu^2) \\ &\times\; x_b f^{\rm unsub}_{b/P_B}(x_b, b;\mu,\zeta_2/\nu^2)\,{\rm Tr}\left[\boldsymbol{S}_{ab\to cd}(b;\mu,\nu)\cdot\boldsymbol{H}_{ab\to cd}(P_\perp;\mu)\right] \\ &\times J_c(P_\perp R;\mu) S_c^{\rm cs}(b,R;\mu) J_d(P_\perp R;\mu) S_d^{\rm cs}(b,R;\mu)\,,\end{aligned} \tag{4.93}$$

In this expression, $\boldsymbol{H}_{ab\to cd}(P_\perp;\mu)$ is the hard function, while $\boldsymbol{S}_{ab\to cd}(b;\mu,\nu)$ is a global soft function. Note that both the hard function $\boldsymbol{H}_{ab\to cd}$ and the global soft function $\boldsymbol{S}_{ab\to cd}$ are expressed in the matrix form in the color space and the trace $\mathrm{Tr}[\cdots]$ is over the color. Such factorization of the hard and soft function into matrix form is essential to capture evolution effects between the hard scale $\sim P_\perp$ and the imbalance scale $\sim q_\perp$ [240]. Here μ and ν denotes renormalization and rapidity scales, separately. The rapidity scale ν arises because both the TMD PDFs and the global soft functions have rapidity divergence [241, 62], which are canceled between them as demonstrated below. This cancellation allows us to define rapidity divergence independent $\tilde{\boldsymbol{S}}_{ab\to cd}(b;\mu)$ by

$$\boldsymbol{S}_{ab\to cd}(b;\mu,\nu) = \tilde{\boldsymbol{S}}_{ab\to cd}(b;\mu) S_{ab}(b;\mu,\nu)\,, \tag{4.94}$$

where $S_{ab}(b;\mu,\nu)$ is the standard soft function appearing in usual Drell-Yan and Semi-Inclusive DIS processes. Through this definition, we can perform the soft subtraction [36]

$$\begin{aligned} &f^{\mathrm{unsub}}_{a/P_A}(x_a,b;\mu,\zeta_1/\nu^2)\, f^{\mathrm{unsub}}_{b/P_B}(x_b,b;\mu,\zeta_2/\nu^2)\, S_{ab}(b;\mu,\nu) \\ &\qquad = f_{a/P_A}(x_a,b;\mu,\zeta_1)\, f_{b/P_B}(x_b,b;\mu,\zeta_2)\,. \end{aligned} \tag{4.95}$$

The jet functions $J_c(P_\perp R;\mu)$ and $J_d(P_\perp R;\mu)$ in Eq. (4.93) describe the creation of anti-k_T jets from the massless partons c and d, respectively. Finally, $S^{\mathrm{cs}}_c(k_{c\perp},R;\mu)$ and $S^{\mathrm{cs}}_d(k_{d\perp},R;\mu)$ are the collinear-soft functions. If one performs the integration over the azimuthal angle of the vector $\boldsymbol{b}$, we obtain the following expression

$$\begin{aligned} \frac{d\sigma}{dy_c dy_d dP_\perp^2 d^2q_\perp} =& \sum_{abcd} \frac{1}{16\pi^2\hat{s}^2}\frac{1}{N_{\mathrm{init}}}\frac{1}{1+\delta_{cd}}\frac{1}{2\pi}\int_0^\infty db\, b\, J_0(q_\perp b) \\ &\times x_a f_{a/P_A}(x_a,b;\mu,\zeta_1)\, x_b f_{b/P_B}(x_b,b;\mu,\zeta_2) \\ &\times \mathrm{Tr}\left[\tilde{\boldsymbol{S}}_{ab\to cd}(b;\mu)\cdot \boldsymbol{H}_{ab\to cd}(P_\perp;\mu)\right] J_c(P_\perp R;\mu) S^{\mathrm{cs}}_c(b,R;\mu) J_d(P_\perp R;\mu) \\ &\times S^{\mathrm{cs}}_d(b,R;\mu)\,. \end{aligned} \tag{4.96}$$

It is well-known [223, 224, 242, 243] that the so-called Glauber mode will result in the TMD factorization breaking contributions to Eq. (4.90). In this section, we write down a theoretical formalism in Eq. (4.93) using SCET with the factorization breaking effects

from the Glauber mode ignored. By careful comparison between the predictions from our theoretical framework with the precision experimental data in the future, we can probe the size of the factorization breaking effects. In principle, such effects can be systematically accounted for in SCET by including explicitly the Glauber mode [45]. How exactly this works for dijet production remains to be investigated.

4.3.2.2 Dijet Sivers asymmetry

In the transversely polarized proton-proton collisions, the Sivers function will lead to a spin asymmetry in the cross section when one flips the transverse spin of the incoming proton. We thus define the difference in the cross section as $d\Delta\sigma(S_\perp) = [d\sigma(S_\perp) - d\sigma(-S_\perp)]/2$. One can write down a similar factorized formula for such a spin-dependent differential cross section following Eq. (4.90), and it is given by

$$\begin{aligned}\frac{d\Delta\sigma(S_\perp)}{dy_c dy_d dP_\perp^2 d^2q_\perp} =& \sum_{abcd} \frac{1}{16\pi^2\hat{s}^2}\frac{1}{N_{\text{init}}}\frac{1}{1+\delta_{cd}}\int_\perp \frac{1}{M}\epsilon_{\alpha\beta}\, S_\perp^\alpha\, k_{a\perp}^\beta\, x_a f_{1T\, a/P_A}^{\perp,\,\text{unsub}}(x_a, k_{a\perp};\mu,\zeta_1/\nu^2) \\ &\times x_b f_{b/P_B}^{\text{unsub}}(x_b, k_{a\perp};\mu,\zeta_2/\nu^2)\text{Tr}\left[\boldsymbol{S}_{ab\to cd}(\lambda_\perp;\mu,\nu)\cdot \boldsymbol{H}_{ab\to cd}^{\text{Sivers}}(P_\perp;\mu)\right] \\ &\times J_c(P_\perp R;\mu) S_c^{\text{cs}}(k_{c\perp}, R;\mu) J_d(P_\perp R;\mu) S_d^{\text{cs}}(k_{d\perp}, R;\mu)\,, \end{aligned} \tag{4.97}$$

where $\epsilon_{\alpha\beta}$ is a two-dimensional asymmetric tensor with $\epsilon_{12} = +1$.

In writing down this spin-dependent formalism, we start from the unpolarized factorized formalism in Eq. (4.90) with the replacement of the unpolarized TMD PDF by the Sivers function following the so-called Trento convention [244],

$$f_{a/P_A}^{\text{unsub}}(x_a, k_{a\perp};\mu,\zeta_1/\nu^2) \to \frac{1}{M}\epsilon_{\alpha\beta}\, S_\perp^\alpha\, k_{a\perp}^\beta\, f_{1T,\, a/P_A}^{\perp a,\,\text{unsub}}(x_a, k_{a\perp};\mu,\zeta_1/\nu^2)\,, \tag{4.98}$$

where the subscript $ab \to cd$ in the Sivers function on the right-hand side represents the so-called process-dependence of the Sivers function, as discovered by [245, 246, 134, 133, 229, 230, 36]. In Chapter 3, we saw that one can either absorb the pole contributions into the Sivers function or in the partonic cross section. Therefore, we are free to use the usual Sivers function from Semi-Inclusive DIS and derive a novel hard function. Once this is done, we will have a new hard function $\boldsymbol{H}_{ab\to cd}^{\text{Sivers}}(P_\perp;\mu)$, which would be different from the unpolarized

hard function, $\boldsymbol{H}_{ab\to cd}(P_\perp;\mu)$. We explain in details how we derive the hard functions $\boldsymbol{H}^{\rm Sivers}_{ab\to cd}$ for different partonic processes in the next section, where we show non-trivial structures are expressed in terms of matrix forms in the color space. To a large degree, our formalism for the spin-dependent case can be regarded as an extension of the generalized TMD formalism introduced earlier in [245, 246, 134, 133], but with a matrix form for both hard and soft functions.

At this point, I would like to note that the soft function can in principle also be different for di-jets. In general, one needs to consider emissions from each section (jet, collinear, soft, soft-collinear) and then introduce the additional gluon. In fact, Ref. [225] shows in explicit calculations at one-loop level that soft functions in the polarized case are different from the unpolarized counterpart beyond leading logarithmic accuracy, which is an indication of TMD factorization breaking. However, the change in soft function comes from the Glauber gluon which we ignore as explained above. In this respect, our starting point Eq. (4.97) will be the best assumption at hand that takes a factorized form. We show the RG consistency for this factorized form, and we also demonstrate how we derive the process-dependent hard functions $\boldsymbol{H}^{\rm Sivers}_{ab\to cd}(P_\perp;\mu)$ for the polarized scattering. We leave a detailed study on the numerical impact of any TMD factorization breaking effects for future investigation.

Performing Fourier transform from the transverse momentum space into the b-space, we obtain

$$\begin{aligned}\frac{d\Delta\sigma(S_\perp)}{dy_c dy_d dP_\perp^2 d^2q_\perp} =& \sum_{abcd}\frac{1}{16\pi^2\hat{s}^2}\frac{1}{N_{\rm init}}\frac{1}{1+\delta_{cd}}\epsilon_{\alpha\beta}\,S_\perp^\alpha\int\frac{d^2\boldsymbol{b}}{(2\pi)^2}\,e^{i\boldsymbol{q}_\perp\cdot\boldsymbol{b}}\,x_a f^{\perp\,(\beta)}_{1T\,a/P_A}(x_a,b;\mu,\zeta_1)\\ &\times\, x_b f_{b/P_B}(x_b,b;\mu,\zeta_2)\,{\rm Tr}\left[\tilde{\boldsymbol{S}}_{ab\to cd}(b;\mu)\cdot\boldsymbol{H}^{\rm Sivers}_{ab\to cd}(P_\perp;\mu)\right]\\ &\times\, J_c(P_\perp R;\mu)S_c^{\rm cs}(b,R;\mu)J_d(P_\perp R;\mu)S_d^{\rm cs}(b,R;\mu)\,,\end{aligned}\tag{4.99}$$

where we have already used Eq. (4.94) to rewrite the unsubtracted unpolarized TMD PDF and Sivers function in terms of the properly defined versions which are free of rapidity divergence. Here $f^{\perp\,(\beta)}_{1T\,a/P_A}(x_a,b;\mu,\zeta_1)$ is the Fourier transform of the Sivers function,

$$f^{\perp\,(\beta)}_{1T\,a/P_A}(x_a,b;\mu,\zeta_1)=\frac{1}{M}\int d^2\boldsymbol{k}_{a\perp}\,e^{-i\boldsymbol{k}_{a\perp}\cdot\boldsymbol{b}}\,k^\beta_{a\perp}f^\perp_{1T\,a/P_A}(x_a,k_{a\perp};\mu,\zeta_1)\,,$$

$$\equiv \left(\frac{ib^\beta}{2}\right) f^{\perp}_{1T\,a/P_A}(x_a, b; \mu, \zeta_1)\,, \tag{4.100}$$

where we have used the fact that the integration in the first line would be proportional to b^β, and we thus factored b^β out explicitly in the second line. The remaining part of the Sivers function is now denoted as $f^{\perp}_{1T\,a/P_A}(x_a, b; \mu, \zeta_1)$. Note that for the same reason as explained below Eq. (4.95), we do not have the rapidity ν-dependence in the above equation. It is also instructive to emphasize that $f^{\perp\,\mathrm{unsub}}_{1T\,a/P_A}(x_a, b; \mu, \zeta_1/\nu^2)$ follows the same TMD evolution equations as the unpolarized TMD PDF $f^{\mathrm{unsub}}_{a/P_A}(x_a, b; \mu, \zeta_1/\nu^2)$, which enables us to evolve the Sivers function from some initial scale μ_0 to the relevant scale μ. We now plug Eq. (4.100) into Eq. (4.99), and integrate over the azimuthal angle of the vector $\boldsymbol{b}$, we obtain

$$\begin{aligned}\frac{d\Delta\sigma(S_\perp)}{dy_c dy_d dP_\perp^2 d^2q_\perp} =& \sin(\phi_q - \phi_S) \sum_{abcd} \frac{1}{16\pi^2 \hat{s}^2} \frac{1}{N_{\mathrm{init}}} \frac{1}{1+\delta_{cd}} \left(-\frac{1}{4\pi}\right) \int_0^\infty db\, b^2\, J_1(q_\perp b) \\ &\times\; x_a\, f^{\perp\,a}_{1T}(x_a, b; \mu, \zeta_1) x_b\, f_{b/P_B}(x_b, b; \mu, \zeta_2)\, \mathrm{Tr}\left[\tilde{\boldsymbol{S}}_{ab\to cd}(b; \mu) \cdot \boldsymbol{H}^{\mathrm{Sivers}}_{ab\to cd}(P_\perp; \mu)\right] \\ &\times\; J_c(P_\perp R; \mu) S^{\mathrm{cs}}_c(b, R; \mu) J_d(P_\perp R; \mu) S^{\mathrm{cs}}_d(b, R; \mu)\,, \end{aligned} \tag{4.101}$$

where J_1 is the Bessel function of order one, and we have used the identity

$$\epsilon_{\alpha\beta} S^\alpha_\perp\, \hat{q}^\beta_\perp = \sin(\phi_q - \phi_S)\,, \tag{4.102}$$

with $\hat{q}_\perp$ the unit vector along the direction of the imbalance $\boldsymbol{q}_\perp$. In general, the so-called single spin asymmetry (the Sivers asymmetry) A_N for dijet production will be then given by

$$A_N = \frac{d\Delta\sigma(S_\perp)}{dy_c dy_d dP_\perp^2 d^2q_\perp} \Big/ \frac{d\sigma}{dy_c dy_d dP_\perp^2 d^2q_\perp}\,. \tag{4.103}$$

4.3.2.3 Remarks

We will provide detailed expressions and discuss the evolution of all the relevant functions in the next section. Here, let us emphasize the following points on our factorized formalism:

- There will be non-global structures from quantum correlations between in-jet and out-of-jet radiations: exclusive jet production will be sensitive on the correlation effects

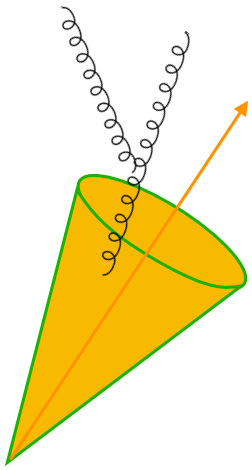

Figure 4.8: Illustration of first non-global logarithms from quantum correlation of in-jet and out-of-jet radiation.

between in-jet and out-of-jet radiations, which is first discovered in [162]. There, it was shown that non-global logarithms first appear at NNLO order through a correlated emission from a heavy mass hemisphere to a light mass hemisphere. We observe similar non-global logarithms first at NNLO through a correlated emission from the higher scaled in-jet to the lower scaled out-of-jet emission as shown in Fig. 4.8, which is given at NNLO by [130]

$$-\frac{C_A C_a}{2}\left(\frac{\alpha_s}{\pi}\right)^2 \frac{\pi^2}{24}\ln^2\left(\frac{P_\perp^2}{\mu_b^2}\right) , \tag{4.104}$$

where $C_a = C_F$ and C_A for the quark and gluon jet, respectively. To generalize the analysis of these non-global logarithms to general resummation order, the factorization and resummation formula need to include multi-Wilson-line structures [247, 248]. The multi-Wilson-line formalism then gives rise to the non-linear evolution equation [249] for non-global logarithms (NGLs) resummation. The TMD factorization formula including such effects have been given in [250, 164, 251]. Numerically, the leading-logarithmic NGLs resummation can be solved using parton shower methods [162, 252, 253, 254] or BMS equations [255, 256]. In our phenomenology, we have included the contributions from leading-logarithmic NGLs as discussed in Section 4.3.5.

- Our formalism for unpolarized dijet production in Eqs. (4.93) is similar to those in [234, 235]. Here, by taking the small-R limit, we refactorize the TMD R-dependence soft function [234, 235] as the product of the R-independent global TMD soft function and the R-dependent collinear-soft function [135, 164]. In addition, the R-dependent hard function in [234, 235] has been further factorized into a R-independent hard function as above and the jet functions which naturally capture all the R-dependence. In this regard, the factorized formula presented here is more transparent and intuitive. Such refactorizations are essential to resum logarithms of R for small radius jets.

- After performing the refactorization mentioned in the above item, both the single logarithmic anomalous dimensions of the global and collinear-soft function not only depend on the magnitude $|\boldsymbol{b}|$ but also the azimuthal angle ϕ_b of the vector $\boldsymbol{b}$ [135, 164]. Especially, after taking into account QCD evolution effects the ϕ_b integral is divergent in some phase space region. In order to regularize such divergences, we can first take ϕ_b averaging in both the global and collinear-soft function, and then explicit ϕ_b dependence will vanish. Therefore, one can avoid such divergence in the resummation formula directly. This ϕ_b averaging method will not change the RG consistency at the one-loop order. The other methods to avoid such divergence have been discussed in [164], and no significant numerical differences are found at the NLL accuracy. The similar ϕ_b averaging methods have also been used in [257, 258, 259] to simplify the calculation of the TMD soft function.

4.3.3 Hard Functions in unpolarized and polarized scattering

In this section, we derive the hard functions for both unpolarized and polarized scatterings, i.e. $\boldsymbol{H}_{ab\to cd}(P_\perp;\mu)$ and $\boldsymbol{H}^{\rm Sivers}_{ab\to cd}(P_\perp;\mu)$ in Eqs. (4.96) and (4.101), respectively. They are matrices in the color space. We first review the results for the hard functions $\boldsymbol{H}_{ab\to cd}$ in the unpolarized scattering, which are well-known in the literature, see e.g. Refs. [260, 261]. We then derive the hard function matrices $\boldsymbol{H}^{\rm Sivers}_{ab\to cd}$ in the polarized scattering case. These hard functions properly take into account the process-dependence of the Sivers functions [245,

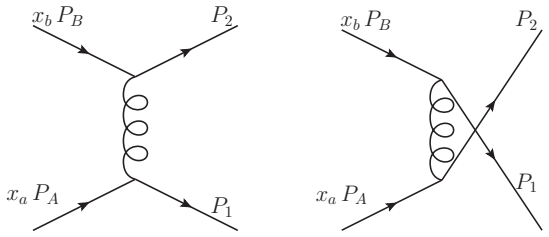

Figure 4.9: Unpolarized scattering amplitudes for the $qq \to qq$ subprocess. From left the right, the scattering amplitude is provided for the t- and u-channel processes.

246, 134, 133, 229, 230, 36]. To get started, we define the Mandelstam variables for the partonic scattering process, $a(p_1) + b(p_2) \to c(p_3) + d(p_4)$, as follows

$$\hat{s} = (p_1 + p_2)^2 = (p_3 + p_4)^2 = 4P_\perp^2 \cosh^2\left(\frac{\Delta y}{2}\right) = x_a x_b s\,, \tag{4.105a}$$

$$\hat{t} = (p_1 - p_3)^2 = (p_2 - p_4)^2 = -2P_\perp^2 e^{-\Delta y/2} \cosh\left(\frac{\Delta y}{2}\right)\,, \tag{4.105b}$$

$$\hat{u} = (p_1 - p_4)^2 = (p_2 - p_3)^2 = -2P_\perp^2 e^{\Delta y/2} \cosh\left(\frac{\Delta y}{2}\right)\,, \tag{4.105c}$$

where $\Delta y = y_c - y_d$ is the rapidity difference of the two jets. In the following, the expressions for the hard functions will be written in terms of these Mandelstam variables.

4.3.3.1 Unpolarized Hard Matrices

Four quark subprocesses

We start with the partonic subprocesses that involve four quarks, such as $qq \to qq$. In Tab. 4.1, we organize each of the four quark subprocesses into a color basis. The color basis operators acting on particles i and j are denoted as $\Gamma_{n,ij}$ which are used to generate the hard and soft matrices. For the four quark interactions, two operators, $n = 1, 2$, are required to span the color space. As seen in the table, this results in 12 total color matrices. Using the fact that hard function for the unpolarized case is invariant under the charge conjugation, the bottom row can easily be computed from the top row. Furthermore, once the hard matrices have been calculated for the first column, crossing symmetry can be applied in order to obtain the hard color matrices for the second and third column. It is then only

$12 \to 34$	Color Basis	$12 \to 34$	Color Basis	$12 \to 34$	Color Basis
$qq' \to qq'$		$q\bar{q} \to q'\bar{q}'$		$q\bar{q}' \to \bar{q}'q$	
$qq' \to q'q$	$\Gamma_{n,31}\Gamma_{n,42}$	$q\bar{q}' \to q\bar{q}'$	$\Gamma_{n,21}\Gamma_{n,34}$	$q\bar{q} \to \bar{q}'q'$	$\Gamma_{n,41}\Gamma_{n,23}$
$qq' \to qq$		$q\bar{q} \to q\bar{q}$		$q\bar{q} \to \bar{q}q$	
$\bar{q}\bar{q}' \to \bar{q}\bar{q}'$		$\bar{q}q \to \bar{q}'q'$		$\bar{q}q' \to q'\bar{q}$	
$\bar{q}\bar{q}' \to \bar{q}'\bar{q}$	$\Gamma_{n,13}\Gamma_{n,24}$	$\bar{q}q' \to \bar{q}q'$	$\Gamma_{n,12}\Gamma_{n,43}$	$\bar{q}q \to q'\bar{q}'$	$\Gamma_{n,14}\Gamma_{n,32}$
$\bar{q}\bar{q}' \to \bar{q}\bar{q}$		$\bar{q}q \to \bar{q}q$		$\bar{q}q \to q\bar{q}$	

Table 4.1: The choice of basis for each of the four quark subprocesses. $\Gamma_{n,ij}$ are operators in color space which join the fermion lines i and j. For the four quark subprocesses, two operators, $\Gamma_{1,ij}$ and $\Gamma_{2,ij}$, are required to span the color space.

necessary to explicitly calculate the hard matrices for the subprocesses associated with the color basis $\Gamma_{n,31}\Gamma_{n,42}$. For our calculation, we follow the conventions used in Refs. [261, 260] to choose $\Gamma_{1,ij} = (t^a)_{ij}$ and $\Gamma_{2,ij} = \delta_{ij}$, so that the color basis is spanned by the orthogonal basis

$$\theta_1 = (t^a)_{ij}(t^a)_{kl}\,, \qquad \theta_2 = \delta_{ij}\delta_{kl}\,, \tag{4.106}$$

$$\theta_1^\dagger = (t^a)_{ji}(t^a)_{lk}\,, \qquad \theta_2^\dagger = \delta_{ji}\delta_{lk}\,. \tag{4.107}$$

We note that other bases have been used in the literature [262]. We now explicitly perform the calculation for the $qq' \to qq'$, $qq' \to q'q$, and $qq \to qq$ subprocesses. For these subprocesses,

we can write

$$\mathcal{M} = \mathcal{M}_t^{\text{kin}} \left(t^b\right)_{31} \left(t^b\right)_{42} + \mathcal{M}_u^{\text{kin}} \left(t^b\right)_{32} \left(t^b\right)_{41} \tag{4.108}$$

where we have suppressed the $ab \to cd$ subprocess label. The subscript in the $\mathcal{M}$ terms denotes the relevant Mandelstam variable ($\hat{t}$ or $\hat{u}$) for the channel that contributes to the subprocess as shown in the Fig. 4.9. To arrive at this expressions, we have separated the color parts from the kinematic parts (denoted with the superscript kin). These kinematic scattering amplitudes are defined by

$$\mathcal{M}_t^{\text{kin}} = \begin{cases} -\dfrac{g_s^2}{\hat{t}} \bar{u}(P_1)\gamma^\mu u(x_a\, P_A)\bar{u}(P_2)\gamma_\mu u(x_b\, P_B) & ab \to cd = qq' \to qq' \\ 0 \qquad\qquad \text{for} & ab \to cd = qq' \to q'q \\ -\dfrac{g_s^2}{\hat{t}} \bar{u}(P_1)\gamma^\mu u(x_a\, P_A)\bar{u}(P_2)\gamma_\mu u(x_b\, P_B) & ab \to cd = qq \to qq\,, \end{cases} \tag{4.109}$$

$$\mathcal{M}_u^{\text{kin}} = \begin{cases} 0 & ab \to cd = qq' \to qq' \\ -\dfrac{g_s^2}{\hat{u}} \bar{u}(P_2)\gamma^\mu u(x_a\, P_A)\bar{u}(P_1)\gamma_\mu u(x_b\, P_B) \qquad \text{for} & ab \to cd = qq' \to q'q \\ \dfrac{g_s^2}{\hat{u}} \bar{u}(P_2)\gamma^\mu u(x_a\, P_A)\bar{u}(P_1)\gamma_\mu u(x_b\, P_B) & ab \to cd = qq \to qq\,. \end{cases} \tag{4.110}$$

We can now decompose these scattering amplitudes in color space as

$$\mathcal{M} = \mathcal{M}_1\, \theta_1 + \mathcal{M}_2\, \theta_2 \qquad \mathcal{M}^\dagger = \mathcal{M}_1^\dagger\, \theta_1^\dagger + \mathcal{M}_2^\dagger\, \theta_2^\dagger\,, \tag{4.111}$$

where

$$\mathcal{M}_1 = \frac{\text{Tr}\left[\mathcal{M}\theta_1^\dagger\right]}{\text{Tr}\left[\theta_1\theta_1^\dagger\right]} \quad \mathcal{M}_2 = \frac{\text{Tr}\left[\mathcal{M}\theta_2^\dagger\right]}{\text{Tr}\left[\theta_2\theta_2^\dagger\right]} \quad \mathcal{M}_1^\dagger = \frac{\text{Tr}\left[\mathcal{M}^\dagger\theta_1\right]}{\text{Tr}\left[\theta_1\theta_1^\dagger\right]} \quad \mathcal{M}_2^\dagger = \frac{\text{Tr}\left[\mathcal{M}^\dagger\theta_2\right]}{\text{Tr}\left[\theta_2\theta_2^\dagger\right]}\,. \tag{4.112}$$

To obtain the expressions in Eq. (4.112), we have exploited the orthogonality of our chosen color basis in Eqs. (4.106) and (4.107). Then we will have $|\mathcal{M}|^2$ as

$$|\mathcal{M}|^2 = \text{Tr}\left[\boldsymbol{H}_{ab\to cd} \cdot \boldsymbol{S}_{ab\to cd}\right]\,, \tag{4.113}$$

where the hard matrix is given by

$$\boldsymbol{H}_{ab\to cd} = \begin{bmatrix} |\mathcal{M}_1|^2 & \mathcal{M}_1\mathcal{M}_2^\dagger \\ \mathcal{M}_2\mathcal{M}_1^\dagger & |\mathcal{M}_2|^2 \end{bmatrix}\,, \tag{4.114}$$

$12 \to 34$	Basis	$12 \to 34$	Basis	$12 \to 34$	Basis	$12 \to 34$	Basis	$12 \to 34$	Basis	$12 \to 34$	Basis
$q\bar{q} \to gg$	$\Gamma^{ab}_{n,21}$	$qg \to gq$	$\Gamma^{ab}_{n,41}$	$qg \to qg$	$\Gamma^{ab}_{n,31}$	$gq \to gq$	$\Gamma^{ab}_{n,42}$	$gq \to qg$	$\Gamma^{ab}_{n,32}$	$gg \to q\bar{q}$	$\Gamma^{ab}_{n,43}$
$\bar{q}g \to \bar{q}g$	$\Gamma^{ab}_{n,21}$	$\bar{q}g \to g\bar{q}$	$\Gamma^{ab}_{n,41}$	$\bar{q}q \to gg$	$\Gamma^{ab}_{n,31}$	$gg \to \bar{q}q$	$\Gamma^{ab}_{n,42}$	$g\bar{q} \to \bar{q}g$	$\Gamma^{ab}_{n,32}$	$g\bar{q} \to g\bar{q}$	$\Gamma^{ab}_{n,43}$

Table 4.2: The choice of basis for each of two quark two gluon subprocesses. Three operators $\Gamma^{ab}_{1,ij}$,$\Gamma^{ab}_{2,ij}$,$\Gamma^{ab}_{3,ij}$ are required to span the color space for each subprocess.

and the leading order soft matrix as

$$\boldsymbol{S}_{ab\to cd} = \begin{bmatrix} \mathrm{Tr}\left[\theta_1\theta_1^\dagger\right] & \mathrm{Tr}\left[\theta_1\theta_2^\dagger\right] \\ \mathrm{Tr}\left[\theta_2\theta_1^\dagger\right] & \mathrm{Tr}\left[\theta_2\theta_2^\dagger\right] \end{bmatrix} = \begin{bmatrix} \frac{1}{2}N_cC_F & 0 \\ 0 & N_c^2 \end{bmatrix} . \tag{4.115}$$

The hard matrices of the four quark processes in $\Gamma_{31}\Gamma_{42}$ color basis in Tab. 4.1 are given by

$$\boldsymbol{H}_{qq'\to qq'} = \frac{8g_s^4\left(\hat{s}^2+\hat{u}^2\right)}{\hat{t}^2}\begin{bmatrix} 1 & 0 \\ 0 & 0 \end{bmatrix} , \tag{4.116}$$

$$\boldsymbol{H}_{qq'\to q'q} = \frac{8g_s^4\left(\hat{s}^2+\hat{t}^2\right)}{\hat{u}^2C_A^2}\begin{bmatrix} 1 & -C_F \\ -C_F & C_F^2 \end{bmatrix} , \tag{4.117}$$

$$\boldsymbol{H}_{qq\to qq} = \frac{8g_s^4}{\hat{t}^2\hat{u}^2N_c^2}\begin{bmatrix} \hat{t}^4+\hat{s}^2\hat{t}^2-2N_c\hat{s}^2\hat{u}\hat{t}+N_c^2\hat{u}^4+N_c^2\hat{s}^2\hat{u}^2 & -C_F\hat{t}\left(\hat{t}^3+\hat{s}^2\hat{t}-N_c\hat{s}^2\hat{u}\right) \\ -C_F\hat{t}\left(\hat{t}^3+\hat{s}^2\hat{t}-N_c\hat{s}^2\hat{u}\right) & C_F^2\hat{t}^2\left(\hat{s}^2+\hat{t}^2\right) \end{bmatrix} . \tag{4.118}$$

We find these results to be consistent with the expressions in [260]. The remaining hard functions can be obtained from crossing symmetries.

Two quarks and two gluon subprocesses

In Tab. 4.2, we provide a list of subprocesses involving two quarks and two gluons with the color basis operators $\Gamma^{ab}_{n,ij}$. For the two quark and two gluon interactions, three operators,

$n = 1, 2, 3$, are required to span the color space. A convenient choice for the computation is the set of orthogonal operators (primed),

$$\Gamma^{ab\ \prime}_{1,ij} = \frac{\delta^{ab}}{2N_c}\delta_{ij}\,, \qquad \Gamma^{ab\ \prime}_{2,ij} = \frac{1}{2}d^{abc}t^c_{ij}\,, \qquad \Gamma^{ab\ \prime}_{3,ij} = \frac{1}{2}f^{abc}t^c_{ij}\,, \tag{4.119}$$

which has the corresponding orthogonal basis,

$$\theta'_1 = \frac{\delta^{ab}}{2N_c}\delta_{ij}\,, \qquad \theta'_2 = \frac{1}{2}d^{abc}t^c_{ij}\,, \qquad \theta'_3 = \frac{1}{2}f^{abc}t^c_{ij}\,. \tag{4.120}$$

At the same time, we find that the final expressions for the hard matrices take a simpler form when one uses the non-orthogonal basis used in Refs. [261, 260, 262] by defining the basis operators to be (unprimed)

$$\Gamma^{ab}_{1,ij} = (t^a t^b)_{ij}\,, \qquad \Gamma^{ab}_{2,ij} = (t^b t^a)_{ij}\,, \qquad \Gamma^{ab}_{3,ij} = \delta_{ij}\delta^{ab}\,. \tag{4.121}$$

The corresponding basis is given by

$$\theta_1 = (t^a t^b)_{ij}\,, \qquad \theta_2 = (t^b t^a)_{ij}\,, \qquad \theta_3 = \delta_{ij}\delta^{ab}\,. \tag{4.122}$$

We note that the normalization of θ_3 in [262] differs from the normalization of Refs. [261, 260] by a factor of 2. For the choice of basis in Eq. (4.122), the LO soft matrix is given by

$$\boldsymbol{S}_{ab\to cd} = \begin{bmatrix} \mathrm{Tr}\left[\theta_1\theta_1^\dagger\right] & \mathrm{Tr}\left[\theta_1\theta_2^\dagger\right] & \mathrm{Tr}\left[\theta_1\theta_3^\dagger\right] \\ \mathrm{Tr}\left[\theta_2\theta_1^\dagger\right] & \mathrm{Tr}\left[\theta_2\theta_2^\dagger\right] & \mathrm{Tr}\left[\theta_2\theta_3^\dagger\right] \\ \mathrm{Tr}\left[\theta_3\theta_1^\dagger\right] & \mathrm{Tr}\left[\theta_3\theta_2^\dagger\right] & \mathrm{Tr}\left[\theta_3\theta_3^\dagger\right] \end{bmatrix} = \begin{bmatrix} N_c C_F^2 & -\frac{C_F}{2} & N_c C_F \\ -\frac{C_F}{2} & N_c C_F^2 & N_c C_F \\ N_c C_F & N_c C_F & 2N_c^2 C_F \end{bmatrix}. \tag{4.123}$$

In order to exploit the orthogonality condition of the primed basis in Eq. (4.120), but still provide a simple expression for the hard matrices using the unprimed basis in Eq. (4.122), we first compute the hard matrices in the primed basis then obtain the results in the unprimed basis using the relation

$$\boldsymbol{H}_{ab\to cd} = \boldsymbol{R}^\dagger\, \boldsymbol{H}'_{ab\to cd}\, \boldsymbol{R}\,, \qquad \text{where} \quad \boldsymbol{R} = \frac{1}{2N_c}\begin{bmatrix} 0 & 0 & 1 \\ N_c & N_c & -1 \\ -N_c & N_c & 0 \end{bmatrix}. \tag{4.124}$$

We now perform the calculation for the hard matrices for the $q\bar{q} \to gg$ process in the primed orthogonal basis. The scattering amplitude for this subprocess can be written in color space as

$$\mathcal{M} = M_1\theta'_1 + M_2\theta'_2 + M_3\theta'_3 \qquad \mathcal{M}^\dagger = M_1^\dagger\theta'^\dagger_1 + M_2^\dagger\theta'^\dagger_2 + M_3^\dagger\theta'^\dagger_3 \tag{4.125}$$

where

$$\mathcal{M}_1 = \frac{\text{Tr}\left[\mathcal{M}\theta'^\dagger_1\right]}{\text{Tr}\left[\theta'_1\theta'^\dagger_1\right]} \qquad \mathcal{M}_2 = \frac{\text{Tr}\left[\mathcal{M}\theta'^\dagger_2\right]}{\text{Tr}\left[\theta'_2\theta'^\dagger_2\right]}, \qquad \mathcal{M}_3 = \frac{\text{Tr}\left[\mathcal{M}\theta'^\dagger_3\right]}{\text{Tr}\left[\theta'_3\theta'^\dagger_3\right]}, \tag{4.126}$$

$$\mathcal{M}_1^\dagger = \frac{\text{Tr}\left[\mathcal{M}^\dagger\theta'_1\right]}{\text{Tr}\left[\theta'_1\theta'^\dagger_1\right]} \qquad \mathcal{M}_2^\dagger = \frac{\text{Tr}\left[\mathcal{M}^\dagger\theta'_2\right]}{\text{Tr}\left[\theta'_2\theta'^\dagger_2\right]}, \qquad \mathcal{M}_3^\dagger = \frac{\text{Tr}\left[\mathcal{M}^\dagger\theta'_3\right]}{\text{Tr}\left[\theta'_3\theta'^\dagger_3\right]}. \tag{4.127}$$

The hard matrix in the primed basis can therefore be computed as

$$\boldsymbol{H}'_{q\bar{q}\to gg} = \begin{bmatrix} M_1\,M_1^\dagger & M_1\,M_2^\dagger & M_1\,M_3^\dagger \\ M_2\,M_1^\dagger & M_2\,M_2^\dagger & M_2\,M_3^\dagger \\ M_3\,M_1^\dagger & M_3\,M_2^\dagger & M_3\,M_3^\dagger \end{bmatrix}. \tag{4.128}$$

Finally, we now use Eq. (4.124) to obtain the simplified hard functions in the unprimed basis as

$$\boldsymbol{H}_{q\bar{q}\to gg} = 8g_s^4\frac{\left(\hat{t}^2+\hat{u}^2\right)}{\hat{s}^2}\begin{bmatrix} \frac{\hat{u}}{\hat{t}} & 1 & 0 \\ 1 & \frac{\hat{t}}{\hat{u}} & 0 \\ 0 & 0 & 0 \end{bmatrix}. \tag{4.129}$$

The hard matrices for other subprocesses involving two quarks and two gluons, such as $qg \to qg$, can be obtained from this expression using crossing symmetries.

Four gluon subprocesses

For the four gluon subprocesses, $gg \to gg$, we follow the work in Refs. [260, 261] to use the following over-complete basis

$$\begin{aligned}
&\theta_1 = \text{Tr}\left[t^{a_1}t^{a_2}t^{a_3}t^{a_4}\right], && \theta_2 = \text{Tr}\left[t^{a_1}t^{a_2}t^{a_4}t^{a_3}\right], && \theta_3 = \text{Tr}\left[t^{a_1}t^{a_4}t^{a_3}t^{a_2}\right], \\
&\theta_4 = \text{Tr}\left[t^{a_1}t^{a_4}t^{a_2}t^{a_3}\right], && \theta_5 = \text{Tr}\left[t^{a_1}t^{a_3}t^{a_4}t^{a_2}\right], && \theta_6 = \text{Tr}\left[t^{a_1}t^{a_3}t^{a_2}t^{a_4}\right], \\
&\theta_7 = \text{Tr}\left[t^{a_1}t^{a_4}\right]\text{Tr}\left[t^{a_2}t^{a_3}\right], && \theta_8 = \text{Tr}\left[t^{a_1}t^{a_2}\right]\text{Tr}\left[t^{a_3}t^{a_4}\right], && \theta_9 = \text{Tr}\left[t^{a_1}t^{a_3}\right]\text{Tr}\left[t^{a_2}t^{a_4}\right].
\end{aligned} \tag{4.130}$$

We note that a six dimensional basis was chosen in [262]. Using this basis in Eq. (4.130), one can show that the hard matrix takes the following form

$$\boldsymbol{H}_{gg\to gg} = \frac{2g_s^4\left(\hat{s}^4+\hat{t}^4+\hat{u}^4\right)}{\hat{s}^2\hat{u}^2N_c^2C_F^2}\begin{bmatrix} 1 & \frac{\hat{u}}{\hat{t}} & 1 & \frac{\hat{s}}{\hat{t}} & \frac{\hat{u}}{\hat{t}} & \frac{\hat{s}}{\hat{t}} & 0 & 0 & 0 \\ \frac{\hat{u}}{\hat{t}} & \frac{\hat{u}^2}{\hat{t}^2} & \frac{\hat{u}}{\hat{t}} & \frac{\hat{s}\hat{u}}{\hat{t}^2} & \frac{\hat{u}^2}{\hat{t}^2} & \frac{\hat{s}\hat{u}}{\hat{t}^2} & 0 & 0 & 0 \\ 1 & \frac{\hat{u}}{\hat{t}} & 1 & \frac{\hat{s}}{\hat{t}} & \frac{\hat{u}}{\hat{t}} & \frac{\hat{s}}{\hat{t}} & 0 & 0 & 0 \\ \frac{\hat{s}}{\hat{t}} & \frac{\hat{s}\hat{u}}{\hat{t}^2} & \frac{\hat{s}}{\hat{t}} & \frac{\hat{s}^2}{\hat{t}^2} & \frac{\hat{s}\hat{u}}{\hat{t}^2} & \frac{\hat{s}^2}{\hat{t}^2} & 0 & 0 & 0 \\ \frac{\hat{u}}{\hat{t}} & \frac{\hat{u}^2}{\hat{t}^2} & \frac{\hat{u}}{\hat{t}} & \frac{\hat{s}\hat{u}}{\hat{t}^2} & \frac{\hat{u}^2}{\hat{t}^2} & \frac{\hat{s}\hat{u}}{\hat{t}^2} & 0 & 0 & 0 \\ \frac{\hat{s}}{\hat{t}} & \frac{\hat{s}\hat{u}}{\hat{t}^2} & \frac{\hat{s}}{\hat{t}} & \frac{\hat{s}^2}{\hat{t}^2} & \frac{\hat{s}\hat{u}}{\hat{t}^2} & \frac{\hat{s}^2}{\hat{t}^2} & 0 & 0 & 0 \\ 0 & 0 & 0 & 0 & 0 & 0 & 0 & 0 & 0 \\ 0 & 0 & 0 & 0 & 0 & 0 & 0 & 0 & 0 \\ 0 & 0 & 0 & 0 & 0 & 0 & 0 & 0 & 0 \end{bmatrix}. \tag{4.131}$$

The LO soft matrix for this channel is given in Appendix C of [261] for this basis as

$$\boldsymbol{S}_{gg\to gg} = \frac{C_F}{8N_c}\begin{bmatrix} a_0 & b_0 & c_0 & b_0 & b_0 & b_0 & d_0 & d_0 & -e_0 \\ b_0 & a_0 & b_0 & b_0 & c_0 & b_0 & -e_0 & d_0 & b_0 \\ c_0 & b_0 & a_0 & b_0 & b_0 & b_0 & d_0 & d_0 & -e_0 \\ b_0 & b_0 & b_0 & a_0 & b_0 & c_0 & d_0 & -e_0 & d_0 \\ b_0 & c_0 & b_0 & b_0 & a_0 & b_0 & -e_0 & d_0 & d_0 \\ b_0 & b_0 & b_0 & c_0 & b_0 & a_0 & d_0 & -e_0 & d_0 \\ d_0 & -e_0 & d_0 & d_0 & -e_0 & d_0 & d_0e_0 & e_0^2 & e_0^2 \\ d_0 & d_0 & d_0 & -e_0 & d_0 & -e_0 & e_0^2 & d_0e_0 & e_0^2 \\ -e_0 & d_0 & -e_0 & d_0 & d_0 & d_0 & e_0^2 & e_0^2 & d_0e_0 \end{bmatrix}, \tag{4.132}$$

where $a_0 = N_c^4 - 3N_c^2 + 3$, $b_0 = 3 - N_c^2$, $c_0 = 3 + N_c^2$, $d_0 = 2N_c^2C_F$, and $e_0 = N_c$.

4.3.3.2 Polarized Hard Matrices

As we have emphasized in the previous section, Sivers function is non-universal. The well-known example is the sign change between the Sivers function probed in Semi-Inclusive DIS and that in Drell-Yan (DY) process [263, 155, 156],

$$f_{1T\,q/P_A}^{\perp\,(\mathrm{DY})}(x,k_\perp;\mu,\zeta_1) = -f_{1T\,q/P_A}^{\perp\,(\mathrm{SIDIS})}(x,k_\perp;\mu,\zeta_1)\,. \tag{4.133}$$

Such a sign change can be easily taken care of in describing the Drell-Yan Sivers asymmetry,

$$d\Delta\sigma(S_\perp) \propto f_{1T\,q/P_A}^{\perp\,(\mathrm{DY})}(x,k_\perp;\mu,\zeta_1)H(Q;\mu) = f_{1T\,q/P_A}^{\perp\,(\mathrm{SIDIS})}(x,k_\perp;\mu,\zeta_1)\big[-H(Q;\mu)\big]\,, \qquad (4.134)$$

where $H(Q;\mu)$ is the hard function in the Drell-Yan process, and we have applied Eq. (4.133) in the second step. In other words, if we use the Semi-Inclusive DIS Sivers function in a Drell-Yan process, we shift the minus sign (or the process-dependence) into the hard function.

For the partonic subprocesses in the hadronic dijet production, one has much more complicated process-dependence for the Sivers functions involved. This can be seen from the highly nontrivial gauge link structure which has been derived in [246] in the definition of the TMD PDFs. Even in these complicated processes, one can incorporate such process-dependence of the Sivers functions into modified hard functions as in Eq. (4.134) [245, 134, 133, 229, 230]. We follow a similar procedure in this section to include this process-dependence of the Sivers functions into the hard functions in the matrix form.

In Fig. 4.10, we demonstrate the factorization between the Sivers function and modified hard functions. Unlike the unpolarized case, the contributions of the Sivers asymmetry are given by considering the attachment of an additional collinear (to the incoming hadron) gluon to three of the external legs. Such a gluon is part of the gauge link in the definition of the Sivers function, and it is the imaginary part of the Feynman diagram (related to the so-called soft gluonic pole) that contributes to the process-dependence of the Sivers function.

It is important to note that the additional gluon leads to additional complications so that naive crossing symmetry cannot be used to relate one hard function to another, as in the unpolarized case studied above. These complications occur because the contributions to the Sivers asymmetry are only given by attaching the additional gluon to three of the four external legs. Furthermore, since the sign of the interaction (imaginary part) with the external gluon is opposite for quarks and anti-quarks, this sign must also be accounted for when applying crossing symmetry or charge conjugation.

Four quark subprocesses

As in the unpolarized case, the bases for four quark subprocesses are given in Tab. 4.1.

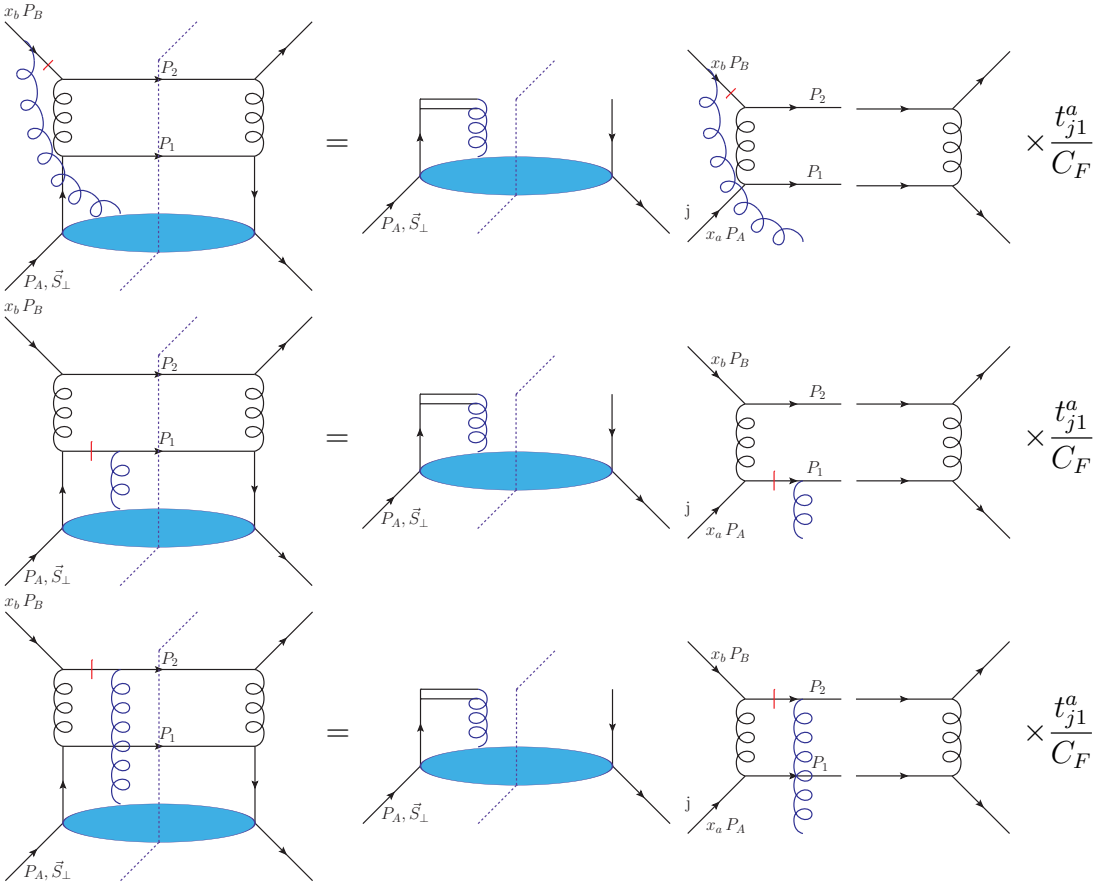

Figure 4.10: A demonstration of the factorization between the Sivers function and the hard function for $qq' \to qq'$ subprocess. The red lines indicate the locations of the soft poles while the blue gluon represents the gauge link which generates the asymmetry.

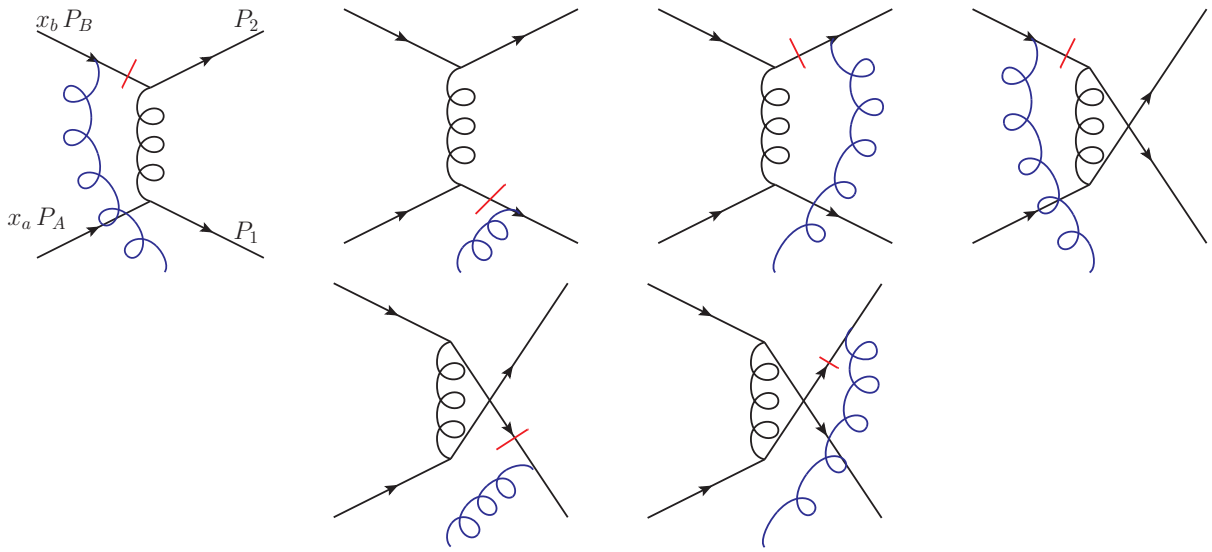

Figure 4.11: Polarized scattering amplitudes for the $qq \to qq$ subprocess. From left the right, the first three graphs give the scattering amplitude for the t-channel for initial-state, final-state 1, and final-state 2 interactions. The remaining channels give the contributions for the u-channel for initial-state, final-state 1, and final-state 2 interactions.

As discussed above, one cannot naively apply crossing symmetry to obtain hard matrices of a general polarized subprocess. For the polarized four quark subprocesses, however, only the sign of each color factor changes under charge conjugation. Therefore, the hard matrices for the bottom row of Tab. 4.1 can be obtained from the results from the top row of this table with the addition of a minus sign.

To demonstrate how $\boldsymbol{H}^{\text{Sivers}}_{ab\to cd}$ are derived, we explicitly perform the calculation for the $qq' \to qq'$, $qq' \to q'q$, and $qq \to qq$ subprocesses as we did for the unpolarized case. Afterwards, we provide the expressions for the remaining subprocesses. To start, it is important to remind ourselves that a non-vanishing Sivers asymmetry requires initial/final state interactions generating a phase. Because all initial and final partonic states relevant for dijet production are colored, both initial and final state interactions have to be taken into account. Such interactions would generate non-trivial gauge link structures, see e.g. Refs. [264, 246, 229]. On the left side of Fig. 4.10, as an example, we show all possible diagrams with one gluon exchange between the remnant of the polarized proton and the

$qq' \to qq'$ hard scattering part, which contribute to the Sivers asymmetry. Now with the presence of the extra gluon scattering (first order of the gauge link expansion), the diagram at the left side of the cut will be denoted as $\mathcal{M}_j^{\text{Sivers},a}$, while the right side is same as the unpolarized case denoted as $\mathcal{M}^\dagger$. Here a is the color for the attached gluon, j is the color index for the incoming quark with momentum $x_a P_A$ on the left side of cut line, while the color index for the incoming quark on the right side of the cut line is given by 1 like in the previous section. In contrast to the unpolarized correlation function, quarks j and 1 do not need to have the same color, because of the presence of the gluon from the gauge link. Now we perform the following expansion to obtain the hard matrix $|\mathcal{M}^{\text{Sivers}}|^2$ for the polarized case,

$$\mathcal{M}_j^{\text{Sivers},a} \mathcal{M}^\dagger = |\mathcal{M}^{\text{Sivers}}|^2 \, t_{1j}^a \,, \tag{4.135}$$

where t_{1j}^a will be included into the quark-quark correlator in the polarized proton to become $\sim \langle PS|\bar{\psi}_1 \, n \cdot A^a t_{1j}^a \, \psi_j|PS\rangle$, see e.g. Ref. [265, 246, 133]. From Eq. (4.135), we thus derive

$$\begin{aligned} |\mathcal{M}^{\text{Sivers}}|^2 =& \frac{1}{\text{Tr}\left[t^a t^a\right]} \mathcal{M}_j^{\text{Sivers},a} \, t_{j1}^a \, \mathcal{M}^\dagger \\ =& \frac{1}{N_c} \cdot \frac{1}{C_F} \mathcal{M}_j^{\text{Sivers},a} \, t_{j1}^a \, \mathcal{M}^\dagger \,. \end{aligned} \tag{4.136}$$

At the same time, we use the convention that N_{init} in the polarized and unpolarized cases are the same. Therefore, the factor of $1/N_c$ in Eq. (4.136) is absorbed into N_{init}. With that in mind, to arrive at the correct normalization of the polarized hard function, we thus obtain

$$|\mathcal{M}^{\text{Sivers}}|^2 \to \frac{1}{C_F} \mathcal{M}_j^{\text{Sivers},a} \, t_{j1}^a \, \mathcal{M}^\dagger \,, \tag{4.137}$$

which is demonstrated on the right-hand side of Fig. 4.10.

Now we need to project $\mathcal{M}_j^{\text{Sivers},a}$ and $\mathcal{M}^\dagger$ into the color basis separately. The polarized scattering amplitude $\mathcal{M}_j^{\text{Sivers},a}$ can be written as

$$\begin{aligned} \mathcal{M}_j^{\text{Sivers},a} =& \, \mathcal{M}_t^{\text{kin}} \left(t^b t^a\right)_{42} \left(t^b\right)_{3j} + \mathcal{M}_t^{\text{kin}} \left(t^b\right)_{42} \left(t^a t^b\right)_{3j} + \mathcal{M}_t^{\text{kin}} \left(t^a t^b\right)_{42} \left(t^b\right)_{3j} \\ &+ \mathcal{M}_u^{\text{kin}} \left(t^b t^a\right)_{32} \left(t^b\right)_{4j} + \mathcal{M}_u^{\text{kin}} \left(t^a t^b\right)_{32} \left(t^b\right)_{4j} + \mathcal{M}_u^{\text{kin}} \left(t^b\right)_{32} \left(t^a t^b\right)_{4j} \,, \end{aligned} \tag{4.138}$$

where $\mathcal{M}_t^{\text{kin}}$ and $\mathcal{M}_u^{\text{kin}}$ are the same as the expressions in Eqs. (4.109) and (4.110). From left to right on the top line of this expression, these terms give the scattering amplitudes for the initial-state, final-state 1, and final-state 2 interaction for the t-channel, corresponding to the first three diagrams of Fig. 4.11 in the same order. Likewise from left to right on the bottom line, the terms give the scattering amplitude for the initial-state, final-state 1, and final-state 2 interaction for the u-channel, corresponding to the last three diagrams of Fig. 4.11 in the same order. Using the Feynman rules for the gauge link color factors given in Fig. 6 of [133], we easily arrive at Eq. (4.138) from these diagrams. From the unpolarized scattering amplitude given in Eq. (4.108), we write the conjugate amplitude as

$$\mathcal{M}^\dagger = \mathcal{M}_t^{\text{kin}\dagger} \left(t^b\right)_{24} \left(t^b\right)_{13} + \mathcal{M}_u^{\text{kin}\dagger} \left(t^b\right)_{23} \left(t^b\right)_{14} . \tag{4.139}$$

Analogous to the unpolarized scattering amplitude, the scattering amplitude can be decomposed into the orthogonal basis given in Eq. (4.106) as

$$\mathcal{M}_j^{\text{Sivers},a} t_{j1}^a = \mathcal{M}_1^{\text{Sivers}} \theta_1 + \mathcal{M}_2^{\text{Sivers}} \theta_2 \,, \tag{4.140}$$

$$\mathcal{M}^\dagger = \mathcal{M}_1^\dagger \theta_1^\dagger + \mathcal{M}_2^\dagger \theta_2^\dagger \,, \tag{4.141}$$

where we have

$$\mathcal{M}_1^{\text{Sivers}} = \frac{\text{Tr}\left[\mathcal{M}_j^{\text{Sivers},a} t_{j1}^a \, \theta_1^\dagger\right]}{\text{Tr}\left[\theta_1 \, \theta_1^\dagger\right]} \,, \qquad \mathcal{M}_2^{\text{Sivers}} = \frac{\text{Tr}\left[\mathcal{M}_j^{\text{Sivers},a} t_{j1}^a \, \theta_2^\dagger\right]}{\text{Tr}\left[\theta_2 \, \theta_2^\dagger\right]} \,, \tag{4.142}$$

$$\mathcal{M}_1^\dagger = \frac{\text{Tr}\left[\mathcal{M}^\dagger \, \theta_1\right]}{\text{Tr}\left[\theta_1 \, \theta_1^\dagger\right]} \,, \qquad \mathcal{M}_2^\dagger = \frac{\text{Tr}\left[\mathcal{M}^\dagger \, \theta_2\right]}{\text{Tr}\left[\theta_2 \, \theta_2^\dagger\right]} \,. \tag{4.143}$$

After performing this decomposition, we can now write

$$|\mathcal{M}^{\text{Sivers}}|^2 = \text{Tr}\left[\boldsymbol{H}_{ab\to cd}^{\text{Sivers}} \cdot \boldsymbol{S}_{ab\to cd}\right] \,, \tag{4.144}$$

where $\boldsymbol{H}_{ab\to cd}^{\text{Sivers}}$ is given by

$$\boldsymbol{H}_{ab\to cd}^{\text{Sivers}} = \frac{1}{C_F} \begin{bmatrix} \mathcal{M}_1^{\text{Sivers}} \, M_1^\dagger & \mathcal{M}_1^{\text{Sivers}} \, M_2^\dagger \\ \mathcal{M}_2^{\text{Sivers}} \, M_1^\dagger & \mathcal{M}_2^{\text{Sivers}} \, M_2^\dagger \end{bmatrix} \tag{4.145}$$

and $\boldsymbol{S}$ is the same as the unpolarized case.

From these expressions, we can obtain the polarized hard matrices for the $qq' \to qq'$, $qq' \to q'q$, and $qq \to qq$ subprocesses as

$$\boldsymbol{H}^{\text{Sivers}}_{qq'\to qq'} = \frac{4g_s^4\left(\hat{s}^2+\hat{u}^2\right)}{\hat{t}^2 N_c C_F}\begin{bmatrix} N_c^2-5 & 0 \\ 2C_F & 0 \end{bmatrix}, \tag{4.146}$$

$$\boldsymbol{H}^{\text{Sivers}}_{qq'\to q'q} = -\frac{4g_s^4\left(\hat{s}^2+\hat{t}^2\right)}{\hat{u}^2 N_c^3 C_F}\begin{bmatrix} N_c^2+3 & -\left(N_c^2+3\right)C_F \\ -\left(3-N_c^2\right)C_F & \left(3-N_c^2\right)C_F^2 \end{bmatrix}, \tag{4.147}$$

$$\boldsymbol{H}^{\text{Sivers}}_{qq\to qq} = \boldsymbol{H}^{\text{Sivers}}_{qq'\to qq'} + \boldsymbol{H}^{\text{Sivers}}_{qq'\to q'q} + \frac{4\hat{s}^2 g_s^4}{\hat{t}\hat{u}N_c^2 C_F}\begin{bmatrix} 8 & -\left(5-N_c^2\right)C_F \\ -\left(5-N_c^2\right)C_F & 2C_F^2 \end{bmatrix}. \tag{4.148}$$

Since $qq \to qq$ subprocess receives contributions from both t- and u-channels (as well as their interference), its expression is the most complicated among the three subprocesses computed. One can show that after performing the trace with the soft color matrix, the expressions are consistent with the squared amplitude of [133]. The color matrices for the remaining four quark subprocesses in the top row of Tab. 4.1 can be computed in the same spirit and we obtain the following expressions

$$\boldsymbol{H}^{\text{Sivers}}_{q\bar{q}\to q'\bar{q}'} = \frac{4\left(N_c^2+1\right)g_s^4\left(\hat{t}^2+\hat{u}^2\right)}{\hat{s}^2 N_c C_F}\begin{bmatrix} 1 & 0 \\ 0 & 0 \end{bmatrix}, \tag{4.149}$$

$$\boldsymbol{H}^{\text{Sivers}}_{q\bar{q}'\to q\bar{q}'} = \frac{4g_s^4\left(\hat{s}^2+\hat{u}^2\right)}{\hat{t}^2 N_c^3 C_F}\begin{bmatrix} N_c^2+1 & -\left(N_c^2+1\right)C_F \\ 2N_c C_F^2 & -2N_c C_F^3 \end{bmatrix}, \tag{4.150}$$

$$\boldsymbol{H}^{\text{Sivers}}_{q\bar{q}\to q\bar{q}} = \boldsymbol{H}^{\text{Sivers}}_{q\bar{q}\to q'\bar{q}'} + \boldsymbol{H}^{\text{Sivers}}_{q\bar{q}'\to q\bar{q}'} - \frac{8\hat{u}^2 g_s^4}{\hat{s}\hat{t}N_c^2 C_F^2}\begin{bmatrix} \left(N_c^2+1\right)C_F & -\frac{1}{2}\left(N_c^2+1\right)C_F^2 \\ N_c C_F^3 & 0 \end{bmatrix}, \tag{4.151}$$

$$\boldsymbol{H}^{\text{Sivers}}_{q\bar{q}'\to \bar{q}'q} = -\frac{4g_s^4\left(\hat{s}^2+\hat{t}^2\right)}{\hat{u}^2 N_c C_F}\begin{bmatrix} N_c^2-3 & 0 \\ 2C_F & 0 \end{bmatrix}, \tag{4.152}$$

$$\boldsymbol{H}^{\text{Sivers}}_{q\bar{q}\to \bar{q}'q'} = \frac{4\left(N_c^2+1\right)g_s^4\left(\hat{t}^2+\hat{u}^2\right)}{\hat{s}^2 N_c^3 C_F}\begin{bmatrix} 1 & -C_F \\ -C_F & C_F^2 \end{bmatrix}, \tag{4.153}$$

$$\boldsymbol{H}^{\text{Sivers}}_{q\bar{q}\to \bar{q}q} = \boldsymbol{H}^{\text{Sivers}}_{q\bar{q}'\to \bar{q}'q} + \boldsymbol{H}^{\text{Sivers}}_{q\bar{q}\to \bar{q}'q'} - \frac{8\hat{t}^2 g_s^4}{\hat{s}\hat{u}N_c^2 C_F}\begin{bmatrix} 2 & -\frac{1}{2}\left(3-N_c^2\right)C_F \\ -\frac{1}{2}\left(N_c^2+3\right)C_F & C_F^2 \end{bmatrix}. \tag{4.154}$$

After performing charge conjugation, the hard color matrices for the subprocesses in the bottom row of Tab. 4.1 can be obtained from these expressions.

Two quarks and two gluon subprocesses

All twelve of the two quark and two gluon subprocesses are given in Tab. 4.2. As we have mentioned in Sec. 4.3.1, we neglect the gluon Sivers contribution in this section. This means that all subprocesses with a gluon incoming from the polarized proton will be neglected. There are then six remaining subprocesses to compute. However, we find that under charge conjugation, the polarized hard functions once again only change by an overall minus sign. Thus, we only need to perform the calculation for three of the hard matrices.

In order to further demonstrate our method for calculating the polarized hard matrices, we now perform the calculation for the $q\bar{q} \to gg$ subprocess. We then provide the expressions for the remaining hard matrices. For the unpolarized process the scattering amplitude has three channels. After the addition of the external gluon, there are then nine polarized process to be considered. At the cross section level, this results in 27 hard interactions which need to be considered. Despite this complication, we can once again write

$$|\mathcal{M}^{\text{Sivers}}|^2 = \frac{1}{C_F} \mathcal{M}_j^{\text{Sivers}\, a} t_{j1}^a \mathcal{M}^\dagger \,. \tag{4.155}$$

Just like in the unpolarized case, we begin the calculation by decomposing the amplitudes into the primed basis first. Then to simplify our result, we rotate into the unprimed basis. The scattering amplitudes for the process can then be written as

$$\mathcal{M}_j^{\text{Sivers}\, a} t_{j1}^a = \mathcal{M}_1^{\text{Sivers}} \theta_1' + \mathcal{M}_2^{\text{Sivers}} \theta_2' + \mathcal{M}_3^{\text{Sivers}} \theta_3' \,, \tag{4.156}$$

$$\mathcal{M}_i^\dagger = \mathcal{M}_1^\dagger \theta_1'^\dagger + \mathcal{M}_2^\dagger \theta_2'^\dagger + \mathcal{M}_3^\dagger \theta_3'^\dagger \,, \tag{4.157}$$

where

$$\mathcal{M}_1^{\text{Sivers}} = \frac{\text{Tr}\left[\mathcal{M}_j^{\text{Sivers},a} t_{j1}^a \, \theta_1'^\dagger\right]}{\text{Tr}\left[\theta_1' \, \theta_1'^\dagger\right]} \,, \; \mathcal{M}_2^{\text{Sivers}} = \frac{\text{Tr}\left[\mathcal{M}_j^{\text{Sivers},a} t_{j1}^a \, \theta_2'^\dagger\right]}{\text{Tr}\left[\theta_2' \, \theta_2'^\dagger\right]} \,, \; \mathcal{M}_3^{\text{Sivers}} = \frac{\text{Tr}\left[\mathcal{M}_j^{\text{Sivers},a} t_{j1}^a \, \theta_3'^\dagger\right]}{\text{Tr}\left[\theta_3' \, \theta_3'^\dagger\right]} \,, \tag{4.158}$$

$$\mathcal{M}_1^\dagger = \frac{\mathrm{Tr}\left[\mathcal{M}^\dagger\,\theta_1'\right]}{\mathrm{Tr}\left[\theta_1'\,\theta_1'^\dagger\right]}\,, \qquad \mathcal{M}_2^\dagger = \frac{\mathrm{Tr}\left[\mathcal{M}^\dagger\,\theta_2'\right]}{\mathrm{Tr}\left[\theta_2'\,\theta_2'^\dagger\right]}\,. \qquad \mathcal{M}_3^\dagger = \frac{\mathrm{Tr}\left[\mathcal{M}^\dagger\,\theta_3'\right]}{\mathrm{Tr}\left[\theta_3'\,\theta_3'^\dagger\right]}\,. \tag{4.159}$$

The hard matrix in the primed basis can then be computed as

$$\boldsymbol{H}_{q\bar{q}\to gg}^{\text{Sivers}\,\prime} = \frac{1}{C_F}\begin{bmatrix} \mathcal{M}_1^{\text{Sivers}}\,M_1^\dagger & \mathcal{M}_1^{\text{Sivers}}\,M_2^\dagger & \mathcal{M}_1^{\text{Sivers}}\,M_3^\dagger \\ \mathcal{M}_2^{\text{Sivers}}\,M_1^\dagger & \mathcal{M}_2^{\text{Sivers}}\,M_2^\dagger & \mathcal{M}_2^{\text{Sivers}}\,M_3^\dagger \\ \mathcal{M}_3^{\text{Sivers}}\,M_1^\dagger & \mathcal{M}_3^{\text{Sivers}}\,M_2^\dagger & \mathcal{M}_3^{\text{Sivers}}\,M_3^\dagger \end{bmatrix}\,. \tag{4.160}$$

In order to obtain the hard matrix in the unprimed basis we apply the transformation

$$\boldsymbol{H}_{q\bar{q}\to gg} = \boldsymbol{R}^\dagger\,\boldsymbol{H}'_{q\bar{q}\to gg}\,\boldsymbol{R} \qquad \boldsymbol{R} = \begin{bmatrix} 1 & 1 & -1 \\ 1 & 1 & 1 \\ 2N_c & 0 & 0 \end{bmatrix}^{-1}\,. \tag{4.161}$$

The final result for all of the two quark and two gluon interactions hard matrices are given by

$$\boldsymbol{H}_{q\bar{q}\to gg}^{\text{Sivers}} = -\frac{4g_s^4\left(\hat{s}^2+\hat{u}^2\right)}{\hat{s}\hat{t}^2\hat{u}N_cC_F}\begin{bmatrix} 2\hat{s}^2N_cC_F & 2\hat{s}\hat{u}N_cC_F & 0 \\ -\hat{s}\hat{u}\left(N_c^2+1\right) & -\hat{u}^2\left(N_c^2+1\right) & 0 \\ \hat{s}^2N_c & \hat{s}\hat{u}N_c & 0 \end{bmatrix}\,, \tag{4.162}$$

$$\boldsymbol{H}_{qg\to gq}^{\text{Sivers}} = \frac{4g_s^4\left(\hat{s}^2+\hat{t}^2\right)}{\hat{s}\hat{t}\hat{u}^2N_cC_F}\begin{bmatrix} 2\hat{s}^2N_cC_F & 2\hat{s}\hat{t}N_cC_F & 0 \\ -\hat{s}\hat{t}\left(N_c^2+1\right) & -\hat{t}^2\left(N_c^2+1\right) & 0 \\ \hat{s}^2N_c & \hat{s}\hat{t}N_c & 0 \end{bmatrix}\,, \tag{4.163}$$

$$\boldsymbol{H}_{q\bar{q}\to gg}^{\text{Sivers}} = \frac{4g_s^4\left(\hat{t}^2+\hat{u}^2\right)}{\hat{s}^2\hat{t}\hat{u}N_cC_F}\begin{bmatrix} \hat{u}^2\left(N_c^2+1\right) & \hat{t}\hat{u}\left(N_c^2+1\right) & 0 \\ \hat{t}\hat{u}\left(N_c^2+1\right) & \hat{t}^2\left(N_c^2+1\right) & 0 \\ \hat{s}\hat{u}N_c & \hat{s}\hat{t}N_c & 0 \end{bmatrix}\,, \tag{4.164}$$

$$\tag{4.165}$$

After performing charge conjugation, the hard color matrices for the remaining subprocesses can be obtained from these expressions.

Simplification in the one-dimensional color space

We note that for processes in which the color space is one dimensional, i.e. single color basis in the decomposition, such as Drell-Yan, Semi-Inclusive DIS, and color singlet boson-jet

processes, the decomposition of scattering amplitude is trivial. We have

$$\mathcal{M} = \mathcal{M}^{\text{kin}}\,\theta_1\,, \tag{4.166}$$

where $\mathcal{M}^{\text{kin}} = \mathcal{M}_s^{\text{kin}} + \mathcal{M}_t^{\text{kin}} + \mathcal{M}_u^{\text{kin}}$ in general receives contribution from different channels as above. The kinematic parts can be trivially extracted by

$$\mathcal{M}^{\text{kin}} = \frac{\text{Tr}\left[\mathcal{M}\theta_1^\dagger\right]}{\text{Tr}\left[\theta_1\theta_1^\dagger\right]}\,, \qquad \mathcal{M}^{\text{kin}\dagger} = \frac{\text{Tr}\left[\mathcal{M}^\dagger\theta_1\right]}{\text{Tr}\left[\theta_1\theta_1^\dagger\right]}\,. \tag{4.167}$$

Therefore the unpolarized hard matrices can be constructed simply by

$$\boldsymbol{H} = \left|\mathcal{M}^{\text{kin}}\right|^2\left[1\right]\,, \qquad \boldsymbol{S} = \left[\text{Tr}\left[\theta_1\theta_1^\dagger\right]\right]\,. \tag{4.168}$$

In these expressions, we have suppressed the subprocess subscript since these expressions are true for all subprocesses with a one-dimensional color space. The differential cross section is then given by

$$\left|\mathcal{M}\right|^2 = \text{Tr}\left[\boldsymbol{H}\cdot\boldsymbol{S}\right] = C^u\left|\mathcal{M}^{\text{kin}}\right|^2 \tag{4.169}$$

where in the second line we have defined $C^u = \text{Tr}\left[\theta_1\theta_1^\dagger\right]$. Similarly, for the polarized hard matrix, we can write

$$\left|\mathcal{M}^{\text{Sivers}}\right|^2 = \frac{\text{Tr}\left[\mathcal{M}^{\text{Sivers,a}}t^a_{j1}\theta_1^\dagger\right]}{\text{Tr}\left[\theta_1\theta_1^\dagger\right]} = \text{Tr}\left[\boldsymbol{H}^{\text{Sivers}}\cdot\boldsymbol{S}\right] = \frac{C^{\text{Sivers}}}{C^u}\left|\mathcal{M}^{\text{kin}}\right|^2\,, \tag{4.170}$$

where $C^{\text{Sivers}}\mathcal{M}^{\text{kin}} = \text{Tr}\left[\mathcal{M}^{\text{Sivers,a}}t^a_{j1}\theta_1^\dagger\right]$. Therefore, the hard functions of the polarized and unpolarized scatterings are related by an overall color constant,

$$\boldsymbol{H}^{\text{Sivers}} = \frac{C^{\text{Sivers}}}{C^u}\boldsymbol{H}\,. \tag{4.171}$$

Here, C^{Sivers} can further be decomposed into color factors arising from gauge link gluons interacting with different external colored partons, as seen in [266, 133, 267, 207].

4.3.3.3 Evolution equations

Hard functions can be related to the Wilson coefficients C_I^Γ in the color basis $\{\theta_I\}$ of section 4.3.3 by $H_{IJ} = \sum_\Gamma C_I^\Gamma C_J^{\Gamma *}$. Here Γ represents different helicity states of the incoming and outgoing particles. Explicit expressions of the Wilson coefficients at next-to-leading order can be found in [260, 261], but we do not present them as we are only using the tree-level hard functions for our study. We do, however, include the renormalization group (RG) evolution of the hard functions coming from the 1-loop anomalous dimensions. Then the Wilson coefficients satisfy the RG evolution equations [260, 261, 268, 269]

$$\mu \frac{d}{d\mu} C_I^\Gamma = \left[\left(\Gamma_{\text{cusp}} \frac{c_H}{2} \ln \frac{-\hat{t}}{\mu^2} + \gamma_H \right) \delta_{IJ} + \Gamma_{\text{cusp}} M_{IJ} \right] C_J^\Gamma \,. \tag{4.172}$$

Here, $\Gamma_{\text{cusp}} = \frac{\alpha_s}{\pi} + \cdots$ is the cusp anomalous dimensions and $c_H = C_a + C_b + C_c + C_d$. The non-cusp anomalous dimension is defined as

$$\gamma_H = -\frac{1}{2} \left(\gamma_\mu^a \left[\alpha_s(\mu)\right] + \gamma_\mu^b \left[\alpha_s(\mu)\right] + \gamma_\mu^c \left[\alpha_s(\mu)\right] + \gamma_\mu^d \left[\alpha_s(\mu)\right] \right) \,, \tag{4.173}$$

where $\gamma_\mu^i[\alpha_s(\mu)] = \frac{\alpha_s}{\pi}\gamma_i + \cdots$, with $\gamma_q = \frac{3}{2}C_F$ and $\gamma_g = \frac{\beta_0}{2}$. Lastly, the matrix $\boldsymbol{M}$ takes the form

$$\boldsymbol{M} = -\sum_{i<j} \boldsymbol{T}_i \cdot \boldsymbol{T}_j \left[L(s_{ij}) - L(\hat{t}) \right] \,, \tag{4.174}$$

where $s_{12} = s_{34} = \hat{s}$, $s_{13} = s_{24} = \hat{t}$, and $s_{14} = s_{23} = \hat{u}$ and

$$L(\hat{t}) = \ln\left(\frac{-\hat{t}}{\mu^2}\right) \,, \qquad L(\hat{u}) = \ln\left(\frac{-\hat{u}}{\mu^2}\right) \,, \qquad L(\hat{s}) = \ln\left(\frac{\hat{s}}{\mu^2}\right) - i\pi \,. \tag{4.175}$$

From the RG evolution of the Wilson coefficients given in Eq. (4.172), we can arrive at the RG evolution equations for hard matrix $\boldsymbol{H}$ as

$$\mu \frac{d}{d\mu} \boldsymbol{H} = \boldsymbol{\Gamma}^H \cdot \boldsymbol{H} + \boldsymbol{H} \cdot \boldsymbol{\Gamma}^{H\dagger} \,, \tag{4.176}$$

where $\boldsymbol{\Gamma}^H$ is given by

$$\boldsymbol{\Gamma}^H = \left(\Gamma_{\text{cusp}} \frac{c_H}{2} \ln \frac{-\hat{t}}{\mu^2} + \gamma_H \right) \boldsymbol{I} + \Gamma_{\text{cusp}} \boldsymbol{M} \,. \tag{4.177}$$

4.3.4 QCD resummation and evolution formalism

In this section, we present the renormalization group (RG) equations for the rest of the key ingredients in the factorized formalism. These include the TMD PDFs, global soft functions, jet functions, and collinear-soft functions. After presenting their NLO perturbative results and RG evolution equations, we check the RG consistency. In the end, we present our resummation formula for dijet production.

4.3.4.1 TMDs and global soft functions

The unsubtracted TMD PDFs in the factorized formula in Eq. (4.93) describe the radiation along the incoming beams. They satisfy the RG evolution equations

$$\mu\frac{d}{d\mu}\ln f_i^{\rm unsub}(x,b;\mu,\zeta_1/\nu^2) = \Gamma_\mu^{f_i}(\mu,\nu)\,, \tag{4.178}$$

$$\nu\frac{d}{d\nu}\ln f_i^{\rm unsub}(x,b;\mu,\zeta_1/\nu^2) = \Gamma_\nu^{f_i}(\mu)\,, \tag{4.179}$$

where its μ- and ν-anomalous dimensions are given by

$$\Gamma_\mu^{f_i}(\mu,\nu,\zeta_i) = \Gamma_{\rm cusp} C_i\, L_{\zeta_i} + \gamma_\mu^i[\alpha_s(\mu)]\,, \tag{4.180}$$

$$\Gamma_\nu^{f_i}(\mu,\nu) = \frac{\alpha_s C_i}{\pi} L\,. \tag{4.181}$$

As we will see in this subsection, the rapidity divergences of the unsubtracted TMDs will be exactly canceled by the rapidity divergences of the global soft functions, which will allow us to identify the standard TMDs with subtracted rapidity divergence as in Eq. (4.95) above.

Suppressing the label $ab \to cd$ for convenience, the global soft functions up to 1-loop are given by

$$\boldsymbol{S}^{(0)}(b) = \boldsymbol{I}\,, \tag{4.182}$$

$$\boldsymbol{S}^{\rm bare,(1)}(b) = \sum_{i<j} \boldsymbol{T}_i\cdot\boldsymbol{T}_j\,\mathcal{I}_{ij}^{(1)}(b)\,, \tag{4.183}$$

where [184]

$$\mathcal{I}_{12}^{(1)}(b) = \frac{\alpha_s}{2\pi}\left[2\left(\frac{2}{\eta}-L_\nu\right)\left(\frac{1}{\epsilon}+L\right) - \frac{2}{\epsilon^2} + L^2 + \frac{\pi^2}{6}\right]\,, \tag{4.184}$$

$$\mathcal{I}_{13}^{(1)}(b) = \frac{\alpha_s}{2\pi}\left[\left(\frac{2}{\eta} - L_\nu - 2y_c\right)\left(\frac{1}{\epsilon} + L\right) - \frac{2}{\epsilon^2} - \frac{1}{\epsilon}L + \frac{\pi^2}{6}\right], \tag{4.185}$$

$$\mathcal{I}_{34}^{(1)}(b) = \frac{\alpha_s}{2\pi}\left[4\left(\frac{1}{\epsilon} + L\right)\ln\big(2\cosh(\Delta y/2)\big) - \frac{2}{\epsilon^2} - \frac{2}{\epsilon}L - L^2 + \Delta y^2 - 4\ln^2\big(2\cosh(\Delta y/2)\big) + \frac{\pi^2}{6}\right], \tag{4.186}$$

$$\mathcal{I}_{14}^{(1)}(b) = \mathcal{I}_{13}^{(1)}(b)(y_c \to y_d)\,, \quad \mathcal{I}_{23}^{(1)}(b) = \mathcal{I}_{13}^{(1)}(b)(y_c \to -y_c)\,, \quad \mathcal{I}_{24}^{(1)}(b) = \mathcal{I}_{14}^{(1)}(b)(y_d \to -y_d)\,. \tag{4.187}$$

The explicit matrix forms of tree-level soft functions in Eq. (4.182) for some color basis $\{\theta_I\}$ can be computed as

$$(I)_{IJ} = \theta_I \theta_J^\dagger\,, \tag{4.188}$$

which is equivalent to the matrix forms of the LO soft functions found in section 4.3.3. The matrix $\boldsymbol{T}_i \cdot \boldsymbol{T}_j$ of the eq. (4.183) was also computed in the color bases used in section 4.3.3 and can be found in [261, 260]. The renormalized global soft functions satisfy the RG evolution equations

$$\mu\frac{d}{d\mu}\boldsymbol{S}(b;\mu,\nu) = \boldsymbol{\Gamma}_\mu^{S\dagger}\cdot\boldsymbol{S} + \boldsymbol{S}\cdot\boldsymbol{\Gamma}_\mu^S\,, \tag{4.189}$$

$$\nu\frac{d}{d\nu}\boldsymbol{S}(b;\mu,\nu) = \boldsymbol{\Gamma}_\nu^{S\dagger}\cdot\boldsymbol{S} + \boldsymbol{S}\cdot\boldsymbol{\Gamma}_\nu^S\,, \tag{4.190}$$

$$\tag{4.191}$$

From Eqs. (4.182) - (4.187) and using $\sum_i \boldsymbol{T}_i = 0$, we then find

$$\begin{aligned}\boldsymbol{\Gamma}_\mu^S =& -\frac{\alpha_s}{2\pi}\left[C_a\left(\ln\frac{-\hat{t}}{x_a^2 S} - L_\nu\right) + C_b\left(\ln\frac{-\hat{t}}{x_b^2 S} - L_\nu\right) + (C_c + C_d)\left(\ln\frac{-\hat{t}}{P_\perp^2} - L\right)\right]\boldsymbol{I} \\ & - \frac{\alpha_s}{\pi}\boldsymbol{M} + \frac{\alpha_s}{\pi}\left(\boldsymbol{T}_1\cdot\boldsymbol{T}_2 + \boldsymbol{T}_3\cdot\boldsymbol{T}_4\right)i\pi \\ =& -\frac{\Gamma_{\text{cusp}}}{2}\left[C_a\left(\ln\frac{-\hat{t}}{x_a^2 S} - L_\nu\right) + C_b\left(\ln\frac{-\hat{t}}{x_b^2 S} - L_\nu\right) + (C_c + C_d)\left(\ln\frac{-\hat{t}}{P_\perp^2} - L\right)\right]\boldsymbol{I} \\ & - \Gamma_{\text{cusp}}\boldsymbol{M} + \Gamma_{\text{cusp}}\left(\boldsymbol{T}_1\cdot\boldsymbol{T}_2 + \boldsymbol{T}_3\cdot\boldsymbol{T}_4\right)i\pi\,,\end{aligned} \tag{4.192}$$

$$\boldsymbol{\Gamma}_\nu^S = -\frac{\alpha_s(C_a + C_b)}{2\pi}L\boldsymbol{I}\,, \tag{4.193}$$

where $\boldsymbol{M}$ was given in Eq. (4.174) and we promoted $\frac{\alpha_s}{\pi} \to \Gamma_{\text{cusp}}$, which is consistent with the factorization consistency relation below. Note that Eq. (4.192) is strictly real and the imaginary term $\sim i\pi$ cancels exactly with the imaginary term found in $\boldsymbol{M}$.

We note that $\mathbf{\Gamma}^S_\nu \sim \boldsymbol{I}$ and that this is expected as the hard functions do not have any rapidity divergence. Thus, we can write

$$\nu\frac{d}{d\nu}\boldsymbol{S}(b;\mu,\nu) = \mathbf{\Gamma}^{S\dagger}_\nu \cdot \boldsymbol{S} + \boldsymbol{S}\cdot\mathbf{\Gamma}^S_\nu = -\frac{\alpha_s(C_a+C_b)}{\pi}L\boldsymbol{S}(b;\mu,\nu)\,, \tag{4.194}$$

which has the same rapidity anomalous dimensions as the back-to-back soft functions $S_{ab}(b;\mu,\nu)$ found in standard Drell-Yan and Semi-Inclusive DIS process [62]. As expected, the rapidity divergence of the global soft function $\boldsymbol{S}(b;\mu,\nu)$ in Eq. (4.194) exactly cancels the rapidity anomalous dimensions for the unsubtracted TMDs $f_{a/P_A}(b;\mu,\nu)$ and $f_{b/P_B}(b;\mu,\nu)$ given in Eq. (4.181). Therefore, as discussed in the introduction, we can define $\tilde{\boldsymbol{S}}(b;\mu)$ absent of the rapidity divergence such that

$$\boldsymbol{S}(b;\mu,\nu) = \tilde{\boldsymbol{S}}(b;\mu)S_{ab}(b;\mu,\nu)\,. \tag{4.195}$$

Then as in Eq. (4.95), $S_{ab}(b;\mu,\nu)$ is combined with the unsubtracted TMDs to identify standard TMDs free of the rapidity divergences.

4.3.4.2 Jet and collinear-soft functions

Both jet and collinear-soft functions describe the radiation which resolves the produced jets. The jet functions [270, 271] encode the collinear radiations inside anti-k_T jet with radius R. The NLO expressions are given by

$$J_i(P_\perp R;\mu) = 1 + \frac{\alpha_s}{\pi}\left[\frac{C_i}{4}\ln^2\left(\frac{\mu^2}{P_\perp^2R^2}\right) + \frac{\gamma_i}{2}\ln\left(\frac{\mu^2}{P_\perp^2R^2}\right) + d_i\right]\,, \tag{4.196}$$

where the algorithmic dependent terms d_i for anti-k_T algorithm are

$$d_q = \left(\frac{13}{4} - \frac{3\pi^2}{8}\right)C_F\,, \tag{4.197}$$

$$d_g = \left(\frac{67}{18} - \frac{3\pi^2}{8}\right)C_A - \frac{23}{36}n_f\,. \tag{4.198}$$

The jet functions satisfy the RG evolution equations

$$\mu\frac{d}{d\mu}J_i(P_\perp R;\mu) = \Gamma^{J_i}_\mu(\mu)J_i(P_\perp R;\mu)\,, \tag{4.199}$$

where the anomalous dimension is given by

$$\Gamma_\mu^{J_i}(\mu) = \Gamma_{\rm cusp} C_i \ln\left(\frac{\mu^2}{P_\perp^2 R^2}\right) + \gamma_\mu^i[\alpha_s(\mu)]\,. \tag{4.200}$$

The collinear-soft functions [135, 164] describe the soft radiation along the jet direction and resolves the jet cone R. The NLO expressions are given by

$$S_i^{cs,(1)}(b,R;\mu) = 1 - \frac{\alpha_s C_i}{4\pi}\left[\ln^2\left(\frac{\mu^2}{\mu_b^2 R^2}\right) - \frac{\pi^2}{6}\right]. \tag{4.201}$$

The collinear-soft functions satisfy the RG evolution equations

$$\mu\frac{d}{d\mu} S_i^{\rm cs}(b,R;\mu) = \Gamma_\mu^{cs_i}(\mu) S_i^{\rm cs}(b,R;\mu)\,, \tag{4.202}$$

where its anomalous dimension takes the form

$$\Gamma_\mu^{cs_i}(\mu) = \Gamma_{\rm cusp} C_i \ln\left(\frac{\mu^2}{\mu_b^2 R^2}\right). \tag{4.203}$$

4.3.4.3 RG consistency at 1loop

With the anomalous dimensions presented for all the ingredients, we now show that our factorized formula given in Eq. (4.93) satisfy the consistency relations for the RG evolutions. The cancellation of the rapidity divergences was already checked around Eq. (4.194). We also expect μ-divergence of the various functions to cancel and satisfy the consistency equation

$$\mu\frac{d}{d\mu}\ln\big(\mathrm{Tr}\left[\boldsymbol{S}(b;\mu,\nu)\cdot\boldsymbol{H}(P_\perp;\mu)\right]\big) + \Gamma_\mu^{f_{a/P_A}} + \Gamma_\mu^{f_{b/P_B}} + \Gamma_\mu^{cs_c} + \Gamma_\mu^{cs_d} + \Gamma_\mu^{J_c} + \Gamma_\mu^{J_d} = 0\,. \tag{4.204}$$

From Eqs. (4.176), (4.177), (4.189), (4.192), we immediately find at 1-loop,

$$\begin{aligned}
&\mu\frac{d}{d\mu}\ln\big(\mathrm{Tr}\big[\boldsymbol{S}(b;\mu,\nu)\cdot\boldsymbol{H}(P_\perp;\mu)\big]\big) \\
&\qquad = \frac{\mathrm{Tr}\left[\boldsymbol{\Gamma}_\mu^{S\dagger}\cdot\boldsymbol{S}\cdot\boldsymbol{H} + \boldsymbol{S}\cdot\boldsymbol{\Gamma}_\mu^{S}\cdot\boldsymbol{H} + \boldsymbol{S}\cdot\boldsymbol{\Gamma}^{H}\cdot\boldsymbol{H} + \boldsymbol{S}\cdot\boldsymbol{H}\cdot\boldsymbol{\Gamma}^{H\dagger}\right]}{\mathrm{Tr}\left[\boldsymbol{S}(b;\mu,\nu)\cdot\boldsymbol{H}(P_\perp;\mu)\right]} \\
&\qquad = -\frac{\alpha_s}{\pi}\left[C_a\ln\left(\frac{\nu^2}{x_a^2 S}\right) + C_b\ln\left(\frac{\nu^2}{x_b^2 S}\right) - (C_c+C_d)\ln\left(\frac{P_\perp^2}{\mu_b^2}\right)\right] + 2\gamma_H\,.
\end{aligned} \tag{4.205}$$

One can then easily check from the μ-anomalous dimensions of the other functions given in Eqs. (4.180), (4.200), (4.203) that Eq. (4.204) is explicitly satisfied at 1-loop.

4.3.4.4 Resummation formula

Based on the above discussions and RG renormalization group methods in SCET, we can now derive the expression for the all-order resummed result. Explicitly, we calculate the cross section at the NLL accuracy, where we will use the two-loop cusp and one-loop single logarithmic anomalous dimension and the matching coefficients are kept at leading order. On the other hand, the color structures inside the hard and soft function will mix with each other under the RG evolution, which was first studied in [240]. In this section, we will apply the same methods in [260] to solve the RG equations. For the unpolarized cross section, the resummation formula has the form as follows:

$$\begin{aligned}
\frac{d\sigma}{dy_c dy_d dP_\perp^2 d^2q_\perp} &= \sum_{abcd} \frac{1}{16\pi^2\hat{s}^2}\frac{1}{N_{\text{init}}}\frac{1}{1+\delta_{cd}}\frac{1}{2\pi}\int_0^\infty db\, b\, J_0(q_\perp b)\, x_a f_{a/P_A}(x_a;\mu_{b_*})\, x_b f_{b/P_B}(x_b;\mu_{b_*}) \\
&\times \exp\left\{-\int_{\mu_{b_*}}^{\mu_h}\frac{d\mu}{\mu}\left[\Gamma_{\text{cusp}}(\alpha_s)c_H \ln\frac{|\hat{t}|}{\mu^2}+2\Gamma_H(\alpha_s)\right]\right\} \\
&\times \sum_{KK'}\exp\left[-\int_{\mu_{b_*}}^{\mu_h}\frac{d\mu}{\mu}\Gamma_{\text{cusp}}(\alpha_s)(\lambda_K+\lambda_{K'}^*)\right] H_{KK'}(P_\perp;\mu_h)\tilde{S}_{K'K}(b_*;\mu_{b_*}) \\
&\times \exp\left[-\int_{\mu_{b_*}}^{\mu_j}\frac{d\mu}{\mu}\Gamma_\mu^{J_c}(\alpha_s)-\int_{\mu_{b_*}}^{\mu_{cs}}\frac{d\mu}{\mu}\Gamma_\mu^{cs_c}(\alpha_s)\right] U_{\text{NG}}^c(\mu_{cs};\mu_j)\, J_c(P_\perp R;\mu_j) S_c^{\text{cs}}(b_*,R;\mu_{cs}) \\
&\times \exp\left[-\int_{\mu_{b_*}}^{\mu_j}\frac{d\mu}{\mu}\Gamma_\mu^{J_d}(\alpha_s)-\int_{\mu_{b_*}}^{\mu_{cs}}\frac{d\mu}{\mu}\Gamma_\mu^{cs_d}(\alpha_s)\right] U_{\text{NG}}^d(\mu_{cs};\mu_j)\, J_d(P_\perp R;\mu_j) S_d^{\text{cs}}(b_*,R;\mu_{cs}) \\
&\times \exp\left[-S_{\text{NP}}^a(b,\sqrt{\hat{s}},Q_0)-S_{\text{NP}}^b(b,\sqrt{\hat{s}},Q_0)\right], \qquad (4.206)
\end{aligned}$$

where λ_K is the eigenvalue of the matrix M_{IJ} in the hard anomalous dimension (4.172) and $H_{KK'}$ and $\tilde{S}_{K'K}$ are the hard and soft function in the diagonal basis as defined in [260]. In our numerical calculation, we use the LAPACK library [272] to obtain their value at different phase-space points. We have applied the b_*-prescription to prevent the Landau pole from being reached in the b-integral. Here, we define b_* as

$$b_* = b/\sqrt{1+b^2/b_{\text{max}}^2}\,, \qquad (4.207)$$

where b_{max} is chosen [120] to be 1.5 GeV^{-1}. Our perturbative Sudakov factor come from solving the renormalization group evolution equations for different functions from their intrinsic

scales, which are chosen for the hard, jet and collinear-soft function as

$$\mu_h = \sqrt{\hat{s}}, \quad \mu_j = P_\perp R, \quad \mu_{cs} = \mu_{b_*} R. \tag{4.208}$$

Note that $\sqrt{\hat{s}} \sim P_\perp$ is completely fixed by the measured quantities y_c, y_d and $P_\perp$ as seen from Eq. (4.92). Another choice of $\mu_h \sim P_\perp$ leads to similar numerical results.

The nonperturbative Sudakov factor in Eq. (4.206) was fitted to experimental data in [92]. The extracted functions are given by

$$S_{\rm NP}^{a,b}(b,\mu,Q_0) = g_1^f b^2 + \frac{g_2}{2}\frac{C_{a,b}}{C_F}\ln\frac{\mu}{Q_0}\ln\frac{b}{b_*}, \quad \text{with } g_1^f = 0.106,\ g_2 = 0.84,\ Q_0^2 = 2.4\,\text{GeV}^2. \tag{4.209}$$

We also incorporate NGLs resummation effects included by the function $U_{\rm NG}^{c,d}$. In order to include NGLs resummation effects at NLL accuracy, we also need to consider the extra one-loop single logarithmic anomalous dimension $\hat{\mathbf{\Gamma}}$ from the non-linear evolution parts. However, in [247, 248] this anomalous dimension was shown to cancel between the jet and collinear-soft function up to two-loop order. The explicit operator-based derivation of RG consistency including $\hat{\mathbf{\Gamma}}$ can be found in [273, 164, 251]. In the large N_c limit, the non-linear evolution equation can be solved using the parton shower algorithm [274]. Especially, at the NLL accuracy the evolution is totally determined by the one-loop anomalous dimension $\hat{\mathbf{\Gamma}}$, which is equivalent to the one appearing in the light jet mass distribution at the e^+e^- collider. Therefore, we can use the same fitting function form given in [162] to capture NGLs resummation contributions after setting proper initial and final evolution scales. In our case, these two scales are the jet scale μ_j and the collinear-soft scale μ_{cs}. Explicitly, the function is

$$U_{\rm NG}^k(\mu_{cs};\mu_j) = \exp\left[-C_A C_k \frac{\pi^2}{3} u^2 \frac{1+(au)^2}{1+(bu)^c}\right], \tag{4.210}$$

where the superscript $k = q$ and g denote the (anti-)quark and gluon jet, respectively, and with $C_q = C_F$ and $C_g = C_A$. The parameters a, b and c are fitting parameters which are given as $a = 0.85\,C_A$, $b = 0.86\,C_A$ and $c = 1.33$. The variable $u = \frac{1}{\beta_0}\log\frac{\alpha_s(\mu_{cs})}{\alpha_s(\mu_j)}$ is the

evolution scale measuring the separation of the scales μ_{cs} and μ_j. As shown in eq. (4.208), b_* prescription for μ_{cs} keeps u from reaching a nonperturbative scale.

As we have done for the unpolarized cross section, we also derive a similar resummation formula for the spin-dependent cross section

$$\begin{aligned}
\frac{d\Delta\sigma(S_\perp)}{dy_c dy_d dP_\perp^2 d^2q_\perp} =& \sin(\phi_q-\phi_S)\sum_{abcd}\frac{1}{16\pi^2\hat{s}^2}\frac{1}{N_{\rm init}}\frac{1}{1+\delta_{cd}}\left(-\frac{1}{4\pi}\right)\int_0^\infty db\, b^2\, J_1(q_\perp b)\\
&\times\ x_a T_{a,F}(x_a,x_a;\mu_{b_*})\, x_b f_{b/P_B}(x_b;\mu_{b_*})\ \exp\left\{-\int_{\mu_{b_*}}^{\mu_h}\frac{d\mu}{\mu}\left[\Gamma_{\rm cusp}(\alpha_s)c_H\ln\frac{|\hat{t}|}{\mu^2}+2\Gamma_H(\alpha_s)\right]\right\}\\
&\times\sum_{KK'}\exp\left[-\int_{\mu_{b_*}}^{\mu_h}\frac{d\mu}{\mu}\Gamma_{\rm cusp}(\alpha_s)(\lambda_K+\lambda^*_{K'})\right]H_{KK'}(P_\perp;\mu_h)\tilde{S}_{K'K}(b_*;\mu_{b_*})\\
&\times\exp\left[-\int_{\mu_{b_*}}^{\mu_j}\frac{d\mu}{\mu}\Gamma_\mu^{J_c}(\alpha_s)-\int_{\mu_{b_*}}^{\mu_{cs}}\frac{d\mu}{\mu}\Gamma_\mu^{cs_c}(\alpha_s)\right]U^c_{\rm NG}(\mu_{cs};\mu_j)\, J_c(P_\perp R;\mu_j)S_c^{\rm cs}(b_*,R;\mu_{cs})\\
&\times\exp\left[-\int_{\mu_{b_*}}^{\mu_j}\frac{d\mu}{\mu}\Gamma_\mu^{J_d}(\alpha_s)-\int_{\mu_{b_*}}^{\mu_{cs}}\frac{d\mu}{\mu}\Gamma_\mu^{cs_d}(\alpha_s)\right]U^d_{\rm NG}(\mu_{cs};\mu_j)\, J_d(P_\perp R;\mu_j)S_d^{\rm cs}(b_*,R;\mu_{cs})\\
&\times\exp\left[-S^s_{\rm NP}(b,\sqrt{\hat{s}},Q_0)-S^b_{\rm NP}(b,\sqrt{\hat{s}},Q_0)\right],
\end{aligned}\tag{4.211}$$

where at the NLL accuracy we keep the LO matching coefficient in Eq. 3.71. It involves the parametrization for the Sivers function, which depends on the collinear Qiu-Sterman function $T_{q,F}(x_a,x_a;\mu_{b_*})$ and a different non-perturbative Sudakov factor $S^s_{\rm NP}$. The relevant parametrization has been determined from a recent global analysis of the Sivers asymmetry of Semi-Inclusive DIS and Drell-Yan processes [10]. The non-perturbative Sudakov factor is given by

$$S^s_{\rm NP}(b,\mu,Q_0)=g_1^s b^2+\frac{g_2}{2}\ln\frac{\mu}{Q_0}\ln\frac{b}{b_*},\quad \text{with } g_1^s=0.18.\tag{4.212}$$

4.3.5 Phenomenology

In this section we will present the numerical results using the resummation formula in Eqs. (4.206) and (4.211), where intrinsic scales for the hard, jet and collinear-soft function are defined in Eq. (4.208). In the numerical study, we will focus on the Sivers asymmetry for the dijet production at the RHIC with $\sqrt{s}=200$ GeV, where the jet events are reconstructed

by using anti-k_T algorithm with jet radius $R = 0.6$. The transverse momentum $P_\perp$ and the rapidity $y_{c,d}$ of jets are

$$P_\perp > 4\,\text{GeV}, \quad -1 < y_{c,d} < 2. \tag{4.213}$$

For the unpolarized proton, we use the HERAPDF20NLO parton distribution functions [98]. The numerical Bessel transforms in Eqs. (4.206) and (4.211) are performed using the algorithm in [275]. Furthermore, the Eq. (4.96) is derived after neglecting the power corrections from $\mathcal{O}(q_\perp^2/P_\perp^2)$. In other words, in the large $q_\perp$ region, the full results should include corrections from the so-called Y-term, which can be obtained from perturbative QCD calculations [276]. In this section we focus on the contribution from back-to-back dijet production. In order to select such kinematics, we require the transverse momentum $q_\perp$ for the dijet system $|q_\perp| < q_\perp^{\text{cut}}$. In the numerical calculations, we fix the value of $q_\perp^{\text{cut}} = 2$ GeV.

As shown in the Fig. 4.7, the transverse-polarized proton moves on $+z$-direction and its spin points to $+y$-direction with $\phi_S = \pi/2$. The transverse momentum vector $\boldsymbol{q}_\perp$ lies in the $x-y$ plane, and the Sivers asymmetry is defined as the difference of the events between $q_{\perp,x} > 0$ and $q_{\perp,x} < 0$ hemispheres, that is the same as the measurements by STAR collaboration [228]. Explicitly, we have

$$A_N(y_{\text{sum}}) = \frac{\int_0^{q_\perp^{\text{cut}}} dq_\perp \int_0^{2\pi} d\phi_q \int d\mathcal{PS} \frac{d\Delta\sigma}{dq_\perp d\phi_q dy_c dy_d dP_\perp} \Big[\theta(\cos\phi_q) - \theta(-\cos\phi_q)\Big]}{\int_0^{q_\perp^{\text{cut}}} dq_\perp \int_0^{2\pi} d\phi_q \int d\mathcal{PS} \frac{d\sigma}{dq_\perp d\phi_q dy_c dy_d dP_\perp}}, \tag{4.214}$$

with $\int d\mathcal{PS} = \int dy_c dy_d dP_\perp \delta(y_{\text{sum}} - y_c - y_d)$ represents the transverse momenta and rapidities integral for dijets. In the numerator, the ϕ_q-integral with $\theta(\cos\phi_q)$ and $\theta(-\cos\phi_q)$ corresponds $q_{\perp,x} > 0$ and $q_{\perp,x} < 0$, respectively.

In the Fig. 4.12, we show the numerical results of the Sivers asymmetry for dijet processes, where we neglect the charm and bottom jet events. The red and blue curves represent the asymmetry contributed from u- and d-quark Sivers function, respectively. As is expected, we find that the asymmetry is enhanced in the large y_{sum} region, i.e. the forward scattering region, due to the larger fractional contribution of Sivers function in the valence region. Besides, the contributions from u- and d-quark Sivers function are opposite from each other, which causes a huge cancellation of the asymmetry, as shown by the black curves in Fig. 4.12.

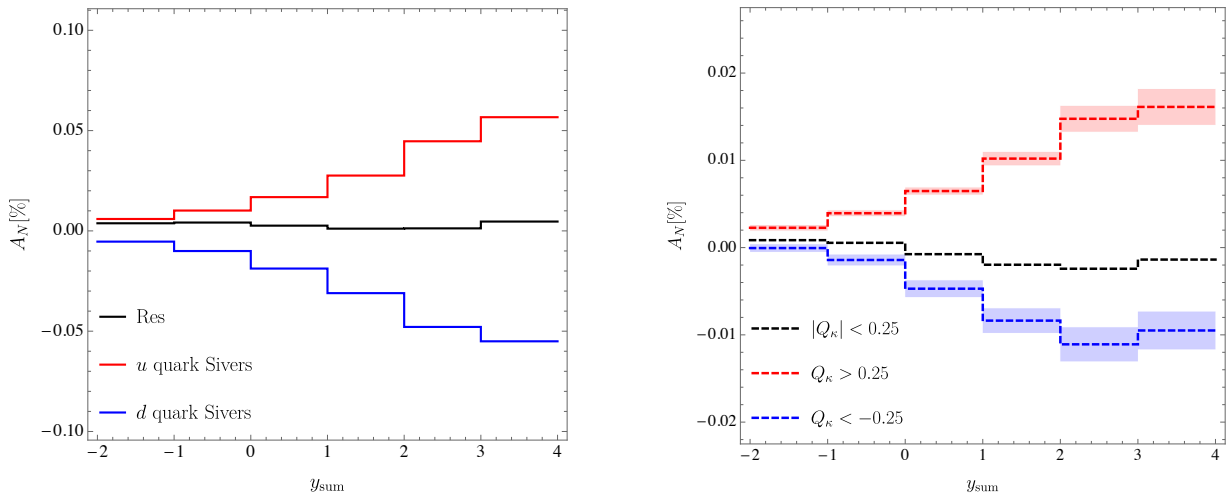

Figure 4.12: Theoretical predictions of the Sivers asymmetry for dijet production at the RHIC with $\sqrt{s} = 200$ GeV. In the left plot red and blue curves are the results from u- and d- quark Sivers function, and the black curve includes all the contributions. In the right plot we show the Sivers asymmetry distribution within three different jet charge Q_κ bins. The red and blue bands indicate the theoretical uncertainties using the 200 replicas of the quark Sivers function [10]. At each point in calculation of our theoretical prediction, we retain the middle 68% of the replicas.

In the calculation, most of the asymmetries come from the partonic scattering process $qg \to qg$ where the initial quark comes from the polarized proton. Especially, the more forward jet is associated with the parton from the polarized proton moving in the same direction. Hence, if we can tag parton species initiating the more forward jet, then we can separate u- and d-quark Sivers functions and avoid the accidental cancellation as shown in the left plot of Fig. 4.12.

In order to achieve jet flavor separation mentioned above, one possible method is applying the electric charge information of jets, which has been proposed in [277, 231, 237]. In this section, we will use the standard jet electric charge definition given in [278, 279]

$$Q_\kappa = \sum_{h \in \text{jet}} z_h^\kappa Q_h \,, \tag{4.215}$$

where z_h is the transverse momentum ratio between hadrons and the jet. κ is an input

parameter, which is fixed by $\kappa = 0.3$ [237] in our calculations. As shown in [237], after measuring the jet charge information, the theory formula is slightly modified by replacing the jet function $J_i(P_\perp R;\mu)$ in Eq. (4.101) by the charge-tagged jet function $\mathcal{G}_i(Q_\kappa, P_\perp R;\mu)$ as

$$\frac{d\Delta\sigma}{dQ_\kappa d^2q_\perp} = \int d\mathcal{P}\mathcal{S}\, T_{a,F}\otimes f_{b/P_B}\otimes \mathrm{Tr}[\boldsymbol{H}\cdot\boldsymbol{S}]\otimes S_c^{cs}\otimes S_d^{cs}\left[\mathcal{G}_c\, J_d\,\theta(y_c-y_d)+J_c\,\mathcal{G}_d\,\theta(y_d-y_c)\right], \tag{4.216}$$

with the normalization as $\int_{-\infty}^{\infty} dQ_\kappa\, \mathcal{G}_i(Q_\kappa, P_\perp R;\mu) = J_i(P_\perp R;\mu)$ required by the probability conservation. Here we only replace the more forward jet function with the charge-tagged jet function, which corresponds to the insertion of the step function. We define the jet charge bin fraction as

$$r_i^{\mathrm{bin}} = \frac{\int_{\mathrm{bin}} dQ_\kappa\, \mathcal{G}_i(Q_\kappa, P_\perp R;\mu)}{J_i(P_\perp R;\mu)}. \tag{4.217}$$

Then the Sivers asymmetry A_N in different jet charge bins is given as, in terms of jet charge bin fraction

$$A_N^{\pm,0} = \frac{\sum_{i=u,d,g,\cdots} r_i^{\pm,0}\Delta\sigma_i}{\sigma}, \tag{4.218}$$

where we suppress the phase space integral shown in Eq. (4.214). The index i denotes the parton species initiating the more forward jet. Here we use the same jet charge bins defined in [237], where $+,-$ and 0 indicate $Q_\kappa > 0.25, Q_\kappa < -0.25$ and $|Q_\kappa| < 0.25$ bins, separately. Such jet charge bin fraction can be fitted from the unpolarized cross section for back-to-back dijet events at the RHIC. In [231], the authors have shown the preliminary results from the measurements as $\kappa = 0$. In the theory calculation, one can use Monte-Carlo event generators such as Pythia8 [280] to estimate these numbers. In the Tab. 4.3 we give the results of jet charge bin fractions $r_i^{\pm,0}$ for various jet flavors used in our numerical calculations, where the jet charges are defined using all charged hadrons inside the jet.

In the right plot of Fig. 4.12 we show the result of A_N within the different jet charge bins. After selecting the charge of the more forward jet $Q_\kappa > 0.25$, the contribution from the u-quark Sivers function is enhanced compared to the case without the jet charge measurement

	u	$\bar{u}$	d	$\bar{d}$	s	$\bar{s}$	g
r_i^+	0.61	0.16	0.15	0.51	0.15	0.50	0.37
r_i^-	0.10	0.54	0.48	0.14	0.49	0.16	0.37
r_i^0	0.29	0.30	0.37	0.35	0.36	0.34	0.26

Table 4.3: The jet charge bin fractions $r_i^{\pm,0}$ for various jet flavors from Pythia8 simulation, where the jet charges are defined using all charged-hadrons inside the jet.

(the black curve in the left plot). A similar size enhancement from the d-quark Sivers function is also observed in $Q_\kappa < -0.25$ charge bin as shown by the blue curve. Besides, we find the Sivers asymmetries from $Q_\kappa > 0.25$ bins are positive and $Q_\kappa < -0.25$ bins are negative, which are consistent with the preliminary STAR measurements [231]. In the forward region, the Sivers asymmetry can achieve $\mathcal{O}(0.01\%)$, and size of our calculation is also around the same order of the data. Furthermore, we have also plotted the theoretical uncertainty which is related to the extraction of the Sivers function obtained in [10]. To generate this uncertainty, we have considered the 200 replicas from this reference. For each replica, we generate our theoretical prediction. We then retain the middle 68% at each point. We plot the uncertainty as red and blue bands for the positive and negative jet charge bins in the Fig. 4.12, respectively. Taken together, our calculation suggests that the dijet production at the hadron collider is an important process to extract the information about the Siver function and deserves further studies on the theoretical framework about the remarks discussed in 4.3.2.3.

4.3.6 Conclusions

We study the single spin asymmetries of dijet production in the back-to-back region in transversely polarized proton-proton collisions. In the back-to-back region, the dijet transverse momentum imbalance $q_\perp$ is much smaller than the transverse momentum $P_\perp$ of the jets. In this case, the conventional perturbative QCD calculations in the expansion of coupling constant α_s generate large logarithms in the form of $\alpha_s^n \ln^m (P_\perp^2/q_\perp^2)$ with $m \leq 2n-1$, which

have to be resummed in order to render the convergence of the perturbative computations. We propose a QCD formalism in terms of transverse momentum dependent (TMD) parton distribution functions for dijet production in both unpolarized and polarized proton-proton collisions. Such a formalism allows us to resum the aforementioned large logarithms, and further takes into account the non-universality or process-dependence of the Sivers functions in the case of the transversely polarized scattering. It is well-known that hadronic dijet production in back-to-back region suffers from TMD factorization breaking effects. Thus, to write down the QCD "seemingly factorized" formalism for resumming large logarithms mentioned above, we make a couple of approximations. First of all, we neglect the Glauber mode in the formalism which are known to be the main reason for the TMD factorization breaking. Secondly, we have assumed that the soft gluon radiation that is encoded in the global soft function in our formalism is spin-independent, i.e., they are the same between the unpolarized and polarized scatterings. Since the precise method for dealing with the TMD factorization breaking effects is still not known, we feel that the proposed formalism in this section is a reasonable starting point for further investigation.

With such a formalism at hand, we compute the Sivers asymmetry for the dijet production in the kinematic region that is relevant to the proton-proton collisions at the Relativistic Heavy Ion Collider (RHIC), and find that the spin asymmetry is very small due to the cancellation between u- and d-quark Sivers functions, which are similar in size but opposite in sign. However, we find that the individual contribution from u- and d-quark Sivers functions can lead to an asymmetry of size $\mathcal{O}(\pm 0.05\%)$ in the forward rapidity region, which seems feasible at the RHIC. Motivated by this, we compute the Sivers asymmetry of dijet production in the positive and negative jet charge bins, i.e., when the jet charge Q_κ for the jet with the larger rapidity of two is in the bins $Q_\kappa > 0.25$ and $Q_\kappa < -0.25$, respectively. By selecting the positive (negative) jet charge bin, we enhance the contribution from u- (d)-quark Sivers function and thus enhance the size of the asymmetry. Our calculation shows that Sivers asymmetries in such positive (negative) jet charge bins lead to asymmetries of size $\mathcal{O}(+0.01\%)$ ($\mathcal{O}(-0.01\%)$), respectively. The sign of such asymmetries seem to be consistent

with the preliminary STAR measurements at the RHIC. The size of our calculations is also around the same order of the experimental data. This give us a great hope to further investigate the single spin asymmetries for hadronic dijet production at the RHIC.

4.4 Jet fragmentation functions for Z-tagged jets

4.4.1 Introduction

The momentum distribution of hadrons inside a fully reconstructed jet, commonly referred to as jet fragmentation function (JFF), serves as a novel way of probing fragmentation. Recently, jet fragmentation functions have been measured for single inclusive jet produced in unpolarized proton-proton collisions at the Large Hadron Collider (LHC) for light hadrons [281, 282], for open heavy flavor mesons [283, 284, 285], and for heavy quarkonium [286, 287]. Such measurements have already started to constrain the fragmentation functions for open heavy flavor mesons [288, 289], and to pin down non-relativistic QCD (NRQCD) long-distance matrix elements, which characterize the hadronization process for heavy quarkonium production [290, 291].

The same measurements in heavy ion collisions show a strong modification of the JFF [292, 293] in the existence of the hot and dense medium, the quark-gluon plasma, and thus serve as a novel probe for the medium. Jet fragmentation functions can also be measured in transversely polarized proton-proton collisions. For example, the measurements by the STAR collaboration at the Relativistic Heavy Ion Collider (RHIC) study the azimuthal distribution of hadrons inside the jet [214] and provide information for the so-called Collins fragmentation functions [140, 294, 295].

Single inclusive jet production at the LHC involves a large fraction of gluon jets [296]. In order to further disentangle quark and gluon jets, one can study e.g., photon-tagged jet production and the JFF in photon-tagged jets. These processes are more sensitive to the quark jets, or quark-to-hadron fragmentation functions. See [293] for recent JFF measurement for photon-tagged jets. More recently the LHCb collaboration at the LHC has measured both

longitudinal and transverse momentum distribution of charged hadrons produced inside Z-tagged jets in the forward rapidity region in proton-proton collisions, $p + p \to Z + \text{jet} + X$. Experimental requirements are placed on the Z-jet pair to better identify events that correspond to a two-to-two partonic hard scattering process, i.e. the Z-jet pair is required to be nearly back-to-back in azimuth such that $|\Delta\phi_{Z-\text{jet}}| > 7\pi/8$. In our previous work [135], we developed a factorized framework for back-to-back photon-jet production within Soft-Collinear Effective Theory (SCET) [54, 55, 53, 56, 239]. Such a framework can be generalized to study back-to-back Z-jet production [164], as well as JFF in Z-tagged jets.

In this paper, we use SCET to derive a factorization and resummation formalism for JFF in which

the longitudinal momentum fraction z_h of the jet carried by the hadron and the transverse momentum $j_\perp$ with respect to the jet direction. We demonstrate how the z_h-dependence is connected to the standard collinear fragmentation functions, while the $j_\perp$-dependence is associated with the transverse momentum dependent (TMD) fragmentation functions. For the phenomenology, we find good agreement for the intermediate z_h region. For $j_\perp$-dependence, we suggest binning in both z_h and $j_\perp$, which would lead to a more direct probing of TMD fragmentation functions. The rest of the paper is organized as follows. In Sec. 4.4.2, we generalize our QCD formalism developed for photon-jet production to describe back-to-back Z-jet cross section, as well as the jet fragmentation functions in Z-tagged jets. Numerical results are presented in Sec. 4.4.3, where we compare our calculations with the LHCb experimental data. We conclude our paper in Sec. 4.4.4.

4.4.2 Theoretical framework

We consider hadron distribution inside Z-tagged jets in proton-proton collisions, as illustrated in Fig. 4.13,

$$p(p_A) + p(p_B) \to Z(\eta_Z, \boldsymbol{p}_{ZT}) + \text{jet}(\eta_J,\ \boldsymbol{p}_{JT}, R)\ h(z_h, \boldsymbol{j}_\perp) + X\,, \tag{4.219}$$

where $s = (p_A + p_B)^2$ is the center-of-mass energy squared, the Z-boson is produced with the rapidity η_Z and transverse momentum $\boldsymbol{p}_{ZT}$, while the jet is reconstructed in the usual anti-k_T algorithm [193] with the jet radius parameter R, and the jet has the rapidity η_J and the transverse momentum $\boldsymbol{p}_{JT}$. One further observes a hadron inside the jet, which carries a longitudinal momentum fraction z_h of the jet, and a transverse momentum $\boldsymbol{j}_\perp$ with respect to the jet direction.

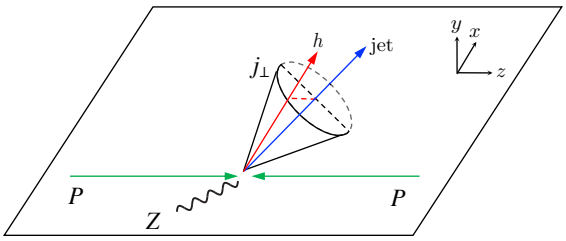

Figure 4.13: Illustration for the distribution of hadrons inside jets in Z-tagged jet production in proton-proton collisions.

One usually defines the imbalance $\boldsymbol{q}_T$ between the transverse momenta of the Z-boson and the jet, and the average of the transverse momenta $\boldsymbol{p}_T$ as

$$\boldsymbol{q}_T \equiv \boldsymbol{p}_{ZT} + \boldsymbol{p}_{JT}, \qquad \boldsymbol{p}_T = \frac{\boldsymbol{p}_{ZT} - \boldsymbol{p}_{JT}}{2}. \tag{4.220}$$

To be consistent with the experimental setup [11], we only consider the region where the Z-boson and the jet are produced back-to-back. In such a region, the imbalance is much smaller than the average transverse momentum, $q_T \ll p_T$, where the perturbative computations receive contributions of large logarithms of the form $\alpha_s^n \ln^{2n}(p_T/q_T)$, which have to be resummed. In the following, we first review the QCD formalism that achieves this purpose. We then generalize to the case of hadron distribution inside the jets, for both longitudinal z_h-distribution and the transverse momentum $j_\perp$-distribution.

4.4.2.1 Ztagged jet cross section

A formalism has been developed to resum the logarithms of the form $\alpha_s^n \ln^{2n}(p_T/q_T)$ as well as the logarithms of jet radius $\ln R$ in our previous work [135] for back-to-back photon-

tagged jet cross section. This formalism can be generalized to the Z-tagged jet production, $p + p \to Z + \text{jet} + X$.

In such a formalism, the differential cross section can be written as

$$\begin{aligned}\frac{d\sigma}{d\mathcal{PS}} =& \sum_{a,b,c} \int d\phi_J \int \prod_{i=1}^{4} d^2\boldsymbol{k}_{iT} \delta^{(2)} \left(\boldsymbol{q}_T - \sum_i^4 \boldsymbol{k}_{iT} \right) \\ & \times f_{a/p_a}^{\text{unsub}}(x_a, k_{1T}; \mu, \zeta_1/\nu^2) f_{b/p_B}^{\text{unsub}}(x_b, k_{2T}; \mu, \zeta_2/\nu^2) \\ & \times S_{n\bar{n}n_J}^{\text{global}}(\boldsymbol{k}_{3T}; \mu, \nu) S_{n_J}^{cs}(\boldsymbol{k}_{4T}, R; \mu) H_{ab\to cZ}(p_T, m_Z; \mu)\, J_c(p_{JT}R; \mu)\,, \end{aligned} \tag{4.221}$$

where the phase space $d\mathcal{PS} = d\eta_J d\eta_Z dp_T d^2\boldsymbol{q}_T$, and ϕ_J is the azimuthal angle of the jet. Besides different hard functions $H_{ab\to cZ}$, the above formalism is the same as that for photon-tagged jet production developed in [135]. See also Ref. [164], where the authors further study the impact of the so-called non-global logarithms [162].

We include both partonic channels $q\bar{q} \to gZ$ and $qg \to qZ$ at the next-to-leading order (NLO) for the hard functions $H_{ab\to cZ}$ [297, 178].

Let us now discuss the jet function J_c, which encodes collinear radiations inside the jet. The NLO results for quark and gluon jet functions can be found in e.g. [270, 271]. For completeness, the quark jet function J_q for anti-k_T algorithm is given by

$$J_q(p_{JT}R; \mu) = 1 + \frac{\alpha_s}{\pi} C_F \left(L_{\text{JT}}^2 - \frac{3}{2} L_{\text{JT}} + \frac{13}{4} - \frac{3\pi^2}{8} \right), \tag{4.222}$$

where L_{JT} is the logarithm defined as

$$L_{\text{JT}} = \ln\left(\frac{p_{JT}R}{\mu} \right). \tag{4.223}$$

Thus the natural scale of the jet function is given by

$$\mu_J \sim p_{JT}R. \tag{4.224}$$

At the same time, the jet function satisfies the renormalization group equation

$$\mu \frac{d}{d\mu} J_i(p_{JT}R; \mu) = \gamma_J^i(\mu)\, J_i(p_{JT}R; \mu), \tag{4.225}$$

which leads to the following solution

$$J_i(p_{JT}R;\mu) = J_i(p_{JT}R;\mu_J)\exp\left[\int_{\mu_J}^{\mu}\frac{d\mu'}{\mu'}\gamma_J^i(\mu')\right], \tag{4.226}$$

with $i = q, g$ for quark and gluon jets. The anomalous dimensions γ_J^i are given by

$$\gamma_J^i(\mu) = -2\,\Gamma^i_{\rm cusp}(\alpha_s)\,L_{\rm JT} + \gamma^i(\alpha_s), \tag{4.227}$$

with $\Gamma^i_{\rm cusp}$ and γ^i the cusp and non-cusp anomalous dimensions. They have the perturbative expansions $\Gamma^i_{\rm cusp} = \sum_n \Gamma^i_{n-1}\left(\frac{\alpha_s}{4\pi}\right)^n$ and $\gamma^i = \sum_n \gamma^i_{n-1}\left(\frac{\alpha_s}{4\pi}\right)^n$ [298, 299, 300, 301, 302]. For example,

$$\Gamma^q_0 = 4C_F, \qquad \gamma^q_0 = 6C_F, \tag{4.228}$$

$$\Gamma^g_0 = 4C_A, \qquad \gamma^g_0 = 2\beta_0, \tag{4.229}$$

where $\beta_0 = \frac{11}{3}C_A - \frac{4}{3}T_F n_f$, with $T_F = \frac{1}{2}$ and n_f the number of active quark flavors.

4.4.2.2 Hadron distribution inside Ztagged jets: $z_h$dependence

Now if we measure the longitudinal (along the jet direction) z_h distribution of hadrons inside the Z-tagged jet, the factorized formalism can be written as

$$\begin{aligned}\frac{d\sigma^h}{d\mathcal{P}\mathcal{S}\,dz_h} =& \sum_{a,b,c}\int d\phi_J \int\prod_{i=1}^{4} d^2\boldsymbol{k}_{iT}\,\delta^{(2)}\left(\boldsymbol{q}_T - \sum_i^4 \boldsymbol{k}_{iT}\right)\\ &\times f^{\rm unsub}_{a/p_a}(x_a, k_{1T};\mu,\zeta_1/\nu^2) f^{\rm unsub}_{b/p_B}(x_b, k_{2T};\mu,\zeta_2/\nu^2)\\ &\times S^{\rm global}_{n\bar{n}n_J}(\boldsymbol{k}_{3T};\mu,\nu) S^{cs}_{n_J}(\boldsymbol{k}_{4T}, R;\mu) H_{ab\to cZ}(p_T, m_Z;\mu)\,\mathcal{G}^h_c(z_h, p_{JT}R;\mu)\,,\end{aligned} \tag{4.230}$$

where we replace the jet function J_c in Eq. (4.221) by the fragmenting jet function $\mathcal{G}^h_c$ [288, 300]. Here $z_h = p_h^+/p_J^+$, with p_h^+ and p_J^+ the large light-cone component of the hadron and the jet, respectively. The fragmenting jet function $\mathcal{G}^h_i$ will no longer be purely perturbative since it involves the hadron in the jet, which is non-perturbative. However, $\mathcal{G}^h_i$ can be matched onto the standard collinear fragmentation functions (FFs) $D_{h/i}$,

$$\mathcal{G}^h_i(z_h, p_{JT}R;\mu) = \sum_j \int_{z_h}^1 \frac{dz}{z}\mathcal{J}_{ij}(z, p_{JT}R;\mu)\,D_{h/j}\left(\frac{z_h}{z};\mu\right), \tag{4.231}$$

where one can find the coefficients $\mathcal{J}_{ij}$ at NLO in [288, 279]. For later convenience, let us reproduce the expression for $\mathcal{J}_{qq}$ here,

$$\mathcal{J}_{qq}(z, p_{JT}R; \mu) = \delta(1-z) \tag{4.232}$$
$$+ \frac{\alpha_s}{\pi} C_F \left[\delta(1-z) \left(L_{\rm JT}^2 - \frac{\pi^2}{24} \right) + \frac{1+z^2}{(1-z)_+} \left(L_{\rm JT} + \ln z \right) + \frac{1-z}{2} + (1+z^2) \left(\frac{\ln(1-z)}{1-z} \right)_+ \right] .$$

At the same time, it is important to realize that $\mathcal{G}_i^h$ follows the same renormalization group equation as the jet function J_i in Eq. (4.227),

$$\mu \frac{d}{d\mu} \mathcal{G}_i^h(z_h, p_{JT}R; \mu) = \gamma_J^i(\mu)\, \mathcal{G}_i^h(z_h, p_{JT}R; \mu) \,, \tag{4.233}$$

which would evolve $\mathcal{G}_i^h$ from its natural scale, again $\mu_J \sim p_{JT}R$, up to the hard scale μ as

$$\mathcal{G}_i^h(z_h, p_{JT}R; \mu) = \mathcal{G}_i^h(z_h, p_{JT}R; \mu_J) \exp\left[\int_{\mu_J}^{\mu} \frac{d\mu'}{\mu'} \gamma_J^i(\mu') \right] . \tag{4.234}$$

4.4.2.3 Hadron distribution inside Ztagged jets: $j_\perp$dependence

Finally if we measure both the longitudinal z_h and transverse momentum $j_\perp$ distribution of hadrons inside the Z-tagged jet, the factorized formalism can be written as

$$\frac{d\sigma^h}{d\mathcal{P}\mathcal{S}\, dz_h\, d^2\boldsymbol{j}_\perp} = \sum_{a,b,c} \int d\phi_J \int \prod_{i=1}^{4} d^2\boldsymbol{k}_{iT} \delta^{(2)} \left(\boldsymbol{q}_T - \sum_i^4 \boldsymbol{k}_{iT} \right)$$
$$\times f_{a/p_a}^{\rm unsub}(x_a, k_{1T}; \mu, \zeta_1/\nu^2) f_{b/p_B}^{\rm unsub}(x_b, k_{2T}; \mu, \zeta_2/\nu^2)$$
$$\times S_{n\bar{n}\bar{n}_J}^{\rm global}(\boldsymbol{k}_{3T}; \mu, \nu) S_{n_J}^{cs}(\boldsymbol{k}_{4T}, R; \mu) H_{ab\to cZ}(p_T, m_Z; \mu)\, \mathcal{G}_c^h(z_h, \boldsymbol{j}_\perp, p_{JT}R; \mu, \zeta_3) \,, \tag{4.235}$$

where this time we have a TMD fragmenting jet function $\mathcal{G}_c^h$, and $\boldsymbol{j}_\perp$ is the transverse component of the hadron momentum with respect to the jet direction. We are interested in the small $j_\perp$ region, $j_\perp \ll p_{JT}R$, where $\mathcal{G}_c^h$ receives contributions from both collinear, and collinear-soft modes [303]. It can be further factorized as [303, 136]

$$\mathcal{G}_i^h(z_h, \boldsymbol{j}_\perp, p_{JT}R; \mu, \zeta_3) = \int d^2\boldsymbol{k}_\perp d^2\boldsymbol{\lambda}_\perp \delta^2\left(z_h\boldsymbol{\lambda}_\perp + \boldsymbol{k}_\perp - \boldsymbol{j}_\perp \right)$$
$$\times D_{h/i}^{\rm unsub}(z_h, \boldsymbol{k}_\perp; \mu, \zeta_3/\nu^2) S_i(\boldsymbol{\lambda}_\perp; \mu, \nu R),$$

where the collinear mode is described by the usual TMD FFs $D_{h/i}$, and the collinear-soft mode is captured by the soft function S_i. Besides the usual renormalization scale μ, the scale ν is again associated with the rapidity divergence. Here it might be instructive to point out the difference between the above refactorization and those for TMD hadron distribution inside a single inclusive jet produced in proton-proton collisions, $p+p \to \text{jet}+h+X$, in [136], where an additional hard factor arises that captures out-of-jet radiation with characteristic scale $\sim p_{JT}R$. Here since we are studying Z+jet production in the back-to-back region, such out-of-jet radiation is not allowed at leading-power. This is because any out-of-jet radiation would generate Z-jet imbalance of the order $p_{JT}R \gg q_T$, which would thus move Z-jet away from the back-to-back configuration.

Following the usual wisdom in TMD physics, we transform the above expression in the transverse momentum space into the coordinate $\boldsymbol{b}$-space as follows

$$\mathcal{G}_i^h(z_h, \boldsymbol{j}_\perp, p_{JT}R; \mu, \zeta_3) = \int \frac{d^2\boldsymbol{b}}{(2\pi)^2}\, e^{i\boldsymbol{j}_\perp\cdot\boldsymbol{b}/z_h} D_{h/i}^{\text{unsub}}(z_h, \boldsymbol{b}; \mu, \zeta_3/\nu^2) S_i(\boldsymbol{b}; \mu, \nu R), \tag{4.236}$$

where the Fourier transform is defined as follows

$$D_{h/i}^{\text{unsub}}(z_h, \boldsymbol{b}; \mu, \zeta_3/\nu^2) = \frac{1}{z_h^2}\int d^2\boldsymbol{k}_\perp e^{-i\boldsymbol{k}_\perp\cdot\boldsymbol{b}/z_h} D_{h/i}^{\text{unsub}}(z_h, \boldsymbol{k}_\perp; \mu, \zeta_3/\nu^2)\,, \tag{4.237}$$

$$S_i(\boldsymbol{b}; \mu, \nu R) = \int d^2\boldsymbol{\lambda}_\perp e^{-i\boldsymbol{\lambda}_\perp\cdot\boldsymbol{b}} S_i(\boldsymbol{\lambda}_\perp; \mu, \nu R)\,. \tag{4.238}$$

The perturbative results up to next-to-leading order and the renormalization for both $D_{h/i}^{\text{unsub}}$ and S_i have been carefully studied in [136]. Over there we define the "proper" in-jet TMD fragmentation function $\mathcal{D}_{h/i}^R$ as

$$\mathcal{D}_{h/i}^R(z_h, \boldsymbol{b}; \mu, \zeta_3) = D_{h/i}^{\text{unsub}}(z_h, \boldsymbol{b}; \mu, \zeta_3/\nu^2) S_i(\boldsymbol{b}; \mu, \nu R)\,, \tag{4.239}$$

where the rapidity divergence cancels between $D_{h/i}^{\text{unsub}}$ and S_i, and thus there is no rapidity divergence and thus no ν-dependence on the left-hand side. We also find that $\mathcal{D}_{h/i}^R$ evolves as follows

$$\mathcal{D}_{h/i}^R(z_h, \boldsymbol{b}; \mu, \zeta_3) = \hat{\mathcal{D}}_{h/i}(z_h, \boldsymbol{b}; \mu_J, \zeta_3) \exp\left[\int_{\mu_J}^{\mu} \frac{d\mu'}{\mu'}\left(-2\Gamma_{\text{cusp}}^i(\alpha_s) L_{\text{JT}} + \gamma^i(\alpha_s)\right)\right],$$

$$=\hat{\mathcal{D}}_{h/i}(z_h, \boldsymbol{b}; \mu_J, \zeta_3) \exp\left[\int_{\mu_J}^{\mu} \frac{d\mu'}{d\mu'} \gamma_J^i(\mu')\right] . \tag{4.240}$$

where the equation holds when $\mu_J = p_{JT}R$, and $\hat{\mathcal{D}}_{h/i}$ are the "properly"-defined TMD FFs, i.e., those measured in semi-inclusive deep inelastic scattering and/or back-to-back hadron pair production in e^+e^- collisions [36]. Plug this result into Eq. (4.236), we obtain

$$\begin{aligned}\mathcal{G}_i^h(z_h, \boldsymbol{j}_\perp, p_{JT}R; \mu, \zeta_3) =& \left[\int \frac{d^2\boldsymbol{b}}{(2\pi)^2} e^{i\boldsymbol{j}_\perp\cdot\boldsymbol{b}/z_h} \hat{\mathcal{D}}_{h/i}(z_h, \boldsymbol{b}; \mu_J, \zeta_3)\right] \exp\left[\int_{\mu_J}^{\mu} \frac{d\mu'}{d\mu'} \gamma_J^i(\mu')\right] , \\ \equiv& \hat{\mathcal{D}}_{h/i}(z_h, \boldsymbol{j}_\perp; \mu_J, \zeta_3) \exp\left[\int_{\mu_J}^{\mu} \frac{d\mu'}{d\mu'} \gamma_J^i(\mu')\right] . \end{aligned} \tag{4.241}$$

One of the most important observations is that the evolution factor, i.e., the exponential part on the right-hand side is the same for the jet function J_i in Eq. (4.226), the fragmenting jet function $\mathcal{G}_i^h$ in Eq. (4.234), and the TMD fragmenting jet function $\mathcal{G}_i^h$ in Eq. (4.241). In other words, the renormalization group equation is the same for all of them. This is consistent with the factorized formalism, since the rest of the factors are the same for all three cases in Eqs. (4.221), (4.230), and (4.235). This factor is different from the hadron distribution inside jets for single inclusive jet production, as extensively studied in e.g. Refs. [290, 296, 136, 304, 305]. For single inclusive jet production, the renormalization group equations for the relevant jet functions follow time-like DGLAP equations.

For the proper TMD fragmentation functions $\hat{\mathcal{D}}_{h/i}$, we use the same parametrization as in [136],

$$\begin{aligned}\hat{\mathcal{D}}_{h/i}(z_h, \boldsymbol{j}_\perp; \mu_J, \zeta_3) =& \frac{1}{z_h^2} \int \frac{bdb}{2\pi} J_0(j_\perp b/z_h) \\ & \times C_{j\leftarrow i} \otimes D_{h/j}(z_h; \mu_{b_*}) e^{-S^i_{\rm pert}(b;\mu_{b_*},\mu_J,\mu^2_{b_*},\mu^2_J) - S^i_{\rm NP}(z_h,b,\mu_J,Q_0)} , \end{aligned} \tag{4.242}$$

where we have used so-called b_*-prescription to avoid Landau pole of strong coupling α_s [306], $C_{j\leftarrow i}$ are the coefficient functions, $S^i_{\rm pert}$ is the perturbative Sudakov factor, and $S^i_{\rm NP}$ is the non-perturbative Sudakov factor. Their expressions are all given in [136], where TMD FFs are computed at next-to-leading order for $C_{j\leftarrow i}$ and at next-to-leading logarithmic level for $S^i_{\rm pert}$. The integration in Eq. (4.242) involves Bessel function J_0 which is oscillating and we thus have used an optimized Ogata quadrature method developed in [275] to handle the integration for better numerical convergence and reliability.

4.4.3 Phenomenology at the LHC

In this section, we present numerical results for hadron distribution inside Z-tagged jets in proton-proton collisions and compare to the experimental measurements by the LHCb collaboration at the LHC.

The LHCb collaboration has performed measurements for hadron distribution inside Z-tagged jets in proton-proton collisions at the center-of-mass energy $\sqrt{s} = 8$ TeV in the forward rapidity regions at the LHC. The jet rapidity is integrated over $2.5 < \eta_J < 4.0$, while the Z-boson rapidity is integrated over $2.0 < \eta_Z < 4.5$. The jets are reconstructed using the anti-k_T algorithm with a jet size parameter of $R = 0.5$ [11]. For the longitudinal distribution of hadrons inside jets, we define the jet fragmentation function as

$$F(z_h) = \frac{d\sigma^h}{d\mathcal{PS}\, dz_h} \Big/ \frac{d\sigma}{d\mathcal{PS}}\,, \tag{4.243}$$

where the numerator and the denominator are given by Eqs. (4.230) and (4.221), respectively, and we have suppressed the dependence on the rapidity and transverse momentum for both the Z-boson and the jet in $F(z_h)$. At the same time, for the $j_\perp$-dependence of the hadrons inside the jet, we define

$$F(z_h, j_\perp) = \frac{d\sigma^h}{d\mathcal{PS}\, dz_h dj_\perp} \Big/ \frac{d\sigma}{d\mathcal{PS}}\,. \tag{4.244}$$

Note that the numerator can be easily computed from Eq. (4.235), with the azimuthal angle of $\boldsymbol{j}_\perp$ integrated over, and further multiplied by a factor of $j_\perp$. In the numerical computations, we use NLO DSS fragmentation functions for charged hadrons from [307]. Other fragmentation functions such as NNFF1.1 [308] give similar results.

In Fig. 4.14, we plot $F(z_h)$ as a function of z_h. We make the default scale choices of $\mu = \sqrt{p_T^2 + m_Z^2}$ and $\mu_J = p_{JT}R$. We explore the scale uncertainty by varying μ and μ_J independently by a factor of two around their default values and by taking the envelope of these variations. From left to right, the three panels correspond to different jet transverse momenta: $20 < p_{JT} < 30$ GeV (left), $30 < p_{JT} < 50$ GeV (middle), and $50 < p_{JT} < 100$ GeV (right). We find that for the intermediate $0.1 \lesssim z_h \lesssim 0.5$, our results describe the LHCb

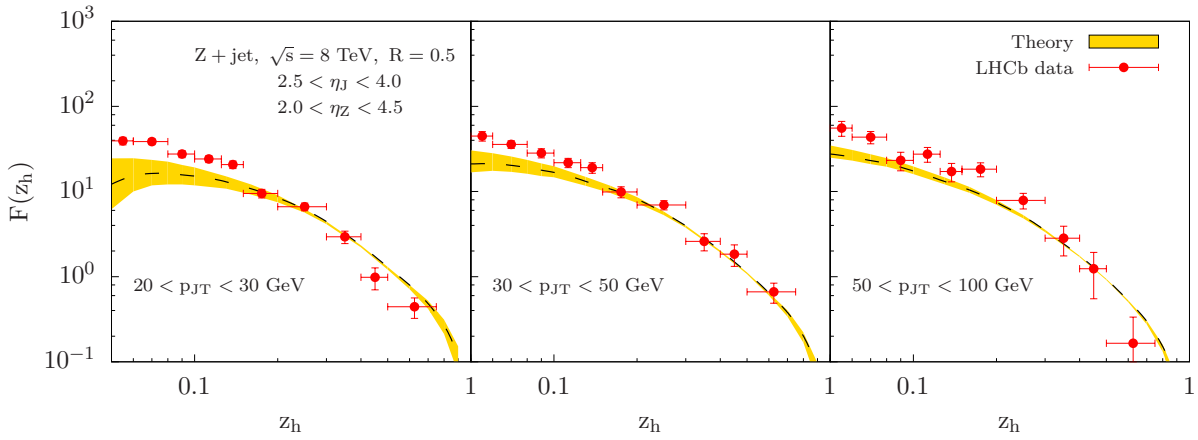

Figure 4.14: Hadron distributions inside Z-tagged jets $F(z_h)$ in Eq. (4.230) are plotted as functions of z_h. From left to right, the three panels correspond to different jet transverse momenta: $20 < p_{JT} < 30$ GeV, $30 < p_{JT} < 50$ GeV, and $50 < p_{JT} < 100$ GeV. The yellow band is the theoretical uncertainty from the scale variation as explained in the text. The red solid data points are from LHCb collaboration [11].

data reasonably well. However, when z_h is either very small ($z_h \ll 1$) or very large ($z_h \to 1$), the description becomes worse. This is easily understood. From Eqs. (4.230) and (4.232), the coefficient functions such as $\mathcal{J}_{qq}$ contains $\ln z$ and $\left(\frac{\ln(1-z)}{1-z}\right)_+$, which become important for $z \ll 1$ and $z \to 1$, respectively. Thus one has to resum such types of logarithms: one might follow [309] for $\ln z$ resummation, while for large-z one could get insights from [310]. We leave such studies for future publication.

For the $j_\perp$-distribution of hadrons inside Z-tagged jets, LHCb formally integrates over the entire $0 < z_h < 1$ region. [4] From Eq. (4.242), this would require that we know well the standard collinear fragmentation function $D_{h/i}$ for the entire $0 < z_h < 1$ region. However, typical global analysis for fragmentation functions only constrains the fragmentation functions for $z_h \gtrsim 0.05$. This fact thus hinders a more direct and transparent comparison between our theoretical calculations and the LHCb data, as we have observed previously [136] for hadron distribution in inclusive jet production. To help the situation, in Fig. 4.15 we

[4] There is a lower cut at a very small z_h, since LHCb only selects hadrons with $p_T^h > 0.25$ GeV.

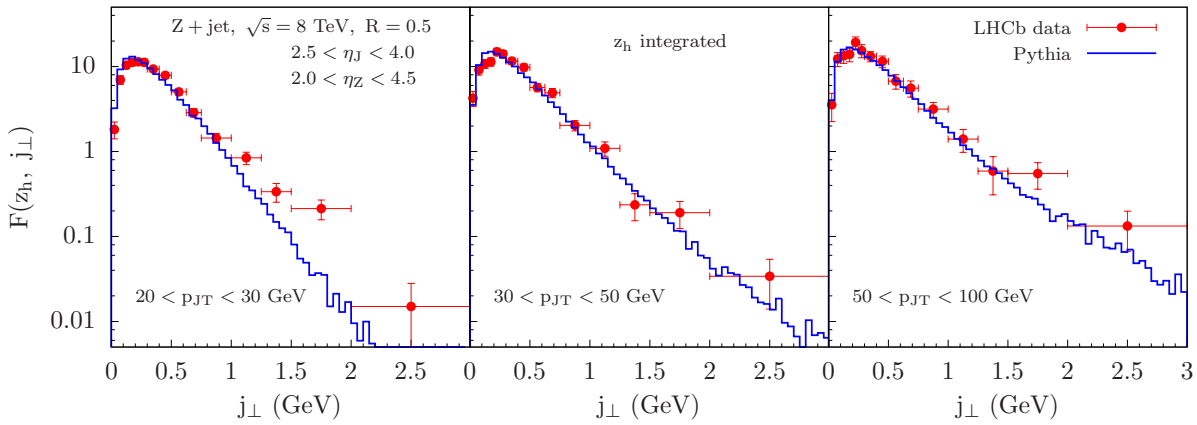

Figure 4.15: The comparison between the LHCb data (red solid points) and the Pythia simulation (blue histogram) for hadron $j_\perp$ distribution. We integrate over the entire z_h range.

make a comparison between the LHCb data and the Pythia 8 simulation [280]. In the Pythia simulation, we make the same cuts as in the experiments and integrate over the entire z_h range. As one can see clearly from Fig. 4.15, the Pythia simulation gives a good description for the hadron $j_\perp$-distribution in the small and intermediate region.

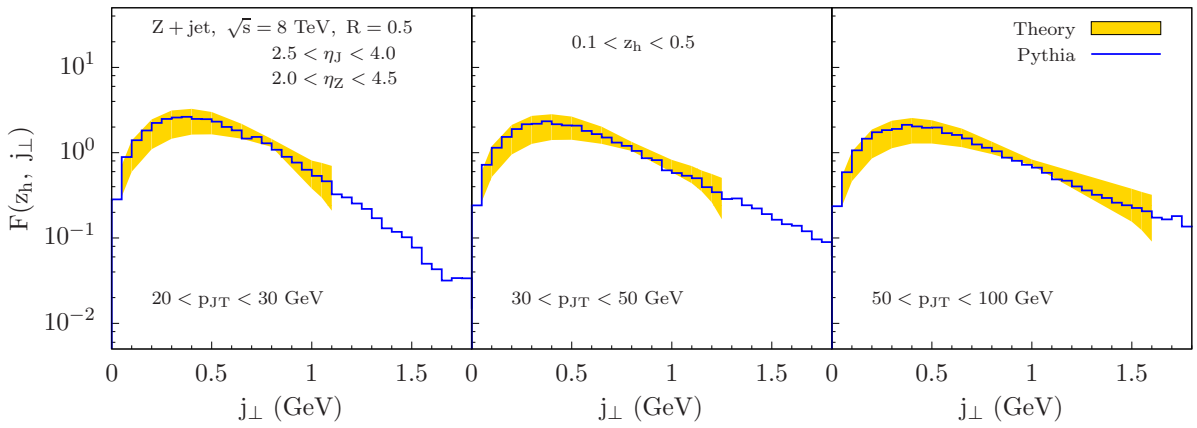

Figure 4.16: The comparison between our theoretical computations (yellow bands) and the Pythia simulation (blue histogram) for hadron $j_\perp$ distribution. We integrate z_h over the range $0.1 < z_h < 0.5$.

Since Pythia simulations give such good descriptions of the LHCb data on hadron $j_\perp$-dependence, we thus could use Pythia 8 to simulate the hadron $j_\perp$-dependence, integrated

for an appropriate z_h range, which is suitable for comparison with our theoretical results. With this in mind, we perform such Pythia simulations and integrate over $0.1 < z_h < 0.5$. The simulations are presented in blue histograms in Fig. 4.16. At the same time, we present our theoretical computations as yellow bands, which are generated the same as in Fig. 4.14, i.e., from the scale variation of μ and μ_J from their corresponding natural scales. We find that our TMD calculations agree well with the Pythia simulations. Note that our factorized formalism works only for the small $j_\perp \ll p_{JT}R$ region. For the relatively large $j_\perp$ region, one expects the so-called Y-term [36] to become important and has to be included to describe the data. This is why our theoretical curves stop at certain $j_\perp$ values.

4.4.4 Conclusion

We study back-to-back Z-jet production in proton-proton collisions at the LHC. In particular, we concentrate on the longitudinal z_h and transverse momentum $j_\perp$ distribution of hadrons inside Z-tagged jets. We find that the z_h-dependence is sensitive to the standard collinear fragmentation functions, while the $j_\perp$-dependence probes the transverse momentum dependent fragmentation functions (TMD FFs). The numerical calculations based on our theoretical formalism give good descriptions of the LHCb data for intermediate z_h region. For $j_\perp$-dependence, since the experimental data are integrated over the entire $0 < z_h < 1$ region, the direct comparison is nontrivial if not impossible. For integrating over the intermediate $0.1 < z_h < 0.5$ region, our results agree well with the Pythia simulations for the relatively small $j_\perp$ region. For future measurements, we suggest to set up the binning in both z_h and $j_\perp$, as this would lead to a more direct probing of TMD FFs. We expect our work to have important applications in studying fragmentation functions in vector-boson-tagged jet production in both proton-proton and nucleus-nucleus collisions.

CHAPTER 5

Lambda Baryons for Proton Structure

5.1 Introduction

We saw in the case of Semi-Inclusive DIS that in order to perform QCD tomography for the spin-dependent hadrons, that we needed to understand the hadronization effects. In principle to access the non-perturbative information for the full spin dependence of the proton in Semi-Inclusive DIS, one would also need to simultaneously understand the full spin dependence for hadronization. This is one of the reasons why hadronization has remained one of the most active and important areas of research in the field of nuclear physics, for recent reviews, see Refs [311, 312]. However, the primary issue with performing imaging for spin-dependent hadronization is that experimentalists need to be able to re-construct the spin of the polarized hadron, which introduces additional experimental uncertainties. However, it has been known for some time that Λ and $\bar{\Lambda}$ baryons, which I will collectively refer to as Λs, undergo self-analyzing decay. Namely these baryons decay as $\Lambda \to p + \pi$ and the momentum of the final-state proton is correlated with the direction of the spin. As a result, Λ baryons serve as our primary window into spin-dependent fragmentation. One of the primary goals of the future EIC [68, 313, 314] is to measure TMD FFs over wide kinematic regions at unprecedented experimental precision. In this paper, we aim to study the role that the future EIC can play in constraining TMD FFs which are associated with transversely polarized Λ production. While I focus on transverse polarization, in principle the same techniques can also be used for longitudinal TMD FFs as well, see for instance Ref. [315].

The BELLE collaboration recently measured the transverse polarization of the Λ in e^+e^-

annihilation [316]. They have measured such a polarization of both Λ and $\bar{\Lambda}$ in single Λ production (with respect to the thrust axis), $e^- + e^+ \to \Lambda/\bar{\Lambda} + X$, as well as in DIA. While the TMD factorization formalism exists for DIA [17, 36], single Λ production with respect to the thrust axis could involve a more complicated factorization structure [317], if the thrust variable is also measured. Nevertheless, there is an attempt at factorization within the standard TMD formalism [318] for single Λ production. This experimental data for DIA allowed for the phenomenological extractions of the TMD PFF in [319, 12, 320]. These extraction were a major goal of the TMD community, as it represents one of eight leading-twist TMDs for the TMD FFs, and thus provides three-dimensional imaging of hadrons in association with the fragmentation process.

The understanding of these spin-transverse momentum correlations gives rise to interesting phenomenological differences between TMD FFs and the TMD parton distribution functions (PDFs). To demonstrate this, let's examine the number density for a spin-dependent TMD PDF and TMD FF

$$\Phi^{\text{unsub}}\left(x, \boldsymbol{k}_\perp, \boldsymbol{S}; \mu, \zeta/\nu^2\right) = \left(f - \frac{\epsilon_\perp^{\rho\sigma} k_{\perp\rho} S_{\perp\sigma}}{M} f_{1T}^\perp\right) \frac{\not{\bar{n}}}{4} + \dots , \tag{5.1}$$

$$\Delta\left(z, \boldsymbol{p}_\perp, \boldsymbol{S}_h; \mu, \zeta/\nu^2\right) = \left(D - \frac{\epsilon_T^{\rho\sigma} p_{\perp\rho} S_{\perp\sigma}}{zM} D_{1T}^\perp\right) \frac{\not{n}}{4} + \dots . \tag{5.2}$$

In this expression, I have introduced the TMD PFF as $D_{1T}^\perp$. We can see from these two expressions that the TMD PFF is the analog of the Sivers function for hadronization, there is an unpolarized parton and a transversely polarized hadron. We saw previously that there was a sign change for the Sivers function between the Semi-Inclusive DIS and Drell-Yan processes [155, 156, 321]. As we previously discussed, this behavior occurred because the spin asymmetry for Sivers was generated due the soft poles of the three parton correlation function. The analog of these two processes for hadronization are Semi-Inclusive DIS and DIA. As a result, naively one would expect that the TMD PFFs should be opposite in Semi-Inclusive DIS and DIA. However, studies have shown that the TMD PFF is not generated by the appearance of a soft pole. As a result, the TMD PFF should be universal with respect to these two processes [322, 323, 324, 325]. The experimental verification of this fact is

vital for understanding the universality arguments of the TMD FFs. In fact, Ref. [325] has precisely suggested studies of both back-to-back $\Lambda + h$ production and Semi-Inclusive DIS to test the universality of the TMD PFFs. In this paper, we provide a prediction for the transverse polarization in Semi-Inclusive DIS, which can be used for the first experimental confirmation of the universality of the TMD PFFs.

While the Belle data can be used to obtain information for the TMD PFFs, the COMPASS collaboration performed recent measurements of the transverse spin transfer in Semi-Inclusive DIS for Λ production in Ref. [13]. In the transverse spin-transfer, a transverse quark leads to a correlation of the transverse spins of the incoming and outgoing hadrons. As a result, this process opens the possibility of performing the first extraction of the quark transversity TMD FF for Λ production. In addition, the STAR experiment also reported their measurements on transverse spin transfer for single inclusive $\Lambda/\bar{\Lambda}$ hyperon production in proton-proton collisions at $\sqrt{s} = 200$ GeV [326]. However, while the STAR measurement can be used as a probe of the collinear transversity PDF and transversity FF, the process is described by the collinear factorization formalism [327, 33] and not by the TMD factorization formalism.

While the future EIC offers the possibility of measuring spontaneous Λ polarization and the transverse spin transfer in Semi-Inclusive DIS, recently back-to-back electron-jet production in electron-proton, $e + p$, collisions has been explored as a probe of the TMD PDFs in Refs. [130, 163]. Furthermore, in Refs. [136, 328, 137] the authors discuss that by measuring the distribution of hadrons relative to the jet axis, one de-correlates the TMD FF in the TMD fragmenting jet function and the other TMDs in the process. As a result, in Ref. [142, 137], it was proposed to measure the distribution of hadrons in a jet in back-to-back electron-jet production as a probe of TMD FFs.

To address the role that the future EIC can play in constraining the TMD PFF, in this paper we perform an EIC impact study for the Semi-Inclusive DIS process in extracting the TMD PFF. In such a study, we will characterize the required luminosity for constraining these distributions. Furthermore, we use the recent COMPASS measurement for the trans-

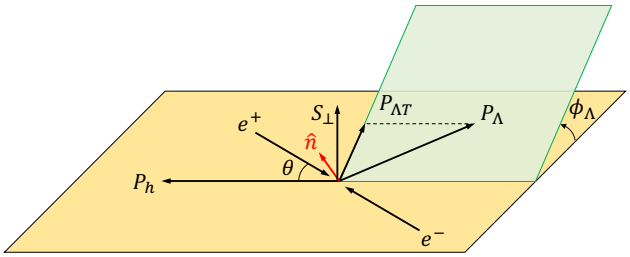

Figure 5.1: Kinematics of the leptonic center-of-mass frame for back-to-back two-hadron production in e^-e^+ annihilation, $e^- + e^+ \to h(P_h) + \Lambda(P_\Lambda) + X$.

verse spin transfer to perform the first extraction of the quark-to-Λ transversity TMD FF. Using this extraction, we compare our theoretical uncertainties against our projections for the statistical uncertainties at the future EIC. Finally, we also provide projections at the future EIC for back-to-back electron-jet production for both spontaneous Λ polarization in unpolarized ep collisions, as well as the transverse spin transfer in transversely polarized ep scattering.

This chapter is organized as follows. In 5.2.1 I provide the relevant formalism and detail the calculation of the Λ transverse polarization observable $P_\perp^\Lambda$ in DIA. In 5.2.2 I give the parametrization of our TMD PFFs and discuss the fit procedure, and fit results. In Sec. 5.3, I provide the formalism for Semi-Inclusive DIS and perform the first extraction of the transversity TMD FF. In Sec. 5.4.1, I provide the theoretical formalism for back-to-back electron-jet production. In Sec. 5.4.2, I provide the details for the simulated experimental setup. In Sec. 5.4.3, I provide the details and results of our EIC impact study for the TMD PFF. In Sec. 5.4.5 we provide our projections for spontaneous Λ in jet polarization as well as the transverse spin transfer. I summarize our findings and conclude in Sec. 5.5.

5.2 Global Analysis of the TMD PFF

5.2.1 Formalism

Let's begin by defining the momenta of the DIA process as

$$e^-(\ell) + e^+(\ell') \to \gamma^*(q) \to h(P_h) + \Lambda(P_\Lambda, \boldsymbol{S}_\perp) + X. \tag{5.3}$$

Following [329], we choose a leptonic center-of-mass frame where the light hadron P_h has no transverse momentum. The leptons and the light hadron form the so-called *leptonic plane*. The angle between P_h and $(\ell,\ \ell')$ is given by θ, as illustrated in Fig. 5.1. On the other hand, P_h and P_Λ span the so-called *hadronic plane*. In this frame, the Λ particle has transverse momentum $\boldsymbol{P}_{\Lambda T}$, at an azimuthal angle ϕ_Λ with respect to the leptonic plane. We have

$$\boldsymbol{P}_{\Lambda T} = -z_\Lambda \boldsymbol{q}_\perp, \tag{5.4}$$

where $\boldsymbol{q}_\perp$ is related to the "transverse" component of the virtual photon momentum, defined as

$$q_t^\mu = q^\mu - \frac{P_h \cdot q}{P_h \cdot P_\Lambda} P_\Lambda^\mu - \frac{P_\Lambda \cdot q}{P_\Lambda \cdot P_h} P_h^\mu, \tag{5.5}$$

with $q_\perp^2 = -q_t^\mu q_{t\mu}$. The expression for the QCD factorization formalism for the unpolarized differential cross is given by section [17, 325]

$$\frac{d\sigma}{d\mathcal{P}\mathcal{S} d^2\boldsymbol{q}_\perp} = \sigma_0 \, \mathcal{C}^{\mathrm{DIA}} \left[D_{\Lambda/q} D_{h/\bar{q}} \right] . \tag{5.6}$$

In the expression for the cross section, the point-like scattering cross section is given by

$$\sigma_0 = \frac{N_c \pi \alpha_{\mathrm{em}}^2}{2Q^2} \left(1 + \cos^2\theta\right) , \tag{5.7}$$

and $d\mathcal{P}\mathcal{S} = dz_\Lambda \, dz_h \, d(\cos\theta)$ is the phase space element. In this expression θ is the angle between P_h and ℓ' while the parton fraction variables are defined as

$$z_\Lambda = 2P_\Lambda \cdot q/Q^2, \qquad z_h = 2P_h \cdot q/Q^2. \tag{5.8}$$

The $\mathcal{C}^{\rm DIA}$ denotes the convolutional integral for DIA and is defined as

$$\mathcal{C}^{\rm DIA}\left[c\,A\,B\right] = H^{\rm DIA}(Q;\mu)\,z_\Lambda^2\,z_h^2\sum_q e_q^2\int d^2k_{h\perp}d^2k_{\Lambda\perp}\delta^{(2)}(\boldsymbol{k}_{\Lambda\perp}+\boldsymbol{k}_{h\perp}-\boldsymbol{q}_\perp)$$
$$\times\, c\left(z_h,z_\Lambda,\boldsymbol{k}_{h\perp},\boldsymbol{k}_{\Lambda\perp}\right)c\left(z_h,z_\Lambda,p_{h\perp},p_{\Lambda\perp}\right)A_{h/\bar{q}}\left(z_h,p_{h\perp};\mu,\zeta_1\right)\,B_{\Lambda/q}\left(z_\Lambda,p_{\Lambda\perp};\mu,\zeta_2\right)\,. \quad (5.9)$$

In this expression $H^{\rm DIA}$ is the hard contribution to the cross section and $Q^2=q^2$. I'll note however, that since the partonic cross section for DIA and Drell-Yan are identical that the hard functions for these processes are also equal. In this expression, I have introduced two TMD FFs, $D_{h/q}$ and $D_{\Lambda/q}$, which are the unpolarized TMD FFs for h and Λ, respectively. The $\boldsymbol{k}_{i\perp}$ with $i=h,\Lambda$ are the transverse momenta of the fragmenting quarks in the frame where the hadron has zero transverse momentum. Similarly, the $\boldsymbol{p}_{i\perp}$ are the transverse momenta of the hadrons in the frame where the fragmenting quarks have zero transverse momentum. These momenta are related to one another by $\boldsymbol{p}_{i\perp}=-z_i\boldsymbol{k}_{i\perp}$.

To obtain the cross section for the polarized process, we simply replace the unpolarized TMD FF for Λ with the spin-dependent density in Eq. 5.2. With the short-hand notation in Eq. 5.6, we have the expression for the transverse-spin dependent differential cross section

$$\frac{d\sigma(\boldsymbol{S}_\perp)}{d\mathcal{P}\mathcal{S}d^2\boldsymbol{q}_\perp} = \sigma_0\Big\{\mathcal{C}^{\rm DIA}\left[DD\right]+|\boldsymbol{S}_\perp|\sin(\phi_S-\phi_\Lambda)\frac{1}{z_\Lambda M_\Lambda}\mathcal{C}^{\rm DIA}\left[\hat{\boldsymbol{P}}_{\Lambda T}\cdot\boldsymbol{p}_{\Lambda\perp}D_{1T}^\perp D_h\right]+\cdots\Big\}\,, \quad (5.10)$$

where $\hat{\boldsymbol{P}}_{\Lambda T}=\boldsymbol{P}_{\Lambda T}/|\boldsymbol{P}_{\Lambda T}|$ is the unit vector along the transverse momentum of the Λ particle, as defined in Fig. 5.1.

In trying to connect the theoretical formalism above with the BELLE collaboration's experimental measurement of Λ polarization, one encounters several subtleties. First is the direction with respect to which BELLE measures Λ polarization. Defining $\boldsymbol{m}=-\hat{\boldsymbol{P}}_h$, with $\hat{\boldsymbol{P}}_h$ ($\hat{\boldsymbol{P}}_\Lambda$) the unit vector along the momentum of the hadron h (the Λ), we see that BELLE measures Λ polarization along the direction $\hat{\boldsymbol{n}}\propto\boldsymbol{m}\times\hat{\boldsymbol{P}}_\Lambda$, perpendicular to the hadronic plane in Fig. 5.1. On the other hand, the polarization vector $\boldsymbol{S}_\perp$ in the above formalism is transverse with respect to the leptonic plane in Fig. 5.1. Because of this, we need to perform an additional projection onto the $\hat{\boldsymbol{n}}$-direction.

Second of all, there are additional terms as denoted by "$\cdots$" in Eq. 5.10 [329]. One such term involves a convolution of transversity FFs $H_{1,\Lambda/q}(z_\Lambda, p_{\Lambda\perp}; Q, Q^2)$ for the Λ hadron with the Collins FFs $H^\perp_{1,h/\bar{q}}(z, p_{h\perp}; Q, Q^2)$ for the light hadron h. Such a term has an azimuthal dependence of $\sin(\phi_S + \phi_\Lambda)$. In principle, the optimal strategy to isolate, and thus extract unambiguously, the PFFs $D^\perp_{1T,\Lambda/q}$ would be to measure and disentangle all of these different azimuthal dependencies, just like in the usual Semi-Inclusive DIS spin measurements [86]. This has not yet been done by the BELLE collaboration. Surprisingly, though, if one integrates over $\boldsymbol{q}_\perp$ in the formalism, all the other terms vanish and we are left with only the term involving the PFF $D^\perp_{1T,\Lambda/q}$ for the spin-dependent cross section [1].

Since the experimental data are expressed only as a function of z_Λ and z_h, and are inclusive over $\boldsymbol{q}_\perp$, our analysis of the experimental data to extract the PFFs is thus justified. Eventually with the transverse momentum integrated, the measured Λ polarization denoted as $P^\Lambda_\perp$ will be given by

$$P^\Lambda_\perp(z_\Lambda, z_h) = \frac{d\Delta\sigma(\boldsymbol{S}_\perp)}{d\mathcal{PS}} \Big/ \frac{d\sigma}{d\mathcal{PS}}\,, \tag{5.11}$$

where $\Delta\sigma(\boldsymbol{S}_\perp) = [\sigma(\boldsymbol{S}_\perp) - \sigma(-\boldsymbol{S}_\perp)]/2$, and the denominator is the unpolarized cross section.

5.2.2 Fitting Procedure

In this section, we first provide the parametrization used for the extraction of polarizing fragmentation functions, and give an expression for the asymmetry $P^\Lambda_\perp(z_\Lambda, z_h)$ within our model. We then describe our fitting procedure and the fitted results. Finally, we make a prediction for the Λ polarization in semi-inclusive deep inelastic scattering.

5.2.2.1 Fitting scheme

All available data are measured at the same hard scale $Q = 10.58$ GeV at the BELLE experiment; thus, TMD evolution for the relevant TMD FFs is not needed. Because of this, we can model these TMD FFs using simple Gaussians and extract them at this particular

[1] We thank D. Boer and H. Matevosyan for very insightful communication concerning this point.

scale Q. We model the unpolarized TMD FFs as Gaussians

$$D_{h/q}(z_h, p_{h\perp}^2; Q, Q^2) = D_{h/q}(z_h; Q)\, \frac{e^{-p_{h\perp}^2/\langle p_{h\perp}^2\rangle}}{\pi\langle p_{h\perp}^2\rangle}, \tag{5.12}$$

$$D_{\Lambda/q}(z_\Lambda, p_{\Lambda\perp}^2; Q, Q^2) = D_{\Lambda/q}(z_\Lambda; Q)\, \frac{e^{-p_{\Lambda\perp}^2/\langle p_{\Lambda\perp}^2\rangle}}{\pi\langle p_{\Lambda\perp}^2\rangle}, \tag{5.13}$$

where we take $\langle p_{h\perp}^2\rangle = 0.19$ GeV^2 from [330] for the light hadrons h. For Λ, we assume $\langle p_{\Lambda\perp}^2\rangle = \langle p_{h\perp}^2\rangle$ in this paper. We model the polarizing fragmentation functions $D_{1T,\Lambda/q}^\perp$ according to the equation

$$D_{1T,\Lambda/q}^\perp(z_\Lambda, p_{\Lambda\perp}; Q, Q^2) = D_{1T,\Lambda/q}^\perp(z_\Lambda; Q)\frac{e^{-p_{\Lambda\perp}^2/\langle M_D^2\rangle}}{\pi\langle M_D^2\rangle}. \tag{5.14}$$

Here we write the polarized collinear function $D_{1T,\Lambda/q}^\perp(z_\Lambda; Q)$ simply as a modulation of the unpolarized collinear function $D_{\Lambda/q}(z_\Lambda; Q)$ by an additional collinear function $\mathcal{N}_q(z_\Lambda)$

$$D_{1T,\Lambda/q}^\perp(z_\Lambda; Q) = \mathcal{N}_q(z_\Lambda) D_{\Lambda/q}(z_\Lambda; Q)\,, \tag{5.15}$$

and we parametrize $\mathcal{N}_q(z_\Lambda)$ by the formula

$$\mathcal{N}_q(z_\Lambda) = N_q z_\Lambda^{\alpha_q}(1-z_\Lambda)^{\beta_q}\frac{(\alpha_q+\beta_q-1)^{\alpha_q+\beta_q-1}}{(\alpha_q-1)^{\alpha_q-1}\beta_q{}^{\beta_q}}. \tag{5.16}$$

The Gaussian width $\langle M_D^2\rangle$ differs from the unpolarized width $\langle p_{\Lambda\perp}^2\rangle$ by an auxiliary width M_1 obeying the equality [331, 220]

$$\langle M_D^2\rangle \equiv \left(\frac{1}{\langle p_{\Lambda\perp}^2\rangle} + \frac{1}{M_1^2}\right)^{-1} = \frac{M_1^2\langle p_{\Lambda\perp}^2\rangle}{M_1^2 + \langle p_{\Lambda\perp}^2\rangle}, \tag{5.17}$$

from which it is clear that M_1 characterizes the scale of spin corrections to $\langle p_{\Lambda\perp}^2\rangle$. We choose to fit $\langle M_D^2\rangle$ – of course, M_1 can be easily determined once $\langle M_D^2\rangle$ is known.

In order to maintain the interpretation of the spin-dependent fragmentation functions $\hat{D}_{\Lambda/q}(z, \boldsymbol{p}_{\Lambda\perp}, \boldsymbol{S}_\perp; Q, Q^2)$ as probability densities, the positivity bound

$$\frac{p_{\Lambda\perp}}{z_\Lambda M_\Lambda}\left|D_{1T,\Lambda/q}^\perp(z_\Lambda, p_{\Lambda\perp}^2; Q, Q^2)\right| \le D_{\Lambda/q}(z_\Lambda, p_{\Lambda\perp}^2; Q, Q^2) \tag{5.18}$$

given in [332, 311], must be satisfied. We thus implement the fit constraints

$$\alpha_q > 1\,,\ \beta_q > 0\,,\ \langle M_D^2\rangle < \langle p_{\Lambda\perp}^2\rangle\,, \qquad |N_q| \le \sqrt{2e}\frac{\langle M_D^2\rangle}{\langle p_{\Lambda\perp}^2\rangle}\frac{M_\Lambda}{M_1}\,, \tag{5.19}$$

which are sufficient conditions for the enforcement of the positivity bound. Moreover, it is useful to define the $p_{\Lambda\perp}$-moment of the TMD PFFs

$$\begin{aligned} D_{1T,\Lambda/q}^{\perp(1)}(z_\Lambda;Q) &\equiv \int d^2\boldsymbol{p}_{\Lambda\perp}\frac{p_{\Lambda\perp}}{2z_\Lambda^2 M_\Lambda^2}D_{1T,\Lambda/q}^{\perp}(z_\Lambda,p_{\Lambda\perp};Q,Q^2) \\ &= \frac{\langle M_D^2\rangle}{2z_\Lambda^2 M_\Lambda^2}D_{1T,\Lambda/q}^{\perp}(z_\Lambda;Q). \end{aligned} \tag{5.20}$$

Using our parametrization, all momenta can be integrated out analytically, so that the cross sections take on the forms

$$\frac{d\sigma}{d\mathcal{P}\mathcal{S}} = \sigma_0 H(Q)\sum_q e_q^2 D_{\Lambda/q}(z_\Lambda;Q)D_{h/\bar{q}}(z_h;Q), \tag{5.21}$$

$$\frac{d\Delta\sigma(\boldsymbol{S}_\perp)}{d\mathcal{P}\mathcal{S}} = \sigma_0 H(Q)\frac{z_h\sqrt{\pi}}{2z_\Lambda}\frac{\langle M_D^2\rangle}{M_\Lambda\sqrt{z_h^2\langle M_D^2\rangle + z_\Lambda^2\langle p_{h\perp}^2\rangle}}\sum_q e_q^2 D_{1T,\Lambda/q}^{\perp}(z_\Lambda;Q)D_{h/\bar{q}}(z_h;Q). \tag{5.22}$$

As such, we finally obtain the following expression for the Λ polarization $P_\perp^\Lambda(z_\Lambda,z_h)$ from Eq. 5.11,

$$P_\perp^\Lambda(z_\Lambda,z_h) = \frac{z_h\sqrt{\pi}}{2z_\Lambda}\frac{\langle M_D^2\rangle}{M_\Lambda\sqrt{z_h^2\langle M_D^2\rangle + z_\Lambda^2\langle p_{h\perp}^2\rangle}}\frac{\sum_q e_q^2 D_{1T,\Lambda/q}^{\perp}(z_\Lambda;Q)D_{h/\bar{q}}(z_h;Q)}{\sum_q e_q^2 D_{\Lambda/q}(z_\Lambda;Q)D_{h/\bar{q}}(z_h;Q)}. \tag{5.23}$$

To compute $P_\perp^\Lambda(z_\Lambda,z_h)$, we use the AKK08 parametrization [333] of the collinear Λ fragmentation functions. Currently, there are no available collinear fragmentation functions which separate the Λ and $\bar{\Lambda}$ contributions. While the work in [318] took $D_{\bar{\Lambda}/q} = D_{\Lambda/\bar{q}} = 0$ with $q = u,d,s$, this scheme does not adequately describe $\Lambda + h$ production. For example, in the $e^- + e^+ \to \Lambda + \pi^+ + X$ process, one of the dominant contributions to the cross-section is given by the $D_{\Lambda/\bar{u}}(z_\Lambda;Q)$. Since the work in [318] neglected all sea quark contributions, this would lead to a very small asymmetry, which conflicts with the BELLE data. For this paper, we assume $D_{\Lambda/q} = D_{\bar{\Lambda}/q} = \frac{1}{2}D_{\Lambda/\bar{\Lambda}\leftarrow q}$ for all quark flavors.

For the fragmentation functions of pions, we choose the DSS14 parametrization given in [99], which is an update of the previous DSS07 fragmentation functions [307]. As such an update is not available for kaons, we choose the DSS07 parametrizations for the fragmentation functions of kaons.

In order to fit the non-perturbative TMD PFFs $D_{1T,\Lambda/q}^{\perp}(z_\Lambda,p_{\Lambda\perp};Q,Q^2)$, we use the typical flavor-dependent parameters N_q, α_q, and β_q, similar to the parametrization used in [80] for

the Sivers functions. In this paper, for the polarization of the Λ, we fit the 11 parameters N_u, N_d, N_s, N_{sea}, α_u, α_d, α_s, α_{sea}, β_{val}, β_{sea}, and $\langle M_D^2 \rangle$. The parameters labeled sea apply to the remaining considered flavors, namely $\bar{u}$, $\bar{d}$, and $\bar{s}$. Furthermore, in order to fit the $\bar{\Lambda}$ polarization, we take $D^{\perp}_{1T,\bar{\Lambda}/\bar{q}}(z_\Lambda, p_{\Lambda\perp}; Q, Q^2) = D^{\perp}_{1T,\Lambda/q}(z_\Lambda, p_{\Lambda\perp}; Q, Q^2)$, by invariance under charge conjugation. To generate the uncertainty band for the fit, we once again use the replica method in Ref. [70].

5.2.2.2 Results

To sample the χ^2, we once again use the `MINUIT` package [116] from `CERNLIB` to perform the fit. The parameters as well as the $\chi^2/d.o.f$ of the fit are presented in 5.1. The $\chi^2/d.o.f$ of 1.694 suggests that the fit is of reasonably good quality. One must note that we have restricted ourselves to fit the experimental data with $z_h < 0.5$, for a total of 96 data points. It is also important to note that when these parameters are used to describe the data globally, without removing the $z_h > 0.5$ data, we have $\chi^2/d.o.f = 2.421$. This could indicate a sizable contribution of threshold logarithms [334] and target mass corrections [335, 336, 337] in this region.

While the advertised $\chi^2/d.o.f$ is 1.694, a large contribution of the χ^2 comes from two "problematic" points, the point at $z_h = 0.243$, $z_\Lambda = 0.35$ for the $\Lambda + K^+$ process and the point at $z_h = 0.245$, $z_\Lambda = 0.35$ for the $\bar{\Lambda} + K^-$ process. If the χ^2 contributions from these points are removed, the $\chi^2/d.o.f$ becomes 1.499. In fact removing these points from the fitting procedure altogether leads to a $\chi^2/d.o.f$ of 1.180. In the future, it would be interesting to investigate these two points in more detail.

In Fig. 5.2, I have included a histograms of the distributions of fit parameters, which are determined by the fits to the replicated data sets. We find that the modes of the histograms agree well with the determined values of the central fit. This agreement indicates that the values of the parameters are well-constrained, and not appreciably sensitive to variations of the central point within the experimental uncertainties.

In Figs. 5.3 and 5.4 we plot the experimental data, as well as the result of our fit for the

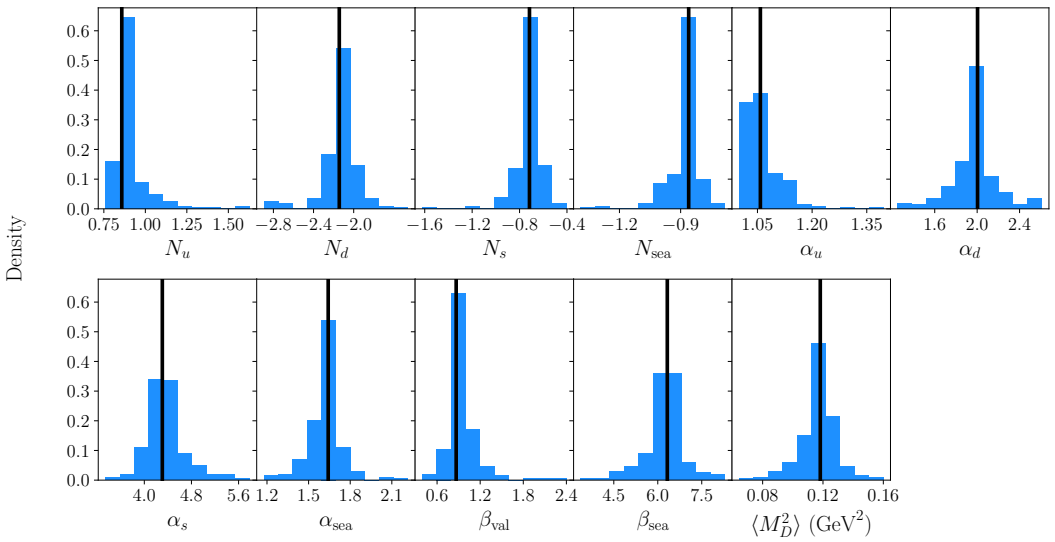

Figure 5.2: Distributions of `MINUIT` parameters from 200 replicas. The black lines represent the parameter values which are determined from the best fit of the actual experimental data. Each histogram is normalized such that the heights of its bars sum to unity.

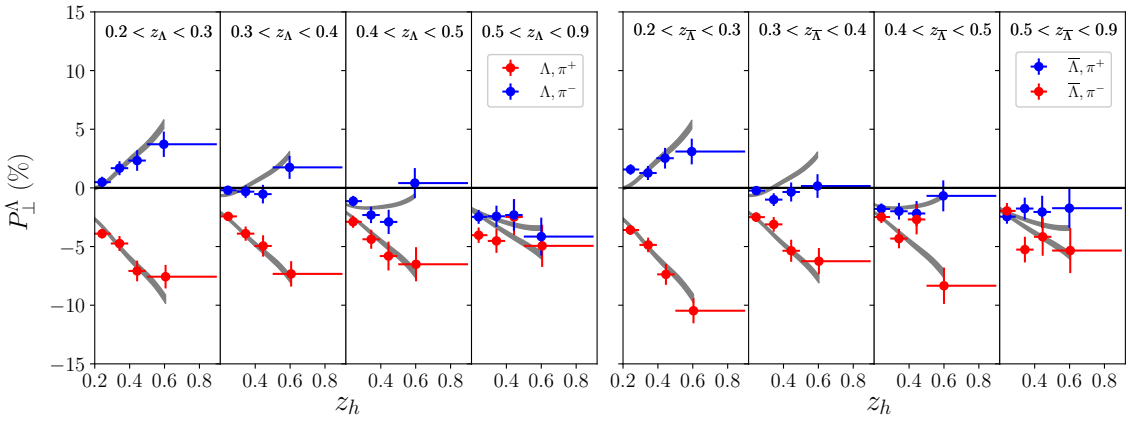

Figure 5.3: The fit to the experimental data for π mesons is shown, with the gray uncertainty band displayed is generated by the replicas at 68% confidence. The left plots are for the production of $\Lambda + \pi^\pm$, while the right plots are for the production of $\bar{\Lambda} + \pi^\pm$.

Λ polarization $P_\perp^\Lambda$ in the back-to-back production of $\Lambda(\bar{\Lambda}) + \pi^\pm$ and $\Lambda(\bar{\Lambda}) + K^\pm$, respectively. The gray uncertainty bands displayed are generated by the replicas at 68% confidence. For 5.3, the left plots correspond to $\Lambda + \pi^\pm$ production, while the right plots correspond to $\bar{\Lambda} + \pi^\pm$ production. Likewise, the left (right) plots are for the Λ ($\bar{\Lambda}$) production associated with $K^\pm$.

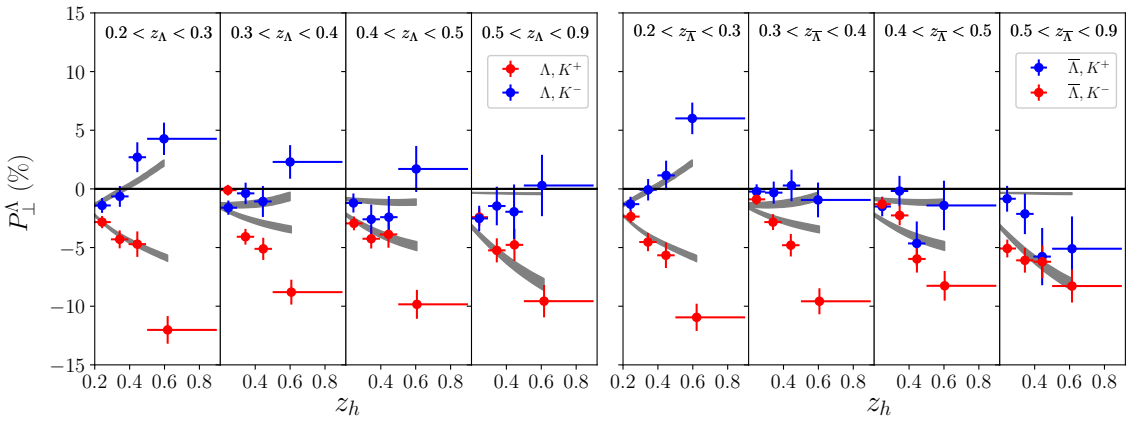

Figure 5.4: Same as 5.3 but for the production of $\Lambda + K^\pm$ (left) and $\bar\Lambda + K^\pm$ (right).

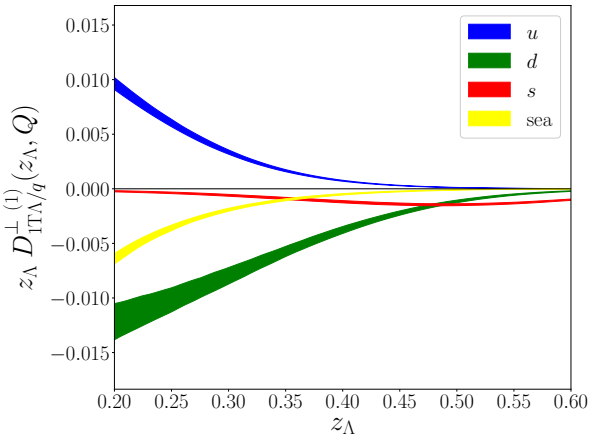

Figure 5.5: The polarizing fragmentation functions $z_\Lambda D_{1T,\Lambda/q}^{\perp(1)}(z_\Lambda; Q)$, defined in Eq. 5.20, are plotted as functions of z_Λ for different quark flavors, at 68% confidence.

One should note that the data points with $z_h > 0.5$ are not included in our fit, and thus we see that the global comparison with our theoretical results is of slightly lower quality. We further observe that our model seems to describe the $\Lambda(\bar\Lambda) + \pi^\pm$ data better than the $\Lambda(\bar\Lambda) + K^\pm$ data; indeed, we find $\chi^2/ndata = 1.223$ for pions, and 1.802 for kaons.

In 5.5, we plot $z_\Lambda D_{1T,\Lambda/q}^{\perp(1)}(z_\Lambda; Q)$, defined in Eq. 5.20, as a function of z_Λ for u, d, s and sea quarks, at 68% confidence. We find that the PFF for the u quark is positive, while those of the d and s quarks are negative. We also find a sizable negative sea quark contribution. These signs are consistent with the qualitative analysis in the BELLE experimental paper [316]. In

$$\chi^2/d.o.f = 1.694$$

$N_u = 0.858^{+0.108}_{-0.011}$	$N_d = -2.144^{+0.156}_{-0.088}$
$N_s = -0.716^{+0.070}_{-0.068}$	$N_{\rm sea} = -0.861^{+0.026}_{-0.086}$
$\alpha_u = 1.058^{+0.050}_{-0.044}$	$\alpha_d = 2.004^{+0.123}_{-0.196}$
$\alpha_s = 4.306^{+0.326}_{-0.185}$	$\alpha_{\rm sea} = 1.641^{+0.053}_{-0.102}$
$\beta_{\rm val} = 0.866^{+0.218}_{-0.046}$	$\beta_{\rm sea} = 6.325^{+0.240}_{-0.522}$
$\langle M_D^2 \rangle = 0.118^{+0.007}_{-0.012}$ GeV^2	

Table 5.1: Listed are the parameter values with uncertainties. The central values are taken from the fit with the actual BELLE data [316] (no Gaussian noise), while the uncertainties are calculated from the middle 68% of parameter values generated from 200 replicas (see the discussion in Sec. 5.2.2.1).

terms of the magnitude of the PFFs, we find that the u and d quarks are comparable, while the PFF for the s quark is smaller by almost an order of magnitude, and it plays a more important role in the relatively large $z_\Lambda \gtrsim 0.4$. The PFFs for sea quarks are sizable mostly in the relatively small $z_\Lambda \lesssim 0.3$ region.

One can understand these findings qualitatively. For example, the $\Lambda + \pi^-$ processes are dominated by the contribution of $D_{1T,\Lambda/u}^{\perp} D_{\pi^-/\bar{u}}$ in Eq. 5.23. As this subset of BELLE data has large positive Λ polarization ($z_\Lambda \lesssim 0.4$), we find that the sign of the u-quark PFF is positive. Likewise, the $\Lambda + \pi^+$ processes are dominated by the contribution of $D_{1T,\Lambda/d}^{\perp} D_{\pi^+/\bar{d}}$. Due to the large negative polarization, we find that the sign of the d-quark PFF is negative. Finally the $\Lambda + K^+$ process is dominated by the contribution of $D_{1T,\Lambda/s}^{\perp} D_{K^+/\bar{s}}$. We then determine the sign of the s-quark PFF to be negative, although our best fit gives a very small PFF for the s-quark. Finally the sea quarks usually play more important roles in the relatively small z_Λ region. In this set of BELLE data, it starts to become more important for $z_\Lambda \lesssim 0.3$. We find negative PFFs for sea quarks, which are smaller in size compared with those for u and d quarks. It is worth noting at this point that in Ref. [320], feed down

mechanisms were discussed and the authors found that they could set the u and d TMD PFFs to be equal to one another and obtain a good quality fit. However, in this analysis, the authors considered c contributions and found that they were quite large.

5.3 Λ Baryons in Semi-Inclusive DIS

5.3.1 Factorization Theorems

Let's define the kinematics for Semi-Inclusive DIS as

$$e(\ell) + p(P, \boldsymbol{s}_\perp) \to e(\ell') + \Lambda(P_h, \boldsymbol{s}_{\Lambda\perp}) + X\,,$$

where $\boldsymbol{s}_\perp$ is the transverse spin of the incoming proton, while $\boldsymbol{s}_{\Lambda\perp}$ is the transverse spin of the final produced Λ baryon. We take the frame choice such that the proton moves in the positive z direction while the incoming virtual photon moves in the negative z direction, see Fig. 1 of Ref. [120] for our convention, alternatively see Ref. [244] for the so-called Trento conventions. In the proton-photon COM frame, the differential cross section can be written as

$$\frac{d\sigma(\boldsymbol{s}_\perp, \boldsymbol{s}_{\Lambda\perp})}{d\mathcal{P}\mathcal{S}\, d^2P_{h\perp}} = \sigma_0^{\text{DIS}}\Big[F_{UU} + \sin(\phi_S - \phi_\Lambda) F_{UT}^{\sin(\phi_S-\phi_\Lambda)} + \cos(\varphi_S - \phi_S)\, D(y)\, F_{TT}^{\cos(\varphi_S-\phi_S)}\Big], \tag{5.24}$$

$$D(y) = \frac{2(1-y)}{1+(1-y)^2}\,. \tag{5.25}$$

In Eq. 5.24, the terms φ_S and ϕ_S in the superscript of the $F_{TT}^{\cos(\varphi_S-\phi_S)}$ structure function denote the azimuthal angles for $\boldsymbol{s}_\perp$ and $\boldsymbol{s}_{\Lambda\perp}$, respectively. Furthermore the ϕ_Λ term in the superscript of the $F_{UT}^{\sin(\phi_S-\phi_\Lambda)}$ structure function denotes the azimuthal angle of the transverse momentum of the Λ baryon, which is denoted $\boldsymbol{P}_{h\perp}$.

The experimentally measured spontaneous transverse polarization P_Λ and the transverse spin transfer S_Λ for Λ production are given by

$$P_\Lambda = \frac{F_{UT}^{\sin(\phi_S-\phi_\Lambda)}}{F_{UU}}\,, \qquad S_\Lambda = D(y)\,\frac{F_{TT}^{\cos(\varphi_S-\phi_S)}}{F_{UU}}\,, \tag{5.26}$$

respectively. We note at this point that the COMPASS measurement in Ref. [13] did not include the depolarization factor $D(y)$ in the definition of the transverse spin transfer.

Within the usual TMD factorization, these new structure functions can be written as

$$F_{UT}^{\sin(\phi_S-\phi_\Lambda)} = H^{\rm DIS}(Q;\mu)\,\mathcal{C}^{\rm DIS}\left[\frac{\hat{\mathbf{P}}_{h\perp}\cdot\boldsymbol{p}_\perp}{z_\Lambda M_\Lambda} f\, D_{1T}^{\perp}\right], \tag{5.27}$$

$$F_{TT}^{\cos(\varphi_S-\phi_S)} = H_\perp^{\rm DIS}(Q;\mu)\,\mathcal{C}^{\rm DIS}\left[h\,H\right]. \tag{5.28}$$

The function $H_\perp^{\rm DIS}(Q)$ is the hard function for a transversely polarized quark channels, which is normalized to 1 at Leading Order (LO). In the third expression, I have introduced $h_{q/p}$ and $H_{\Lambda/q}$, the transversity TMD PDF and TMD FF, respectively. It is worthwhile noting that there is another term which contributes to the Λ transverse polarization in unpolarized ep collisions and results in a $\sin(\phi_S+\phi_\Lambda)$-azimuthal modulation. This contribution arises from the Boer-Mulders function in the proton convoluted with the transversity TMD FF [338].

5.4 TMD PFF for EIC Phenomenology

5.4.1 QCD Factorization

In this section, we first review the TMD factorization formalism for spontaneous Λ polarization as well as the transverse spin transfer in SIDIS. We then provide the factorization formalism for Λ production inside the jet in back-to-back electron-jet production in ep collisions, with which we study two aforementioned spin configurations. We demonstrate that the spontaneous Λ polarization allows us to probe TMD PFF, while the transverse spin transfer is sensitive to Λ transversity TMD FF.

5.4.1.1 Λ Baryons inside a jet

We will now discuss the factorization formalism for transverse Λ production inside a jet for the back-to-back electron-jet production in ep collisions

$$e(\ell)+p(P,\boldsymbol{s}_\perp)\to e(\ell')+(\text{jet}(p_J)\,\Lambda(P_h,\boldsymbol{s}_{\Lambda\perp}))+X\,.$$

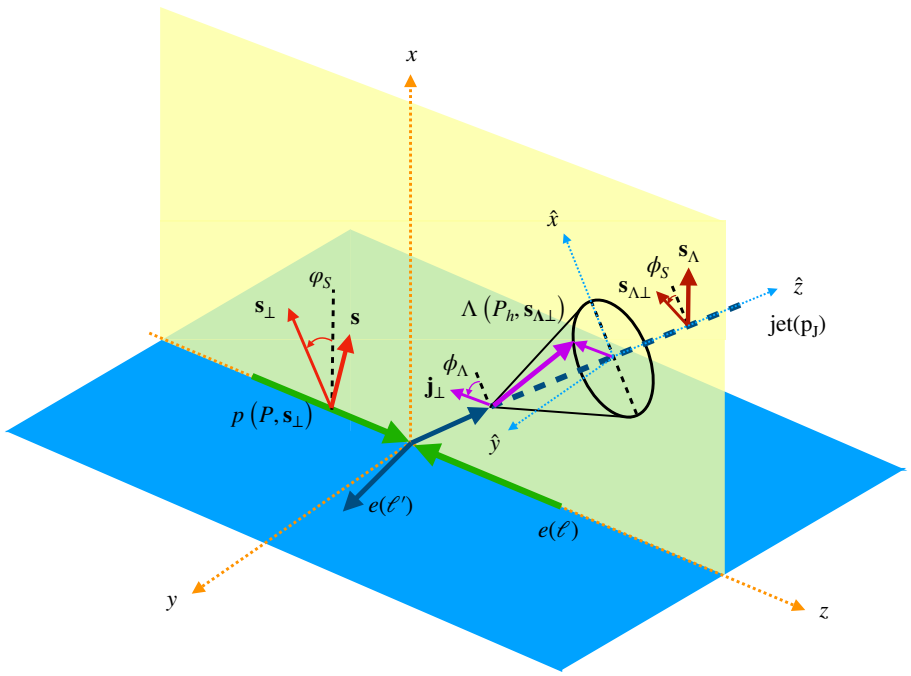

Figure 5.6: Kinematic configuration for back-to-back lepton-jet production.

In Fig. 5.6, we have included a plot which demonstrates the kinematic configuration of this process. The jet is constructed via a proper jet algorithm such as anti-k_T algorithm [238] with the jet radius R. For this process, we denote the transverse momentum of the jet direction as $\boldsymbol{p}_{J\perp}$ while $\boldsymbol{\ell}'_\perp$ represents the transverse momentum of the final state lepton. In both cases, the transverse momenta are defined in the center-of-mass frame of the incoming electron and the incoming nucleon. In this frame $\boldsymbol{q}_\perp = \boldsymbol{\ell}'_\perp + \boldsymbol{p}_{J\perp}$ represents the transverse momentum imbalance of the outgoing electron and the jet. The back-to-back electron-jet configuration occurs at a small transverse momentum imbalance, $|\boldsymbol{q}_\perp| \ll \ell'_\perp \sim p_{J\perp}$ [130, 142]. Additionally, for this process it is convenient to measure the transverse momentum of the Λ baryon relative to the jet axis, which we denote $\boldsymbol{j}_\perp$. The TMD region for Λ production in the jet occurs in the kinematic region where $j_\perp \ll p_{J\perp} R$ [136].

By studying the partonic process for jet production, one can see that the direction of the jet is directly sensitive to the TMD PDF. By measuring the transverse momenta of Λ

baryons within this jet, we also gain sensitivity to the TMD FFs. This process offers the advantage that since the jet and the Λ baryons are measured with respect to different axes, the factorization structure for this process will lead to a deconvolution of the TMD PDF and TMD FF, thus allowing us to probe these structures more independently.

Following the work of [339, 296, 303, 136, 140, 328, 139], the relevant cross section can be written as

$$\frac{\mathrm{d}\sigma(\boldsymbol{s}_\perp, \boldsymbol{s}_{\Lambda\perp})}{d\mathcal{PS}\, d^2\boldsymbol{q}_\perp\, dz_{J\Lambda}\, d^2\boldsymbol{j}_\perp} = \sigma_0 \Big[W_{UU} \sin(\phi_S - \phi_\Lambda) + W_{UT}^{\sin(\phi_S-\phi_\Lambda)} + \cos\left(\varphi_{\mathcal{S}} - \phi_S\right)\, D(\hat{s},\hat{t},\hat{u})\, W_{TT}^{\cos(\varphi_{\mathcal{S}}-\phi_S)} \Big] ,$$

In this expression $d\mathcal{PS} = dy_e\, d^2\boldsymbol{\ell}'_\perp$ is the phase space element in rapidity and transverse momentum of the outgoing electron in the center-of-mass frame of incoming electron and the nucleon. The variable $z_{J\Lambda}$ represents the fraction of the momentum of the jet which is carried by the Λ baryon. The $z_{J\Lambda}$ and $\boldsymbol{j}_\perp$ variables can be related to the momenta of the Λ baryon and jet through the relations

$$z_{J\Lambda} = \boldsymbol{P}_h \cdot \boldsymbol{p}_J / |\boldsymbol{p}_J|^2 , \qquad \boldsymbol{j}_\perp = \boldsymbol{P}_h \times \boldsymbol{p}_J / |\boldsymbol{p}_J| , \tag{5.29}$$

where $\boldsymbol{P}_h$ and $\boldsymbol{p}_J$ represent the three momenta of the Λ baryon and the jet respectively.

On the other hand, in 5.29, we have

$$\sigma_0 = \frac{\alpha_{\mathrm{em}}^2}{sQ^2} \frac{2(\hat{s}^2 + \hat{u}^2)}{Q^4} , \tag{5.30}$$

where the partonic Mandelstam variables are given by

$$\hat{s} = x_B S_{\mathrm{ep}} , \qquad \hat{t} = -\sqrt{S_{\mathrm{ep}}}\, \ell'_\perp e^{y_e} , \qquad \hat{u} = -x_B \sqrt{S_{\mathrm{ep}}}\, \ell'_\perp e^{-y_e} , \tag{5.31}$$

where S_{ep} is the center of mass energy of the electron-proton pair while $Q^2 = -\hat{t}$. Furthermore, we define

$$D(\hat{s},\hat{t},\hat{u}) = -\frac{2\hat{s}\hat{u}}{\hat{s}^2 + \hat{u}^2} . \tag{5.32}$$

For this process, W denote the structure functions and we follow the same labelling convention for the subscripts as outlined in the previous section. The polarization and spin transfer for back-to-back electron-jet production in ep collisions can be written in terms of these structure functions as

$$P_\Lambda = \frac{W_{UT}^{\sin(\phi_S-\phi_\Lambda)}}{W_{UU}}\,, \tag{5.33}$$

$$S_\Lambda = D(\hat{s},\hat{t},\hat{u})\,\frac{W_{TT}^{\cos(\varphi_S-\phi_S)}}{W_{UU}}\,, \tag{5.34}$$

respectively.

The expression for the unpolarized structure function can be obtained from Ref. [142] as

$$\begin{aligned} W_{UU} =\; & H(Q;\mu)\sum_q e_q^2\,\mathcal{G}_{\Lambda/q}(z_{J\Lambda}, j_\perp;\mu_J,\mu,\zeta_2) \\ & \times\int\frac{d^2b}{(2\pi)^2}\,e^{i\boldsymbol{q}_\perp\cdot\boldsymbol{b}}\,f_{q/p}(x_B,b;\mu,\zeta_1)\,S(b,y_J,R;\mu)\,. \end{aligned} \tag{5.35}$$

In this expression, H and U are the hard function and the b-space soft functions for this process. Furthermore, x_B is the usual Bjorken variable which is related to the variables in the phase space element through the relation

$$x_B = \frac{Q^2}{2P\cdot q} = \frac{\ell'_\perp e^{y_e}}{\sqrt{S_{\rm ep}} - \ell'_\perp e^{-y_e}}\,. \tag{5.36}$$

For later convenience, we also define the inelasticity y as

$$y = 1 - \frac{\ell'_\perp}{\sqrt{S_{\rm ep}}}e^{-y_e}\,. \tag{5.37}$$

The rapidity of the jet, y_J, can also be defined in terms of the kinematic variables entering into the phase space through the relation

$$y_J = -\frac{1}{2}\ln\left(\frac{\hat{t}}{x\hat{u}}\right). \tag{5.38}$$

Furthermore, μ and μ_J are the renormalization and the jet scales, respectively. For the remainder of this chapter, we will always choose the renormalization scale to be given by $\mu = p_{J\perp}$ while the jet scale will be given by $\mu_J = p_{J\perp}R$. The function $\mathcal{G}_{\Lambda/q}$ entering into 5.35 is the TMD fragmenting jet function [340, 136, 328, 139], which describes the distribution

of Λ particles inside the jet. Following the results of Ref. [142], this distribution function is related to the usual unpolarized TMD FF through the relation

$$\mathcal{G}_{\Lambda/q}(z_{J\Lambda}, j_\perp; \mu_J, \mu, \zeta_2) = \exp\left(\int_{\mu_J}^{\mu} \frac{d\mu'}{\mu'}\gamma_J(\mu')\right) \int \frac{d^2b}{(2\pi)^2} e^{i\boldsymbol{j}_\perp\cdot\boldsymbol{b}/z_{J\Lambda}} D_{\Lambda/q}(z_{J\Lambda}, b; \mu_J, \zeta_2)\,, \quad (5.39)$$

where γ_J is the anomalous dimension of the TMD fragmenting jet function, to be given below in Sec. 5.4.5.

For spontaneous Λ polarization, we follow the procedure in Ref. [341] to replace the TMD FF in 5.39 by the relevant density associated with the distribution of transversely polarized Λ baryons. Explicitly, we make the replacement

$$D_{\Lambda/q}(z_{J\Lambda}, b; \mu_J, \zeta_2) \to -\frac{M_\Lambda \epsilon_{\perp\rho\sigma} b^\rho S_\perp^\sigma}{z_{J\Lambda}^2} D_{1T,\Lambda/q}^{\perp(1)}(z_{J\Lambda}, b; \mu_J, \zeta_2)\,,$$

where $D_{1T,\Lambda/q}^{\perp(1)}$ is the first moment of the TMD PFF in b-space [341]. After making this replacement, the structure function for spontaneous Λ polarization is given by

$$\begin{aligned} W_{UT}^{\sin(\phi_S-\phi_\Lambda)} &= H(Q;\mu)\sum_q e_q^2\, \mathcal{G}_{1T,\Lambda/q}^{\perp}(z_{J\Lambda}, j_\perp; \mu_J, \mu, \zeta_2) \\ &\times \int \frac{d^2b}{(2\pi)^2}\, e^{i\boldsymbol{q}_\perp\cdot\boldsymbol{b}}\, f_{q/p}(x_B, b; \mu, \zeta_1)\, S(b, y_J, R; \mu)\,, \end{aligned} \quad (5.40)$$

where

$$\begin{aligned} \mathcal{G}_{1T,\Lambda/q}^{\perp}(z_{J\Lambda}, j_\perp; \mu_J, \mu, \zeta_2) &= \frac{M_\Lambda}{z_{J\Lambda}} \exp\left(\int_{\mu_J}^{\mu} \frac{d\mu'}{\mu'}\gamma_J(\mu')\right) \\ &\times \frac{\partial}{\partial j_\perp} \int \frac{d^2b}{(2\pi)^2} e^{i\boldsymbol{j}_\perp\cdot\boldsymbol{b}/z_{J\Lambda}}\, D_{1T,\Lambda/q}^{\perp(1)}(z_{J\Lambda}, b; \mu_J, \zeta_2)\,. \end{aligned} \quad (5.41)$$

Finally, we define the transverse spin transfer structure function as

$$\begin{aligned} W_{TT}^{\cos(\varphi_S-\phi_S)} &= H_\perp(Q;\mu)\sum_q e_q^2\, \mathcal{G}_{\Lambda/q}^{T}(z_{J\Lambda}, j_\perp; \mu_J, \mu, \zeta_2) \\ &\times \int \frac{d^2b}{(2\pi)^2}\, e^{i\boldsymbol{q}_\perp\cdot\boldsymbol{b}}\, h_{q/p}(x_B, b; \mu, \zeta_1)\, S(b, y_J, R; \mu)\,, \end{aligned} \quad (5.42)$$

where

$$\mathcal{G}_{\Lambda/q}^{T}(z_{J\Lambda}, j_\perp; \mu_J, \mu, \zeta_2) = \exp\left(\int_{\mu_J}^{\mu} \frac{d\mu'}{\mu'}\gamma_J(\mu')\right) \int \frac{d^2b}{(2\pi)^2} e^{i\boldsymbol{j}_\perp\cdot\boldsymbol{b}/z_{J\Lambda}} H_{\Lambda/q}(z_{J\Lambda}, b; \mu_J, \zeta_2)\,, \quad (5.43)$$

provides the distribution of transversely polarized Λ baryons in a jet which is initiated by a transversely polarized quark and $H_\perp(Q;\mu)$ is the hard function associated with the transversely polarized quark hard process.

5.4.2 Experimental Setup

In this section, we present the details of our simulation for generating the event statistics. The present study is based on the four baseline energy configurations which are discussed in EIC Yellow Report [342]. The four configurations are 5 GeV × 41 GeV, 5 GeV × 100 GeV, 10 GeV × 100 GeV, and 18 GeV × 275 GeV, where the first energy is the electron beam energy while the second energy is the proton beam energy. The *ep* event simulation that we present here is based on the PYTHIA eRHIC Monte Carlo program which is a modified version of PYTHIA-6.4.28 [152] with the PDFs input from the LHAPDF [343] library. Furthermore, for the back-to-back lepton-jet process, we perform jet reconstruction using the FASTJET [238] package. The kinematics have been constrained in the following ranges: $Q > 1$ GeV, $0.05 < y < 0.95$, $W > 2$ GeV. The constrains on Q^2 and W are used to select valid SIDIS events, whereas the y selection avoids phase space where either radiative corrections become large or the event cannot be reliably reconstructed.

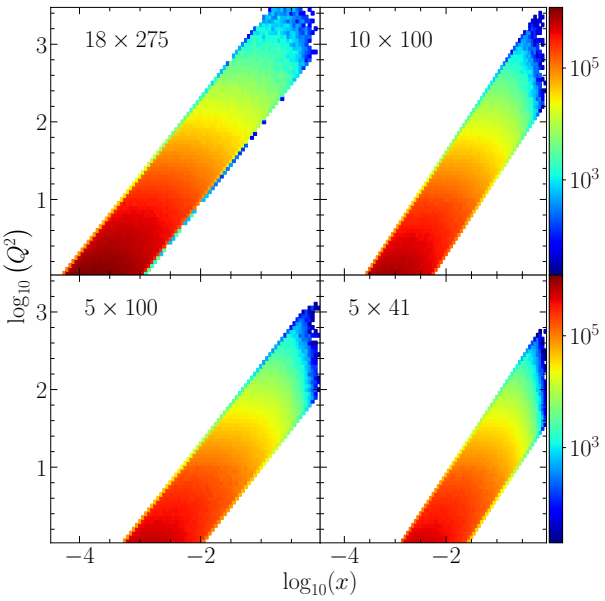

Figure 5.7: The ranges in the square of the transferred photon momentum Q^2 versus the parton momentum fraction x accessible for different collision energies. The z-scale (density) indicates the number of events with at least one $\Lambda/\bar{\Lambda}$ in pseudo-rapidity range -3.5< η <3.5.

Figure 5.7 shows the x_B vs. Q^2 distribution with the y constraint applied for different

collision energies. The Λ hyperons are reconstructed from its charged final state decay products, proton (anti-proton), and negative (positive) pion. The 2-D distributions in p_T, the transverse momentum in the lab frame, and η, the pseudo-rapidity space for proton and charged pion, are shown in Fig. 5.8 (left and middle). The assumed EIC detector will cover the full azimuth in a finite pseudo-rapidity range $-3.5 < \eta < 3.5$. The lowest transverse momentum is set to be 0.1 GeV. To ensure the applicability of TMD factorization [36], the condition, $P_{h\perp}/z < Q/4$ is also applied. The distribution of $P_{h\perp}/z_\Lambda$ versus $Q/4$ is shown in Fig. 5.9 with the dashed line indicating the selection cut. To reduce the contribution from the beam remnant, the Feynman-x, $x_F = 2p_L^\Lambda/W$, is required to be positive. As shown in Fig. 5.10, the fraction of the Λ originating from target fragmentation in the final sample is only a few percent. This study relies on fast simulations, where the efficiency is not impacted by the displacement between the decay vertex of the hyperon and the primary vertex. As shown in Fig. 5.11, the decay vertex can be removed from the primary vertex by several centimeters which might impact the detection efficiency of a compact tracking system proposed for the EIC [344]. To account for this effect, we apply a quite conservative overall efficiency factor of 50% for the projected statistical uncertainties.

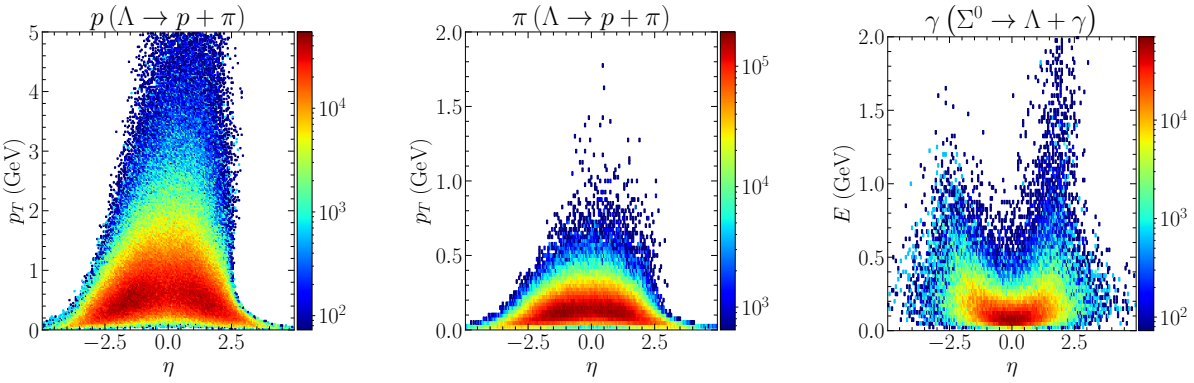

Figure 5.8: Final state particle distributions in transverse momentum (energy) and pseudo-rapidity space for proton (left), pion (middle), and photon from Σ^0 decay (right). Here we display the results at the collision energy 18×275 GeV^2 and we note that the distributions for other energy configurations are similar.

For Λ production at EIC energies, feed-down from heavier particles is not negligible.

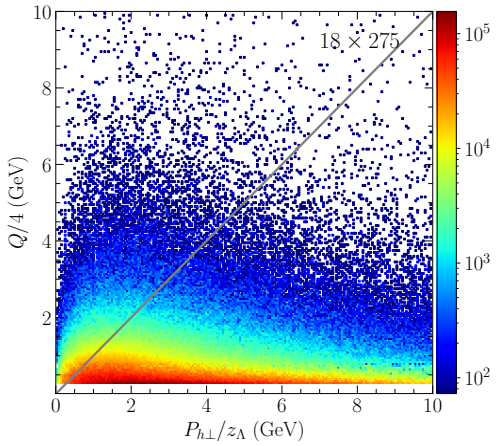

Figure 5.9: Illustration of the impact of the constraint $P_{h\perp}/z_\Lambda < Q/4$. Only events above the line are accepted. The efficiency of this cut depends on the hard scale Q^2 and is approximately 7% for $Q^2 > 1$ GeV^2, 25% for $Q^2 > 10$ GeV^2 and 50% for $Q^2 > 100$ GeV^2. Here, we provide the result for the 18×275 GeV^2 energy configuration while we note that the results for the other collision energies configurations are similar.

Figure 5.10, shows the origins of the detected Λ, according to the event list provided by the PYTHIA generator, for the top energy 18×275 GeV^2. After selection cuts, about 1/3∼1/2 of the Λ candidates are promptly produced from string fragmentation. Most of the remainder, about half of the total, originates from the feed-down of Σ^0 hyperons, excited Σ^* states and Ξ hyperons. Additional contributions, less than 10 % come from heavy quark decays, e.g. Λ_c and diquarks from the target remnant. In principle, the fragmentation formalism used in this work, does not apply to hyperons produced in the weak decay of heavier states. This includes most of the feed-down except for feed-down from Σ^*, which predominantly decays strongly into Λ. However, to our knowledge, all previous experimental measurements, except for Ref. [316], did not separate between weak and strong production. Consequently, previous phenomenological work integrated over all Λ, extracting in some sense effective fragmentation functions. For these reasons, we will also integrate over all Λ ancestries and will not assign a systematic uncertainty to the feed-down contributions.

For an eventual feed-down correction, the contributions from the various decays would

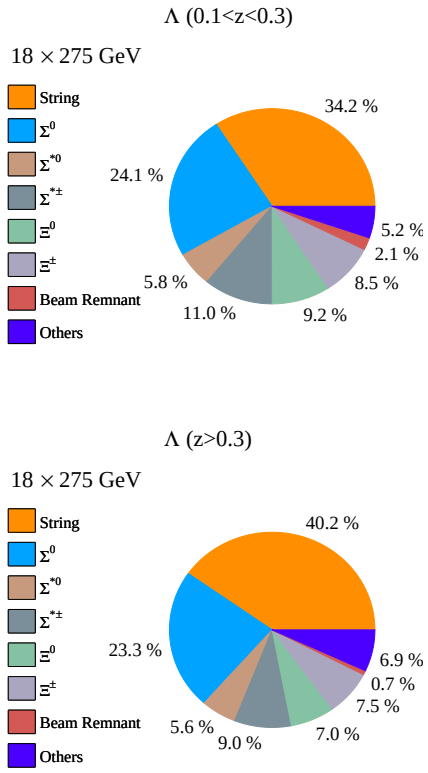

Figure 5.10: Origins of Λ for $0.1 < z < 0.3$ and $z > 0.3$ according to the event records provided by the PYTHIA event generator for the 18×275 GeV^2 energy configuration.

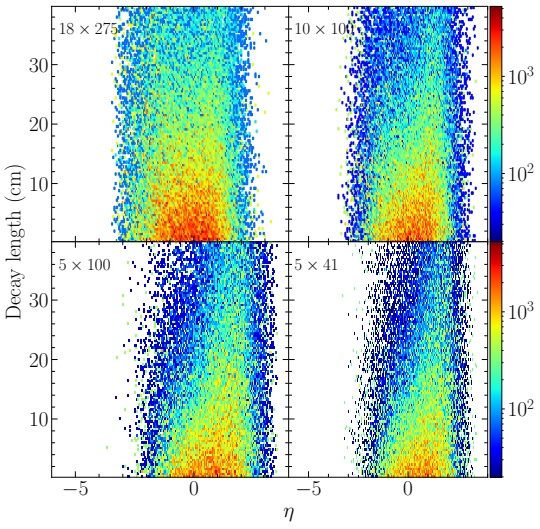

Figure 5.11: Correlations between Λ and $\bar{\Lambda}$ decay length and pseudo-rapidity at different collision energies.

have to be identified in data. For Σ^0, which decays nearly always to $\Lambda + \gamma$, we investigated therefore the feasibility of reconstructing this decay. As shown in Fig. 5.8 right panel, the final state γ are emitted predominantly at or near the central pseudo-rapidity range with a relative low energy, mostly < 0.5 GeV. While the detection of these photons is challenging, with the detector performance requirements outlined in the Yellow Report, it should be feasible to reconstruct Σ^0 hyperons with sufficient mass resolution. More than half of the feed-down from Ξ hyperons originate from the decay $\Xi^0 \rightarrow \Lambda + \pi^0$, which is difficult to reconstruct, due to combinatorial background in the π^0 reconstruction. The decay $\Xi^{\pm} \rightarrow \Lambda + \pi^{\pm}$ can be reconstructed with sufficient efficiency, however, this decay makes up less than 10%. We note that additional systematic uncertainties are expected to come from the uncertainty on the beam polarization for the spin transfer measurement as well as from wrongly reconstructed Λ hyperons as well as detector effects. For the Λ in jet measurements, the Jet Energy Resolution (JER) will impact the reconstruction of kinematic variables. Following studies in the Yellow Report, the relative uncertainty on the beam polarization can be assumed to be less than 3 %, which makes this systematic negligible compared with the expected statistical

uncertainties. The JER should be about 10%. Since the extracted quantities are not strongly dependent on kinematics derived from the jet energy, we also assume that this systematic is negligible. Finally, based on experience from previous measurements of Λ polarization, we also assume that systematics due to detector effects and wrongly reconstructed Λ hyperons are negligible compared to our projected statistical uncertainties. These assumptions have to be revisited for the eventual measurement.

5.4.3 Reweighting Analysis for the TMD PFF and Transversity TMD FF

Having summarized the details of our experimental simulation in the previous section, we now present our SIDIS re-weighting analysis at the EIC. In Sec. 5.4.3.1, we provide the numerical input for the re-weighting analysis. In Sec. 5.4.3.2, we provides the results of our projections for the uncertainties for the TMD PFF from this analysis as well as the comparison with the experimental data. In Sec. 5.4.4, I provide the parameterization, fit results, and EIC impact study for the transversity TMD FF in Semi-Inclusive DIS.

5.4.3.1 Numerical Input for the TMD PFF

For this chapter, we will always use LO matching. This is motivated by the fact that the one loop expression for the TMD PFF has not yet been performed. At this perturbative order, the hard function can be replaced by

$$H^{\mathrm{DIS}}(Q;\mu) = 1\,. \tag{5.44}$$

To quantify the contribution of the EIC in constraining the TMD PFFs, we perform two fits in this section. Our baseline fit contains only the experimental data from the Belle collaboration while the re-weighted fit contains both the experimental data from Belle and the pseudo-data generated in the previous section. For this section, we take the integrated luminosity of the EIC pseudo-data to be 40 fb^{-1}.

At this point, I would like to note a major point. In our analysis of the Belle data, all data points were at a single scale $Q = 10.58$ GeV. As a result, we used a simple Gaussian

model to perform the extraction. In our analysis for the EIC impact study, we will continue to ignore contributions from evolution and thus perform this analysis in a Gaussian model.

To parameterize the TMD PDF in the polarization case, I will use the parameterization

$$f_{q/p}(x_B, k_\perp^2; \mu, \zeta_1) = f_{q/p}(x_B; Q) \frac{e^{-k_\perp^2/\langle k_\perp^2 \rangle}}{\pi \langle k_\perp^2 \rangle} \,. \tag{5.45}$$

where we use $\langle k_\perp^2 \rangle = 0.61$ from [330]. Using this expression, the spontaneous Λ polarization in Eq. 5.26 can be written as

$$P_\Lambda(x_B, y, z_\Lambda, P_{h\perp}) = \frac{\sum_q e_q^2 f_{q/p}(x_B; Q)\, \omega_q(z_\Lambda; P_{h\perp})\, D_{\Lambda/q}(z_\Lambda, Q)}{\sum_q e_q^2 f_{q/p}(x_B; Q) D_{\Lambda/q}(z_\Lambda; Q)} \,. \tag{5.46}$$

In this expression

$$\omega_q(z_\Lambda, P_{h\perp}) = \frac{P_{h\perp}}{z_\Lambda\, M} \frac{\langle M_D^2 \rangle \langle P_{h\perp}^2 \rangle}{\langle \Delta P_{h\perp}^2 \rangle^2} \mathcal{N}_q(z_\Lambda) \times \exp\left[P_{h\perp}^2 \left(\frac{1}{\langle P_{h\perp}^2 \rangle} - \frac{1}{\langle \Delta P_{h\perp}^2 \rangle} \right) \right] \tag{5.47}$$

are the weighting functions while

$$\langle P_{h\perp}^2 \rangle = \langle k_\perp^2 \rangle z_\Lambda^2 + \langle p_\perp^2 \rangle \,, \tag{5.48}$$

$$\langle \Delta P_{h\perp}^2 \rangle = \langle k_\perp^2 \rangle z_\Lambda^2 + \langle M_D^2 \rangle \,, \tag{5.49}$$

are the Gaussian widths associated with the unpolarized and polarized processes, respectively.

In this analysis, we follow the parameterization in Ref. [12] with fit parameters N_u, N_d, N_s, N_{sea}, α_u, α_d, α_s, α_{sea}, β_{val}, β_{sea}, and $\langle M_D^2 \rangle$. To perform the fit of the generated pseudo-data, we integrate the numerator and denominator of 5.46 in x, y, and $P_{h\perp}$. Namely to generate the pseudo-data, events are binned into $1 > x_B > 10^{-1}$, $10^{-1} > x_B > 10^{-2}$, $10^{-2} > x_B > 10^{-3}$, and $10^{-3} > x_B > 10^{-4}$. To generate our theoretical predictions, we integrate over these ranges of x values. pseudo-data are also generated using the constraint that $0.05 < y < 0.95$. Using the relation $x_B\, y\, S_{\rm ep} = Q^2$, for each data point in our prediction, we integrate over $0.05 < y < 0.95$ under the condition that $Q > 1$ GeV. Finally, to generate

the pseudo-data, we have also applied the kinematic constraint that $P_{h\perp}/z_\Lambda < 0.25\,Q$, which is associated with the TMD factorization region. For each point, we integrate over this kinematic region in our fitting procedure.

To perform both of the fits, we use the Migrad fit in the `Minuit` package [345] to minimize the χ^2. Furthermore, to generate the theoretical results, we use the replica method [346, 347] with 200 replicas. For each of the replicas, we initialize the fit parameters using a Monte Carlo sampler.

5.4.3.2 Results for the TMD PFF

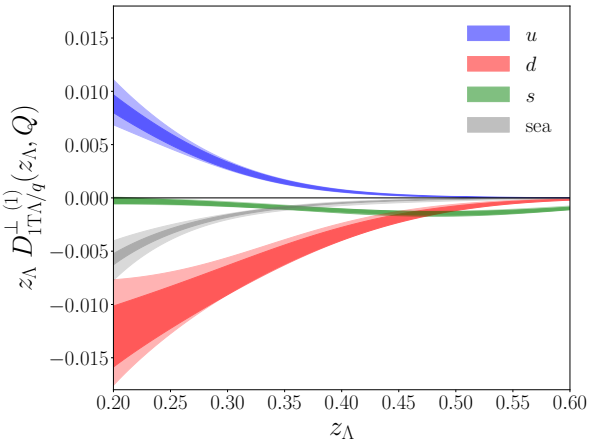

Figure 5.12: The first moment of the TMD PFF at $Q = 10.58$ GeV. The light bands represent the uncertainty from the fit to Belle data in Ref. [12], while the dark bands represent the uncertainty obtained from the simultaneous fit of the Belle data and the EIC pseudo-data.

In Fig. 5.12, we plot the first moment of the TMD PFF which was obtained from the baseline fit as a light band. In the darker band, we plot the result from the simultaneous fit to the Belle data as well as the EIC pseudo-data. The theoretical uncertainty for the first moment, $\delta D_{1T}^{\perp\,(1)}$, is obtained from the set of replicas by calculating the standard deviation at each point. Furthermore, we define the average value of the extracted first moment as $D_{1T}^{\perp\,(1)}$. As we can see, from this plot, the uncertainty is significantly reduced in the simultaneous analysis. In order to further quantify the size of this reduction of the theoretical uncertainties,

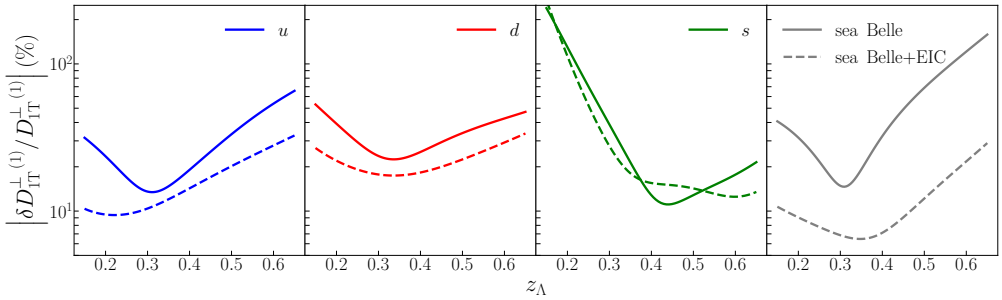

Figure 5.13: The ratio of the uncertainty of the TMD PFF for each flavor at $Q = 10.58$ GeV. The solid lines represent the results from the fit to Belle data while the dashed line represents the result from the fit to the Belle data and the EIC pseudo-data.

we also plot the ratio $\delta D_{1T}^{\perp\,(1)}/D_{1T}^{\perp\,(1)}$ in Fig. 5.13. As we see in this figure, the pseudo-data generated from the EIC kinematics leads to a significant reduction of the theoretical uncertainty for the u and sea quarks. The large reduction in the theoretical uncertainties in the sea quark TMD PFF is occurring because the parameterization in Ref. [12] assumes charge symmetry. Thus $D_{1T,\Lambda/q}^{\perp\,(1)} = D_{1T,\bar{\Lambda}/\bar{q}}^{\perp\,(1)}$ and $D_{1T,\Lambda/\bar{q}}^{\perp\,(1)} = D_{1T,\bar{\Lambda}/q}^{\perp\,(1)}$. Since the analysis that we perform here uses a proton beam, the fit with the pseudo-data allows us to strongly constrain the $D_{1T,\bar{\Lambda}/u}^{\perp\,(1)}$ and $D_{1T,\bar{\Lambda}/d}^{\perp\,(1)}$ functions. From the charge symmetry assumption, this leads to a large reduction in the uncertainties for the $D_{1T,\Lambda/\bar{u}}^{\perp\,(1)}$ and $D_{1T,\Lambda/\bar{d}}^{\perp\,(1)}$ functions. As a result, the uncertainties for the sea quark distributions are dramatically reduced. However, because the strange distribution in the PDF is small, we find that the theoretical uncertainties $D_{1T,\Lambda/s}^{\perp\,(1)}$ are unchanged with the introduction of pseudo-data. Furthermore, we find that the reduction in the theoretical uncertainties for the d quark distribution is smaller than those for the u and sea quarks. However, we note that in principle the theoretical uncertainty for this flavor can be further reduced by considering experimental data from a ^{3}He nuclear beam. Namely by using a ^{3}He beam and tagging the two protons in the forward region, a neutron can be isolated in the hadron beam. This procedure would allow future extractions to spontaneous Λ production for electron-neutron scattering which is extremely useful for studying the d-quark TMD PFF.

In Fig. 5.14, we plot the pseudo-data that was obtained in the previous section for Λ

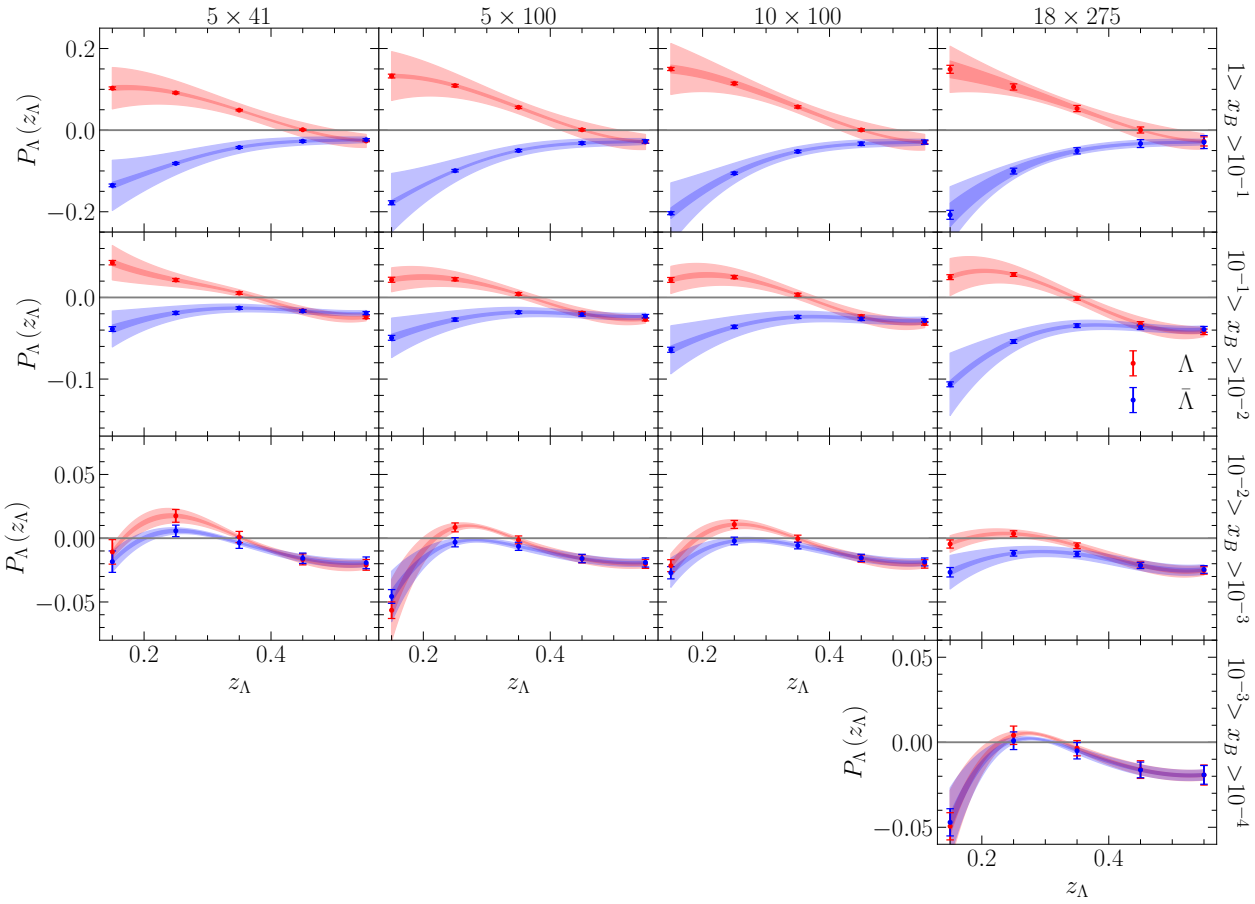

Figure 5.14: Theoretical predictions are compared against the pseudo-data generated in the reweighting method at 40 fb^{-1}. The rows are grouped by the range of x_B while the columns are group by the energy configuration of the collision where the first number represents the energy of the lepton beam in GeV and the second number represents the energy of the hadron beam in GeV. The light band represents the theoretical uncertainty from the baseline fit to the Belle data while the dark band represents the theoretical uncertainty from the fit including the pseudo-data.

in red and $\bar{\Lambda}$ in blue. Once again, the light band represents the theoretical uncertainty obtained from the baseline fit. The dark band represents the theoretical uncertainty from the simultaneous fit. To calculate the theoretical uncertainties, we compute the standard deviation of replicas at each point. We bin each row (column) of this plot according to its x_B range (energy configuration). The top row contains the pseudo-data generated from events with $1 > x_B > 10^{-1}$. As we can see in this region, the size of the projected polarization is relatively large and positive for Λ production. Furthermore, the polarization is large and negative for the $\bar{\Lambda}$ production. The large and positive polarization for Λ production is occurring because the contribution from the u quark is dominant for this process and is also positive. The large and negative polarization for $\bar{\Lambda}$ production is occurring because the large contribution from the u quark TMD PDF is being weighted with the sea contribution for the TMD PFF. Since the sea contribution is negative, the resulting asymmetry is large and negative. As the binned value of x_B decreases as we move down the rows in Fig. 5.14, we can see that the polarization for Λ tends to decrease in magnitude. This behavior occurs because there are large cancellations between the u and sea quarks in this kinematic region.

5.4.4 Numerical Input and Results for the Transversity TMD FF

To characterize the theoretical uncertainty which can be obtained by current experimental data, we first use the current experimental data from COMPASS to constrain the transversity TMD FF for Λ baryon production.

In this section, we first begin by providing the numerical recipe used for the extraction of the transversity TMD FF. To perform this analysis, we work at LO accuracy for the matching and Next-to-Leading-Logarithmic (NLL) accuracy for the logarithmic resummation. Beyond the Gaussian approximation, it is convenient to work in b-space. The expressions for the unpolarized structure function at LO becomes

$$F_{UU} = \sum_q e_q^2 \int \frac{db\, b}{2\pi} J_0\left(\frac{bP_{h\perp}}{z_\Lambda}\right) D_{\Lambda/q}(z_\Lambda, b; Q, Q^2) f_{q/p}(x_B, b; Q, Q^2)\,.$$

At the perturbative accuracy that we use in this section, the TMDs can be matched onto

the collinear distributions using the relations

$$f_{q/p}(x_B, b; Q, Q^2) = f_{q/p}(x_B; \mu_{b_*}) \exp\left(-S_{\rm pert}(b; \mu_{b_*}, Q, \mu_{b_*}^2, Q^2) - S_{\rm NP}^f(b, Q, Q_0)\right) , \quad (5.50)$$

$$D_{\Lambda/p}(z_\Lambda, b; Q, Q^2) = \frac{1}{z_\Lambda^2} D_{\Lambda/q}(z_\Lambda; \mu_{b_*}) \times \exp\left(-S_{\rm pert}(b; \mu_{b_*}, Q, \mu_{b_*}^2, Q^2) - S_{\rm NP}^D(z_\Lambda, b, Q, Q_0)\right) . \quad (5.51)$$

The unpolarized structure function can be written as

$$F_{UU} = \sum_q e_q^2 \frac{1}{z_\Lambda^2} \int \frac{db\, b}{2\pi} J_0\left(\frac{bP_{h\perp}}{z_\Lambda}\right) D_{\Lambda/q}(z_\Lambda; \mu_{b_*})\, f_{q/p}(x_B; \mu_{b_*}) \times \exp\left[-2S_{\rm pert}(b; \mu_{b_*}, Q, \mu_{b_*}^2, Q^2) - S_{\rm NP}^D(z_\Lambda, b, Q, Q_0) - S_{\rm NP}^f(b, Q, Q_0)\right] . \quad (5.52)$$

Following a similar analysis for the transverse spin transfer process, one can write the structure function associated with this process as

$$F_{TT}^{\cos(\varphi_S - \phi_S)} = \sum_q e_q^2 \frac{1}{z_\Lambda^2} \int \frac{db\, b}{2\pi} J_0\left(\frac{bP_{h\perp}}{z_\Lambda}\right) H_{\Lambda/q}(z_\Lambda; \mu_{b_*})\, h_{q/p}(x_B; \mu_{b_*}) \times \exp\left[-2S_{\rm pert}(b; \mu_{b_*}, Q, \mu_{b_*}^2, Q^2) - S_{\rm NP}^H(z_\Lambda, b, Q, Q_0) - S_{\rm NP}^h(b, Q, Q_0)\right] \quad (5.53)$$

where $h_{q/p}$ and $H_{\Lambda/q}$ are the collinear transversity PDF and FF while $S_{\rm NP}^H$ and $S_{\rm NP}^h$ are the non-perturbative Sudakov factors for these distributions.

Several extraction in the literature for the transversity TMD PDF. In this work, we follow the work in Ref. [120] to parameterize the transversity PDF as

$$h_{q/p}(x; \mu_0) = N_q^h x^{\alpha_q^h} (1-x)^{\beta_q^h} \frac{(\alpha_q^h + \beta_q^h)^{\alpha_q^h + \beta_q^h}}{{\alpha_q^h}^{\alpha_q^h} {\beta_q^h}^{\beta_q^h}} \frac{1}{2} \left[f_{q/p}(x; \mu_0) + g_{q/p}(x; \mu_0)\right] . \quad (5.54)$$

In this expression, N_q^h, α_q^h, β_q^h are fit parameters which were obtained in this reference for the u and d quarks while the contributions of the sea quarks were set to zero. Furthermore, we have defined the initial scale of the parameterization to be μ_0.

The transversity PDF in Eq. 5.54 can in general have a non-trivial x dependence. This non-trivial dependence enters because, while the collinear PDF f and the helicity PDF g have simply polynomial dependencies on x at their initial scales, when these initial scales differ

from μ_0, evolution effects in f and g will complicate this parameterization. The simplest parameterization the one could take would be to choose the scale μ_0 such that it corresponds to the intrinsic scales of both f and g. This constraint limits the number of parameterizations that we can use for these distributions. While there are a large number of parameterization for f available on the market, there are relatively few parameterization for g. In this analysis, we take the DSSV parameterization from Ref. [348]. The initial scale of this parameterization is 1 GeV. Of the available PDFs, we find that the MSTW parameterization shares the same initial scale as the DSSV parameterization. We have therefore chosen to use this set for the entire paper. As a result of this choice, the x dependence of our parameterization of the transversity PDF can be shown to be given by a polynomial at μ_0.

In order to evolve $h_{q/p}$ from the initial scale to μ_{b_*} in Eq. 5.53, we must solve the DGLAP evolution equation for this distribution. However, as was stated in Ref. [349], there is no gluon transversity at leading power. As a result, the DGLAP evolution equation of the quark transversity does not mix with the gluon distribution. Therefore, the evolution equation does not contain splitting function which mix quarks and gluons and the DGLAP evolution equation is simply given by

$$\frac{\partial}{\partial \ln \mu^2} h_{q/p}(x;\mu) = \frac{\alpha_s}{2\pi} \int_x^1 \frac{d\hat{x}}{\hat{x}} P^h_{q\to q}(\hat{x})\, h_{q/p}\left(\frac{x}{\hat{x}};\mu\right) , \tag{5.55}$$

where the splitting kernel for the transversity PDF is given by

$$P^h_{q\to q}(x) = C_F \left[\frac{2\hat{x}}{(1-\hat{x})_+} + \frac{3}{2}\delta(1-\hat{x}) \right] . \tag{5.56}$$

As in the case for the Sivers we simplify the evolution in Eq. 5.55 by working in Mellin space. Because our parameterization for the transversity PDF resulted in polynomial dependence on x at $\mu_0 = 1$ GeV, the Mellin transform for the transversity PDF can be performed analytically at $\mu_0 = 1$ GeV. As a result, evolving our parameterization for the transversity PDF from μ_0 to μ_{b_*} can be accomplished by performing a single numerical integral which is associated with an inverse Mellin transformation.

To parameterize the transverse momentum dependence on the transversity TMD PDF, we follow the parameterization in Ref. [120]. Explicitly, we parameterize the non-perturbative

Sudakov for the transversity TMD PDF as

$$S^h_{\rm NP}(b,Q,Q_0) = S^f_{\rm NP}(b,Q,Q_0)\,, \tag{5.57}$$

which sets the non-perturbative Sudakov to be the same for unpolarized TMD PDF and the transversity TMD PDF.

Having parameterized the transversity TMD PDF, we now turn our attention to the transversity TMD FF. As the COMPASS measurement is consistent with zero [13], these experimental data can provide relatively little input on the size and shape of $H_{\Lambda/q}$. Therefore, we choose the relatively simple parameterization

$$H_{\Lambda/q}(z;Q) = N^H_q\, D_{\Lambda/q}(z;Q)\,, \tag{5.58}$$

where N^H_q represents parameters to be fit which control the overall size of the transversity FF.

Because the parameterization for the transversity TMD PDF in Eq. 5.54 has only non-zero contributions from the u and d quarks, only the N^H_u and N^H_d parameters can be constrained in this analysis. As such, we take all other quark contributions to be zero. Due to these assumptions, our model will predict zero transverse spin transfer for $\bar{\Lambda}$ production. Therefore, we do not consider the $\bar{\Lambda}$ production data for this process.

To parameterize the non-perturbative Sudakov term for the transversity TMD FF, we follow the procedure that was done in in Ref. [120] to set the non-perturbative Sudakov term to be the same for the unpolarized TMD PDF and the transversity TMD PDF. For the transversity TMD FF, we explicitly take

$$S^H_{\rm NP}(z_\Lambda,b,Q,Q_0) = S^D_{\rm NP}(z_\Lambda,b,Q,Q_0)\,. \tag{5.59}$$

In order to fit the N^H_u and N^H_d parameters, we use iMinuit [345, 350]. Furthermore, in order to generate the uncertainty band from the extraction, we use the replica method [346, 347] with 200 replicas. Using this simple model, we arrive at a $\chi^2/d.o.f = 1.108$ for 12 points. The fitted values for the parameters are given by $N^H_u = -0.028 \pm 0.061$ and $N^H_d = -0.089 \pm 0.210$.

In Fig. 5.15, we plot our theoretical comparison against the COMPASS experimental data. The grey band represents our theoretical uncertainty which is obtained by calculating one standard deviation away from the mean of the replicas at each point. As we see in this plot, in each kinematic region, our extraction for the transverse spin transfer is consistent with zero. In Fig. 5.16, we plot the extracted collinear transversity FF as a function of z_Λ for $Q = 2$ GeV for the u quark in red and the d quark in blue. The dashed and dotted lines represent the average over the replicas for the u and the d quark transversity FFs, respectively. Due to the experimental measurement being consistent with zero, we see that the transversity FF is also consistent with zero within our theoretical error bars.

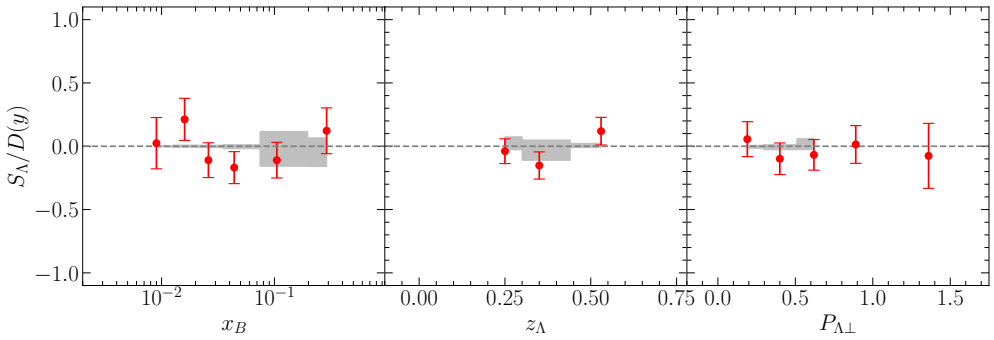

Figure 5.15: The comparison of our fitted transverse spin transfer and the experimental data at COMPASS [13]. The grey band represents our theoretical uncertainty which is obtained using the replica method, while the red error bars are the experimental data from COMPASS.

In Fig. 5.17, we plot our theoretical prediction at the future EIC for the transverse spin transfer for Λ production in SIDIS in the large x region where the valence quarks should dominate. The red band represents the theoretical uncertainty from our extraction while the black line line represents the average of the replicas. The black error bars represent our projected statistical uncertainties at the future EIC. In order to obtain the statistical uncertainties for these kinematic ranges, we have divided the statistical uncertainties from the spontaneous polarization section by a factor of 70% in order to account for the uncertainties associated with the proton beam polarization. We note that the theoretical uncertainty which we display in this analysis stems only from the parameters N_u^H and N_d^H parameters.

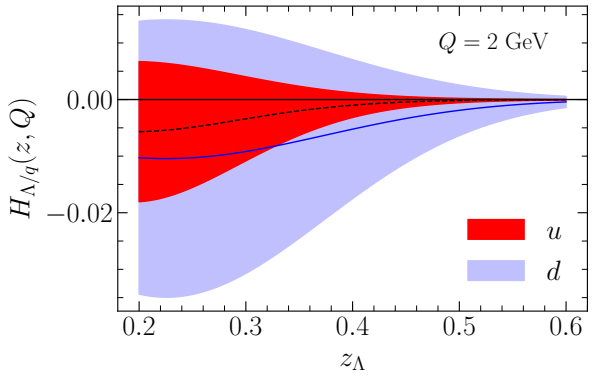

Figure 5.16: The collinear transversity FF extracted from the COMPASS measurement. The red and blue bands represent the theoretical uncertainties from our extraction which was obtained using the replica method for the u and d quarks, respectively. The dashed and solid lines represent the average of the replicas for the u and d quarks.

The full theoretical uncertainties should also contain contributions from the uncertainties from the transversity TMD PDF as well as the unpolarized TMDs and even the collinear distributions. As a result, these theoretical uncertainties underestimate the total theoretical uncertainty. However, as we see in this figure, the theoretical uncertainties are more than an order of magnitude larger than the projected statistical uncertainties at the EIC. This indicates that the EIC could potentially be used to perform the first measurement of the transverse spin transfer which is not consistent with zero and that such data would be extremely important in constraining the transversity TMD FF.

5.4.5 Projections for Λ in Jet

In this section, I first present our parameterization for spontaneous Λ polarization as well as the transverse spin transfer for Λ baryon production within the produced jet. I then present the results of our projections at the future EIC.

The definition of spontaneous Λ polarization is given in 5.33. This expression relies on the unpolarized structure functions W_{UU} in 5.35, and the structure function for spontaneous polarization $W_{UT}^{\sin(\phi_S - \phi_\Lambda)}$ in 5.40. At this point, we first provide the parameterization for

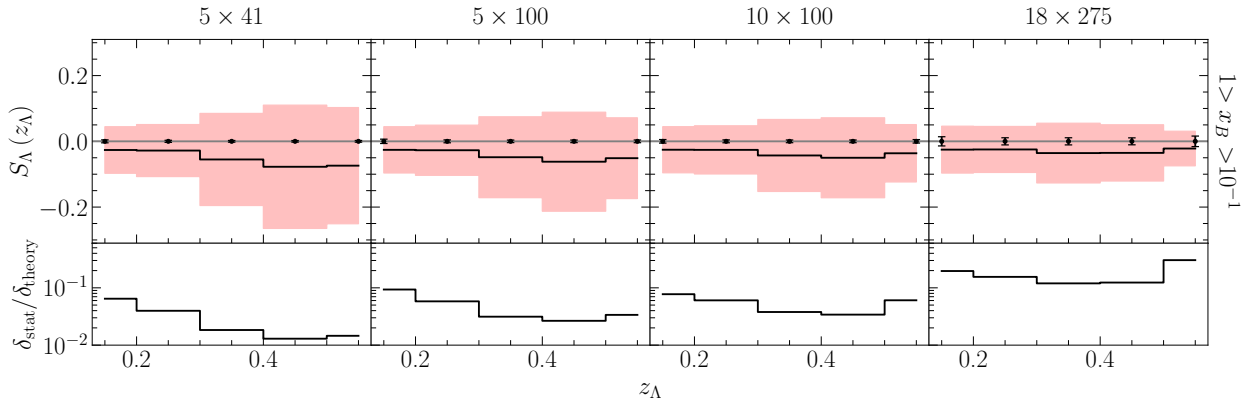

Figure 5.17: Prediction for the transverse spin transfer for Λ production at the future EIC. The label above each sub plot provides the electron beam energy $\times$ the proton beam energy. The label to the right indicates the kinematic region for x_B. In each subplot, the red bars represents the theoretical uncertainty from our extraction at one standard deviation. The black line represents the average over the replicas. The black error bars represent the projected statistical uncertainties at 40 fb^{-1}.

the unpolarized structure function.

In this section, we once again work at LO+NLL perturbative order. At LO matching, the hard functions in 5.35 and 5.42 are

$$H(Q;\mu) = 1\,, \qquad H_\perp(Q;\mu) = 1\,. \tag{5.60}$$

For this process, there are two separate soft function which contribute to $\boldsymbol{q}_\perp$. The first contribution is the well-known global soft function, which we will denote $S_{\rm global}$. This function is associated with wide angle soft gluon emissions. The second contributions is known as the collinear soft function, which we denote $S_{\rm sc}$, is associated with soft gluon exiting the jet, see for instance Ref. [135] for more details. The global soft and collinear-soft functions for this process are given up to NLO+NLL accuracy in Ref. [137] along with the anomalous dimensions. At LO+NLL accuracy, these functions are given by

$$S_{\rm global}(b;\mu) = \exp\left(\int_{\mu_{b_*}}^{\mu} \frac{d\mu'}{\mu'}\gamma_{\rm global}(b;\mu')\right)\,, \tag{5.61}$$

$$S_{\rm sc}(b, y_J, R; \mu) = \exp\left(\int_{\mu_{b_*}}^{\mu} \frac{d\mu'}{\mu'} \gamma_{\rm sc}(b, y_J, R; \mu')\right) , \tag{5.62}$$

where the anomalous dimensions for these functions are given at NLL accuracy by

$$\gamma_{\rm global}(b; \mu) = 2\frac{\alpha_s C_F}{\pi} y_J + \gamma_{\rm cusp} C_F \ln\frac{\mu^2}{\mu_b^2} , \tag{5.63}$$

$$\gamma_{\rm sc}(b, y_J, R; \mu) = -\gamma_{\rm cusp} C_F \ln\frac{\mu^2}{\mu_b^2 R^2} . \tag{5.64}$$

with $\mu_b = 2e^{-\gamma_E}/b$. In the b-space, the soft functions combine as a product so that the total soft function entering into this process, i.e. $S(b, y_J, R; \mu)$ in Eqs. 5.35, 5.40 and 5.42, is given by

$$S(b, y_J, R; \mu) = S_{\rm global}(b; \mu) S_{\rm sc}(b, y_J, R; \mu) . \tag{5.65}$$

In our numerical analysis, we will always take the jet radius $R = 1$ so that the anomalous dimension of U is simply given by the sum of the global and collinear-soft anomalous dimensions.

In order to obtain the final expression for the unpolarized structure functions in 5.35, we now use the collinear matching expression in 5.51 to write the unpolarized TMD fragmenting jet function as

$$\begin{aligned}\mathcal{G}_{\Lambda/q}(z_{J\Lambda}, j_\perp; \mu_J, \mu, \zeta_2) = \exp\left(\int_{\mu_J}^{\mu} \frac{d\mu'}{\mu'} \gamma_J(\mu')\right) \int \frac{db\, b}{2\pi} J_0\left(\frac{b j_\perp}{z_{J\Lambda}}\right) D_{\Lambda/q}(z_{J\Lambda}; \mu_{b_*}) \\ \times \exp\left(-S_{\rm pert}(b; \mu_{b_*}, \mu_J, \mu_{b_*}, \mu_J) - S^D_{\rm NP}(z_{J\Lambda}, b, Q_0, \mu_J)\right) .\end{aligned} \tag{5.66}$$

At NLL, the anomalous dimension for the TMD fragmenting jet function is given by

$$\gamma_J(\mu) = -\gamma_{\rm cusp}(\alpha_s) \ln\left(\frac{\mu_J^2}{\mu^2}\right) - \gamma_V(\alpha_s) . \tag{5.67}$$

In addition, we also include contributions from the non-global logarithms, see Refs. [162, 130, 135, 351, 164] for details. Finally, in order to obtain the structure function for unpolarized Λ production, we also apply the matching relation for the TMD PDF in 5.50 onto the expression in 5.35. After performing the matching, the unpolarized structure function is given by

$$W_{UU} = \sum_q e_q^2 \mathcal{G}_{\Lambda/q}(z_{J\Lambda}, j_\perp; \mu_J, \mu, \zeta_2) \int \frac{db\, b}{(2\pi)} J_0(b\, q_\perp) f_{q/p}(x_B; \mu_{b_*}) S(b, y_J, R; \mu)$$

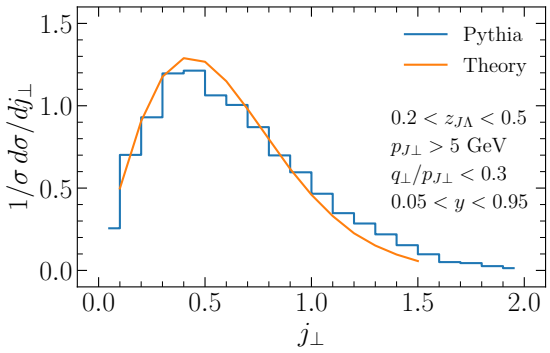

Figure 5.18: The $j_\perp$ distribution for unpolarized Λ baryons in a jet for back-to-back lepton-jet production in ep collisions. The orange line represents our theoretical prediction while the blue histogram represents the Pythia simulation. The integrated phase space is also displayed on the right side of this figure.

$$\times \exp\left(-S_{\rm pert}(b;\mu_{b_*},\mu_J,\mu_{b_*}^2,\mu_J^2) - S_{\rm NP}^f(b,Q_0,\mu)\right) . \tag{5.68}$$

To obtain numerical results for this section, we use the same parameterization for the unpolarized TMDs as in Sec. 5.3.

In order to verify the validity of our formalism so far, we have included a comparison with Pythia in Fig. 5.18. In this figure, we plot our $j_\perp$ distribution for unpolarized Λ production inside the jet. In our Monte Carlo analysis where we generated the pseudo-data for this process, we have examined events which satisfy the constraints $0.05 < y < 0.95$, $p_{J\perp} > 5$ GeV, $q_\perp/p_{J\perp} < 0.3$, and $0.2 < z_{J\Lambda} < 0.5$. Therefore, in order to generate our theoretical prediction for this data, we integrate the structure functions entering into the polarization over these kinematic regions. To perform the integration in y, we simply use the relation in 5.37 to relate the lepton rapidity to the inelasticity. To perform the integration in $p_{J\perp}$, we note that up to power corrections of $q_\perp/p_{j\perp}$ that $\ell'_\perp = p_{j\perp}$ so that we can simply perform the integration in the jet transverse momentum. We have also taken $R = 1$ for the jet radius. In this figure, the Pythia histogram as well as our theoretical curve have been normalized by integrating over $j_\perp < 1.5$ GeV. As we can see in this figure, the shape of the $j_\perp$ distribution matches the result of the Pythia simulation extremely well.

Using the collinear matching relation for the TMD PDF, the structure function for spontaneous Λ polarization can be written as

$$W_{UT}^{\sin(\phi_S-\phi_\Lambda)} = \sum_q e_q^2 \, \mathcal{G}^{\perp}_{1T,\Lambda/q}(z_{J\Lambda}, j_\perp; \mu_J, \mu, \zeta_2) \int \frac{db\, b}{(2\pi)} \, J_0(b\, q_\perp) \, f_{q/p}(x_B; \mu_{b_*}) \, S(b, y_J, R; \mu) \\ \times \exp\left(-S_{\rm pert}(b; \mu_{b_*}, \mu_J, \mu_{b_*}^2, \mu_J^2) - S^f_{\rm NP}(b, Q_0, \mu_J)\right) . \tag{5.69}$$

In order to simplify the TMD polarizing fragmenting jet function, we introduce the collinear matching relation for the TMD PFF

$$D^{\perp(1)}_{1T,\Lambda/q}\left(z, b; Q, Q^2\right) = \frac{\langle M_D^2\rangle}{2z^2 M_\Lambda^2} D^{\perp}_{1T,\Lambda/q}(z; \mu_{b_*}) \\ \times \exp\left(-S_{\rm pert}(b; \mu_{b_*}, \mu_J, \mu_{b_*}^2, \mu_J^2) - S^{\perp}_{\rm NP}(z, b, Q_0^{\perp}, Q)\right) , \tag{5.70}$$

where $Q_0^{\perp}$ is the initial scale of the TMD PFF which is given by 10.58. Using this collinear matching relation, the TMD fragmenting jet function can be written as

$$\mathcal{G}^{\perp}_{1T,\Lambda/q}(z_{J\Lambda}, j_\perp; \mu_J, \mu, \zeta_2) = -\frac{\langle M_D^2\rangle}{2z_{J\Lambda}^4 M_\Lambda} \sin\left(\phi_s - \phi_\Lambda\right) \exp\left(\int_{\mu_J}^{\mu} \frac{d\mu'}{\mu'} \gamma_J(\mu')\right) \int \frac{db\, b}{2\pi} J_1\left(\frac{b j_\perp}{z_{J\Lambda}}\right) \\ \times D^{\perp}_{1T,\Lambda/q}(z_{J\Lambda}; \mu_{b_*}) \exp\left(-S_{\rm pert}(b; \mu_{b_*}, \mu_J, \mu_{b_*}^2, \mu_J^2) - S^{\perp}_{\rm NP}(z_{J\Lambda}, b, Q_0, \mu_J)\right) . \tag{5.71}$$

In Fig. 5.19, we plot our theoretical prediction for spontaneous Λ polarization for back-to-back electron-jet production. The red and blue curves represent the theoretical uncertainty for Λ and $\bar{\Lambda}$ production in which we obtain from the baseline fit in Sec. 5.4.3.2. The red and blue error bars represent the statistical uncertainties for Λ and $\bar{\Lambda}$ production at an integrated luminosity of 100 fb^{-1}. To generate each curve, we integrate over the kinematic region $j_\perp < 1.5$ GeV, $q_\perp/p_{J\perp} < 0.3$, $p_{J\perp} > 5$ GeV, and $0.05 < y < 0.95$ following the same procedure as in the unpolarized case. From left to right, we impose the kinematic constraint that $0.01 < x_B < 0.05$, $0.05 < x_B < 0.10$, and $0.10 < x_B < 0.80$. In each of these plots, we see that the polarization for Λ is positive at small $z_{J\Lambda}$, while the polarization becomes negative at large $z_{J\Lambda}$. Furthermore, we also find that the polarization for Λ is more positive at small $z_{J\Lambda}$ and large x_B. These qualitative behaviors can be seen by studying Fig. 5.12. At small $z_{J\Lambda}$, the contribution from the u quark will dominate the polarization due to the electro-magnetic coupling of the u quark as well as the size of the u quark TMD PDF. As a

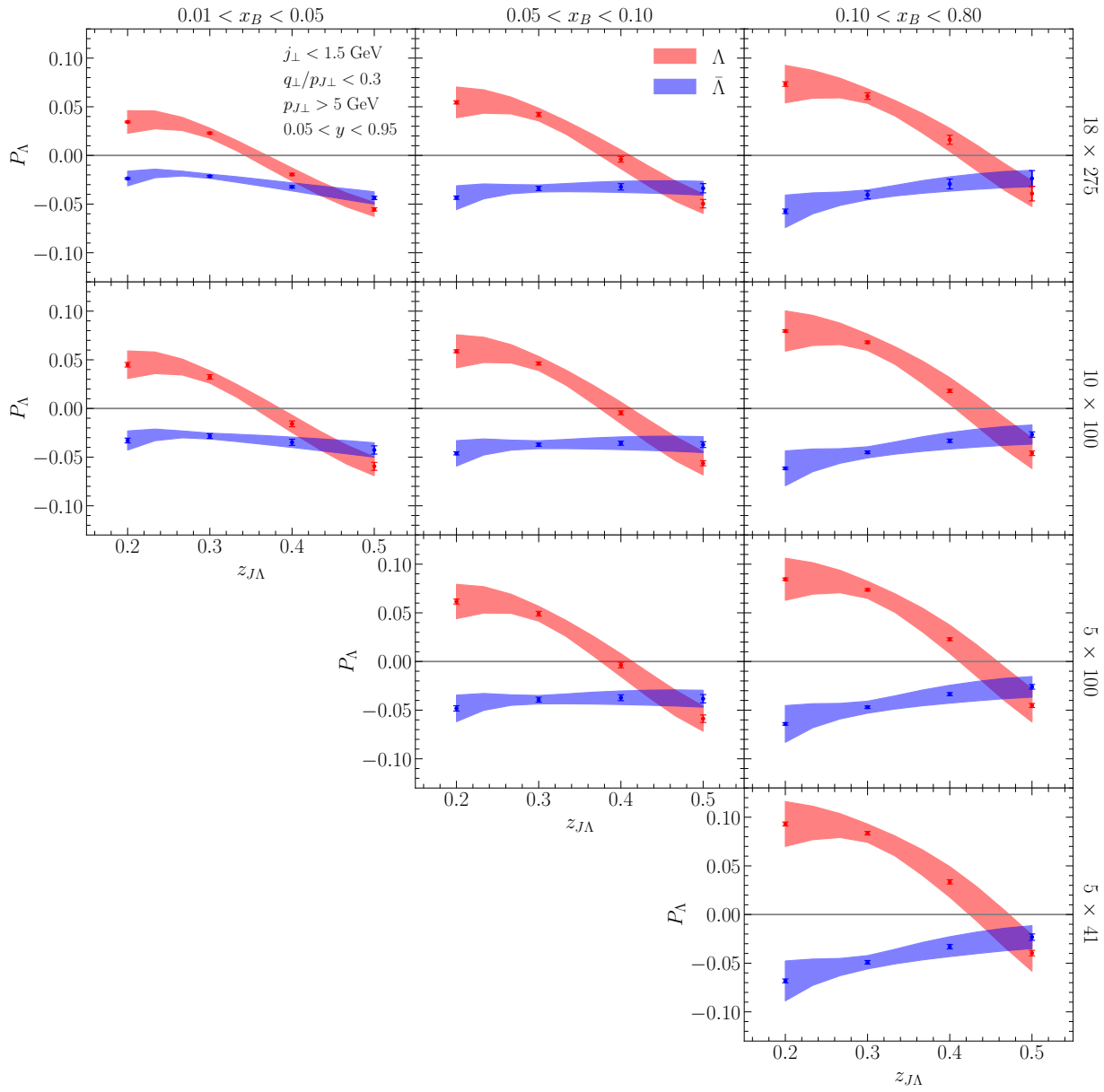

Figure 5.19: Our projections for spontaneous Λ polarization. The red band and blue bands represents our theoretical uncertainty using the parameters obtained from the baseline fit in Sec. 5.4.3.2 for Λ and $\bar{\Lambda}$ production, respectively. The error bars represent our projected statistical uncertainties at an integrated luminosity of 100 fb^{-1}. To obtain these results, we integrate over the kinematic regions listed in the top right of the left plot. Furthermore, we also impose the conditions that x_B is within each of the listed regions.

result, the polarization is large and positive at small $z_{J\Lambda}$. At large $z_{J\Lambda}$ the contributions from the other quark flavors overcome the u quark and the polarization becomes negative. Since the contribution from the u quark is largest in the large x_B region, the polarization is more positive at large x_B. For $\bar{\Lambda}$ production, the u and d are sea contributions to the TMD PFF. As a result, the contributions from the u and d quarks give large negative contributions to the polarization. We see in these plots that the size of the statistical uncertainties is smaller than the theoretical uncertainties in the region of small x_B. This is an indication that experimental data gathered in that particular region can be useful in further constraining the TMD PFF. However, the displayed theoretical uncertainties stem only from the the uncertainties from the fit parameters for the TMD PFF. Other theoretical uncertainties stemming from the unpolarized TMD PDF as well as the collinear distributions will also contribute to this prediction.

After performing the collinear matching for the transversity TMD PDF, the structure function associated with the transverse spin transfer is given by

$$W_{TT}^{\cos(\varphi_S-\phi_S)} = \sum_q e_q^2\, \mathcal{G}^T_{\Lambda/q}(z_{J\Lambda}, j_\perp; \mu_J, \mu, \zeta_2) \int \frac{db\, b}{2\pi}\, J_0(b\, q_\perp)\, h_{q/p}(x_B; \mu_{b_*}) S(b, y_J, R; \mu) \\ \times \exp\left(-S_{\rm pert}(b; \mu_{b_*}, \mu_J, \mu^2_{b_*}, \mu^2_J) - S^h_{\rm NP}(b, Q_0, \mu)\right) . \tag{5.72}$$

In this expression, the TMD fragmenting jet function is given by

$$\mathcal{G}^T_{\Lambda/q}(z_{J\Lambda}, j_\perp; \mu_J, \mu, \zeta_2) = \exp\left(\int_{\mu_J}^{\mu} \frac{d\mu'}{\mu'} \gamma_J(\mu')\right) \frac{1}{z^2_{J\Lambda}} \int \frac{db\, b}{2\pi} J_0\left(\frac{b j_\perp}{z_{J\Lambda}}\right) H_{\Lambda/q}(z_{J\Lambda}; \mu_{b_*}) \\ \times \exp\left(-S_{\rm pert}(b; \mu_{b_*}, \mu_J, \mu^2_{b_*}, \mu^2_J) - S^H_{\rm NP}(z_{J\Lambda}, b, Q_0, \mu_J)\right) . \tag{5.73}$$

To generate our theoretical prediction for back-to-back lepton-jet production, we use the extracted transversity FF from Sec. 5.3 while we once again use the parameterization from Ref. [120] for the transversity TMD PDF.

In Fig. 5.20, we plot our projected transverse spin transfer in the region of large x_B where the contribution from the valence quarks should dominate. The red bar represents the theoretical uncertainty for our fit to the N_u^H and N_d^H parameters while the error bar is

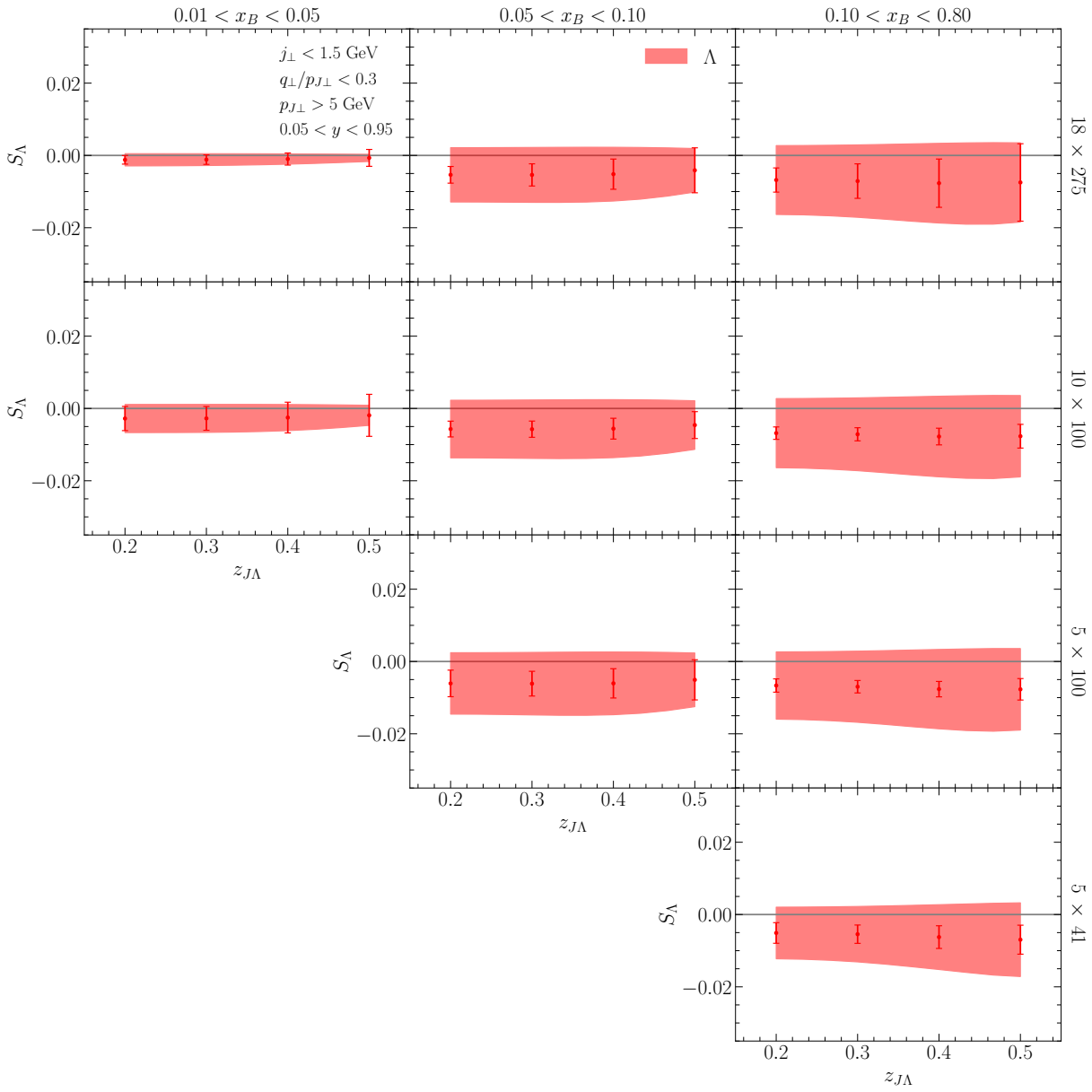

Figure 5.20: Our projection for the transverse spin transfer for Λ production for back-to-back lepton-jet production at the future EIC. The red bar represents our theoretical uncertainties which we obtain from our extraction of the N_u^H and N_d^H parameters. The error bars represent the projected statistical uncertainties at 100 fb^{-1}. We have obtained these statistical uncertainties by dividing the uncertainties from Fig. 5.19 by 70% to account for beam polarization uncertainty.

the projected statistical uncertainty. To generate the statistical uncertainties for this measurement, we use the statistical uncertainties used in Fig. 5.19, while dividing by a factor of 70% to account for the uncertainty in the polarization of the proton beam. We once again emphasize that the advertised theoretical uncertainty stems only from the parameters that enter into our fit while we expect additional large uncertainties originating from the transversity TMD PDF, the unpolarized TMDs, as well as the unpolarized collinear distributions also contribute to this measurement.

5.5 Conclusion

In this chapter we have studied Λ production at the future EIC for spontaneous transverse Λ polarization as well as transverse spin transfer in the TMD formalism. Furthermore, we have studied each of these spin configurations in SIDIS as well as back-to-back lepton-jet production. For each of these processes, we have discussed the impact of the future EIC in constraining the TMD PFF as well as the transversity TMD FF.

In order to characterize the size of the contribution that the future EIC data will have on constraining the TMD PFF, we have performed an EIC impact study. As a baseline we have performed a fit to the experimental data at Belle. While in order to test the impact of the EIC data, we have performed a Pythia analysis to generate projections for the statistical uncertainties at the future EIC. Using these statistical uncertainties, we have performed a simultaneous fit to the Belle data as well as the pseudo-data. By performing this fit, we have demonstrated a significant reduction in the theoretical uncertainties for the u and sea TMD PFF. We have also discussed how potential measurements with a ^{3}He beam can be used to significantly reduce the uncertainty for the d TMD PFF.

In order to study the impact of future EIC data on the transversity TMD FF, we have performed an extraction of this function from the recent COMPASS measurement [13] in the SIDIS process. We find that the current statistical precision from the COMPASS measurement is not high enough for an extraction of the transversity TMD FF. By providing

projections for the statistical uncertainties for Λ polarization in the SIDIS process at the future EIC, we demonstrate that the statistical uncertainties for this process at the future EIC will be roughly an order of magnitude smaller than the current theoretical uncertainties for this process. Thus, the EIC data presents the possibility of being the first significant measurement of the transversity TMD FF.

In addition, we have provided projections for Λ in jet production in back-to-back lepton-jet production. We have generated projected statistical uncertainties at the future EIC for spontaneous Λ production at an integrated luminosity of 100 fb^{-1}. We find that in the region of low x_B that the statistical precision for this process can be used to further constrain the TMD PFF. Finally, we have also provided projections for the transverse spin transfer for Λ in jets in the scattering of an electron and a transversely polarized proton at the future EIC, and we emphasize its importance in constraining the transversity TMD FF.

CHAPTER 6

Evolution of Twist-3 TMDs

6.1 Introduction

The formulation of TMD factorization theorems relies heavily on the neglecting power corrections of order $q_\perp/Q$ and M/Q. In all of the formalism that I have presented up to this point, this has been the case. When considering power corrections to the differential cross section, at twist-3 for instance, the formalism becomes much more complicated and subtle due to the large number of additional areas at which power correction enter. These power corrections introduce a wide range of new distributions which can be experimentally probed, and which provide additional insight into the structure of hadrons. As I will discuss in this chapter, these sub-leading power distributions are named 'intrinsic', 'kinematic', and 'dynamical' distributions. Establishing QCD factorization and resummation theorems beyond leading power allows us to pursue precision in a novel direction and serves to challenge our current understanding of the IR behavior of QCD. Despite the challenges that sub-leading power contributions provide, the TMD community over the past decade has been pushing for an ever greater precision determination of QCD dynamics in hadrons.

To provide some context, currently the perturbative contributions for twist-2 TMDs have been carried out to four loops, see for instance Refs. [352] and [353] for a calculation of the four loop rapidity anomalous dimension for instance [354] for a phenomenological application of these calculations. So far however, NLP corrections to the TMD cross section have only been carried out in Semi-Inclusive DIS and Drell-Yan at LO in QCD in [355, 86, 356]. Over the past few years, many interesting developments have emerged in this direction. Recently, NLP corrections have been studied in a SCET formalism in Ref. [357] at the Lagrangian

level for Semi-Inclusive DIS. Additionally in Ref. [358], the authors studied the evolution of the dynamical twist-3 distributions at one loop. Despite this progress, it still remains to be seen if the standard methods that we use to perform calculations of twist-2 cross sections can be applied at twist-3. In Semi-Inclusive DIS, an analysis was performed by Bacchetta et al. in [359] where attention was given to azimuthal and polarization dependence. In this study the authors found that there were mismatches between the collinear factorization region where $q_\perp \sim Q$ and the TMD region where $q_\perp \ll Q$ for the Cahn effect [360, 361]. More recently in Ref. [362], the authors conjectured that the soft function at NLP should be the same as the soft function at LP and as a result, one can match between the collinear and TMD factorization regions at sub-leading twist. The result of this study indicated that the techniques which are used at twist-2 can be applied to higher twists. Nevertheless, so far explicit one loop calculations of these results have not been performed to verify this assumption.

In our ongoing work, we establish a complete factorization for Semi-Inclusive DIS and Drell-Yan at twist-3 beyond tree level. We explicitly calculate the hard, soft, and collinear TMDs at one loop to obtain the evolution equations for these processes at NLO+NLL accuracy for the intrinsic and kinematic sub-leading TMDs. Furthermore, we explicitly calculate the Collins-Soper (rapidity) evolution equation for the 'dynamical' sub-leading twist distributions. From this analysis, we clarify subtleties in the assumption that was made in Ref. [362]. Within this analysis however, we find factorization breaking effects and we also discover that gauge invariance does not manifest diagram by diagram in perturbation theory for the intrinsic and kinematic distributions. These results indicate that the current formulations of the twist-3 factorization theorems are incorrect. In this chapter, I will discuss the various twist-3 contributions to the cross section and explicitly calculate the evolution equations for the hard, collinear, and soft contributions to the cross section at NLP.

6.2 Distributions at Twist-3

6.2.1 Overview

To illustrate how NLP contributions enter into the cross section, it is convenient to begin by examining the hadronic tensor for inclusive DIS as an illustrative example

$$W^{\mu\nu} = \frac{1}{2\pi}\int d^4x e^{iq\cdot x}\langle P\left|\mathcal{T}j^{\mu}(x)j^{\nu}(0)\right|P\rangle\,. \tag{6.1}$$

If we were to perform an operator product expansion of this expression, we would obtain

$$W^{\mu\nu} = \sum_i C_i(Q^2)\langle P\left|\theta_i\right|P\rangle\,, \tag{6.2}$$

where C_i are the Wilson coefficients and θ_i are local operators. The twist of each operator can be obtained by a simple power counting procedure. In the previous sections, we saw that the operators $\theta = \bar{\psi}n_\mu\gamma^\mu\psi$, $\theta = \bar{\psi}n_\mu\gamma^\mu\gamma^5\psi$, and $\theta = in_\mu\sigma^{\mu k}\gamma^5$ provide leading twist contributions to the cross section. By performing a power counting, one can see that the matrix elements must be proportional to $n\cdot P$ while the Wilson coefficient function will scale like Q^{-m} where m is some arbitrary power. Therefore, the leading power terms scale like $n\cdot P/Q^m \sim Q^{-m+1}$ since $n\cdot P \sim Q$. If we were to examine operators of the form $\theta = \bar{\psi}\psi$, we would find that the matrix elements would be proportional to a scalar. Since the only scalar with mass dimensions in massless QCD is the hadron mass, the matrix elements would be proportional to M and the contributions of these terms in the hadronic tensor would scale as $M/Q \times Q^{-m+1}$, producing a power suppression in comparison with the leading power contribution. Furthermore, we could examine operators of the form $\theta = \bar{\psi}\gamma^k\psi$ where k is a transverse index. The matrix elements for this operator would scale as $q_\perp^k$ where $\boldsymbol{q}_\perp$ is a transverse momentum. While in DIS we would integrate over $\boldsymbol{q}_\perp$, these contributions would not enter. However, for TMD observables, these operators then lead to a power suppression of $q_\perp/Q$ in the TMD region where $q_\perp \ll Q$. The insertion of terms which lead to a direct mass or $q_\perp$ suppression from the insertion of the quark field operators in the OPE are known as the 'intrinsic' sub-leading TMDs. Additionally, we could also consider examining operators of the form $\theta = \bar{\psi}A_\perp n_\mu\gamma^\mu\psi$ where $A_\perp$ is a transverse gluon field. Due to the power counting,

we know that $A_\perp \sim q_\perp$. Through a dimensional analysis argument, the Wilson coefficient function would then need an additional power of Q in the denominator, leading to a $q_\perp/Q$ suppression in the hadronic tensor. The distribution which is generated with the introduction of this transverse gluon field is known as the dynamical sub-leading distribution.

Lastly, it was discussed in Chapter 2 that the φ field can be integrated out of the SCET Lagrangian through the equations of motion. Specifically, the equation of motion is given by

$$\not{D}_\perp \frac{\not{n}}{2}\xi(x) = n\cdot D\,\varphi(x)\,, \qquad \bar{\xi}(x)\frac{\not{\bar{n}}}{2}\not{D}_\perp = \bar{\varphi}(x)\,n\cdot D\,. \tag{6.3}$$

As I will demonstrate in the next section, the intrinsic sub-leading distributions are associated with the φ field while the dynamical distributions are associated with the field configuration $A_\perp\xi$. However, there are still 'kinematic' suppressed field configurations that are associated with $\not{\partial}_\perp\not{n}/2\,\xi$ field configurations. These fields were considered in Ref. [357], where the authors considered such terms by introducing transverse derivative to the current in the OPE and treated the power corrections using SCET.

In this chapter, I will mainly focus on the factorization and evolution associated with the intrinsic and kinematic suppressed distributions while I'll leave many aspects of the dynamical suppressed distributions for a later study.

6.2.2 Intrinsic Sub-Leading TMDs

To introduce the intrinsic sub-leading distributions in full QCD, it is useful to re-visit the definition of the intrinsic sub-leading field

$$\xi^c(x) = \frac{\not{\bar{n}}\not{n}}{4}\psi^c(x)\,, \qquad \varphi^c(x) = \frac{\not{n}\not{\bar{n}}}{4}\psi^c(x)\,, \tag{6.4}$$

such that $\psi^c(x) = \xi^c(x) + \varphi^c(x)$, where ξ^c and φ^c are the so-called good and bad field components of ψ^c and $\not{\bar{n}}\not{n}/4$ and $\not{n}\not{\bar{n}}/4$ are idempotent operators. Performing an OPE in a similar way that was discussed in the previous section and expressing $\psi^c(x)$ in terms of φ^c and ξ^c we are left with the four field configurations

$$\langle P,\boldsymbol{S}|\bar{\xi}^c\theta\xi^c|P,\boldsymbol{S}\rangle\,, \qquad \langle P,\boldsymbol{S}|\bar{\varphi}^c\theta\xi^c|P,\boldsymbol{S}\rangle\,, \tag{6.5}$$

Twist 2	Twist 3	Twist 4
$\frac{1}{2}\not{n}$, $\frac{1}{4}\not{\bar{n}}$	$\frac{1}{2}$,$\frac{1}{2}$	$\frac{1}{2}\not{\bar{n}}$, $\frac{1}{4}\not{n}$
$\frac{1}{2}\not{n}\gamma^5$, $\frac{1}{4}\gamma^5\not{\bar{n}}$	$\frac{1}{2}\gamma^5$, $\frac{1}{2}\gamma^5$	$\frac{1}{2}\not{\bar{n}}\gamma^5$, $\frac{1}{4}\gamma^5\not{n}$
$\frac{i}{2}\sigma^{k+}\gamma^5$, $\frac{i}{4}\gamma^5\sigma_{-k}$	$\frac{1}{2}\gamma^k$, $\frac{1}{2}\gamma_k$	$\frac{i}{2}\sigma^{k-}\gamma^5$, $\frac{i}{4}\gamma^5\sigma_{+k}$
	$\frac{1}{2}\gamma^k\gamma^5$, $\frac{1}{2}\gamma^5\gamma_k$	
	$\frac{i}{2}\sigma^{kl}\gamma^5$, $\frac{i}{4}\gamma^5\sigma_{lk}$	
	$\frac{i}{4}\sigma^{+-}\gamma^5$, $\frac{i}{4}\gamma^5\sigma_{+-}$	

Table 6.1: The operators entering into the Fierz decomposition organized by twist for P_1. We note that the operators for P_2 can be obtained simply by interchanging n and $\bar{n}$. The operators are organized as Γ, $\bar{\Gamma}$. In this chapter k and l represent transverse indices. The operators listed in this table with a single transverse Lorentz index represent two distinct operators in the Fierz decomposition. In total, this results in 16 distinct operators.

$$\langle P, \boldsymbol{S}|\bar{\xi}^c\theta\varphi^c|P, \boldsymbol{S}\rangle\,, \qquad \langle P, \boldsymbol{S}|\bar{\varphi}^c\theta\varphi^c|P, \boldsymbol{S}\rangle\,.$$

If we were to take θ to be one of the operators in the 'Twist 2' column of Tab. 6.1, using the idempotence of the projection operators we could easily demonstrate that the matrix elements will vanish for all field configurations with the exception of the top left one in Eq. (6.5). Similarly, if we were to insert θ from the 'Twist 3' column, we would find that only the top right and bottom left field configurations would lead to a non-vanishing matrix elements. Finally, we could also consider the twist-4 case where the bottom right field configuration can contribute.

Since we know the exact operators which generate matrix elements of the intrinsic twist-3

distributions, we can parameterize the twist-3 TMD PDF

$$\begin{aligned}\Phi^{(3)}_{\text{unsub}}(x,\boldsymbol{k}_\perp,\boldsymbol{S};\mu,\zeta/\nu^2) =& \frac{M}{P^+}\Bigg[\left(e-\frac{\epsilon_\perp^{\rho\sigma}k_{\perp\rho}S_{\perp\sigma}}{M}e_T^\perp\right)\frac{1}{2}-i\left(\lambda_g e_L-\frac{\boldsymbol{k}_\perp\cdot\boldsymbol{S}_\perp}{M}e_\perp\right)\frac{\gamma^5}{2} \\ &+\left(\frac{k_\perp^k}{M}f^\perp-\epsilon_\perp^{kl}S_{\perp l}f'_\perp-\frac{\epsilon_\perp^{kl}k_{\perp l}}{M}\left(\lambda_g f_L^\perp-\frac{\boldsymbol{k}_\perp\cdot\boldsymbol{S}_\perp}{M}f_\perp^\perp\right)\right)\frac{\gamma_k}{2} \\ &+\left(g'_\perp S_\perp^k-\frac{\epsilon_\perp^{kl}k_{\perp l}}{M}g^\perp+\frac{k_\perp^k}{M}\left(\lambda_g g_L^\perp-\frac{\boldsymbol{k}_\perp\cdot\boldsymbol{S}_\perp}{M}g_\perp^\perp\right)\right)\frac{\gamma^5\gamma_k}{2} \\ &+\left(\frac{S_\perp^k k_\perp^l}{M}h_\perp^\perp\right)\frac{i\gamma^5\sigma_{lk}}{4}+\left(h+\lambda_g h_L-\frac{\boldsymbol{k}_\perp\cdot\boldsymbol{S}_\perp}{M}h^\perp\right)\frac{i\gamma^5\sigma_{+-}}{4}\Bigg].\end{aligned} \tag{6.6}$$

where the superscript in the expression for Φ at the left-hand side denotes the twist. The functions entering into this decomposition are known as the intrinsic sub-leading distributions. In this chapter, I will mainly focus on the $f^\perp$ distribution as an illustrative example. This distribution is known to generate the Cahn effect in the TMD region, see for instance [86]. At the cross section level, the Cahn effect in Drell-Yan is generated by terms of the form

$$d\sigma_{\text{Cahn}} \sim \frac{k_\perp^k}{P^+}f^\perp \otimes f \otimes H_{\text{int}} \otimes S_{\text{int}}\,, \tag{6.7}$$

where H_{int} and S_{int} are the intrinsic hard and soft functions.

6.2.3 Kinematic Sub-leading Distributions

I will now discuss the kinematic suppressed fields, which are given by

$$\xi^c_{\text{kin}}(x) = \frac{i\partial\!\!\!/_\perp \bar{n}\!\!\!/}{2in\cdot\partial}\xi^c(x)\,, \qquad \xi^{\bar{c}}_{\text{kin}}(x) = \frac{i\partial\!\!\!/_\perp n\!\!\!/}{2i\bar{n}\cdot\partial}\xi^{\bar{c}}(x)\,. \tag{6.8}$$

In momentum space, it can be directly seen that these fields are suppressed by a factor of λ relative to the ξ fields. We can define kinematic suppressed correlators by replacing one good field in the twist-2 correlator with a kinematic suppressed field. In the case of the collinear correlation function, we have

$$\Phi^{\text{kin}}_{jj'\,\text{unsub}}(x,\boldsymbol{k}_\perp,\boldsymbol{S};\mu,\zeta/\nu^2) = \int\frac{d^4\xi}{(2\pi)^4}\,e^{ik\cdot\xi}\,\delta\left(\xi^+\right) \tag{6.9}$$

$$\times \left[\left\langle P, \boldsymbol{S} \left| \bar{\xi}^c_{j'}(\xi) \mathcal{U}^{\bar{n}}_{(\xi^-,-\infty;\boldsymbol{\xi}_\perp)} \mathcal{U}^T_{(\boldsymbol{\xi}_\perp,\mathbf{0};-\infty)} \mathcal{U}^{\bar{n}}_{(-\infty,0,\mathbf{0}_\perp)} \xi^c_{\text{kin j}}(0) \right| P, \boldsymbol{S} \right\rangle \right.$$
$$\left. + \left\langle P, \boldsymbol{S} \left| \bar{\xi}^c_{\text{kin j}'}(\xi) \mathcal{U}^{\bar{n}}_{(\xi^-,-\infty;\boldsymbol{\xi}_\perp)} \mathcal{U}^T_{(\boldsymbol{\xi}_\perp,\mathbf{0};-\infty)} \mathcal{U}^{\bar{n}}_{(-\infty,0,\mathbf{0}_\perp)} \xi^c_j(0) \right| P, \boldsymbol{S} \right\rangle \right] .$$

In a covariant gauge where the transverse Wilson line vanishes, we can integrate in the transverse direction by parts. In doing so, we can write the correlator as

$$\Phi^{\text{kin}}_{jj'\,\text{unsub}}(x, \boldsymbol{k}_\perp, \boldsymbol{S}; \mu, \zeta/\nu^2) = \sum_a \bar{\Gamma}^a_{jj'} \int \frac{d^4\xi}{(2\pi)^4} e^{ik\cdot\xi} \delta\left(\xi^+\right) \tag{6.10}$$
$$\times \left\langle P, \boldsymbol{S} \left| \bar{\xi}^c(\xi) \mathcal{U}^{\bar{n}}_{(\xi^-,-\infty;\boldsymbol{\xi}_\perp)} \mathcal{U}^{\bar{n}}_{(-\infty,0,\mathbf{0}_\perp)} \Gamma^{[a]} \xi^c(0) \right| P, \boldsymbol{S} \right\rangle ,$$

where $\Gamma^{[a]} = [\Gamma^a, \not{k}_\perp \not{n}/2k^+]$ and we have inserted a complete set of operators. In Tab. 6.2, we have provided $\Gamma^{[a]}$ and $\bar{\Gamma}^a$ for each operator entering into the Fierz decomposition. The $\bar{\Gamma}^a$ operators enter into the hard part of the calculation while the $\Gamma^{[a]}$ operators enter into the trace with the quark correlation function. Analogous to the case for the intrinsic sub-leading correlation function, the contribution of these functions at the cross section go like

$$d\sigma_{\text{Cahn}} \sim \frac{k^k_\perp}{P^+} f^{\text{kin}} \otimes f \otimes H_{\text{kin}} \otimes S_{\text{kin}} , \tag{6.11}$$

where f^{kin} is closely analogous to the unpolarized TMD PDF except it is a correlator of a kinematic suppressed field and a good field and H_{kin} and S_{kin} are the kinematic hard and soft functions.

6.2.4 Dynamical Sub-leading Distributions

At the cross section level, the introduction of an additional transverse gluon alters the current operators and the hadronic tensor in Drell-Yan for instance can be written as

$$W^{(3)}_{\mu\nu} = \frac{1}{(2\pi)^4} \int d^4x\, e^{-iqx} \left\langle P_1\,, P_2 \left| \left(J^{(3)\,\dagger}_\mu(x)\, J^{(2)}_\nu(0) + J^{(2)\,\dagger}_\mu(x)\, J^{(3)}_\nu(0) \right) \right| P_1\,, P_2 \right\rangle , \tag{6.12}$$

where $J^{(3)}_\mu$ is the current associated with the three parton interactions while $J^{(2)}_\mu$ is the current associated with two partons. In Fig. 6.1, we have included the relevant tree level diagrams for this current. By examining this hadronic tensor in momentum space, we can write this expression as

Twist 2	Twist 3	Twist 4
$0\ ,\ \frac{1}{4}\not{\bar{n}}$	$0,\ \frac{1}{2}$	$-\frac{\not{k}_\perp}{k^+}\ ,\ \frac{1}{4}\not{n}$
$0,\ \frac{1}{4}\gamma^5\not{\bar{n}}$	$0,\ \frac{1}{2}\gamma^5$	$-\frac{\not{k}_\perp}{k^+}\gamma^5,\ \frac{1}{4}\gamma^5\not{n}$
$0,\ \frac{i}{4}\gamma^5\sigma_{-k}$	$\frac{k_\perp^i}{k^+}\frac{\not{n}}{2},\ \frac{1}{2}\gamma_k$	$\frac{i}{2}\sigma^{k-}\gamma^5\ ,\ \frac{i}{4}\gamma^5\sigma_{+k}$
	$\frac{k_\perp^i}{k^+}\frac{\not{n}}{2}\gamma^5,\ \frac{1}{2}\gamma^5\gamma_k$	
	$\frac{k_\perp^k}{k^+}\frac{i}{2}\sigma^{+l}\gamma^5-\frac{k_\perp^l}{k^+}\frac{i}{2}\sigma^{+k}\gamma^5,\ \frac{i}{4}\gamma^5\sigma_{lk}$	
	$-\frac{k_{\perp\,i}}{k^+}\frac{i}{2}\sigma^{+i}\gamma^5,\ \frac{i}{4}\gamma^5\sigma_{+-}$	

Table 6.2: The operators entering into the Fierz decomposition organized by twist for P_1. We note that the operators for P_2 can be obtained simply by interchanging n and $\bar{n}$. The operators are organized as $\Gamma^{[a]}$, $\bar{\Gamma}^a$. In this chapter k and l represent transverse indices.

$$W_3^{\mu\nu} = \frac{1}{N_c}\sum_q e_q^2 \int d^2\boldsymbol{k}_{1\perp}\, d^2\boldsymbol{k}_{2\perp}\, d^2\boldsymbol{\lambda}_\perp \delta^{(2)}(\boldsymbol{k}_{1\perp}+\boldsymbol{k}_{2\perp}+\boldsymbol{\lambda}_\perp-\boldsymbol{q}_\perp)\, S\left(\boldsymbol{\lambda}_\perp;\mu,\nu\right) \tag{6.13}$$
$$\times\left\{\int dp_1^+ \,\mathrm{Tr}\left[\gamma_\rho \frac{-\not{k}_2-\not{p}_1}{(k_2+p_1)^2+i\epsilon}\gamma^\nu \Phi^\rho_{A\,\mathrm{unsub}}(x_1,x_1',\boldsymbol{k}_{1\perp};\mu,\zeta_1/\nu^2)\gamma^\mu \Phi_{\mathrm{unsub}}(x_2,\boldsymbol{k}_{2\perp};\mu,\zeta_2/\nu^2)\right]\right.$$
$$\left.+\ldots\right.,$$

where the explicit expression listed here is the top left diagram of Fig. 6.1 dots contain the contributions of the additional diagram. To interpret this expression, it is useful to introduce the three parton correlation function

$$\Phi^\alpha_{F,jj'\,\mathrm{unsub}}\left(x,x',\boldsymbol{k}_\perp,\boldsymbol{S};\mu,\zeta/\nu^2\right) = \int \frac{d^4\xi}{(2\pi)^4}\frac{d^4\eta}{(2\pi)^4}\delta\left(\xi^+\right)\,\delta\left(\eta^+\right)\,P^+ e^{ik\cdot\xi}e^{\frac{i}{2}\sqrt{\zeta}(\xi^--\eta^-)} \tag{6.14}$$
$$\times\left\langle P,\boldsymbol{S}\left|\bar{\xi}_{j'}(\xi)\mathcal{U}^{\bar{n}}_{(\xi^-,-\infty;\boldsymbol{\xi}_\perp)}\mathcal{U}^T_{(\boldsymbol{\xi}_\perp,\boldsymbol{0}_\perp;-\infty)}\mathcal{U}^{\bar{n}}_{(-\infty,\zeta^-;\boldsymbol{0}_\perp)}igF^{+\alpha}(\zeta)\mathcal{U}^{\bar{n}}_{(\zeta^-,0;\boldsymbol{0}_\perp)}\xi_j(0)\right|P,\boldsymbol{S}\right\rangle\,.$$

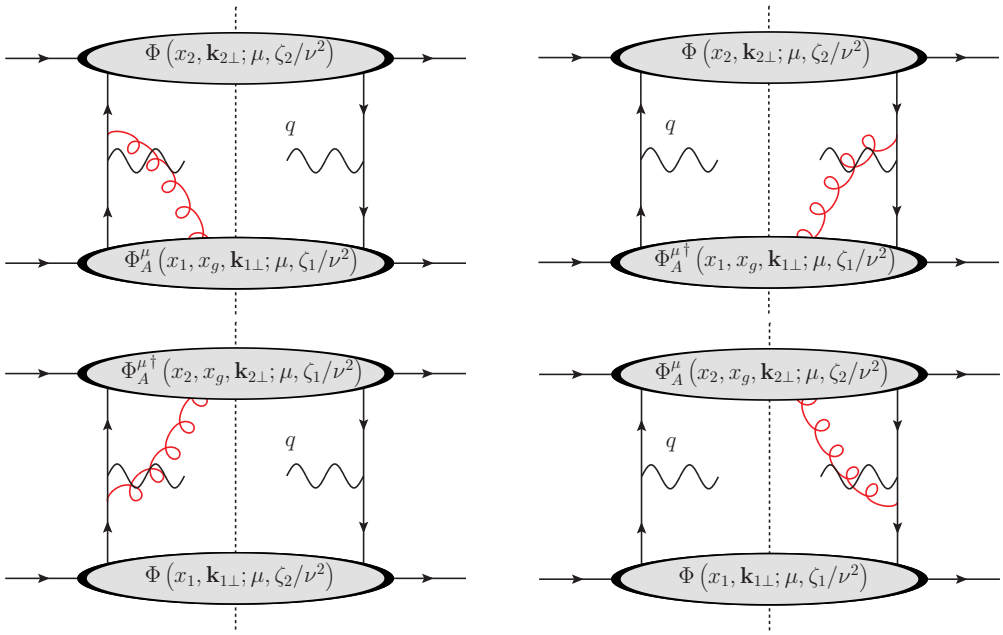

Figure 6.1: The four contributions at tree level for the dynamical twist 3 contributions to the Drell-Yan cross section.

where α is a transverse Lorentz index. It's important to note that k refers to the momentum of the quark which is isolated on one side of the cut away from the gluon. This correlation function can be related to one containing a transverse A^α field trivially in light-cone gauge. We can then parameterize the Φ_A correlator as

$$
\begin{aligned}
&\Phi^{\alpha}_{A\,\text{unsub}}\left(x, x', \boldsymbol{k}_\perp, \boldsymbol{S}; \mu, \zeta/\nu^2\right) = \qquad (6.15)\\
&\frac{xM}{2}\Bigg\{\Bigg[\left(\tilde{f}^{\perp} - i\tilde{g}^{\perp}\right)\frac{k_\perp^\alpha}{M} - \left(\tilde{f}'_{\perp} + i\tilde{g}'_{\perp}\right)\epsilon_{\perp\,\rho\sigma}S_\perp^\sigma\\
&\quad - \left(\lambda\tilde{f}_L^{\perp} - \frac{\boldsymbol{k}_\perp\cdot\boldsymbol{S}_\perp}{M}\tilde{f}_T^{\perp}\right)\frac{\epsilon_{\perp\,\rho\sigma}k_\perp^\sigma}{M} - i\left(\lambda\tilde{g}_L^{\perp} - \frac{\boldsymbol{k}_\perp\cdot\boldsymbol{S}_\perp}{M}\tilde{g}_T^{\perp}\right)\frac{\epsilon_{\perp\,\rho\sigma}k_\perp^\sigma}{M}\Bigg](g_\perp^{\alpha\rho} - i\epsilon_\perp^{\alpha\rho}\gamma_5)\\
&\quad - \left[\left(\lambda\tilde{h}_L^{\perp} - \frac{\boldsymbol{k}_\perp\cdot\boldsymbol{S}_\perp}{M}\tilde{h}_T^{\perp}\right) + i\left(\lambda\tilde{e}_L^{\perp} - \frac{\boldsymbol{k}_\perp\cdot\boldsymbol{S}_\perp}{M}\tilde{e}_T^{\perp}\right)\right]\gamma_\perp^\alpha\gamma_5\\
&\quad + \left[\left(\tilde{h} + i\tilde{e}\right) + \left(\tilde{h}_\perp^{\perp} - i\tilde{e_\perp^{\perp}}\right)\frac{\epsilon_\perp^{\rho\sigma}k_{\perp\rho}S_{\perp\sigma}}{M}\right]i\gamma_\perp^\alpha + \ldots(g_\perp^{\alpha\rho} + i\epsilon_\perp^{\alpha\rho}\gamma_5)\Bigg\}\frac{\not{n}}{2}\,.
\end{aligned}
$$

Therefore, one can show that these terms lead to contributions of the form

$$
d\sigma_{\text{Cahn}} \sim \frac{k_\perp^k}{P^+}\tilde{f}^{\perp}\otimes f\otimes H_{\text{dyn}}\otimes S_{\text{dyn}}\,, \qquad (6.16)
$$

where $H_{\rm dyn}$ and $S_{\rm dyn}$ are the dynamical hard and soft functions. Recently in [357] it was demonstrated that $H_{\rm dyn}$ depends on two collinear variables x and x'.

6.3 Perturbative Corrections and Collinear Matching

In this section, I will explicitly calculate the anomalous dimensions of each of the different regions that enter at NLP. Using these contributions, I will discuss implications for renormalization group consistency.

6.3.1 Hard Corrections for the Two Parton Sub-Process

To obtain the hard contributions to the differential cross section beyond LO, I'll note that the hard contribution enters from the contraction between the leptonic tensor with the trace entering into the hadronic tensor. At tree level for Semi-Inclusive DIS, we can write

$$L_{\mu\nu}^{\rm DIS}\,{\rm Tr}\left[\gamma^\mu\,\bar\Gamma_1^a\,\gamma^\nu\,\bar\Gamma_1^b\right] = Q^2 f(\psi,y)\,H_{\rm DIS}^{(0)}(Q;\mu)\,, \tag{6.17}$$

where $H_{\rm DIS}^{(0)}(Q;\mu)=1$ is the tree level hard function and $f(\psi,y)$ represents the angular correlation which depends on the operators. We note at this point that an analogous expression can also be obtained for Drell-Yan. To account for hard interactions entering into the cross section, it is necessary to account for the virtual interactions between the quarks. To account for these graphs, we make the replacement for the photon-quark vertex in Semi-Inclusive DIS

$$\gamma^\nu \to \gamma^\nu + \frac{\alpha_s C_F}{2\pi} F_{\rm DIS}^\nu\left(Q;\mu\right) + \mathcal{O}\left(\alpha_s^2\right) \tag{6.18}$$

where $F_{\rm DIS}^\nu\left(Q;\mu\right)$ is the one loop QCD form factor for the quark-photon vertex which is explicitly given in dimensional regularization by

$$\begin{aligned} F_{\rm DIS}^\nu\left(Q;\mu\right) = {}& \gamma^\nu\left(1+\frac{1}{2\epsilon}-\frac{1}{2}L_Q\right) + \left(\frac{2}{\epsilon}+2L_Q+3\right)\frac{\bar{n}\!\!\!/\gamma^\nu n\!\!\!/}{4} \\ & + \left(-\frac{1}{\epsilon^2}-\frac{1}{4}L_Q^2-\frac{1}{\epsilon}L_Q-\frac{1}{\epsilon}-L_Q+\frac{\pi^2}{12}-3\right)\frac{\bar{n}\!\!\!/\gamma^\nu n\!\!\!/}{4} + \left(-L_Q-\frac{1}{\epsilon}-1\right)\frac{\bar{n}\!\!\!/\bar{n}^\nu}{4} \\ & + \left(-2L_Q-\frac{2}{\epsilon}-3\right)\frac{n\!\!\!/\bar{n}^\nu}{4} + \left(-L_Q-\frac{1}{\epsilon}-1\right)\frac{n\!\!\!/ n^\nu}{4} + \left(-2L_Q-\frac{2}{\epsilon}-3\right)\frac{\bar{n}\!\!\!/ n^\nu}{4}\,. \end{aligned} \tag{6.19}$$

We also note that the QCD form factor for Drell-Yan can be obtained through the relation $F^{\nu}_{\rm DY}\left(Q;\mu\right) = F^{\nu}_{\rm DIS}\left(iQ;\mu\right)$. Using this expression, the NLO hard contributions to the cross section is given directly by

$$\begin{aligned} H^{(1)}_{\rm DIS}\left(Q;\mu\right) = &\frac{1}{Q^2 f(\psi,y)}\frac{\alpha_s C_F}{2\pi} \\ &\times \left(\mathrm{Tr}\left[F^{\rho}_{\rm DIS}\left(Q;\mu\right)\,\bar{\Gamma}^a_1\,\gamma^{\sigma}\,\bar{\Gamma}^b_1\right] + \mathrm{Tr}\left[\gamma^{\rho}\,\bar{\Gamma}^a_1\,F^{\sigma}_{\rm DIS}\left(Q;\mu\right)\,\bar{\Gamma}^b_1\right]\right) L^{\rm DIS}_{\rho\sigma}\,. \end{aligned} \tag{6.20}$$

Inserting any of the twist-2 operators gives

$$\hat{H}^{\rm LP}_{\rm DIS}(Q;\mu) = 1 + \frac{\alpha_s C_F}{2\pi}\left[-\frac{2}{\epsilon^2} - \frac{3}{\epsilon} - L_Q^2 - \frac{2L_Q}{\epsilon} - 3L_Q + \frac{\pi^2}{6} - 8\right], \tag{6.21}$$

where the hat indicates that the hard function is unsubtracted. We note at this point that the expression for Drell-Yan can be obtained by replacing L_Q^2 with $L_Q^2 - \pi^2$.

For the NLP trace, we use the the combination of operators $\Gamma_a = \not{n}/4$ and $\Gamma_b = \gamma^i/2$ or $\Gamma_a = \gamma^i/2$ and $\Gamma_b = \not{\bar{n}}/4$. In this case, the hard function entering into the cross section is given by

$$\hat{H}^{\rm int}_{\rm DIS}(Q;\mu) = 1 + \frac{\alpha_s C_F}{2\pi}\left[-\frac{1}{\epsilon^2} - \frac{2}{\epsilon} - \frac{1}{2}L_Q^2 - \frac{L_Q}{\epsilon} - 2L_Q + \frac{\pi^2}{12} - 5\right], \tag{6.22}$$

and we once again note that the hard function for Drell-Yan can be obtained by replacing L_Q^2 with $L_Q^2 - \pi^2$.

Using the definition of the unsubtracted hard function, we can obtain the subtracted hard function through multiplicative renormalization as

$$\hat{H}(Q;\mu) = Z(Q;\mu)H(Q;\mu) + \mathcal{O}(\alpha_s^2)\,, \tag{6.23}$$

where the divergences are contained in the multiplicative renormalization factor $Z(Q;\mu)$. This allows us to obtain the subtracted hard functions

$$H_{\rm DIS}(Q;\mu) = 1 + \frac{\alpha_s C_F}{2\pi}\left[-L_Q^2 - 3L_Q + \frac{\pi^2}{6} - 8\right], \tag{6.24}$$

$$H^{\rm int}_{\rm DIS}(Q;\mu) = 1 + \frac{\alpha_s C_F}{2\pi}\left[-\frac{1}{2}L_Q^2 - 2L_Q + \frac{\pi^2}{12} - 5\right], \tag{6.25}$$

and the multiplicative renormalization factors

$$Z_{\rm DIS}(Q;\mu) = 1 + \frac{\alpha_s C_F}{2\pi}\left[-\frac{2}{\epsilon^2} - \frac{3}{\epsilon} - \frac{2L_Q}{\epsilon}\right], \tag{6.26}$$

$$Z^{\rm int}_{\rm DIS}(Q;\mu) = 1 + \frac{\alpha_s C_F}{2\pi}\left[-\frac{1}{\epsilon^2} - \frac{2}{\epsilon} - \frac{L_Q}{\epsilon}\right]. \tag{6.27}$$

The hard anomalous dimensions can be obtained from the multiplicative factors through the relation

$$\Gamma^H_\mu = -\frac{\partial}{\partial \ln\mu} Z(Q;\mu)\,. \tag{6.28}$$

The explicit one loop expression for the hard anomalous dimensions become

$$\Gamma^H_\mu(Q;\mu) = -\frac{\alpha_s C_F}{\pi}\left(2L_Q + 3\right), \qquad \Gamma^{H\,\rm int}_\mu(Q;\mu) = -\frac{\alpha_s C_F}{\pi}\left(L_Q + \frac{1}{2}\right). \tag{6.29}$$

$$\Gamma^H_\mu(Q;\mu) = 2\Gamma_{\rm cusp}(\alpha_s)\ln\left(\frac{Q^2}{\mu^2}\right) + 2\gamma^V(\alpha_s)\,, \tag{6.30}$$

$$\Gamma^{H\,\rm int}_\mu(Q;\mu) = \Gamma_{\rm cusp}(\alpha_s)\ln\left(\frac{Q^2}{\mu^2}\right) + 2\gamma^V_{\rm NLP}(\alpha_s)\,, \tag{6.31}$$

where I define $\gamma^V_{\rm NLP\,0} = -C_F$. We now note a major important point in this chapter. So far in this chapter, we have derived the hard anomalous dimensions which is associated with the intrinsic sub-leading distributions. However, we have demonstrated that the hard anomalous dimension is controlled by the operators $\bar{\Gamma}^a$ and $\bar{\Gamma}^b$. Since these operators for intrinsic sub-leading distributions are the same as those for the kinematic sub-leading distributions, the NLP hard anomalous is left unchanged if we had formulated our cross section using kinematic or intrinsic sub-leading distributions so that we have

$$\Gamma^{H\,\rm kin}_\mu(Q;\mu) = \Gamma^{H\,\rm int}_\mu(Q;\mu)\,. \tag{6.32}$$

6.3.2 Soft Eikonal Approximation for Two Parton Sub-Process

The soft contribution to the differential cross section is obtained at LP by considering soft gluons interacting with the collinear and anti-collinear quark fields. In Fig. 6.2, we provide the diagrams associated with the LP soft interactions for the process. At LP, the relevant

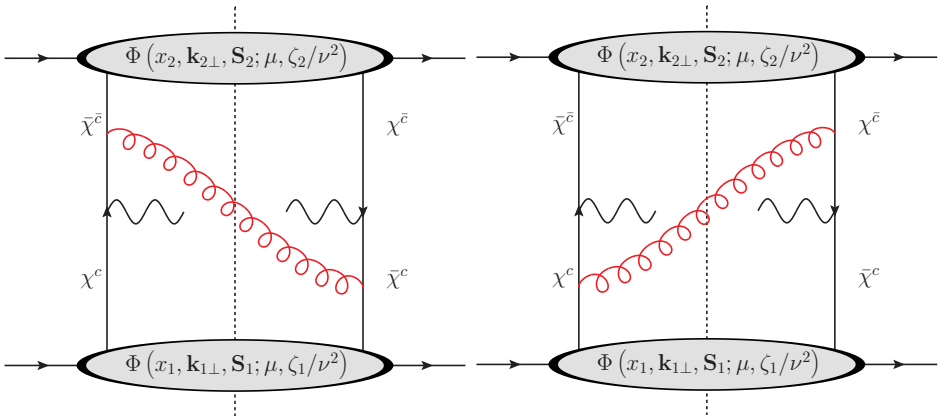

Figure 6.2: The diagrams which give rise to the soft function at NLO+LP in Drell-Yan. We note that for Semi-Inclusive DIS, that the diagrams are the same except that the upper Φ is replaced by the TMD FF quark-quark correlation function. At NLP, one of the good field components, ξ, are replaced by the bad field component φ or the kinematic suppressed field ξ_{kin}.

fields for the interaction are the good components of the collinear and anti-collinear quarks. However at NLP, one good component of the quark field is replaced by a sub-leading quark field, either the bad components $\varphi^{c/\bar{c}}$ or the kinematic suppressed fields $\xi^{c/\bar{c}}_{\text{kin}}$. In this section, we review the interaction of the soft gluons at LP and then demonstrate how soft gluons interact with the sub-leading fields.

We saw in the anomalous dimensions for the unpolarized cross section are given by

$$\Gamma^S_\mu = 2\frac{\alpha_s C_F}{\pi} L_\nu \,, \qquad \Gamma^S_\nu = -2\frac{\alpha_s C_F}{\pi} L \,. \tag{6.33}$$

We also provide the subtracted soft function as

$$S\left(b;\mu,\nu\right) = 1 + \frac{\alpha_s C_F}{2\pi}\left[2LL_\nu - L^2 - \frac{\pi^2}{6}\right] . \tag{6.34}$$

To obtain the soft function for all twist-2 configurations, we note that the soft function is insensitive to the spin configuration. Therefore, the soft function for all twist-2 processes are identical. So we can take

$$S_{\text{LP}}\left(b;\mu,\nu\right) = 1 + \frac{\alpha_s C_F}{2\pi}\left[2LL_\nu - L^2 - \frac{\pi^2}{6}\right] . \tag{6.35}$$

$$\Gamma^S_\mu = 2\frac{\alpha_s C_F}{\pi} L_\nu \,, \qquad \Gamma^S_\nu = -2\frac{\alpha_s C_F}{\pi} L \,. \tag{6.36}$$

To calculate the soft function at twist-3, we simply replace on of the incoming quark fields with a power suppressed quark field. Studying the eikonalization of the quark field, we find

$$\frac{-i\left(\not{p}+\not{l}\right)}{(p+l)^2}\left(-ig\gamma^\mu\right)\varphi^c\left(p\right)A_\mu(l) = -\frac{g}{\bar{n}\cdot l}\frac{\not{\bar{n}}}{2}\frac{\not{n}}{2}\varphi^c(p)\bar{n}\cdot A(l) + \mathcal{O}\left(\lambda\right) \tag{6.37}$$

$$= \mathcal{O}\left(\lambda\right) \,, \tag{6.38}$$

which contains only contributions of order λ since $\varphi^c(p) = \not{n}\not{\bar{n}}/4\,\psi^c(p)$. Since the field φ^c leads to a suppression of the cross section of order λ retaining the additional contributions from the soft function would be at NNLP and should therefore be neglected. Therefore the interaction of soft gluons with the bad components of the quark fields vanishes at NLP. Thus while in Fig. 6.2, there are two diagrams which contribute to the soft function at LP, there will be only one contribution when one considers sub-processes associated with intrinsic sub-leading distributions. This result indicates that

$$\Gamma^{S\,\mathrm{int}}_\mu = \frac{1}{2}\Gamma^S_\mu = \frac{\alpha_s C_F}{\pi} L_\nu \,, \tag{6.39}$$

$$\Gamma^{S\,\mathrm{int}}_\nu = \frac{1}{2}\Gamma^S_\nu = -\frac{\alpha_s C_F}{\pi} L \,. \tag{6.40}$$

Similarly the finite part of the NLO+NLP soft function is

$$S_{\mathrm{int}}\left(b;\mu,\nu\right) = \sqrt{S\left(b;\mu,\nu\right)} = 1 + \frac{\alpha_s C_F}{4\pi}\left[2LL_\nu - L^2 - \frac{\pi^2}{6}\right] \,. \tag{6.41}$$

If we were to formulate the cross section using kinematic suppressed fields, we would have the interaction

$$\frac{-i\left(\not{p}+\not{l}\right)}{(p+l)^2}\left(-ig\gamma^\mu\right)\frac{\not{k}_\perp\not{n}}{2k^+}\xi^c\left(p\right)A_\mu(l) = -\frac{g}{\bar{n}\cdot l}\frac{\not{\bar{n}}}{2}\frac{\not{n}}{2}\frac{\not{k}_\perp\not{n}}{2k^+}\bar{n}\cdot A(l) + \mathcal{O}\left(\lambda\right) \tag{6.42}$$

$$= \mathcal{O}\left(\lambda\right) \,, \tag{6.43}$$

which also vanishes in an analogous way to the bad component. We therefore find that $\Gamma^{S\,\mathrm{kin}}_\mu = \Gamma^{S\,\mathrm{int}}_\mu$, $\Gamma^{S\,\mathrm{kin}}_\nu = \Gamma^{S\,\mathrm{int}}_\nu$, and $S_{\mathrm{kin}} = S_{\mathrm{int}}$.

6.3.3 Evolution in the Two Parton Correlations Functions

To establish both the collinear matching and the evolution of the TMD PDFs, re-factorize the TMD PDF using the Fierz decomposition of the quark line, as in Fig. 2.6. To calculate the anomalous dimensions at one loop, we obtain the divergent part of the integrals

$$\int d^2k_\perp\, e^{-i\boldsymbol{k}_\perp\cdot\boldsymbol{b}}\,\Phi^{[\Gamma^a]\,(1)}_{\rm unsub}\left(x,\boldsymbol{k}_\perp,\boldsymbol{S};\mu,\zeta/\nu^2\right)=\sum_b\int\frac{dx'}{x'}\int d^2k'_\perp\, e^{-i\boldsymbol{k}'_\perp\cdot\boldsymbol{b}}\,\Phi^{\left[\Gamma^b\right]}_{\rm unsub}\left(x',\boldsymbol{k}'_\perp,\boldsymbol{S};\mu,\zeta/\nu^2\right)$$
$$\times\int d^2l_\perp\, e^{i\boldsymbol{l}_\perp\cdot\boldsymbol{b}}\left(\mathrm{I}_{\alpha\beta}\,\mathrm{Tr}\left[\bar\Gamma_b\gamma^\mu\gamma^\alpha\Gamma_a\gamma^\beta\gamma_\mu\right]+\mathrm{II}_\alpha\mathrm{Tr}\left[\bar\Gamma_b\not{n}\gamma^\alpha\Gamma_a\right]\right)\,. \tag{6.44}$$

In this expression, the kinematic part of the integrals are contained in the expressions

$$\mathrm{I}_{\alpha\beta}=-g^2C_F\left(\frac{\mu^2e^{\gamma_E}}{4\pi}\right)^\epsilon\int\frac{dl^+dl^-d^{d-2}l_{\perp\,\epsilon}}{(2\pi)^d}\,\delta\left(x-\frac{p^+}{P^+}+\frac{l^+}{P^+}\right)\,(2\pi)\delta\left(l^2\right)\,\frac{k_\alpha k_\beta}{k^4}\,, \tag{6.45}$$

$$\mathrm{II}_\alpha=-g^2C_F\left(\frac{\mu^2e^{\gamma_E}}{4\pi}\right)^\epsilon\int\frac{dl^+dl^-d^{d-2}l_{\perp\,\epsilon}}{(2\pi)^d}\delta\left(x-\frac{p^+}{P^+}+\frac{l^+}{P^+}\right)\,(2\pi)\delta\left(l^2\right)\,\frac{2k_\alpha}{k^2}\frac{\nu^\eta}{(l^+)^{1+\eta}}\,, \tag{6.46}$$

while the spin dependence and the twist is contained in the trace. The momentum k represents the momentum of the quark entering the hard process and is given by

$$k^\mu=(p-l)^+\,\frac{\bar n^\mu}{2}+(p-l)^-\,\frac{n^\mu}{2}-l_t^\mu-l^\mu_{\perp\epsilon} \tag{6.47}$$

where l is the momentum of the radiated gluon while p is the momentum of the incoming quark and the ϵ subscript on $l^\mu_{\perp\epsilon}$ denotes that the momentum is in a $d-4=-2\epsilon$ direction in dimensional regularization.

Furthermore, we can also obtain the collinear matching for the $k_\perp$-even TMDs by obtaining the finite part of this expression. To obtain these matching for the $k_\perp$-even TMDs, we take

$$\Phi^{\left[\Gamma^b\right]}_{\rm unsub}\left(x',\boldsymbol{k}'_\perp,\boldsymbol{S};\mu,\zeta/\nu^2\right)=\Phi^{\left[\Gamma^b\right]}\left(x',\boldsymbol{S};\mu\right)\,\delta^2(\boldsymbol{k}'_\perp)\,, \tag{6.48}$$

such that the incoming parton has zero transverse momentum. We can therefore write in the case where we are calculating the matching

$$\int d^2k_\perp\, e^{-i\boldsymbol{k}_\perp\cdot\boldsymbol{b}}\,\Phi^{[\Gamma^a]\,(1)}_{\rm unsub}\left(x,\boldsymbol{k}_\perp,\boldsymbol{S};\mu,\zeta/\nu^2\right)=\sum_b\int\frac{dx'}{x'}\,\Phi^{\left[\Gamma^b\right]}\left(x',\boldsymbol{S};\mu\right)$$

$$\times \int d^2 l_\perp \, e^{i \boldsymbol{l}_\perp \cdot \boldsymbol{b}} \left(\mathrm{I}_{\alpha\beta} \, \mathrm{Tr} \left[\bar{\Gamma}_b \gamma^\mu \gamma^\alpha \Gamma_a \gamma^\beta \gamma_\mu \right] + \mathrm{II}_\alpha \mathrm{Tr} \left[\bar{\Gamma}_b \not{n} \gamma^\alpha \Gamma_a \right] \right) . \tag{6.49}$$

The integrals on the right-hand side of this expression can be obtained as follows. Firstly, we integrate over l^+ using the δ function in l^+. We then perform the integration over $l_{\perp\epsilon}$ using the $\delta(l^2)$ term. We note that in order to perform the integration in the angular dependence of the $l^\mu_{\perp\epsilon}$, we group terms according to the powers of $l^\mu_{\perp\epsilon}$ that enter. For instance, integrals of the form

$$\int d^{d-4} l_{\perp\epsilon} \, f^{\mu\nu}(l^-, \boldsymbol{l}_\perp, l^2_{\perp\epsilon}) \, \delta(l^2) \tag{6.50}$$

can be computed trivially using the delta function. In this expression f represents an arbitrary function and the indices μ and ν are associated with directions in the four space time directions. Additionally, terms of the form

$$\int d^{d-4} l_{\perp\epsilon} \, l^\mu_{\perp\epsilon} \, f^\nu(l^-, \boldsymbol{l}_\perp, l^2_{\perp\epsilon}) \, \delta(l^2) \tag{6.51}$$

can be computed trivially by noting that the angular integration in the -2ϵ dimensions must vanish. Once again f represents some arbitrary function. However in this case, the μ index is associated with the -2ϵ dimensions while the ν index is associated with one of the four space time directions. Finally we must also perform calculations of the form,

$$\mathrm{III}^{\mu\nu} \equiv \int d^{d-4} l_{\perp\epsilon} \, l^\mu_{\perp\epsilon} \, l^\nu_{\perp\epsilon} \, f(l^-, \boldsymbol{l}_\perp, l^2_{\perp\epsilon}) \, \delta(l^2) \, . \tag{6.52}$$

To perform these computations we note that the only Lorentz structure which leads to non-vanishing angular integration are those which go like $\mathrm{III}^{\mu\nu} = g^{\mu\nu}_{d-4} \, \mathrm{III}$ such that we can write

$$\mathrm{III}^{\mu\nu} = -\frac{g^{\mu\nu}_{d-4}}{4-2} \int d^{d-4} \, l_{\perp\epsilon} \, l^2_{\perp\epsilon} \, h(l^2_{\perp\epsilon}) \, \delta(l^2) \, . \tag{6.53}$$

where $g^{\mu\nu}_{d-4}$ is the Minkowski metric in $d-4$ dimensions. This metric is defined as

$$g^{\mu\nu}_{d-4} = g^{\mu\nu}_\perp - \hat{x}^\mu \, \hat{x}^\mu - \hat{y}^\mu \, \hat{y}^\mu \, . \tag{6.54}$$

To perform the expansion in momentum space, we use the relations

$$\mu^{2\epsilon} \left(l^2_\perp \right)^{-1-\epsilon} = -\frac{1}{\epsilon} \delta \left(l^2_\perp \right) + \frac{1}{\mu^2} \mathcal{L}_0 \left(\frac{l^2_\perp}{\mu^2} \right) + \mathcal{O}(\epsilon) \, , \tag{6.55}$$

$$\mu^{2\epsilon}\left(l_\perp^2\right)^{-2-\epsilon}=-\frac{1}{1+\epsilon}\frac{\partial}{\partial l_\perp^2}\left[-\frac{1}{\epsilon}\delta\left(l_\perp^2\right)+\frac{1}{\mu^2}\mathcal{L}_0\left(\frac{l_\perp^2}{\mu^2}\right)\right]+\mathcal{O}\left(\epsilon\right)\,, \tag{6.56}$$

and

$$\left(1-\hat{x}\right)^{-1-\eta}=-\frac{1}{\eta}\delta\left(1-\hat{x}\right)+\mathcal{L}_0\left(1-\hat{x}\right)\,. \tag{6.57}$$

In these expressions, we define

$$\mathcal{L}_n\left(z\right)\equiv\left(\frac{1}{z}\ln^n\left(z\right)\right)_+\,, \tag{6.58}$$

which is regularized at $z=0$. The expressions for the integrals in momentum space are given by

$$\begin{aligned}\mathrm{I}^{\alpha\beta}=\frac{\alpha_s C_F}{4\pi^2}\Bigg\{&\left(1-\hat{x}\right)\left[\frac{1}{\epsilon}\delta'\left(l_\perp^2\right)-\frac{1}{\mu^4}\mathcal{L}_0'\left(\frac{l_\perp^2}{\mu^2}\right)\right]l_\perp^\alpha l_\perp^\beta+\left(1-\hat{x}\right)\left[\frac{1}{\epsilon}\delta\left(l_\perp^2\right)-\frac{1}{\mu^2}\mathcal{L}_0\left(\frac{l_\perp^2}{\mu^2}\right)\right]\frac{g_{d-4}^{\alpha\beta}}{2}\\&+\frac{\hat{x}}{4}\left[\frac{1}{\epsilon}\delta\left(l_\perp^2\right)-\frac{1}{\mu^2}\mathcal{L}_0\left(\frac{l_\perp^2}{\mu^2}\right)\right]\left(n^\alpha\bar{n}^\beta+n^\beta\bar{n}^\alpha\right)\\&+\frac{\zeta\hat{x}^2(1-\hat{x})}{4}\left[\frac{1}{\epsilon}\delta'\left(l_\perp^2\right)-\frac{1}{\mu^4}\mathcal{L}_0'\left(\frac{l_\perp^2}{\mu^2}\right)\right]\bar{n}^\alpha\bar{n}^\beta\\&-\frac{1}{2\sqrt{\zeta}}\left[\frac{1}{\epsilon}\delta(l_\perp^2)-\frac{1}{\mu^2}\mathcal{L}_0\left(\frac{l_\perp^2}{\mu^2}\right)\right]\left(l_\perp^\alpha n^\beta+l_\perp^\beta n^\alpha\right)\\&-\frac{\sqrt{\zeta}\hat{x}(1-\hat{x})}{2}\left[\frac{1}{\epsilon}\delta'\left(l_\perp^2\right)-\frac{1}{\mu^4}\mathcal{L}_0'\left(\frac{l_\perp^2}{\mu^2}\right)\right]\left(l_\perp^\alpha\bar{n}^\beta+l_\perp^\beta\bar{n}^\alpha\right)\Bigg\}\end{aligned}$$

and

$$\begin{aligned}\mathrm{II}^{\alpha}=\frac{\alpha_s C_F}{4\pi^2}\Bigg\{&\Bigg[-\frac{\omega^2}{\eta}\delta(1-\hat{x})\frac{1}{\mu^2}\mathcal{L}_0\left(\frac{l_\perp^2}{\mu^2}\right)+\frac{\omega^2}{\eta\epsilon}\delta(l_\perp^2)\delta(1-\hat{x})-\hat{x}\frac{\omega^2}{\epsilon}\delta(l_\perp^2)\mathcal{L}_0\left(1-\hat{x}\right)\\&+\frac{\omega^2}{2\epsilon}L_\zeta\,\delta(l_\perp^2)\,\delta(1-\hat{x})-\frac{L_\zeta}{2}\delta(1-\hat{x})\frac{1}{\mu^2}\mathcal{L}_0\left(\frac{l_\perp^2}{\mu^2}\right)+\hat{x}\mathcal{L}_0\left(1-\hat{x}\right)\frac{1}{\mu^2}\mathcal{L}_0\left(\frac{l_\perp^2}{\mu^2}\right)\Bigg]\bar{n}^\alpha\\&+\Bigg[\frac{2\omega^2}{\eta}\delta(1-\hat{x})\frac{1}{\mu^2}\mathcal{L}_0\left(\frac{l_\perp^2}{\mu^2}\right)-\frac{2\omega^2}{\eta\epsilon}\delta(l_\perp^2)\delta(1-\hat{x})+\frac{2\omega^2}{\epsilon}\delta(l_\perp^2)\mathcal{L}_0(1-\hat{x})\\&+\frac{\omega^2}{\epsilon}L_\zeta\delta(l_\perp^2)\delta(1-\hat{x})+L_\zeta\delta(1-\hat{x})\frac{1}{\mu^2}\mathcal{L}_0\left(\frac{l_\perp^2}{\mu^2}\right)-2\mathcal{L}_0(1-\hat{x})\frac{1}{\mu^2}\mathcal{L}_0\left(\frac{l_\perp^2}{\mu^2}\right)\Bigg]\frac{l_\perp^\alpha}{\sqrt{\zeta}}\Bigg\}\,.\end{aligned}$$

We note that to arrive at these expressions, we have performed an expansion in both η and ϵ. The two traces entering into the matching and evolution expressions will also contain

dependence on ϵ. However, these traces will depend at most linearly on ϵ such that the expansions for the integrals need to be carried out only to order ϵ^0.

To obtain the one loop expression for the TMDs in b-space, we need to take the Fourier transform of the integrals. To perform the Fourier transforms, we note that we must perform integrals of the form

$$\int d^2 l_\perp \, e^{i\boldsymbol{l}_\perp\cdot\boldsymbol{b}} \, l_t^\mu \, f^\nu(l_\perp^2) = -i\frac{\partial}{\partial b_\alpha}\frac{d}{db^2} f(b^2)\,. \tag{6.59}$$

Furthermore, we also need to perform integrals of the form

$$\int d^2 l_\perp \, e^{i\boldsymbol{l}_\perp\cdot\boldsymbol{b}} \, l_t^\mu \, l_t^\nu \, g(l_\perp^2) = -\frac{\partial}{\partial b_\beta}\frac{\partial}{\partial b_\alpha} g(b^2)\,. \tag{6.60}$$

After performing the integration, the kinematic integrals entering into these expressions are given by

$$\begin{aligned}
\tilde{\mathrm{I}}^{\alpha\beta} &= \frac{\alpha_s C_F}{16\pi}\left[\left(\frac{1}{\epsilon}+L\right)\left(2(1-\hat{x})g_{d-4}^{\alpha\beta}+\hat{x}\left(\bar{n}^\beta n^\alpha+\bar{n}^\alpha n^\beta\right)\right)\right] \\
&+ i\frac{\alpha_s C_F}{16\pi}\left[(1-\hat{x})\sqrt{\zeta}\,\left(\bar{n}^\alpha b^\beta+\bar{n}^\beta b^\alpha\right)\left(\frac{1}{\epsilon}+L\right)+\frac{4}{b^2\sqrt{\zeta}}\left(n^\alpha b^\beta+n^\beta b^\alpha\right)\right] \\
&+ \frac{\alpha_s C_F}{4\pi}(1-\hat{x})\left[\left(\frac{1}{\epsilon}+L\right)\frac{g_\perp^{\alpha\beta}}{2}-\frac{b^\alpha b^\beta}{b^2}\right]
\end{aligned}$$

$$\begin{aligned}
\tilde{\mathrm{I}}\!\mathrm{I}^{\alpha} &= \frac{\alpha_s C_F}{16\pi}\left[\left(\frac{4}{\eta}L+\frac{4}{\eta\epsilon}+\frac{2}{\epsilon}L_\zeta+2\,L\,L_\zeta\right)\omega^2\,\delta(1-\hat{x})-4\hat{x}\left(\frac{1}{\epsilon}+L\right)L_0(1-\hat{x})\right]\bar{n}^\alpha \\
&+ i\frac{\alpha_s C_F}{2\pi}\frac{1}{b^2\sqrt{\zeta}}\left[2\left(\frac{1}{\eta}\,\delta(1-\hat{x})-L_0(1-\hat{x})\right)+L_\zeta\delta(1-\hat{x})\right]b^\alpha\,,
\end{aligned}$$

where the tilde means that the kinematic integrals are in b-space. We note that the expression for $I^{\alpha\beta}$ is closely analogous to Eq. (3.9) of Ref. [363] except that terms of the form $\left(\bar{n}^\beta n^\alpha+\bar{n}^\alpha n^\beta\right)$ and $\left(\bar{n}^\alpha b^\beta+\bar{n}^\beta b^\alpha\right)$ did not enter into their expression. However, we note that terms of these forms vanish upon contraction with the traces for leading twist operators. However, these terms need to be considered at NLP. Similarly, for I^α operators of the form b^α do not enter at LP but will be vital to our analysis late in this chapter.

$$\Phi_{\text{unsub}}^{[\Gamma^a]\,(1)}\left(x,\boldsymbol{b},\boldsymbol{S};\mu,\zeta/\nu^2\right)=\sum_b\int\frac{dx'}{x'}\,\Phi_{\text{unsub}}^{[\Gamma^b]}\left(x',\boldsymbol{b},\boldsymbol{S};\mu,\zeta/\nu^2\right) \tag{6.61}$$

$$\times \left(\tilde{\mathrm{I}}_{\alpha\beta}\, \mathrm{Tr}\left[\bar{\Gamma}_b \gamma^\mu \gamma^\alpha \Gamma_a \gamma^\beta \gamma_\mu\right] + \tilde{\mathrm{I}}\mathrm{I}_\alpha \mathrm{Tr}\left[\bar{\Gamma}_b \not{n} \gamma^\alpha \Gamma_a\right] \right) . \tag{6.62}$$

To obtain the anomalous dimensions, we once again perform multiplicative renormalization

$$\hat{\Phi}^{[\Gamma^a]\,(1)}_{\mathrm{unsub}}\left(x, \boldsymbol{b}, \boldsymbol{S}; \mu, \zeta/\nu^2\right) = Z_{\Gamma^a\,\Gamma^b}\left(x, \boldsymbol{b}, \boldsymbol{S}; \mu, \zeta/\nu^2\right) \Phi^{[\Gamma^a]\,(1)}_{\mathrm{unsub}}\left(x, \boldsymbol{b}, \boldsymbol{S}; \mu, \zeta/\nu^2\right) . \tag{6.63}$$

Therefore, we have the evolution equations

$$\frac{\partial}{\partial \ln\mu} \Phi^{[\Gamma^a]\,(1)}_{\mathrm{unsub}}\left(x, \boldsymbol{b}, \boldsymbol{S}; \mu, \zeta/\nu^2\right) = \gamma^\mu_{\Gamma^a\,\Gamma^b}\left(b; \mu, \zeta/\nu^2\right) \Phi^{\left[\Gamma^b\right]\,(1)}_{\mathrm{unsub}}\left(x, \boldsymbol{b}, \boldsymbol{S}; \mu, \zeta/\nu^2\right) , \tag{6.64}$$

$$\frac{\partial}{\partial \ln\nu} \Phi^{[\Gamma^a]\,(1)}\left(x, \boldsymbol{b}, \boldsymbol{S}; \mu, \zeta/\nu^2\right) = \gamma^\nu_{\Gamma^a\,\Gamma^b}\left(b; \mu, \zeta/\nu^2\right) \Phi^{\left[\Gamma^b\right]\,(1)}\left(x, \boldsymbol{b}, \boldsymbol{S}; \mu, \zeta/\nu^2\right) , \tag{6.65}$$

where the anomalous dimensions are defined in terms of the multiplicative renormalization terms as

$$\Gamma^\mu_{\Gamma^a\,\Gamma^b} = -\frac{\partial}{\partial \ln\mu} Z_{\Gamma^a\,\Gamma^b}(b; \mu, \zeta/\nu^2) , \qquad \Gamma^\nu_{\Gamma^a\,\Gamma^b} = -\frac{\partial}{\partial \ln\nu} Z_{\Gamma^a\,\Gamma^b}(b; \mu, \zeta/\nu^2) . \tag{6.66}$$

From the computed anomalous dimensions, we can obtain the renormalization group equations for the intrinsic sub-leading TMD PDFs as follows

$$\frac{\partial}{\partial \ln\mu} \begin{bmatrix} \Phi^{[\not{n}]} \\ \Phi^{\left[\not{n}\gamma^5\right]} \\ \Phi^{\left[i\sigma^{k'+}\gamma^5\right]} \\ \Phi^{[1]} \\ \Phi^{\left[\gamma^5\right]} \\ \Phi^{\left[\gamma^{k'}\right]} \\ \Phi^{\left[\gamma^{k'}\gamma^5\right]} \\ \Phi^{\left[i\sigma^{k'l'}\gamma^5\right]} \\ \Phi^{\left[i\sigma^{+-}\gamma^5\right]} \end{bmatrix} = \frac{\alpha_s C_F}{2\pi} \boldsymbol{\Gamma}^\mu \begin{bmatrix} \Phi^{[\not{n}]} \\ \Phi^{\left[\not{n}\gamma^5\right]} \\ \Phi^{\left[i\sigma^{k+}\gamma^5\right]} \\ \Phi^{[1]} \\ \Phi^{\left[\gamma^5\right]} \\ \Phi^{\left[\gamma^k\right]} \\ \Phi^{\left[\gamma^k\gamma^5\right]} \\ \Phi^{\left[i\sigma^{kl}\gamma^5\right]} \\ \Phi^{\left[i\sigma^{+-}\gamma^5\right]} \end{bmatrix} . \tag{6.67}$$

Here the matrix $\mathbf{\Gamma}^\mu$ have the following form

$$\mathbf{\Gamma}^\mu = \begin{bmatrix} \Gamma_2^\mu & 0 & 0 & 0 & 0 & 0 & 0 & 0 & 0 \\ 0 & \Gamma_2^\mu & 0 & 0 & 0 & 0 & 0 & 0 & 0 \\ 0 & 0 & \Gamma_2^\mu \delta_k^{k'} & 0 & 0 & 0 & 0 & 0 & 0 \\ 0 & 0 & 0 & \Gamma_3^\mu & 0 & 0 & 0 & 0 & 0 \\ 0 & 0 & 0 & 0 & \Gamma_3^\mu & 0 & 0 & 0 & 0 \\ 0 & 0 & 0 & 0 & 0 & \Gamma_3^\mu \delta_k^{k'} & 0 & 0 & 0 \\ 0 & 0 & 0 & 0 & 0 & 0 & \Gamma_3^\mu \delta_k^{k'} & 0 & 0 \\ 0 & 0 & 0 & 0 & 0 & 0 & 0 & \frac{1}{4}\Gamma_3^\mu \left(\delta_k^{k'}\delta_l^{l'} - \delta_k^{l'}\delta_l^{k'}\right) & 0 \\ 0 & 0 & 0 & 0 & 0 & 0 & 0 & 0 & \Gamma_3^\mu \end{bmatrix}. \tag{6.68}$$

The relevant functions in the above matrix are given by

$$\Gamma_2^\mu(\mu,\nu,\zeta) = \frac{\alpha_s(\mu)C_F}{2\pi}\left(2L_\zeta + 3\right) \qquad \Gamma_3^\mu(\mu,\nu,\zeta) = \frac{\alpha_s(\mu)C_F}{2\pi}\left(L_\zeta - \frac{1}{2}\right) \tag{6.69}$$

Similarly, the rapidity evolution equations are given by

$$\frac{\partial}{\partial \ln\nu}\begin{bmatrix} \Phi^{[\not{n}]} \\ \Phi^{\left[\not{n}\gamma^5\right]} \\ \Phi^{\left[i\sigma^{k'+}\gamma^5\right]} \\ \Phi^{[1]} \\ \Phi^{\left[\gamma^5\right]} \\ \Phi^{\left[\gamma^{k'}\right]} \\ \Phi^{\left[\gamma^{k'}\gamma^5\right]} \\ \Phi^{\left[i\sigma^{k'l'}\gamma^5\right]} \\ \Phi^{\left[i\sigma^{+-}\gamma^5\right]} \end{bmatrix} = \frac{\alpha_s C_F}{2\pi}\mathbf{\Gamma}^\nu \begin{bmatrix} \Phi^{[\not{n}]} \\ \Phi^{\left[\not{n}\gamma^5\right]} \\ \Phi^{\left[i\sigma^{k+}\gamma^5\right]} \\ \Phi^{[1]} \\ \Phi^{\left[\gamma^5\right]} \\ \Phi^{\left[\gamma^{k}\right]} \\ \Phi^{\left[\gamma^{k}\gamma^5\right]} \\ \Phi^{\left[i\sigma^{kl}\gamma^5\right]} \\ \Phi^{\left[i\sigma^{+-}\gamma^5\right]} \end{bmatrix}. \tag{6.70}$$

The corresponding anomalous dimensions $\mathbf{\Gamma}^{\nu}$ are givebn by

$$\mathbf{\Gamma}^{\nu} = \begin{bmatrix} 2L & 0 & 0 & 0 & 0 & 0 & 0 & 0 & 0 \\ 0 & 2L & 0 & 0 & 0 & 0 & 0 & 0 & 0 \\ 0 & 0 & 2L\delta_k^{k'} & 0 & 0 & 0 & 0 & 0 & 0 \\ 0 & 0 & 0 & L & 0 & 0 & 0 & 0 & 0 \\ 0 & 0 & \frac{2ib_k}{xP^+}\frac{\partial L}{\partial b^2} & 0 & L & 0 & 0 & 0 & -L \\ \frac{2ib^{k'}}{xP^+}\frac{\partial L}{\partial b^2} & 0 & 0 & 0 & 0 & L\delta_k^{k'} & 0 & 0 & 0 \\ 0 & \frac{2ib^{k'}}{xP^+}\frac{\partial L}{\partial b^2} & 0 & 0 & 0 & 0 & L\delta_k^{k'} & 0 & 0 \\ 0 & 0 & \frac{i}{xP^+}\frac{\partial L}{\partial b^2}\left(b^{l'}\delta_k^{k'} - b^{k'}\delta_k^{l'}\right) & 0 & 0 & 0 & 0 & L\left(\delta_k^{k'}\delta_l^{l'} - \delta_k^{l'}\delta_l^{k'}\right) & 0 \\ 0 & 0 & \frac{2ib_k}{xP^+}\frac{\partial L}{\partial b^2} & 0 & -L & 0 & 0 & 0 & L \end{bmatrix} . \tag{6.71}$$

From Eqs. (6.67) and (6.70) we see the interesting behaviour that the diagonal anomalous dimensions for the NLP distributions are half those for the LP distributions. This interesting behaviour can be traced back to how the sub-leading fields interact with the Wilson lines. The explicit expression for the interaction of the Wilson lines with the intrinsic sub-leading field is given by

$$-g\frac{n^{\mu}}{n\cdot l}\gamma_{\mu}\,\varphi^{c}\left(p\right) = \mathcal{O}\left(\lambda\right) . \tag{6.72}$$

So the result that the anomalous dimension of the intrinsic sub-leading twist TMDs is half of the leading twist TMDs is a consequence of the fact that the interaction of this field with the Wilson line vanishes. We note that this behavior is not limited to the intrinsic NLP distributions but also occurs for the kinematic NLP distributions. This can be seen by examining the interaction of the Wilson line with this field, explicitly the interaction is given by

$$-g\frac{n^{\mu}}{n\cdot l}\gamma_{\mu}\frac{\not{p}_{\perp}\not{n}}{2p^{+}}\xi_{\text{kin}}^{c}\left(p\right) = \mathcal{O}\left(\lambda\right) . \tag{6.73}$$

For the case of the intrinsic sub-leading distributions, we also find that the Collins-Soper evolution equation is not diagonal, which is consistent with the calculation which was performed in Ref. [364]. As a result, solving the rapidity evolution equation is highly non-trivial at twist-3.

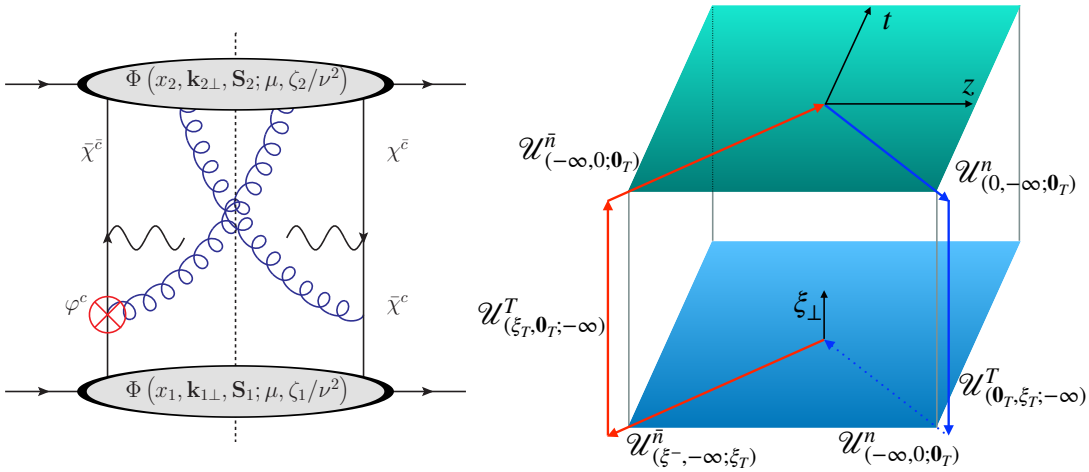

Figure 6.3: Example diagram for the collinear Wilson line structure for Drell-Yan. The red lines represent the Wilson lines for the incoming quark distribution while the blue Wilson lines represent the Wilson lines for the incoming anti-quark distribution. The dashed blue line represents the vanishing Wilson line due to the interaction with the sub-leading field. We note that there is an additional interaction where the bad field enters on the right side of the cut as $\bar{\varphi}^c$.

6.3.4 Soft Subtraction, Factorization Breaking, and Renormalization Group Consistency

In Chapter 2, we saw that the properly defined TMDs are obtained through the relations

$$f(x_1, b; \mu, \zeta_1) f(x_2, b; \mu, \zeta_2) = f^{\text{unsub}}(x_1, b; \mu, \zeta_1/\nu^2)\sqrt{S(b; \mu, \nu)} \tag{6.74}$$

$$\times\, f^{\text{unsub}}(x_2, b; \mu, \zeta_2/\nu^2)\sqrt{S(b; \mu, \nu)}\,, \tag{6.75}$$

where I have used the case of unpolarized hadron production in Drell-Yan as an example. At NLP, we could take the Cahn effect in Drell-Yan as an example process and we would expect that the soft subtraction should go like

$$\frac{k^i_\perp}{P^+} f^\perp(x_1, b; \mu, \zeta_1) f(x_2, b; \mu, \zeta_2) \sim \frac{k^i_\perp}{P^+} f^{\perp\,\text{unsub}}(x_1, b; \mu, \zeta_1/\nu^2)\sqrt{S_{\text{int}}(b; \mu, \nu)} \tag{6.76}$$

$$\times\, f^{\text{unsub}}(x_2, b; \mu, \zeta_2/\nu^2)\sqrt{S_{\text{int}}(b; \mu, \nu)}\,. \tag{6.77}$$

By studying the appearance of the ν dependent term, one can show that for the case of $f^\perp$ that the soft subtraction is well defined. However, since $S_{\text{int}} = \sqrt{S}$, the soft subtraction

for the TMD FF does not cancel all of the appearances of the scale ν. As a result, this naive picture for the soft subtraction fails. This failure can also be seen at the level of the anomalous dimensions. Namely at LP, we know that we have the relation

$$\Gamma_{\nu}^{S\,\mathrm{LP}} + \Gamma_{\nu}^{f} + \Gamma_{\nu}^{f} = 0\,. \tag{6.78}$$

However, at NLP, we would have

$$\Gamma_{S\,\mathrm{int}}^{\nu} + \Gamma_{f}^{\nu} + \Gamma_{f^{\perp}}^{\nu} = \frac{1}{2}\Gamma_{\nu}^{S\,\mathrm{LP}} + \Gamma_{f}^{\nu} + \Gamma_{f^{\perp}}^{\nu} = \Gamma_{f^{\perp}}^{\nu}\,. \tag{6.79}$$

Thus at NLP, this naive picture does not provide renormalization group consistency. To address this issue, let us now study the left panel of Fig. 6.3. In this figure, we examine an example sub-process where the top correlator is a LP one and the bottom correlator is a sub-leading. We have also included the two anti-collinear gluons in blue which are responsible for generating the anti-collinear Wilson lines. These anti-collinear Wilson lines represent the $\otimes$ in diagrams such as Fig. 2.6. In the LP case, there are two non-vanishing interactions in Fig. 6.3 which give rise to the two Wilson line interactions in Fig. 2.6. However, in the case of Fig. 6.3, we must re-examine the interaction of a collinear sub-leading quark field and an anti-collinear gluon. One can easily show that

$$\frac{-i\left(\not{p}+\not{l}\right)}{(p+l)^2}\left(-ig\gamma^{\mu}\right)\varphi^{c}\left(p\right)A_{\mu}(l) = -\frac{g}{\bar{n}\cdot l}\frac{\not{\bar{n}}}{2}\frac{\not{n}}{2}\varphi^{c}(p)\bar{n}\cdot A(l) + \mathcal{O}\left(\lambda\right) \tag{6.80}$$

$$= \mathcal{O}\left(\lambda\right)\,. \tag{6.81}$$

As a result, the field of gluons which is responsible for generating one of the Wilson lines for f vanishes. There are far reaching implications of this result.

Firstly, when one computes the evolution of the LP distribution in the presence of a sub-leading field, one should only consider a single Wilson line interaction. As a result, the UV divergences which are associated with the evolution of the LP distributions should be exactly half the usual ones. Therefore, the anomalous dimensions for the LP TMDs are half the usual ones when considering NLP contributions. This can be explicitly verified by studying the renomalization group consistency equations

$$\Gamma_{S\,\mathrm{int}}^{\nu} + \frac{1}{2}\Gamma_{f}^{\nu} + \Gamma_{f^{\perp}}^{\nu} = 0\,, \tag{6.82}$$

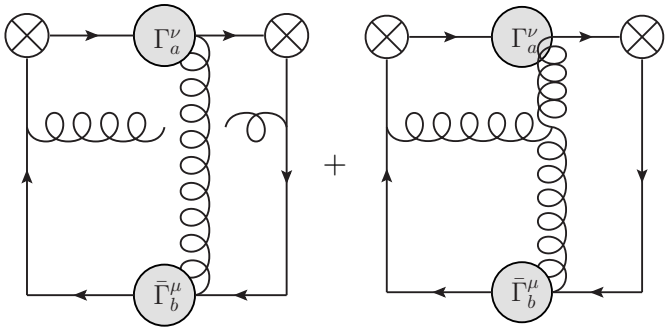

Figure 6.4: Two graphs contributing to the rapidity divergence of the three parton TMDs in light-cone gauge. The $\otimes$ represents the Wilson lines while the operators Γ_a^μ represent the NLP operators in the decomposition of the three parton correlator.

$$\Gamma^\mu_{S\,\text{int}} + \frac{1}{2}\Gamma^\mu_f + \Gamma^\mu_{f^\perp} + \Gamma^\mu_{H\,\text{NLP}} = 0\,. \tag{6.83}$$

Therefore RG consistency is only achieved once we have taken into consideration that the evolution for the LP soft function is different when one introduces an intrinsic sub-leading field. As the idea of factorization theorems is that the distributions should be blind to the total scattering event, the fact that the evolution equations for the TMD PDF are different when one considers sub-leading azimuthal asymmetries indicates that the evolution for the LP distributions is modified. The second issue is much more dramatic. Since the gluons which generate the Wilson line cannot connect to the sub-leading field, the gauge invariance of the LP TMD PDF does not manifest diagram by diagram in perturbation theory. Both of these effects indicate that the naive factorization must be modified at NLP. In the right side of Fig. 6.3, I have included a figure which provides the collinear Wilson loop for the Drell-Yan cross section. The red Wilson lines are those which are associated with $f^\perp$ while the blue Wilson lines are those associated with f in the Cahn effect. The dotted line is the 'missing' Wilson line at sub-leading twist. Finally, while I have discussed these issues for the intrinsic sub-leading distributions, I would also like to note that these issues enter for the kinematic sub-leading distributions as well.

6.3.5 Evolution for the three parton correlator

A final point of our discussion is to examine the rapidity evolution equation for the dynamical twist-3 distributions.

Previously we saw that these distributions are generated when one considers the introduction of an additional transverse gluon in the matrix elements. This gluon introduces additional complications when calculating QCD evolution equation.

$$d^{\mu\nu}(p) = -g^{\mu\nu} + \frac{p^\mu n^\nu + p^\mu n^\nu}{n \cdot p} \tag{6.84}$$

which is the metric associated with gluons in this gauge. Closely analogous to the expression for the two parton correlator, we can express the one loop expression for the three parton TMDs as

$$\begin{aligned}\int d^2k_\perp e^{-i\boldsymbol{k}_\perp\cdot\boldsymbol{b}}\,\Phi^{[\Gamma_a]\,\mu}_{A\,\text{unsub}}\left(x,x_1,\boldsymbol{k}_\perp,\boldsymbol{S};\mu,\zeta/\nu^2\right) = \sum_b \int \frac{dx'}{x'}\int\frac{dx_1'}{x_1'} \\ \int d^2p_\perp\, e^{-i\boldsymbol{p}_\perp\cdot\boldsymbol{b}}\,\Phi^{[\Gamma_b]\,\mu}_{A\,\text{unsub}}\left(x',x_1',\boldsymbol{p}_\perp,\boldsymbol{S},\mu,\zeta/\nu^2\right)\sum_i F^i_{ab}\left(x,x_1,x',x_1',\boldsymbol{b}\right)\,.\end{aligned} \tag{6.85}$$

In this expression i is the index associated with each of the graph which contribute at NLO. In this chapter, we focus on the Collins-Soper equation of the three parton correlator. In light-cone gauge, the two graphs which are responsible for generating the rapidity divergence are given in Fig. 6.4.

$$\begin{aligned}F^1_{ab}\left(x,x_1,x',x_1',\boldsymbol{b}\right) = \frac{g^2}{2}\left(C_F-\frac{C_A}{2}\right)\left(\frac{\mu^2e^{\gamma_E}}{4\pi}\right)^\epsilon\int d^2l_\perp e^{i\boldsymbol{l}_\perp\cdot\boldsymbol{b}}\int\frac{dl^+dl^-d^{d-4}l_{\perp\epsilon}}{(2\pi)^d} \\ \times\ \text{Tr}\left[\bar\Gamma_{\alpha\mu}\gamma_\rho \not{k}_3\Gamma^{\beta\nu}\not{k}\gamma^\sigma\right]\,d_{\rho\sigma}(l)\frac{1}{k^2}\frac{1}{k_3^2}\,\omega^2\left(\frac{l^+}{\nu}\right)^{-\eta}(2\pi)\delta(l^2)\end{aligned} \tag{6.86}$$

$$\times\ \frac{1}{P^+}\delta\left(x-\frac{k^+}{P^+}\right)\delta\left(x_1-\frac{p_1^+}{P^+}\right) \tag{6.87}$$

$$\begin{aligned}F^2_{ab}\left(x,x_1,x',x_1',\boldsymbol{b}\right) = \frac{g^2}{2}\frac{C_A}{2i}\left(\frac{\mu^2e^{\gamma_E}}{4\pi}\right)^\epsilon\int d^2l_\perp e^{i\boldsymbol{l}_\perp\cdot\boldsymbol{b}}\int\frac{dl^+dl^-d^{d-4}l_{\perp\epsilon}}{(2\pi)^d} \\ \times\ \text{Tr}\left[\bar\Gamma_{\alpha\mu}\gamma_\rho\not{k}_3\Gamma^{\beta\nu}\right]\,V^{\alpha\sigma\delta}\left(x_1'P^+,-l,-k_2\right)\,d_{\delta\beta}(k_2)\,d_{\rho\sigma}(l)\end{aligned} \tag{6.88}$$

$$\times\ (2\pi)\delta(l^2)\frac{1}{k_2^2}\frac{1}{k_3^2}\,\omega^2\left(\frac{l^+}{\nu}\right)^{-\eta}\ \frac{1}{P^+}\delta\left(x-\frac{k^+}{P^+}\right)\delta\left(x_1-\frac{p_1^+}{P^+}\right)$$

where

$$V^{\mu\nu\rho}(k_1,k_2,k_3)=i\left[g^{\mu\nu}\left(k1-k2\right)^{\rho}+g^{\mu\nu}\left(k1-k2\right)^{\rho}\right]\,, \tag{6.89}$$

is the kinematic part associated with the three gluon vertex. These integrals can be explicitly performed and the rapidity anomalous dimension can be obtained for $\Phi^{[\Gamma_a]\,\mu}_{A\,\text{unsub}}$ and the evolution equation becomes

$$\frac{\partial}{\partial \ln\nu}\Phi^{[\Gamma_a]\,\mu}_{A\,\text{unsub}}\left(x,x_1,\boldsymbol{k}_\perp,\boldsymbol{S};\mu,\zeta/\nu^2\right)=\Gamma^{\text{dyn}}_{\mu}\Phi^{[\Gamma_a]\,\mu}_{A\,\text{unsub}}\left(x,x_1,\boldsymbol{k}_\perp,\boldsymbol{S};\mu,\zeta/\nu^2\right)\,, \tag{6.90}$$

where we find that the rapidity anomalous dimension of the three parton correlation function is the same as the anomalous dimension of the leading-power TMDs.

6.4 Conclusion

In this chapter, I have presented the relevant distributions which enter at NLP to the cross sections for Semi-Inclusive DIS and Drell-Yan. Through explicit calculation, I have for the first time derived the evolution equations for these distributions as well as for the sub-leading soft and hard functions. We find in our study that for the case of the intrinsic and kinematic sub-leading distributions that while renormalization group consistency can be obtained, that the introduction of the sub-leading fields leads to a modification of the factorization and gauge invariance of the leading distribution, indicating that the full story for TMD factorization at sub-leading twist may be much more complicated than what is currently presented in the literature. Additionally, while in [362], the authors conjectured for the form of the sub-leading soft function for the intrinsic sub-leading distributions, we find through explicit calculation that this assumption is not valid. We do however find that the rapidity anomalous dimension for the dynamical sub-leading twist distribution is the same as the twist-2 distributions, which could indicate that the soft function associated with these distributions is the same as those that are obtained at LP.

CHAPTER 7

Summary and Conclusion

QCD is the fundamental theory of the strong interaction and governs the dynamics of bound quarks and gluons and their relation to the hadronic properties. The EIC will allow us to perform QCD tomography at never before achieved precision, and represents the newest endeavor for humanity to uncover the underlying nature of matter. In this thesis, I have discussed aspects of studying how hadronic spin affects the partonic degrees of freedom by discussing TMDs.

Due to the non-perturbative nature of QCD, to perform full tomography and make predictions at colliders, we rely on factorization theorems. In the language of Collins, Soper, and Sterman, I have demonstrated that these factorization theorems arise due to the appearance of IR divergences in the virtual loop diagrams. The kinematic regions in which these IR divergences occur provide us with a catalog of the QCD modes which provide the asymptotic contributions to QCD amplitudes. We found that there were the appearance of two modes, the soft and collinear modes. Using SCET, we reduce the degrees of freedom of our theoretical formalism by accounting for these QCD modes and integrate out modes which do not contribute to the asymptotic behavior of QCD. For Drell-Yan, I provided an overview of the factorization theorem. We saw in this analysis the appearance of large logarithms in the perturbative expressions and I presented a procedure for performing resummation of these large logarithms. In the case of the TMD PDFs, we saw the appearance of a new soft mode due to the appearance of the infrared rapidity poles. We calculated this new soft function and used it to perform soft subtraction in the TMDs.

Using these perturbative methods, we then performed the highest precision extraction

of the quark Sivers function, which encodes information for how the parent hadron's spin alters the transverse momentum of unpolarized quarks. We saw in this section that the Sivers asymmetry is generated due to multiple parton interactions. Using the global set of data from HERMES, COMPASS, Jefferson Lab, and RHIC, we performed the first global extraction of the Sivers function. Our findings were that the experimental data sets from HERMES, COMPASS, and Jefferson Lab were all consistent with one another. While we found that the size of the RHIC asymmetry was much larger than what the rest of the data was indicating. By performing a thorough analysis, we found that this discrepancy did not occur due to our non-perturbative parameterization. Recently, a re-analysis with additional statistics at RHIC was released. This re-analysis found that the size of asymmetries are much smaller than what the previous analysis indicated. These findings indicate that our original global analysis was not flawed and that the current methods of performing a global analysis of the Sivers function were all well-founded. We then provided projections at the EIC in Semi-Inclusive DIS.

We then moved on to discuss how jets can be used to uncover hadronic structure at the EIC and also in p-p collisions. Since the main interests of the EIC are to uncover the gluon content of hadrons as well as the spin structure, the gluon Sivers function is regarded as a golden measurement at the EIC. Using SCET, we established a factorization and resummation formalism for the gluon Sivers asymmetry at the EIC. We then provided first predictions for this asymmetry and also the unpolarized process at this facility. Additionally, we studied how dijet production in p-p collisions could be used to measure the Sivers function. Using SCET, we established a factorization and resummation formalism. We found in this study that since the Sivers function is related to a three-parton correlation function, the computation even at tree level for the hard contributions was non-trivial. Nevertheless, we established a formalism for calculating these diagrams and used this to provide predictions for the Sivers asymmetry at RHIC at $\sqrt{s} = 200$ GeV. Lastly in this chapter, we studied how jet fragmentation functions can be used to study the distribution of hadrons within jets in Z-tagged jets.

I then moved on to discuss how the transversity TMD FF and the TMD PFF can be obtained at the future EIC for Λ baryons. Using the recent measurement at Belle for spontaneous Λ polarization in DIA, I performed one of the first extractions of the TMD PFF. Using the recent COMPASS measurement of the transverse spin transfer, I performed the first extraction of the transversity TMD FF. We then performed a Pythia re-weighting analysis in order to obtain statistical uncertainties at the EIC. Using these statistical uncertainties, we categorized the required luminosity to reduce fit uncertainties for these distributions. Using the TMD Fragmenting Jet Functions, we provided predictions at the future EIC for spontaneous Λ production and the transverse spin transfer in lepton-jet correlations in lepton-proton collisions. Due to similarities between the Sivers function and the TMD PFF, these measurements will be vital for testing universality of the TMD FFs.

Lastly, I discussed the TMDs at sub-leading power. While virtually all TMD formalisms up to this point neglect power corrections of $q_\perp/Q$ and M/Q, we discussed how sub-leading formalism can be used to probe novel distributions. This study tests whether the LP formalism for factorization and resummation can be naively applied to these higher twist computations. Through explicit computation at the next-to-leading order, we perform the calculation of the hard, collinear, and soft contributions to the differential cross section at sub-leading twist. We found that the introduction of an intrinsic or kinematic sub-leading field causes a modification of both factorization and gauge invariance. We therefore provide evidence that naively applying LP formalism at NLP leads to major issues in the factorization. Nevertheless, we establish renormalization group consistency at one loop for these distributions.

The TMD formalism and simulation tools developed in this thesis will have broad applications in the experimental program at the future Electron-Ion Collider. From these analyses, we will be able to probe the spin structure of the proton in novel processes and at higher precision than what was previously available.

References

[1] A. Ito et al., *Measurement of the Continuum of Dimuons Produced in High-Energy Proton - Nucleus Collisions*, *Phys. Rev. D* **23** (1981) 604–633.

[2] HERMES collaboration, A. Airapetian et al., *Multiplicities of charged pions and kaons from semi-inclusive deep-inelastic scattering by the proton and the deuteron*, *Phys. Rev.* **D87** (2013) 074029, [1212.5407].

[3] COMPASS collaboration, M. Aghasyan et al., *Transverse-momentum-dependent Multiplicities of Charged Hadrons in Muon-Deuteron Deep Inelastic Scattering*, *Phys. Rev.* **D97** (2018) 032006, [1709.07374].

[4] COMPASS collaboration, M. Alekseev et al., *Collins and Sivers asymmetries for pions and kaons in muon-deuteron DIS*, *Phys. Lett.* **B673** (2009) 127–135, [0802.2160].

[5] HERMES collaboration, A. Airapetian et al., *Observation of the Naive-T-odd Sivers Effect in Deep-Inelastic Scattering*, *Phys. Rev. Lett.* **103** (2009) 152002, [0906.3918].

[6] COMPASS collaboration, C. Adolph et al., *Sivers asymmetry extracted in SIDIS at the hard scales of the Drell–Yan process at COMPASS*, *Phys. Lett.* **B770** (2017) 138–145, [1609.07374].

[7] Jefferson Lab Hall A collaboration, X. Qian et al., *Single Spin Asymmetries in Charged Pion Production from Semi-Inclusive Deep Inelastic Scattering on a Transversely Polarized ^{3}He Target*, *Phys. Rev. Lett.* **107** (2011) 072003, [1106.0363].

[8] COMPASS collaboration, M. Aghasyan et al., *First measurement of transverse-spin-dependent azimuthal asymmetries in the Drell-Yan process*, *Phys. Rev. Lett.* **119** (2017) 112002, [1704.00488].

[9] STAR collaboration, L. Adamczyk et al., *Measurement of the transverse single-spin asymmetry in $p^\uparrow + p \to W^\pm/Z^0$ at RHIC*, *Phys. Rev. Lett.* **116** (2016) 132301, [1511.06003].

[10] M. G. Echevarria, Z.-B. Kang and J. Terry, *Global analysis of the Sivers functions at NLO+NNLL in QCD*, *JHEP* **01** (2021) 126, [2009.10710].

[11] LHCb collaboration, R. Aaij et al., *Measurement of charged hadron production in Z-tagged jets in proton-proton collisions at $\sqrt{s} = 8$ TeV*, 1904.08878.

[12] D. Callos, Z.-B. Kang and J. Terry, *Extracting the Transverse Momentum Dependent Polarizing Fragmentation Functions*, 2003.04828.

[13] COMPASS collaboration, M. G. Alexeev et al., *Probing transversity by measuring Λ polarisation in SIDIS*, 2104.13585.

[14] J. Bjorken, *Asymptotic sum rules at infinite momentum*, *Phys. Rev.* **179** (1969) 1547–1553.

[15] R. P. Feynman, *Very high-energy collisions of hadrons*, *Phys. Rev. Lett.* **23** (1969) 1415–1417.

[16] D. Gross and F. Wilczek, *Ultraviolet behavior of non-abelian gauge theories*, *Phys. Rev. Lett.* **30** (1973) 1343–1346.

[17] J. C. Collins and D. E. Soper, *Back-To-Back Jets in QCD*, *Nucl. Phys.* **B193** (1981) 381.

[18] S. Meissner, A. Metz, M. Schlegel and K. Goeke, *Generalized parton correlation functions for a spin-0 hadron*, *JHEP* **0808** (2008) 038, [0805.3165].

[19] S. Meissner, A. Metz and M. Schlegel, *Generalized parton correlation functions for a spin-1/2 hadron*, *JHEP* **0908** (2009) 056, [0906.5323].

[20] C. Lorcé and B. Pasquini, *Structure analysis of the generalized correlator of quark and gluon for a spin-1/2 target*, *JHEP* **09** (2013) 138, [1307.4497].

[21] K. Kanazawa, C. Lorcé, A. Metz, B. Pasquini and M. Schlegel, *Twist-2 generalized transverse-momentum dependent parton distributions and the spin/orbital structure of the nucleon*, *Phys. Rev. D* **90** (2014) 014028, [1403.5226].

[22] X.-d. Ji, *Viewing the proton through 'color' filters*, *Phys.Rev.Lett.* **91** (2003) 062001, [hep-ph/0304037].

[23] A. V. Belitsky, X.-d. Ji and F. Yuan, *Quark imaging in the proton via quantum phase-space distributions*, *Phys. Rev.* **D69** (2004) 074014, [hep-ph/0307383].

[24] C. Lorce and B. Pasquini, *Quark Wigner Distributions and Orbital Angular Momentum*, *Phys.Rev.* **D84** (2011) 014015, [1106.0139].

[25] D. Boer and C. Setyadi, *GTMD model predictions for diffractive dijet production at EIC*, *Phys. Rev. D* **104** (2021) 074006, [2106.15148].

[26] S. Bhattacharya, A. Metz, V. K. Ojha, J.-Y. Tsai and J. Zhou, *Exclusive double quarkonium production and generalized TMDs of gluons*, *Phys. Lett. B* **833** (2022) 137383, [1802.10550].

[27] S. Bhattacharya, A. Metz and J. Zhou, *Generalized TMDs and the exclusive double Drell–Yan process*, *Phys. Lett. B* **771** (2017) 396–400, [1702.04387].

[28] X. Ji, F. Yuan and Y. Zhao, *Hunting the Gluon Orbital Angular Momentum at the Electron-Ion Collider*, *Phys. Rev. Lett.* **118** (2017) 192004, [1612.02438].

[29] Y. Hagiwara, Y. Hatta, B.-W. Xiao and F. Yuan, *Elliptic Flow in Small Systems due to Elliptic Gluon Distributions?*, *Phys. Lett. B* **771** (2017) 374–378, [1701.04254].

[30] Y. Hatta, Y. Nakagawa, F. Yuan, Y. Zhao and B. Xiao, *Gluon orbital angular momentum at small-x*, *Phys. Rev. D* **95** (2017) 114032, [1612.02445].

[31] Y. Hatta, B.-W. Xiao and F. Yuan, *Probing the Small- x Gluon Tomography in Correlated Hard Diffractive Dijet Production in Deep Inelastic Scattering*, *Phys. Rev. Lett.* **116** (2016) 202301, [1601.01585].

[32] M. G. Echevarria, P. A. G. Garcia and I. Scimemi, *GTMDs and the factorization of exclusive double Drell-Yan*, 2208.00021.

[33] J. C. Collins, D. E. Soper and G. F. Sterman, *Factorization of Hard Processes in QCD*, *Adv. Ser. Direct. High Energy Phys.* **5** (1989) 1–91, [hep-ph/0409313].

[34] X.-d. Ji, J.-p. Ma and F. Yuan, *QCD factorization for semi-inclusive deep-inelastic scattering at low transverse momentum*, *Phys. Rev.* **D71** (2005) 034005, [hep-ph/0404183].

[35] L. D. Landau, *On analytic properties of vertex parts in quantum field theory*, *Nucl. Phys.* **13** (1959) 181–192.

[36] J. Collins, *Foundations of perturbative QCD*, *Camb. Monogr. Part. Phys. Nucl. Phys. Cosmol.* **32** (2011) 1–624.

[37] S. Coleman and R. E. Norton, *Singularities in the physical region*, *Nuovo Cim.* **38** (1965) 438–442.

[38] G. T. Bodwin, *Factorization of the Drell-Yan Cross-Section in Perturbation Theory*, *Phys. Rev. D* **31** (1985) 2616.

[39] J. C. Collins, D. E. Soper and G. F. Sterman, *Factorization for Short Distance Hadron - Hadron Scattering*, *Nucl. Phys. B* **261** (1985) 104–142.

[40] J. C. Collins, D. E. Soper and G. F. Sterman, *Soft Gluons and Factorization*, *Nucl. Phys. B* **308** (1988) 833–856.

[41] N. Armesto, F. Dominguez, A. Kovner, M. Lublinsky and V. Skokov, *The Color Glass Condensate density matrix: Lindblad evolution, entanglement entropy and Wigner functional*, *JHEP* **05** (2019) 025, [1901.08080].

[42] V. Vaidya and X. Yao, *Transverse momentum broadening of a jet in quark-gluon plasma: an open quantum system EFT*, *JHEP* **10** (2020) 024, [2004.11403].

[43] M. Li and A. Kovner, *JIMWLK Evolution, Lindblad Equation and Quantum-Classical Correspondence*, *JHEP* **05** (2020) 036, [2002.02282].

[44] G. Ovanesyan and I. Vitev, *An effective theory for jet propagation in dense QCD matter: jet broadening and medium-induced bremsstrahlung*, *JHEP* **06** (2011) 080, [1103.1074].

[45] I. Z. Rothstein and I. W. Stewart, *An Effective Field Theory for Forward Scattering and Factorization Violation*, *JHEP* **08** (2016) 025, [1601.04695].

[46] V. Vaidya, *Effective Field Theory for jet substructure in heavy ion collisions*, *JHEP* **11** (2021) 064, [2010.00028].

[47] T. Becher, A. Broggio and A. Ferroglia, *Introduction to Soft-Collinear Effective Theory*, *Lect. Notes Phys.* **896** (2015) pp.1–206, [1410.1892].

[48] M. Beneke and V. A. Smirnov, *Asymptotic expansion of Feynman integrals near threshold*, *Nucl. Phys. B* **522** (1998) 321–344, [hep-ph/9711391].

[49] V. A. Smirnov, *Applied asymptotic expansions in momenta and masses*, *Springer Tracts Mod. Phys.* **177** (2002) 1–262.

[50] F. Bloch and A. Nordsieck, *Note on the Radiation Field of the electron*, *Phys. Rev.* **52** (1937) 54–59.

[51] T. Kinoshita, *Mass singularities of Feynman amplitudes*, *J. Math. Phys.* **3** (1962) 650–677.

[52] T. D. Lee and M. Nauenberg, *Degenerate Systems and Mass Singularities*, *Phys. Rev.* **133** (1964) B1549–B1562.

[53] C. W. Bauer and I. W. Stewart, *Invariant operators in collinear effective theory*, *Phys. Lett.* **B516** (2001) 134–142, [hep-ph/0107001].

[54] C. W. Bauer, S. Fleming and M. E. Luke, *Summing Sudakov logarithms in B —¿ X(s gamma) in effective field theory*, *Phys. Rev. D* **63** (2000) 014006, [hep-ph/0005275].

[55] C. W. Bauer, S. Fleming, D. Pirjol and I. W. Stewart, *An Effective field theory for collinear and soft gluons: Heavy to light decays*, *Phys. Rev.* **D63** (2001) 114020, [hep-ph/0011336].

[56] C. W. Bauer, D. Pirjol and I. W. Stewart, *Soft collinear factorization in effective field theory*, *Phys. Rev.* **D65** (2002) 054022, [hep-ph/0109045].

[57] M. Beneke, A. P. Chapovsky, M. Diehl and T. Feldmann, *Soft collinear effective theory and heavy to light currents beyond leading power*, *Nucl. Phys.* **B643** (2002) 431–476, [hep-ph/0206152].

[58] M. Beneke and T. Feldmann, *Multipole expanded soft collinear effective theory with nonAbelian gauge symmetry*, *Phys. Lett. B* **553** (2003) 267–276, [hep-ph/0211358].

[59] R. J. Hill and M. Neubert, *Spectator interactions in soft collinear effective theory*, *Nucl. Phys. B* **657** (2003) 229–256, [hep-ph/0211018].

[60] R. D. Tangerman and P. J. Mulders, *Intrinsic transverse momentum and the polarized Drell-Yan process*, *Phys. Rev.* **D51** (1995) 3357–3372, [hep-ph/9403227].

[61] A. V. Manohar, *Deep inelastic scattering as x —¿ 1 using soft collinear effective theory*, *Phys. Rev. D* **68** (2003) 114019, [hep-ph/0309176].

[62] J.-Y. Chiu, A. Jain, D. Neill and I. Z. Rothstein, *A Formalism for the Systematic Treatment of Rapidity Logarithms in Quantum Field Theory*, *JHEP* **05** (2012) 084, [1202.0814].

[63] Particle Data Group collaboration, K. Olive et al., *Review of Particle Physics*, *Chin. Phys. C* **38** (2014) 090001.

[64] D. W. Sivers, *Single Spin Production Asymmetries from the Hard Scattering of Point-Like Constituents*, *Phys. Rev.* **D41** (1990) 83.

[65] D. W. Sivers, *Hard scattering scaling laws for single spin production asymmetries*, *Phys. Rev. D* **43** (1991) 261–263.

[66] J.-w. Qiu and G. F. Sterman, *Single transverse spin asymmetries*, *Phys. Rev. Lett.* **67** (1991) 2264–2267.

[67] J.-w. Qiu and G. F. Sterman, *Single transverse spin asymmetries in direct photon production*, *Nucl. Phys.* **B378** (1992) 52–78.

[68] A. Accardi et al., *Electron Ion Collider: The Next QCD Frontier*, *Eur. Phys. J.* **A52** (2016) 268, [1212.1701].

[69] A. Bacchetta, F. Delcarro, C. Pisano, M. Radici and A. Signori, *Extraction of partonic transverse momentum distributions from semi-inclusive deep-inelastic scattering, Drell-Yan and Z-boson production*, *JHEP* **06** (2017) 081, [1703.10157].

[70] C. Pisano, A. Bacchetta, F. Delcarro, M. Radici and A. Signori, *A first determination of the unpolarized quark TMDs from a global analysis*, *PoS* **QCDEV2017** (2018) 010, [1801.08443].

[71] I. Scimemi and A. Vladimirov, *Analysis of vector boson production within TMD factorization*, *Eur. Phys. J.* **C78** (2018) 89, [1706.01473].

[72] A. Bacchetta, V. Bertone, C. Bissolotti, G. Bozzi, F. Delcarro, F. Piacenza et al., *Transverse-momentum-dependent parton distributions up to N^3LL from Drell-Yan data*, 1912.07550.

[73] I. Scimemi and A. Vladimirov, *Non-perturbative structure of semi-inclusive deep-inelastic and Drell-Yan scattering at small transverse momentum*, 1912.06532.

[74] A. Bacchetta, V. Bertone, C. Bissolotti, G. Bozzi, M. Cerutti, F. Piacenza et al., *Unpolarized Transverse Momentum Distributions from a global fit of Drell-Yan and Semi-Inclusive Deep-Inelastic Scattering data*, 2206.07598.

[75] M. Boglione, A. Dotson, L. Gamberg, S. Gordon, J. Gonzalez-Hernandez, A. Prokudin et al., *Mapping the Kinematical Regimes of Semi-Inclusive Deep Inelastic Scattering*, *JHEP* **10** (2019) 122, [1904.12882].

[76] M. Grewal, Z.-B. Kang, J.-W. Qiu and A. Signori, *Predictive power of transverse-momentum-dependent distributions*, *Phys. Rev. D* **101** (2020) 114023, [2003.07453].

[77] J. Collins, L. Gamberg, A. Prokudin, T. C. Rogers, N. Sato and B. Wang, *Relating Transverse Momentum Dependent and Collinear Factorization Theorems in a Generalized Formalism*, *Phys. Rev.* **D94** (2016) 034014, [1605.00671].

[78] L. Gamberg, A. Metz, D. Pitonyak and A. Prokudin, *Connections between collinear and transverse-momentum-dependent polarized observables within the Collins–Soper–Sterman formalism*, *Phys. Lett. B* **781** (2018) 443–454, [1712.08116].

[79] J. Cammarota, L. Gamberg, Z.-B. Kang, J. A. Miller, D. Pitonyak, A. Prokudin et al., *Origin of single transverse-spin asymmetries in high-energy collisions*, *Phys. Rev. D* **102** (2020) 054002, [2002.08384].

[80] M. G. Echevarria, A. Idilbi, Z.-B. Kang and I. Vitev, *QCD Evolution of the Sivers Asymmetry*, *Phys. Rev.* **D89** (2014) 074013, [1401.5078].

[81] A. Bacchetta, F. Delcarro, C. Pisano and M. Radici, *The three-dimensional distribution of quarks in momentum space*, 2004.14278.

[82] M. Bury, A. Prokudin and A. Vladimirov, *Extraction of the Sivers function from SIDIS, Drell-Yan, and $W^{\pm}/Z$ boson production data with TMD evolution*, *JHEP* **05** (2021) 151, [2103.03270].

[83] M. Bury, A. Prokudin and A. Vladimirov, *Extraction of the Sivers Function from SIDIS, Drell-Yan, and $W^{\pm}/Z$ Data at Next-to-Next-to-Next-to Leading Order*, *Phys. Rev. Lett.* **126** (2021) 112002, [2012.05135].

[84] COMPASS collaboration, C. Adolph et al., *II – Experimental investigation of transverse spin asymmetries in μ -p SIDIS processes: Sivers asymmetries*, *Phys. Lett. B* **717** (2012) 383–389, [1205.5122].

[85] HERMES collaboration, A. Airapetian et al., *Azimuthal single- and double-spin asymmetries in semi-inclusive deep-inelastic lepton scattering by transversely polarized protons*, *JHEP* **12** (2020) 010, [2007.07755].

[86] A. Bacchetta, M. Diehl, K. Goeke, A. Metz, P. J. Mulders and M. Schlegel, *Semi-inclusive deep inelastic scattering at small transverse momentum*, *JHEP* **02** (2007) 093, [hep-ph/0611265].

[87] A. Idilbi and X.-d. Ji, *Threshold resummation for Drell-Yan process in soft-collinear effective theory*, *Phys. Rev. D* **72** (2005) 054016, [hep-ph/0501006].

[88] S. Arnold, A. Metz and M. Schlegel, *Dilepton production from polarized hadron hadron collisions*, *Phys. Rev. D* **79** (2009) 034005, [0809.2262].

[89] Z.-B. Kang and J.-W. Qiu, *Single transverse spin asymmetry of dilepton production near Z0 pole*, *Phys. Rev. D* **81** (2010) 054020, [0912.1319].

[90] M. Anselmino, M. Boglione, U. D'Alesio, S. Melis, F. Murgia and A. Prokudin, *Sivers effect in Drell-Yan processes*, *Phys. Rev. D* **79** (2009) 054010, [0901.3078].

[91] J. Huang, Z.-B. Kang, I. Vitev and H. Xing, *Spin asymmetries for vector boson production in polarized p+p collisions*, *Phys. Rev. D* **93** (2016) 014036, [1511.06764].

[92] P. Sun, J. Isaacson, C. P. Yuan and F. Yuan, *Nonperturbative functions for SIDIS and Drell–Yan processes*, *Int. J. Mod. Phys.* **A33** (2018) 1841006, [1406.3073].

[93] X. Wang, Z. Lu and I. Schmidt, *Transverse momentum spectrum of dilepton pair in the unpolarized $\pi^- N$ Drell-Yan process within TMD factorization*, *JHEP* **08** (2017) 137, [1707.05207].

[94] J. Conway et al., *Experimental Study of Muon Pairs Produced by 252-GeV Pions on Tungsten*, *Phys. Rev. D* **39** (1989) 92–122.

[95] J.-w. Qiu and X.-f. Zhang, *QCD prediction for heavy boson transverse momentum distributions*, *Phys. Rev. Lett.* **86** (2001) 2724–2727, [hep-ph/0012058].

[96] I. Scimemi and A. Vladimirov, *Systematic analysis of double-scale evolution*, *JHEP* **08** (2018) 003, [1803.11089].

[97] M. A. Ebert, J. K. L. Michel, I. W. Stewart and Z. Sun, *Disentangling long and short distances in momentum-space TMDs*, *JHEP* **07** (2022) 129, [2201.07237].

[98] H1, ZEUS collaboration, H. Abramowicz et al., *Combination of measurements of inclusive deep inelastic $e^{\pm}p$ scattering cross sections and QCD analysis of HERA data*, *Eur. Phys. J. C* **75** (2015) 580, [1506.06042].

[99] D. de Florian, R. Sassot, M. Epele, R. J. Hernández-Pinto and M. Stratmann, *Parton-to-Pion Fragmentation Reloaded*, *Phys. Rev. D* **91** (2015) 014035, [1410.6027].

[100] D. de Florian, M. Epele, R. Hernandez-Pinto, R. Sassot and M. Stratmann, *Parton-to-Kaon Fragmentation Revisited*, *Phys. Rev. D* **95** (2017) 094019, [1702.06353].

[101] K. Eskola, V. Kolhinen and C. Salgado, *The Scale dependent nuclear effects in parton distributions for practical applications*, *Eur. Phys. J. C* **9** (1999) 61–68, [hep-ph/9807297].

[102] H1 collaboration, F. Aaron et al., *Inclusive Deep Inelastic Scattering at High Q^2 with Longitudinally Polarised Lepton Beams at HERA*, *JHEP* **09** (2012) 061, [1206.7007].

[103] V. Bertone, S. Carrazza and J. Rojo, *APFEL: A PDF Evolution Library with QED corrections*, *Comput. Phys. Commun.* **185** (2014) 1647–1668, [1310.1394].

[104] Z.-B. Kang and J.-W. Qiu, *Evolution of twist-3 multi-parton correlation functions relevant to single transverse-spin asymmetry*, *Phys. Rev. D* **79** (2009) 016003, [0811.3101].

[105] J. Zhou, F. Yuan and Z.-T. Liang, *QCD Evolution of the Transverse Momentum Dependent Correlations*, *Phys. Rev. D* **79** (2009) 114022, [0812.4484].

[106] W. Vogelsang and F. Yuan, *Next-to-leading Order Calculation of the Single Transverse Spin Asymmetry in the Drell-Yan Process*, *Phys. Rev. D* **79** (2009) 094010, [0904.0410].

[107] V. Braun, A. Manashov and B. Pirnay, *Scale dependence of twist-three contributions to single spin asymmetries*, *Phys. Rev. D* **80** (2009) 114002, [0909.3410].

[108] Z.-B. Kang and J.-W. Qiu, *QCD evolution of naive-time-reversal-odd parton distribution functions*, *Phys. Lett. B* **713** (2012) 273–276, [1205.1019].

[109] Z.-B. Kang, I. Vitev and H. Xing, *Transverse momentum-weighted Sivers asymmetry in semi-inclusive deep inelastic scattering at next-to-leading order*, *Phys. Rev. D* **87** (2013) 034024, [1212.1221].

[110] A. Schafer and J. Zhou, *A Note on the scale evolution of the ETQS function* $T_F(x,x)$, *Phys. Rev. D* **85** (2012) 117501, [1203.5293].

[111] J. Ma, Q. Wang and G. Zhang, *QCD Evolutions of Twist-3 Chirality-Odd Operators*, *Phys. Lett. B* **718** (2013) 1358–1363, [1210.1006].

[112] L.-Y. Dai, Z.-B. Kang, A. Prokudin and I. Vitev, *Next-to-leading order transverse momentum-weighted Sivers asymmetry in semi-inclusive deep inelastic scattering: the role of the three-gluon correlator*, *Phys. Rev. D* **92** (2015) 114024, [1409.5851].

[113] Z.-B. Kang, J.-W. Qiu and H. Zhang, *Quark-gluon correlation functions relevant to single transverse spin asymmetries*, *Phys. Rev. D* **81** (2010) 114030, [1004.4183].

[114] P. Sun and F. Yuan, *Transverse momentum dependent evolution: Matching semi-inclusive deep inelastic scattering processes to Drell-Yan and W/Z boson production*, *Phys. Rev. D* **88** (2013) 114012, [1308.5003].

[115] A. Vogt, *Efficient evolution of unpolarized and polarized parton distributions with QCD-PEGASUS*, *Comput. Phys. Commun.* **170** (2005) 65–92, [hep-ph/0408244].

[116] F. James and M. Roos, *Minuit: A System for Function Minimization and Analysis of the Parameter Errors and Correlations*, *Comput. Phys. Commun.* **10** (1975) 343–367.

[117] F. James and M. Winkler, *MINUIT User's Guide*, .

[118] HERMES collaboration, A. Airapetian et al., *Azimuthal single- and double-spin asymmetries in semi-inclusive deep-inelastic lepton scattering by transversely polarized protons*, 2007.07755.

[119] S. M. Aybat and T. C. Rogers, *TMD Parton Distribution and Fragmentation Functions with QCD Evolution*, *Phys. Rev.* **D83** (2011) 114042, [a].

[120] Z.-B. Kang, A. Prokudin, P. Sun and F. Yuan, *Extraction of Quark Transversity Distribution and Collins Fragmentation Functions with QCD Evolution*, *Phys. Rev.* **D93** (2016) 014009, [1505.05589].

[121] J. C. Collins and T. C. Rogers, *Equality of Two Definitions for Transverse Momentum Dependent Parton Distribution Functions*, *Phys. Rev. D* **87** (2013) 034018, [1210.2100].

[122] Z.-B. Kang, B.-W. Xiao and F. Yuan, *QCD Resummation for Single Spin Asymmetries*, *Phys. Rev. Lett.* **107** (2011) 152002, [1106.0266].

[123] I. Scimemi, A. Tarasov and A. Vladimirov, *Collinear matching for Sivers function at next-to-leading order*, *JHEP* **05** (2019) 125, [1901.04519].

[124] V. Moos and A. Vladimirov, *Calculation of transverse momentum dependent distributions beyond the leading power*, 2008.01744.

[125] G. F. Sterman and S. Weinberg, *Jets from Quantum Chromodynamics*, *Phys. Rev. Lett.* **39** (1977) 1436.

[126] D. Boer and C. Pisano, *Impact of gluon polarization on Higgs boson plus jet production at the LHC*, *Phys. Rev. D* **91** (2015) 074024, [1412.5556].

[127] H1 collaboration, V. Andreev et al., *Measurement of Lepton-Jet Correlation in Deep-Inelastic Scattering with the H1 Detector Using Machine Learning for Unfolding*, *Phys. Rev. Lett.* **128** (2022) 132002, [2108.12376].

[128] D. Gutierrez-Reyes, I. Scimemi, W. J. Waalewijn and L. Zoppi, *Transverse momentum dependent distributions with jets*, *Phys. Rev. Lett.* **121** (2018) 162001, [1807.07573].

[129] D. Gutierrez-Reyes, I. Scimemi, W. J. Waalewijn and L. Zoppi, *Transverse momentum dependent distributions in e^+e^- and semi-inclusive deep-inelastic scattering using jets*, 1904.04259.

[130] X. Liu, F. Ringer, W. Vogelsang and F. Yuan, *Lepton-jet Correlations in Deep Inelastic Scattering at the Electron-Ion Collider*, 1812.08077.

[131] D. Boer and W. Vogelsang, *Asymmetric jet correlations in p p uparrow scattering*, *Phys. Rev. D* **69** (2004) 094025, [hep-ph/0312320].

[132] STAR collaboration, B. I. Abelev et al., *Measurement of transverse single-spin asymmetries for di-jet production in proton-proton collisions at s**(1/2) = 200-GeV*, *Phys. Rev. Lett.* **99** (2007) 142003, [0705.4629].

[133] J.-W. Qiu, W. Vogelsang and F. Yuan, *Single Transverse-Spin Asymmetry in Hadronic Dijet Production*, *Phys. Rev. D* **76** (2007) 074029, [0706.1196].

[134] C. Bomhof, P. Mulders, W. Vogelsang and F. Yuan, *Single-Transverse Spin Asymmetry in Dijet Correlations at Hadron Colliders*, *Phys. Rev. D* **75** (2007) 074019, [hep-ph/0701277].

[135] M. G. A. Buffing, Z.-B. Kang, K. Lee and X. Liu, *A transverse momentum dependent framework for back-to-back photon+jet production*, 1812.07549.

[136] Z.-B. Kang, X. Liu, F. Ringer and H. Xing, *The transverse momentum distribution of hadrons within jets*, *JHEP* **11** (2017) 068, [1705.08443].

[137] Z.-B. Kang, K. Lee, D. Y. Shao and F. Zhao, *Spin asymmetries in electron-jet production at the future electron ion collider*, *JHEP* **11** (2021) 005, [2106.15624].

[138] U. D'Alesio, F. Murgia and C. Pisano, *Testing the universality of the Collins function in pion-jet production at RHIC*, *Phys. Lett. B* **773** (2017) 300–306, [1707.00914].

[139] Z.-B. Kang, K. Lee and F. Zhao, *Polarized jet fragmentation functions*, 2005.02398.

[140] Z.-B. Kang, A. Prokudin, F. Ringer and F. Yuan, *Collins azimuthal asymmetries of hadron production inside jets*, *Phys. Lett.* **B774** (2017) 635–642, [1707.00913].

[141] STAR collaboration, L. Adamczyk et al., *Azimuthal transverse single-spin asymmetries of inclusive jets and charged pions within jets from polarized-proton collisions at* $\sqrt{s} = 500$ *GeV*, *Phys. Rev. D* **97** (2018) 032004, [1708.07080].

[142] M. Arratia, Z.-B. Kang, A. Prokudin and F. Ringer, *Jet-based measurements of Sivers and Collins asymmetries at the future Electron-Ion Collider*, 2007.07281.

[143] D. Boer, P. J. Mulders, C. Pisano and J. Zhou, *Asymmetries in Heavy Quark Pair and Dijet Production at an EIC*, *JHEP* **08** (2016) 001, [1605.07934].

[144] F. Yuan, *Heavy Quarkonium Production in Single Transverse Polarized High Energy Scattering*, *Phys. Rev. D* **78** (2008) 014024, [0801.4357].

[145] A. Mukherjee and S. Rajesh, *J/ψ production in polarized and unpolarized ep collision and Sivers and cos2ϕ asymmetries*, *Eur. Phys. J. C* **77** (2017) 854, [1609.05596].

[146] S. Rajesh, R. Kishore and A. Mukherjee, *Sivers effect in Inelastic J/ψ Photoproduction in $ep^{\uparrow}$ Collision in Color Octet Model*, *Phys. Rev. D* **98** (2018) 014007, [1802.10359].

[147] A. Bacchetta, D. Boer, C. Pisano and P. Taels, *Gluon TMDs and NRQCD matrix elements in J/ψ production at an EIC*, *Eur. Phys. J. C* **80** (2020) 72, [1809.02056].

[148] D. Boer, U. D'Alesio, F. Murgia, C. Pisano and P. Taels, *J/ψ meson production in SIDIS: matching high and low transverse momentum*, *JHEP* **09** (2020) 040, [2004.06740].

[149] U. D'Alesio, F. Murgia, C. Pisano and P. Taels, *Azimuthal asymmetries in semi-inclusive J/ψ + jet production at an EIC*, *Phys. Rev. D* **100** (2019) 094016, [1908.00446].

[150] D. Boer et al., *Gluons and the quark sea at high energies: Distributions, polarization, tomography*, 1108.1713.

[151] L. Zheng, E. Aschenauer, J. Lee, B.-W. Xiao and Z.-B. Yin, *Accessing the gluon Sivers function at a future electron-ion collider*, *Phys. Rev. D* **98** (2018) 034011, [1805.05290].

[152] T. Sjostrand, S. Mrenna and P. Z. Skands, *PYTHIA 6.4 Physics and Manual*, *JHEP* **05** (2006) 026, [hep-ph/0603175].

[153] HERMES collaboration, A. Airapetian et al., *Leading-Order Determination of the Gluon Polarization from high-p_T Hadron Electroproduction*, *JHEP* **08** (2010) 130, [1002.3921].

[154] S. J. Brodsky, D. S. Hwang and I. Schmidt, *Final state interactions and single spin asymmetries in semiinclusive deep inelastic scattering*, *Phys. Lett. B* **530** (2002) 99–107, [hep-ph/0201296].

[155] J. C. Collins, *Leading twist single transverse-spin asymmetries: Drell-Yan and deep inelastic scattering*, *Phys. Lett. B* **536** (2002) 43–48, [hep-ph/0204004].

[156] D. Boer, P. Mulders and F. Pijlman, *Universality of T odd effects in single spin and azimuthal asymmetries*, *Nucl. Phys. B* **667** (2003) 201–241, [hep-ph/0303034].

[157] M. Buffing, A. Mukherjee and P. Mulders, *Generalized Universality of Definite Rank Gluon Transverse Momentum Dependent Correlators*, *Phys. Rev. D* **88** (2013) 054027, [1306.5897].

[158] D. Boer, C. Lorcé, C. Pisano and J. Zhou, *The gluon Sivers distribution: status and future prospects*, *Adv. High Energy Phys.* **2015** (2015) 371396, [1504.04332].

[159] A. Arbuzov et al., *On the physics potential to study the gluon content of proton and deuteron at NICA SPD*, 2011.15005.

[160] A. Banfi, M. Dasgupta and Y. Delenda, *Azimuthal decorrelations between QCD jets at all orders*, *Phys. Lett. B* **665** (2008) 86–91, [0804.3786].

[161] S. D. Ellis and D. E. Soper, *Successive combination jet algorithm for hadron collisions*, *Phys. Rev. D* **48** (1993) 3160–3166, [hep-ph/9305266].

[162] M. Dasgupta and G. P. Salam, *Resummation of nonglobal QCD observables*, *Phys. Lett.* **B512** (2001) 323–330, [hep-ph/0104277].

[163] X. Liu, F. Ringer, W. Vogelsang and F. Yuan, *Lepton-jet Correlation in Deep Inelastic Scattering*, 2007.12866.

[164] Y.-T. Chien, D. Y. Shao and B. Wu, *Resummation of Boson-Jet Correlation at Hadron Colliders*, *JHEP* **11** (2019) 025, [1905.01335].

[165] Z.-B. Kang, K. Lee, D. Y. Shao and J. Terry, *The Sivers Asymmetry in Hadronic Dijet Production*, 2008.05470.

[166] R. F. del Castillo, M. G. Echevarria, Y. Makris and I. Scimemi, *TMD factorization for di-jet and heavy meson pair in DIS*, 2008.07531.

[167] M. A. Ebert, I. W. Stewart and Y. Zhao, *Towards Quasi-Transverse Momentum Dependent PDFs Computable on the Lattice*, *JHEP* **09** (2019) 037, [1901.03685].

[168] B. Jager, M. Stratmann and W. Vogelsang, *Single inclusive jet production in polarized pp collisions at $O(alpha_s^3)$*, *Phys. Rev. D* **70** (2004) 034010, [hep-ph/0404057].

[169] A. Mukherjee and W. Vogelsang, *Jet production in (un)polarized pp collisions: dependence on jet algorithm*, *Phys. Rev. D* **86** (2012) 094009, [1209.1785].

[170] M. Dasgupta, F. A. Dreyer, G. P. Salam and G. Soyez, *Inclusive jet spectrum for small-radius jets*, *JHEP* **06** (2016) 057, [1602.01110].

[171] X. Liu, S.-O. Moch and F. Ringer, *Phenomenology of single-inclusive jet production with jet radius and threshold resummation*, *Phys. Rev. D* **97** (2018) 056026, [1801.07284].

[172] M. G. Echevarria, T. Kasemets, P. J. Mulders and C. Pisano, *QCD evolution of (un)polarized gluon TMDPDFs and the Higgs q_T-distribution*, *JHEP* **07** (2015) 158, [1502.05354].

[173] P. Mulders and J. Rodrigues, *Transverse momentum dependence in gluon distribution and fragmentation functions*, *Phys.Rev.* **D63** (2001) 094021, [hep-ph/0009343].

[174] C. Bomhof and P. J. Mulders, *Non-universality of transverse momentum dependent parton distribution functions*, *Nucl.Phys.* **B795** (2008) 409–427, [0709.1390].

[175] J. G. Korner, E. Mirkes and G. A. Schuler, *QCD Jets at HERA. 1. O (α^-s) Radiative Corrections to Electroweak Cross-sections and Jet Rates*, *Int. J. Mod. Phys.* **A4** (1989) 1781.

[176] E. Mirkes and S. Willfahrt, *Effects of jet azimuthal angular distributions on dijet production cross-sections in DIS*, *Phys. Lett. B* **414** (1997) 205–209, [hep-ph/9708231].

[177] W. Giele and E. Glover, *Higher order corrections to jet cross-sections in e^+e^- annihilation*, *Phys. Rev. D* **46** (1992) 1980–2010.

[178] P. B. Arnold and M. Reno, *The Complete Computation of High p_T W and Z Production in 2nd Order QCD*, *Nucl. Phys. B* **319** (1989) 37–71.

[179] S. Catani, *The Singular behavior of QCD amplitudes at two loop order*, *Phys. Lett. B* **427** (1998) 161–171, [hep-ph/9802439].

[180] T. Becher and M. Neubert, *Infrared singularities of scattering amplitudes in perturbative QCD*, *Phys. Rev. Lett.* **102** (2009) 162001, [0901.0722].

[181] C. Bomhof and P. Mulders, *Gluonic pole cross-sections and single spin asymmetries in hadron-hadron scattering*, *JHEP* **02** (2007) 029, [hep-ph/0609206].

[182] Z.-B. Kang and J.-W. Qiu, *Single transverse-spin asymmetry for D-meson production in semi-inclusive deep inelastic scattering*, *Phys. Rev.* **D78** (2008) 034005, [0806.1970].

[183] U. D'Alesio, L. Maxia, F. Murgia, C. Pisano and S. Rajesh, *Process dependence of the gluon Sivers function in $p^\uparrow p \to J/\psi + X$ within a TMD scheme in NRQCD*, *Phys. Rev. D* **102** (2020) 094011, [2007.03353].

[184] A. Hornig, D. Kang, Y. Makris and T. Mehen, *Transverse Vetoes with Rapidity Cutoff in SCET*, *JHEP* **12** (2017) 043, [1708.08467].

[185] S. Fleming, A. H. Hoang, S. Mantry and I. W. Stewart, *Jets from massive unstable particles: Top-mass determination*, *Phys. Rev. D* **77** (2008) 074010, [hep-ph/0703207].

[186] S. Fleming, A. H. Hoang, S. Mantry and I. W. Stewart, *Top Jets in the Peak Region: Factorization Analysis with NLL Resummation*, *Phys. Rev. D* **77** (2008) 114003, [0711.2079].

[187] C. Lepenik and V. Mateu, *NLO Massive Event-Shape Differential and Cumulative Distributions*, *JHEP* **03** (2020) 024, [1912.08211].

[188] A. Bris, V. Mateu and M. Preisser, *Massive event-shape distributions at N^2LL*, *JHEP* **09** (2020) 132, [2006.06383].

[189] A. H. Hoang, C. Lepenik and M. Stahlhofen, *Two-Loop Massive Quark Jet Functions in SCET*, *JHEP* **08** (2019) 112, [1904.12839].

[190] L. Dai, C. Kim and A. K. Leibovich, *Heavy Quark Jet Fragmentation*, *JHEP* **09** (2018) 109, [1805.06014].

[191] H. T. Li and I. Vitev, *Inclusive heavy flavor jet production with semi-inclusive jet functions: from proton to heavy-ion collisions*, *JHEP* **07** (2019) 148, [1811.07905].

[192] C. Kim, *Exclusive heavy quark dijet cross section*, *J. Korean Phys. Soc.* **77** (2020) 469–476, [2008.02942].

[193] M. Cacciari, G. P. Salam and G. Soyez, *The anti-k_t jet clustering algorithm*, *JHEP* **04** (2008) 063, [0802.1189].

[194] M. Balsiger, T. Becher and A. Ferroglia, *Resummation of non-global logarithms in cross sections with massive particles*, *JHEP* **09** (2020) 029, [2006.00014].

[195] S. Catani and M. Grazzini, *Higgs Boson Production at Hadron Colliders: Hard-Collinear Coefficients at the NNLO*, *Eur. Phys. J. C* **72** (2012) 2013, [1106.4652].

[196] T. Gehrmann, T. Luebbert and L. L. Yang, *Calculation of the transverse parton distribution functions at next-to-next-to-leading order*, *JHEP* **06** (2014) 155, [1403.6451].

[197] T. Lübbert, J. Oredsson and M. Stahlhofen, *Rapidity renormalized TMD soft and beam functions at two loops*, *JHEP* **03** (2016) 168, [1602.01829].

[198] M. G. Echevarria, I. Scimemi and A. Vladimirov, *Unpolarized Transverse Momentum Dependent Parton Distribution and Fragmentation Functions at next-to-next-to-leading order*, *JHEP* **09** (2016) 004, [1604.07869].

[199] M.-X. Luo, T.-Z. Yang, H. X. Zhu and Y. J. Zhu, *Transverse Parton Distribution and Fragmentation Functions at NNLO: the Gluon Case*, *JHEP* **01** (2020) 040, [1909.13820].

[200] M. A. Ebert, B. Mistlberger and G. Vita, *Transverse momentum dependent PDFs at N^3LO*, 2006.05329.

[201] X.-D. Ji, *Gluon correlations in the transversely polarized nucleon*, *Phys. Lett.* **B289** (1992) 137–142.

[202] H. Beppu, Y. Koike, K. Tanaka and S. Yoshida, *Contribution of Twist-3 Multi-Gluon Correlation Functions to Single Spin Asymmetry in Semi-Inclusive Deep Inelastic Scattering*, *Phys. Rev.* **D82** (2010) 054005, [1007.2034].

[203] COMPASS collaboration, C. Adolph et al., *First measurement of the Sivers asymmetry for gluons using SIDIS data*, *Phys. Lett. B* **772** (2017) 854–864, [1701.02453].

[204] M. Burkardt, *Sivers mechanism for gluons*, *Phys. Rev.* **D69** (2004) 091501, [hep-ph/0402014].

[205] U. D'Alesio, F. Murgia and C. Pisano, *Towards a first estimate of the gluon Sivers function from A_N data in pp collisions at RHIC*, *JHEP* **09** (2015) 119, [1506.03078].

[206] E. Aschenauer, U. D'Alesio and F. Murgia, *TMDs and SSAs in hadronic interactions*, *Eur. Phys. J. A* **52** (2016) 156, [1512.05379].

[207] U. D'Alesio, C. Flore, F. Murgia, C. Pisano and P. Taels, *Unraveling the Gluon Sivers Function in Hadronic Collisions at RHIC*, *Phys. Rev. D* **99** (2019) 036013, [1811.02970].

[208] S. Dulat, T.-J. Hou, J. Gao, M. Guzzi, J. Huston, P. Nadolsky et al., *New parton distribution functions from a global analysis of quantum chromodynamics*, *Phys. Rev. D* **93** (2016) 033006, [1506.07443].

[209] STAR collaboration, J. Adams et al., *Cross-sections and transverse single spin asymmetries in forward neutral pion production from proton collisions at s**(1/2) = 200- GeV*, *Phys. Rev. Lett.* **92** (2004) 171801, [hep-ex/0310058].

[210] BRAHMS collaboration, I. Arsene et al., *Single Transverse Spin Asymmetries of Identified Charged Hadrons in Polarized p+p Collisions at s**(1/2) = 62.4-GeV*, *Phys. Rev. Lett.* **101** (2008) 042001, [0801.1078].

[211] STAR collaboration, B. Abelev et al., *Forward Neutral Pion Transverse Single Spin Asymmetries in p+p Collisions at s**(1/2) = 200-GeV*, *Phys. Rev. Lett.* **101** (2008) 222001, [0801.2990].

[212] STAR collaboration, L. Adamczyk et al., *Transverse Single-Spin Asymmetry and Cross-Section for π^0 and η Mesons at Large Feynman-x in Polarized $p+p$ Collisions at $\sqrt{s} = 200$ GeV*, *Phys. Rev. D* **86** (2012) 051101, [1205.6826].

[213] PHENIX collaboration, A. Adare et al., *Measurement of transverse-single-spin asymmetries for midrapidity and forward-rapidity production of hadrons in polarized p+p collisions at $\sqrt{s}$ =200 and 62.4 GeV*, *Phys. Rev. D* **90** (2014) 012006, [1312.1995].

[214] STAR collaboration, L. Adamczyk et al., *Azimuthal transverse single-spin asymmetries of inclusive jets and charged pions within jets from polarized-proton collisions at $\sqrt{s} = 500$ GeV*, *Phys. Rev. D* **97** (2018) 032004, [1708.07080].

[215] G. L. Kane, J. Pumplin and W. Repko, *Transverse Quark Polarization in Large p(T) Reactions, e+ e- Jets, and Leptoproduction: A Test of QCD*, *Phys. Rev. Lett.* **41** (1978) 1689.

[216] C. Kouvaris, J.-W. Qiu, W. Vogelsang and F. Yuan, *Single transverse-spin asymmetry in high transverse momentum pion production in pp collisions*, *Phys. Rev. D* **74** (2006) 114013, [hep-ph/0609238].

[217] Z.-B. Kang, F. Yuan and J. Zhou, *Twist-three fragmentation function contribution to the single spin asymmetry in p p collisions*, *Phys. Lett. B* **691** (2010) 243–248, [1002.0399].

[218] Z.-B. Kang, J.-W. Qiu, W. Vogelsang and F. Yuan, *An Observation Concerning the Process Dependence of the Sivers Functions*, *Phys. Rev. D* **83** (2011) 094001, [1103.1591].

[219] A. Metz and D. Pitonyak, *Fragmentation contribution to the transverse single-spin asymmetry in proton-proton collisions*, *Phys. Lett. B* **723** (2013) 365–370, [1212.5037].

[220] L. Gamberg, Z.-B. Kang and A. Prokudin, *Indication on the process-dependence of the Sivers effect*, *Phys. Rev. Lett.* **110** (2013) 232301, [1302.3218].

[221] K. Kanazawa, Y. Koike, A. Metz and D. Pitonyak, *Towards an explanation of transverse single-spin asymmetries in proton-proton collisions: the role of fragmentation in collinear factorization*, *Phys. Rev. D* **89** (2014) 111501, [1404.1033].

[222] L. Gamberg, Z.-B. Kang, D. Pitonyak and A. Prokudin, *Phenomenological constraints on A_N in $p^\uparrow p \to \pi X$ from Lorentz invariance relations*, *Phys. Lett. B* **770** (2017) 242–251, [1701.09170].

[223] J. Collins and J.-W. Qiu, *k_T factorization is violated in production of high-transverse-momentum particles in hadron-hadron collisions*, *Phys. Rev. D* **75** (2007) 114014, [0705.2141].

[224] T. C. Rogers and P. J. Mulders, *No Generalized TMD-Factorization in Hadro-Production of High Transverse Momentum Hadrons*, *Phys. Rev. D* **81** (2010) 094006, [1001.2977].

[225] X. Liu, F. Ringer, W. Vogelsang and F. Yuan, *Factorization and its Breaking in Dijet Single Transverse Spin Asymmetries in pp Collisions*, 2008.03666.

[226] K. Kanazawa and Y. Koike, *New Analysis of the Single Transverse-Spin Asymmetry for Hadron Production at RHIC*, *Phys. Rev. D* **82** (2010) 034009, [1005.1468].

[227] AnDY collaboration, L. Bland et al., *Cross Sections and Transverse Single-Spin Asymmetries in Forward Jet Production from Proton Collisions at $\sqrt{s} = 500$ GeV*, *Phys. Lett. B* **750** (2015) 660–665, [1304.1454].

[228] STAR collaboration, B. Abelev et al., *Measurement of transverse single-spin asymmetries for di-jet production in proton-proton collisions at s**(1/2) = 200-GeV*, *Phys. Rev. Lett.* **99** (2007) 142003, [0705.4629].

[229] W. Vogelsang and F. Yuan, *Hadronic Dijet Imbalance and Transverse-Momentum Dependent Parton Distributions*, *Phys. Rev. D* **76** (2007) 094013, [0708.4398].

[230] J.-W. Qiu, W. Vogelsang and F. Yuan, *Asymmetric di-jet production in polarized hadronic collisions*, *Phys. Lett. B* **650** (2007) 373–378, [0704.1153].

[231] H. Liu, *Talk given at RIKEN BNL Workshop Jet Observables at the Electron-Ion Collider*, 2020.

[232] PHENIX collaboration, A. Adare et al., *Nonperturbative-transverse-momentum effects and evolution in dihadron and direct photon-hadron angular correlations in p+p collisions at $\sqrt{s}$=510 GeV*, *Phys. Rev. D* **95** (2017) 072002, [1609.04769].

[233] PHENIX collaboration, C. Aidala et al., *Nonperturbative transverse-momentum-dependent effects in dihadron and direct photon-hadron angular correlations in $p+p$ collisions at $\sqrt{s} = 200$ GeV*, *Phys. Rev.* **D98** (2018) 072004, [1805.02450].

[234] P. Sun, C. P. Yuan and F. Yuan, *Soft Gluon Resummations in Dijet Azimuthal Angular Correlations in Hadronic Collisions*, *Phys. Rev. Lett.* **113** (2014) 232001, [1405.1105].

[235] P. Sun, C. P. Yuan and F. Yuan, *Transverse Momentum Resummation for Dijet Correlation in Hadronic Collisions*, *Phys. Rev.* **D92** (2015) 094007, [1506.06170].

[236] Y.-T. Chien, R. Rahn, S. Schrijnder van Velzen, D. Y. Shao, W. J. Waalewijn and B. Wu, *Azimuthal angle for boson-jet production in the back-to-back limit*, 2005.12279.

[237] Z.-B. Kang, X. Liu, S. Mantry and D. Y. Shao, *Jet Charge: A Flavor Prism for Spin Asymmetries at the EIC*, *Phys. Rev. Lett.* **125** (2020) 242003, [2008.00655].

[238] M. Cacciari, G. P. Salam and G. Soyez, *FastJet User Manual*, *Eur. Phys. J. C* **72** (2012) 1896, [1111.6097].

[239] C. W. Bauer, S. Fleming, D. Pirjol, I. Z. Rothstein and I. W. Stewart, *Hard scattering factorization from effective field theory*, *Phys. Rev. D* **66** (2002) 014017, [hep-ph/0202088].

[240] N. Kidonakis, G. Oderda and G. F. Sterman, *Evolution of color exchange in QCD hard scattering*, *Nucl. Phys. B* **531** (1998) 365–402, [hep-ph/9803241].

[241] J.-y. Chiu, A. Jain, D. Neill and I. Z. Rothstein, *The Rapidity Renormalization Group*, *Phys. Rev. Lett.* **108** (2012) 151601, [1104.0881].

[242] S. Catani, D. de Florian and G. Rodrigo, *Space-like (versus time-like) collinear limits in QCD: Is factorization violated?*, *JHEP* **07** (2012) 026, [1112.4405].

[243] J. R. Forshaw, M. H. Seymour and A. Siodmok, *On the Breaking of Collinear Factorization in QCD*, *JHEP* **11** (2012) 066, [1206.6363].

[244] A. Bacchetta, U. D'Alesio, M. Diehl and C. Miller, *Single-spin asymmetries: The Trento conventions*, *Phys. Rev. D* **70** (2004) 117504, [hep-ph/0410050].

[245] A. Bacchetta, C. Bomhof, P. Mulders and F. Pijlman, *Single spin asymmetries in hadron-hadron collisions*, *Phys. Rev. D* **72** (2005) 034030, [hep-ph/0505268].

[246] C. Bomhof, P. Mulders and F. Pijlman, *The Construction of gauge-links in arbitrary hard processes*, *Eur. Phys. J. C* **47** (2006) 147–162, [hep-ph/0601171].

[247] T. Becher, M. Neubert, L. Rothen and D. Y. Shao, *Effective Field Theory for Jet Processes*, *Phys. Rev. Lett.* **116** (2016) 192001, [1508.06645].

[248] T. Becher, M. Neubert, L. Rothen and D. Y. Shao, *Factorization and Resummation for Jet Processes*, *JHEP* **11** (2016) 019, [1605.02737].

[249] G. F. Sterman, *Resummations, power corrections and interjet radiation*, *Acta Phys. Polon.* **B36** (2005) 389–400, [hep-ph/0410014].

[250] T. Becher, R. Rahn and D. Y. Shao, *Non-global and rapidity logarithms in narrow jet broadening*, *JHEP* **10** (2017) 030, [1708.04516].

[251] Z.-B. Kang, D. Y. Shao and F. Zhao, *QCD resummation on single hadron transverse momentum distribution with the thrust axis*, *JHEP* **12** (2020) 127, [2007.14425].

[252] M. Dasgupta and G. P. Salam, *Accounting for coherence in interjet E_T flow: A Case study*, *JHEP* **03** (2002) 017, [hep-ph/0203009].

[253] M. Balsiger, T. Becher and D. Y. Shao, *NLL′ resummation of jet mass*, *JHEP* **04** (2019) 020, [1901.09038].

[254] D. Neill, *Non-Global and Clustering Effects for Groomed Multi-Prong Jet Shapes*, *JHEP* **02** (2019) 114, [1808.04897].

[255] A. Banfi, G. Marchesini and G. Smye, *Away from jet energy flow*, *JHEP* **08** (2002) 006, [hep-ph/0206076].

[256] Y. Hatta, E. Iancu, A. H. Mueller and D. N. Triantafyllopoulos, *Resumming double non-global logarithms in the evolution of a jet*, *JHEP* **02** (2018) 075, [1710.06722].

[257] H. X. Zhu, C. S. Li, H. T. Li, D. Y. Shao and L. L. Yang, *Transverse-momentum resummation for top-quark pairs at hadron colliders*, *Phys. Rev. Lett.* **110** (2013) 082001, [1208.5774].

[258] H. T. Li, C. S. Li, D. Y. Shao, L. L. Yang and H. X. Zhu, *Top quark pair production at small transverse momentum in hadronic collisions*, *Phys. Rev.* **D88** (2013) 074004, [1307.2464].

[259] R. Angeles-Martinez, M. Czakon and S. Sapeta, *NNLO soft function for top quark pair production at small transverse momentum*, *JHEP* **10** (2018) 201, [1809.01459].

[260] R. Kelley and M. D. Schwartz, *1-loop matching and NNLL resummation for all partonic 2 to 2 processes in QCD*, *Phys. Rev. D* **83** (2011) 045022, [1008.2759].

[261] Z. L. Liu, C. S. Li, J. Wang and Y. Wang, *Resummation prediction on the jet mass spectrum in one-jet inclusive production at the LHC*, *JHEP* **04** (2015) 005, [1412.1337].

[262] I. Moult, I. W. Stewart, F. J. Tackmann and W. J. Waalewijn, *Employing Helicity Amplitudes for Resummation*, *Phys. Rev. D* **93** (2016) 094003, [1508.02397].

[263] S. J. Brodsky, D. S. Hwang and I. Schmidt, *Initial state interactions and single spin asymmetries in Drell-Yan processes*, *Nucl. Phys. B* **642** (2002) 344–356, [hep-ph/0206259].

[264] C. J. Bomhof, P. J. Mulders and F. Pijlman, *Gauge link structure in quark-quark correlators in hard processes*, *Phys. Lett.* **B596** (2004) 277–286, [hep-ph/0406099].

[265] C. J. Bomhof, *Azimuthal Spin Asymmetries in Hadronic Processes*, other thesis, Vrije U., 2007.

[266] L. Gamberg and Z.-B. Kang, *Process dependent Sivers function and implications for single spin asymmetry in inclusive hadron production*, *Phys. Lett.* **B696** (2011) 109–118, [1009.1936].

[267] U. D'Alesio, F. Murgia, C. Pisano and P. Taels, *Probing the gluon Sivers function in $p^\uparrow p \to J/\psi\, X$ and $p^\uparrow p \to D\, X$*, *Phys. Rev. D* **96** (2017) 036011, [1705.04169].

[268] T. Becher and M. Neubert, *On the Structure of Infrared Singularities of Gauge-Theory Amplitudes*, *JHEP* **06** (2009) 081, [0903.1126].

[269] G. F. Sterman and M. E. Tejeda-Yeomans, *Multiloop amplitudes and resummation*, *Phys. Lett. B* **552** (2003) 48–56, [hep-ph/0210130].

[270] S. D. Ellis, C. K. Vermilion, J. R. Walsh, A. Hornig and C. Lee, *Jet Shapes and Jet Algorithms in SCET*, *JHEP* **11** (2010) 101, [1001.0014].

[271] X. Liu and F. Petriello, *Resummation of jet-veto logarithms in hadronic processes containing jets*, *Phys. Rev. D* **87** (2013) 014018, [1210.1906].

[272] E. Anderson, Z. Bai, C. Bischof, S. Blackford, J. Demmel, J. Dongarra et al., *LAPACK Users' Guide*. Society for Industrial and Applied Mathematics, Philadelphia, PA, third ed., 1999.

[273] T. Becher, B. D. Pecjak and D. Y. Shao, *Factorization for the light-jet mass and hemisphere soft function*, *JHEP* **12** (2016) 018, [1610.01608].

[274] M. Balsiger, T. Becher and D. Y. Shao, *Non-global logarithms in jet and isolation cone cross sections*, *JHEP* **08** (2018) 104, [1803.07045].

[275] Z.-B. Kang, A. Prokudin, N. Sato and J. Terry, *Efficient Fourier Transforms for Transverse Momentum Dependent Distributions*, 1906.05949.

[276] J. Currie, A. Gehrmann-De Ridder, T. Gehrmann, E. Glover, A. Huss and J. Pires, *Precise predictions for dijet production at the LHC*, *Phys. Rev. Lett.* **119** (2017) 152001, [1705.10271].

[277] E.-C. Aschenauer et al., *The RHIC SPIN Program: Achievements and Future Opportunities*, 1501.01220.

[278] D. Krohn, M. D. Schwartz, T. Lin and W. J. Waalewijn, *Jet Charge at the LHC*, *Phys. Rev. Lett.* **110** (2013) 212001, [1209.2421].

[279] W. J. Waalewijn, *Calculating the Charge of a Jet*, *Phys. Rev. D* **86** (2012) 094030, [1209.3019].

[280] T. Sjostrand, S. Mrenna and P. Z. Skands, *A Brief Introduction to PYTHIA 8.1*, *Comput. Phys. Commun.* **178** (2008) 852–867, [0710.3820].

[281] ATLAS collaboration, G. Aad et al., *Measurement of the jet fragmentation function and transverse profile in proton-proton collisions at a center-of-mass energy of 7 TeV with the ATLAS detector*, *Eur. Phys. J.* **C71** (2011) 1795, [1109.5816].

[282] ATLAS collaboration, M. Aaboud et al., *Measurement of jet fragmentation in 5.02 TeV proton-lead and proton-proton collisions with the ATLAS detector*, *Nucl. Phys.* **A978** (2018) 65, [1706.02859].

[283] ATLAS collaboration, G. Aad et al., *Measurement of $D^{*+/-}$ meson production in jets from pp collisions at sqrt(s) = 7 TeV with the ATLAS detector*, *Phys. Rev.* **D85** (2012) 052005, [1112.4432].

[284] CMS collaboration, C. Collaboration, *Measurement of the radial profile of D^0 mesons in jets produced in pp and PbPb collisions at 5.02 TeV*, .

[285] ALICE collaboration, S. Acharya et al., *Measurement of the production of charm jets tagged with D^0 mesons in pp collisions at $\sqrt{s}$= 7 TeV*, 1905.02510.

[286] LHCb collaboration, R. Aaij et al., *Study of J/ψ Production in Jets*, *Phys. Rev. Lett.* **118** (2017) 192001, [1701.05116].

[287] CMS collaboration, C. Collaboration, *Production of prompt and nonprompt J/ψ mesons in jets in pp collisions at $\sqrt{s} = 5.02$ TeV*, .

[288] Y.-T. Chien, Z.-B. Kang, F. Ringer, I. Vitev and H. Xing, *Jet fragmentation functions in proton-proton collisions using soft-collinear effective theory*, *JHEP* **05** (2016) 125, [1512.06851].

[289] D. P. Anderle, T. Kaufmann, M. Stratmann, F. Ringer and I. Vitev, *Using hadron-in-jet data in a global analysis of D^* fragmentation functions*, *Phys. Rev.* **D96** (2017) 034028, [1706.09857].

[290] Z.-B. Kang, J.-W. Qiu, F. Ringer, H. Xing and H. Zhang, *J/ψ production and polarization within a jet*, *Phys. Rev. Lett.* **119** (2017) 032001, [1702.03287].

[291] R. Bain, L. Dai, A. Leibovich, Y. Makris and T. Mehen, *NRQCD Confronts LHCb Data on Quarkonium Production within Jets*, *Phys. Rev. Lett.* **119** (2017) 032002, [1702.05525].

[292] CMS collaboration, S. Chatrchyan et al., *Measurement of jet fragmentation into charged particles in pp and PbPb collisions at $\sqrt{s_{NN}} = 2.76$ TeV*, *JHEP* **10** (2012) 087, [1205.5872].

[293] ATLAS collaboration, M. Aaboud et al., *Comparison of fragmentation functions for light-quark- and gluon-dominated jets from pp and Pb+Pb collisions in ATLAS*, *Submitted to: Phys. Rev. Lett.* (2019) , [1902.10007].

[294] J. C. Collins, *Fragmentation of transversely polarized quarks probed in transverse momentum distributions*, *Nucl. Phys. B* **396** (1993) 161–182, [hep-ph/9208213].

[295] F. Yuan, *Azimuthal asymmetric distribution of hadrons inside a jet at hadron collider*, *Phys.Rev.Lett.* **100** (2008) 032003, [0709.3272].

[296] Z.-B. Kang, F. Ringer and I. Vitev, *Jet substructure using semi-inclusive jet functions in SCET*, *JHEP* **11** (2016) 155, [1606.07063].

[297] T. Becher, C. Lorentzen and M. D. Schwartz, *Resummation for W and Z production at large pT*, *Phys. Rev. Lett.* **108** (2012) 012001, [1106.4310].

[298] T. Becher, M. Neubert and B. D. Pecjak, *Factorization and Momentum-Space Resummation in Deep-Inelastic Scattering*, *JHEP* **01** (2007) 076, [hep-ph/0607228].

[299] T. Becher and M. D. Schwartz, *Direct photon production with effective field theory*, *JHEP* **02** (2010) 040, [0911.0681].

[300] A. Jain, M. Procura and W. J. Waalewijn, *Parton Fragmentation within an Identified Jet at NNLL*, *JHEP* **05** (2011) 035, [1101.4953].

[301] M. G. Echevarria, A. Idilbi, A. Schäfer and I. Scimemi, *Model-Independent Evolution of Transverse Momentum Dependent Distribution Functions (TMDs) at NNLL*, *Eur. Phys. J.* **C73** (2013) 2636, [1208.1281].

[302] S. Moch, J. A. M. Vermaseren and A. Vogt, *The Three loop splitting functions in QCD: The Nonsinglet case*, *Nucl. Phys.* **B688** (2004) 101–134, [hep-ph/0403192].

[303] R. Bain, Y. Makris and T. Mehen, *Transverse Momentum Dependent Fragmenting Jet Functions with Applications to Quarkonium Production*, *JHEP* **11** (2016) 144, [1610.06508].

[304] Z.-B. Kang, F. Ringer and W. J. Waalewijn, *The Energy Distribution of Subjets and the Jet Shape*, *JHEP* **07** (2017) 064, [1705.05375].

[305] P. Cal, F. Ringer and W. J. Waalewijn, *The jet shape at NLL*, *JHEP* **05** (2019) 143, [1901.06389].

[306] J. C. Collins, D. E. Soper and G. F. Sterman, *Transverse Momentum Distribution in Drell-Yan Pair and W and Z Boson Production*, *Nucl. Phys.* **B250** (1985) 199–224.

[307] D. de Florian, R. Sassot and M. Stratmann, *Global analysis of fragmentation functions for pions and kaons and their uncertainties*, *Phys. Rev.* **D75** (2007) 114010, [hep-ph/0703242].

[308] NNPDF collaboration, V. Bertone, N. P. Hartland, E. R. Nocera, J. Rojo and L. Rottoli, *Charged hadron fragmentation functions from collider data*, *Eur. Phys. J.* **C78** (2018) 651, [1807.03310].

[309] D. P. Anderle, T. Kaufmann, M. Stratmann and F. Ringer, *Fragmentation Functions Beyond Fixed Order Accuracy*, *Phys. Rev.* **D95** (2017) 054003, [1611.03371].

[310] L. Dai, C. Kim and A. K. Leibovich, *Fragmentation to a jet in the large z limit*, *Phys. Rev.* **D95** (2017) 074003, [1701.05660].

[311] A. Metz and A. Vossen, *Parton Fragmentation Functions*, *Prog. Part. Nucl. Phys.* **91** (2016) 136–202, [1607.02521].

[312] M. Anselmino, A. Mukherjee and A. Vossen, *Transverse spin effects in hard semi-inclusive collisions*, 2001.05415.

[313] R. Abdul Khalek et al., *Science Requirements and Detector Concepts for the Electron-Ion Collider: EIC Yellow Report*, 2103.05419.

[314] D. P. Anderle et al., *Electron-ion collider in China*, *Front. Phys. (Beijing)* **16** (2021) 64701, [2102.09222].

[315] K.-b. Chen, Z.-t. Liang, Y.-k. Song and S.-y. Wei, *Longitudinal and transverse polarizations of Λ hyperon in unpolarized SIDIS and e+e- annihilation*, *Phys. Rev. D* **105** (2022) 034027, [2108.07740].

[316] Belle collaboration, Y. Guan et al., *Observation of Transverse $\Lambda/\bar{\Lambda}$ Hyperon Polarization in e^+e^- Annihilation at Belle*, *Phys. Rev. Lett.* **122** (2019) 042001, [1808.05000].

[317] A. Jain, M. Procura and W. J. Waalewijn, *Fully-Unintegrated Parton Distribution and Fragmentation Functions at Perturbative k_T*, *JHEP* **04** (2012) 132, [1110.0839].

[318] M. Anselmino, R. Kishore and A. Mukherjee, *The Polarising Fragmentation Function and the Lambda polarisation in e+ e- processes*, *Phys. Rev.* **D100** (2019) 014029, [1905.02777].

[319] U. D'Alesio, F. Murgia and M. Zaccheddu, *First extraction of the Λ polarising fragmentation function from Belle e^+e^- data*, 2003.01128.

[320] K.-b. Chen, Z.-t. Liang, Y.-l. Pan, Y.-k. Song and S.-y. Wei, *Isospin Symmetry of Fragmentation Functions*, 2102.00658.

[321] Z.-B. Kang and J.-W. Qiu, *Testing the Time-Reversal Modified Universality of the Sivers Function*, *Phys. Rev. Lett.* **103** (2009) 172001, [0903.3629].

[322] A. Metz, *Gluon-exchange in spin-dependent fragmentation*, *Phys. Lett.* **B549** (2002) 139–145, [hep-ph/0209054].

[323] J. C. Collins and A. Metz, *Universality of soft and collinear factors in hard-scattering factorization*, *Phys. Rev. Lett.* **93** (2004) 252001, [hep-ph/0408249].

[324] S. Meissner and A. Metz, *Partonic pole matrix elements for fragmentation*, *Phys. Rev. Lett.* **102** (2009) 172003, [0812.3783].

[325] D. Boer, Z.-B. Kang, W. Vogelsang and F. Yuan, *Test of the Universality of Naive-time-reversal-odd Fragmentation Functions*, *Phys. Rev. Lett.* **105** (2010) 202001, [1008.3543].

[326] STAR collaboration, J. Adam et al., *Transverse spin transfer to Λ and $\bar{\Lambda}$ hyperons in polarized proton-proton collisions at $\sqrt{s} = 200$ GeV*, *Phys. Rev. D* **98** (2018) 091103, [1808.08000].

[327] D. de Florian, J. Soffer, M. Stratmann and W. Vogelsang, *Bounds on transverse spin asymmetries for Lambda baryon production in p p collisions at BNL RHIC*, *Phys. Lett. B* **439** (1998) 176–182, [hep-ph/9806513].

[328] Z.-B. Kang, K. Lee, J. Terry and H. Xing, *Jet fragmentation functions for Z-tagged jets*, *Phys. Lett. B* **798** (2019) 134978, [1906.07187].

[329] D. Boer, R. Jakob and P. J. Mulders, *Asymmetries in polarized hadron production in e+ e- annihilation up to order 1/Q*, *Nucl. Phys.* **B504** (1997) 345–380, [hep-ph/9702281].

[330] M. Anselmino, M. Boglione, J. O. Gonzalez Hernandez, S. Melis and A. Prokudin, *Unpolarised Transverse Momentum Dependent Distribution and Fragmentation Functions from recent HERMES and COMPASS SIDIS Multiplicities*, *PoS* **DIS2014** (2014) 201.

[331] M. Anselmino, M. Boglione, U. D'Alesio, S. Melis, F. Murgia and A. Prokudin, *Simultaneous extraction of transversity and Collins functions from new SIDIS and e+e- data*, *Phys. Rev.* **D87** (2013) 094019, [1303.3822].

[332] A. Bacchetta, M. Boglione, A. Henneman and P. J. Mulders, *Bounds on transverse momentum dependent distribution and fragmentation functions*, *Phys. Rev. Lett.* **85** (2000) 712–715, [hep-ph/9912490].

[333] S. Albino, B. A. Kniehl and G. Kramer, *AKK Update: Improvements from New Theoretical Input and Experimental Data*, *Nucl. Phys.* **B803** (2008) 42–104, [0803.2768].

[334] D. P. Anderle, F. Ringer and W. Vogelsang, *QCD resummation for semi-inclusive hadron production processes*, *Phys. Rev.* **D87** (2013) 034014, [1212.2099].

[335] A. De Rujula, H. Georgi and H. D. Politzer, *Demythification of Electroproduction, Local Duality and Precocious Scaling*, *Annals Phys.* **103** (1977) 315.

[336] A. Accardi and W. Melnitchouk, *Target mass corrections for spin-dependent structure functions in collinear factorization*, *Phys. Lett.* **B670** (2008) 114–118, [0808.2397].

[337] J. V. Guerrero, J. J. Ethier, A. Accardi, S. W. Casper and W. Melnitchouk, *Hadron mass corrections in semi-inclusive deep-inelastic scattering*, *JHEP* **09** (2015) 169, [1505.02739].

[338] J. Zhou, F. Yuan and Z.-T. Liang, *Hyperon Polarization in Unpolarized Scattering Processes*, *Phys. Rev.* **D78** (2008) 114008, [0808.3629].

[339] T. Kaufmann, A. Mukherjee and W. Vogelsang, *Hadron Fragmentation Inside Jets in Hadronic Collisions*, *Phys. Rev. D* **92** (2015) 054015, [1506.01415].

[340] M. Procura and I. W. Stewart, *Quark Fragmentation within an Identified Jet*, *Phys. Rev. D* **81** (2010) 074009, [0911.4980].

[341] L. Gamberg, Z.-B. Kang, D. Y. Shao, J. Terry and F. Zhao, *Transverse Λ polarization in e+e- collisions*, *Phys. Lett. B* **818** (2021) 136371, [2102.05553].

[342] R. A. Khalek et al., *Science requirements and detector concepts for the electron-ion collider: Eic yellow report*, 2103.05419.

[343] M. R. Whalley, D. Bourilkov and R. C. Group, *The Les Houches accord PDFs (LHAPDF) and LHAGLUE*, in *HERA and the LHC: A Workshop on the Implications of HERA and LHC Physics (Startup Meeting, CERN, 26-27 March 2004; Midterm Meeting, CERN, 11-13 October 2004)*, 8, 2005, hep-ph/0508110.

[344] J. Arrington et al., *EIC Physics from An All-Silicon Tracking Detector*, 2102.08337.

[345] F. James and M. Roos, *Minuit – A System for Function Minimization and Analysis of the Parameter Errors and Correlations*, *Computer Physics Communications* **10** (Dec., 1975) 343–367.

[346] NNPDF collaboration, R. D. Ball, L. Del Debbio, S. Forte, A. Guffanti, J. I. Latorre, A. Piccione et al., *A Determination of parton distributions with faithful uncertainty estimation*, *Nucl. Phys. B* **809** (2009) 1–63, [0808.1231].

[347] A. Signori, A. Bacchetta, M. Radici and G. Schnell, *Investigations into the flavor dependence of partonic transverse momentum*, *JHEP* **11** (2013) 194, [1309.3507].

[348] D. de Florian, R. Sassot, M. Stratmann and W. Vogelsang, *Extraction of Spin-Dependent Parton Densities and Their Uncertainties*, *Phys. Rev. D* **80** (2009) 034030, [0904.3821].

[349] M. Stratmann and W. Vogelsang, *Next-to-leading order QCD evolution of transversity fragmentation functions*, *Phys. Rev. D* **65** (2002) 057502, [hep-ph/0108241].

[350] H. Dembinski and P. O. et al., *scikit-hep/iminuit*, .

[351] A. Banfi and M. Dasgupta, *Dijet rates with symmetric E(t) cuts*, *JHEP* **01** (2004) 027, [hep-ph/0312108].

[352] C. Duhr, B. Mistlberger and G. Vita, *The Four-Loop Rapidity Anomalous Dimension and Event Shapes to Fourth Logarithmic Order*, 2205.02242.

[353] I. Moult, H. X. Zhu and Y. J. Zhu, *The Four Loop QCD Rapidity Anomalous Dimension*, 2205.02249.

[354] T. Neumann and J. Campbell, *Fiducial Drell-Yan production at the LHC improved by transverse-momentum resummation at N^4LL+N^3LO*, 2207.07056.

[355] P. Mulders and R. Tangerman, *The Complete tree level result up to order 1/Q for polarized deep inelastic leptoproduction*, *Nucl. Phys. B* **461** (1996) 197–237, [hep-ph/9510301].

[356] Z. Lu and I. Schmidt, *Transverse momentum dependent twist-three result for polarized Drell-Yan processes*, *Phys. Rev. D* **84** (2011) 114004, [1109.3232].

[357] M. A. Ebert, A. Gao and I. W. Stewart, *Factorization for azimuthal asymmetries in SIDIS at next-to-leading power*, *JHEP* **06** (2022) 007, [2112.07680].

[358] S. Rodini and A. Vladimirov, *Definition and evolution of transverse momentum dependent distribution of twist-three*, *JHEP* **08** (2022) 031, [2204.03856].

[359] A. Bacchetta, D. Boer, M. Diehl and P. J. Mulders, *Matches and mismatches in the descriptions of semi- inclusive processes at low and high transverse momentum*, *JHEP* **08** (2008) 023, [0803.0227].

[360] R. N. Cahn, *Azimuthal dependence in leptoproduction: A simple parton model calculation*, *Phys. Lett.* **B78** (1978) 269.

[361] R. N. Cahn, *Critique of Parton Model Calculations of Azimuthal Dependence in Leptoproduction*, *Phys. Rev. D* **40** (1989) 3107–3110.

[362] A. Bacchetta, G. Bozzi, M. G. Echevarria, C. Pisano, A. Prokudin and M. Radici, *Azimuthal asymmetries in unpolarized SIDIS and Drell-Yan processes: a case study towards TMD factorization at subleading twist*, *Phys. Lett. B* **797** (2019) 134850, [1906.07037].

[363] M. A. Ebert, S. T. Schindler, I. W. Stewart and Y. Zhao, *One-loop Matching for Spin-Dependent Quasi-TMDs*, *JHEP* **09** (2020) 099, [2004.14831].

[364] A. P. Chen and J. P. Ma, *Light-Cone Singularities and Transverse-Momentum-Dependent Factorization at Twist-3*, *Phys. Lett. B* **768** (2017) 380–386, [1610.08634].